UNIVERSITE BLAISE PASCAL

U.F.R. Sciences et Technologies

ECOLE DOCTORALE DES SCIENCES FONDAMENTALES N° XXX

THESE

présentée pour obtenir le grade de

DOCTEUR D'UNIVERSITE

Spécialité: Météorologie

Par **Matthieu MASBOU**

D.E.A. Climat et Physico-Chimie de l'atmosphère

LM-PAFOG - a new three-dimensional fog forecast model with parametrised microphysics

Soutenue publiquement le XX Juillet 2008, devant la commission d'examen:

Rapporteur:	Mme Evelyne RICHARD
Rapporteur:	M. Thomas TRAUTMANN
Examinateur:	M. Klass S. de BOER
Examinateur:	M. Steve MILLER
Directeur de thèse:	Mme Andréa FLOSSMANN
Co-directeur de thèse:	M. Andreas BOTT

"Quand deux chemins s'ouvrent à toi, choisis toujours le plus difficile."

Himalaya, l'enfance d'un chef.

Acknowledgements

Contents

Chapter 1

Introduction

1.1 Motivation

Weather can be described in a myriad of dimensions, some of which have a direct effect on humans or on items connected to human well-being. Modern societies have invested in systems to provide information on future weather events. Provision of this information requires expenditure of resources. Societies also wish to understand and assess the real benefits of such forecasts, both as a guide in deciding the most efficient mix of weather products to provide the most useful temporal and spatial dimensions of such forecasts.

Many economical sectors use weather forecasts on a daily or seasonal basis to make decisions. The energy sector uses weather forecasts to estimate fluctuation demands for energy. The household sector uses weather forecasts to make decisions such as what to wear, when and where to go on vacation. The agricultural sector uses precipitation, temperature and frost forecasts to determine when to plant and when to irrigate. The aviation, trucking and shipping sector use weather forecasts to make routing decisions.

Among other weather situations, fog has a significant impact on economical and safety aspects. Numerous traffic management authorities depend strongly on accurate forecasts of fog and visibility (*Andre* et al., 2004; *Pagowski* et al., 2004). A study of the French Observatory for Road Safety points out the aggravating role of fog in case of accidents: accidents occurring in foggy conditions double the material damages and furthermore, in case of accidents involving persons, fog constitutes the most aggravating factor with 12 deaths per 100 accidents (*Chapelon and Loones*, 2001).

Different economic agents request the development of better fog predictions. Studies based on cost/benefit analysis underline the economical value of forecasts on low visibility events (*Leigh*, 1995; *Allan* et al., 2001). The National Oceanic and Atmospheric Administration (NOAA) estimated that improvements of a few hours in forecast for short-term ice formation and fog conditions could save $29 millions per year by rerouting trucks in the transport industry in the United States (*NOAA*, 2002).

Otherwise, fog does not only appear as an economical issue. In regions with scarce water ressources the development of fog collectors could use fog as a sustainable water source (*Schemenauer and Cereceda*, 1994).

In terms of traffic safety and economy, human well-being depends on reliable forecasts

of fog occurrence. Temporal evolution, spatial extension and physical properties of fog are the requested information to supply of a forecast. Such a forecast should respect: high spatial resolution, high temporal resolution and fine parametrisation. However, fog forecast quality is still limited because most of todays forecast systems do not meet all these standards.

Necessary improvements have been widely identified. Cooperation and initiatives in the action 722 of the European Science Foundation (ESF) CO-operation in the field of Scientific and Technical Research (COST) programme ensured numerous developments concerning short range forecasting of fog, visibility and low clouds (*Jacobs* et al., 2005).

A reliable and accurate fog forecast model constitutes an essential support when solving many scientific and socio-economic problems.

1.2   What is fog ?

The presence of fog is defined by a visibility reduction below one kilometer. This mostly happens by suspension of very small, usually microscopic water droplets in the air, reducing the horizontal visibility at the Earth's surface (*WMO*, 1992). The fog water droplets are considered as having a diameter between 5 and 50 μm (*Pruppacher and Klett*, 1997), and settle at velocities of no more than 5 cm s^{-1} (*WMO*, 1996). Generally, most fog events have a Liquid Water Content (LWC) ranging between 0.01 and 0.3 gm^{-3}. More generally, fog formation is considered when water vapour condensates or sublimates on aerosol particles at low altitude.

Fog can be classified into six types depending on its dominating formation process. The processes responsible for the fog formation can be radiative cooling of the ground and the adjacent air masses (radiation fog), cooling of the air parcel below the dew point temperature induced by the advection of air masses over cold surfaces (advection fog), a forced adiabatic cooling of air mass due to topographical obstacles (upslope fog), and atmospheric mixing processes (sea fog, frontal fog and turbulence fog).

Several observation studies of fog have already been done reaching back about 100 years (e.g. *Köppen*, 1916, 1917; *Taylor*, 1917; *Georgii*, 1920; *Willett*, 1928; *Roach* et al., 1976; *Fitzjarrald and Lala*, 1989; *Leipper*, 1994; *Kloesel*, 1992). These studies emphasised the importance of a multitude of meteorological parameters affecting fog formation and development, including the primary role of radiation, microphysics, turbulence and moisture transport over heterogeneous terrain. Formation and dissipation of fog is controlled by continuous interactions between thermodynamic and dynamical factors (*Duynkerke*, 1991; *Roach*, 1994, 1995). Furthermore, fog development is affected by the interaction between the land or sea surface and the lower layers of the atmosphere. Local parameters such as topography, vegetation, soil characteristics and very shallow flows near the surface induce small changes that influence fog generation. The large dependence of fog formation on these surface parameters can induce very local formation of fog patches.

1.3   State of numerical fog modelling

The need of a reliable fog forecast and the particularity of fog has led to the development of different forecasting and nowcasting methods based on observations, numerical forecast models and statistic approaches.

Numerical modelling of fog already has a long tradition. The various existing fog models differ in their complexity describing the relevant thermodynamic and microphysical processes occurring during a fog event. The physical parametrisations of these models focus on partial aspects inducing the formation of fog. *Fisher and Caplan* (1963) developed one of the first fog models simulating fog evolution. However, they neglected the radiative cooling of the atmosphere. *Musson-Genon* (1987) and *Turton and Brown* (1987) concentrated their efforts on a new formulation of the turbulent transport in the calm nocturnal boundary layer. In others approaches, fog microphysics is considered by parametrisation techniques thus only bulk fog water content can be obtained (*Zdunkowski and Nielsen*, 1969; *Zdunkowski and Barr*, 1972; *Lala* et al., 1975; *Brown and Roach*, 1976; *Bergot and Guedalia*, 1994; *Texeira*, 1999; *Koracin* et al., 2001). The bulk microphysics approach is a severe limitation to accurately describe the gravitational settling of fog droplets. Explicit detailed microphysics considering the time evolution of the spectral size distribution of fog droplets was introduced by *Brown* (1980) and further refined in a new approach by *Bott* et al. (1990). Comprehensive description of the interaction between fog and vegetation were developed (*Siebert* et al., 1992a,b; *von Glasow and Bott*, 1999). Most of these models have been developed to improve the understanding of local processes in the fog formation. The high grid resolution and the complex parametrisation need significant computation-time efforts. These models favour the modelling of thermodynamics and microphysics at the expense of dynamical factors causing almost all fog models to be one-dimensional. The limitation to a column allows to compute complex parametrisation induced in the fog formation processes very quickly. The interaction soil-atmosphere as well as the description of the boundary layer is then well considered. However, a one-dimensional forecast approach assumes horizontal homogeneity of all thermodynamic variables and demonstrates large difficulties to consider dynamical influences induced by their surrounding environment.

Guedalia and Bergot (1994) added in their one-dimensional fog model a forcing advection term to better reflect its importance in the timing of the fog evolution. Recently, the coupling of a one-dimensional fog model with a three-dimensional mesoscale model illustrates the actual solution to combine the single-column with the surrounding heterogeneity (*Duynkerke*, 1999; *Texeira and Miranda*, 2001; *Clark and Hopwood*, 2001; *Olsson* et al., 2007). The atmospheric conditions corresponding to the formation of radiative fog (stable boundary layer, weak advection forcing) can be successfully forecasted in an one-dimensional approach. Nevertheless, single column models are not adapted to treat complex three-dimensional flows. Advection of humid air parcels, cold pools in complex orography and the increase or decrease of the overlying cloud cover are essential factors which cannot be considered in such single-column approaches. Advection fog or orographic fog forecasts cannot be considered by such an approach.

Currently, only mesoscale models consider three-dimensional flows. *Ballard* et al. (1991) and *Golding* (1993) used a three-dimensional mesoscale model with parametrised

cloud microphysics to forecast fog. However, fog forecasts using mesoscale models are only possible in a limited way. Such a model can give only coarse information about the formation and dissipation of fog on the scale of a few tens of kilometers. The coarse vertical grid (lowest atmospheric layer typically more than 60 m thick) cannot consider the processes involved in fog formation with the necessary accuracy. The details in various parametrisations are significantly limited by the computing time in the three-dimensional forecast approach. Since mesoscale models are designed for the simulation of processes covering large areas, they do not fullfill all the requirements of fog forecasts in a sufficient way. Local characteristics as well as detailed thermodynamics and microphysics are neglected on behalf of three-dimensional dynamics consideration.

Certain approaches improve the coarse three-dimensional forecast by implementing additional downscaling which considers the local factor in the fog formation. A few models such as the Unified Model (*Cullen*, 1993) and the HIRLAM (*Petersen and Nielsen*, 2000), deliver a direct information on fog presence. The coupling of surface measurements with the mesoscale output can allow effective parametrisation of visibility. However, due to inadequate mesoscale grid resolution, their fog forecasts can only consider cases of widespread fog. In Austria, *Seidl and Kann* (2002) have developed a post-processing scheme based on the experience of forecasters. They improve the model forecast for the low visibility situation in spite of the large vertical grid. These post-processing approaches increase the reliability of the fog forecast, but the final forecast accuracy is still severely limited by the original horizontal grid resolution. Post-processing is activated only if the coarse mesoscale forecast adequately detects the favourable weather situation.

Local measurements associated with statistic schemes commonly provide an interpretation guide for fog forecasts. Statistical methods are based on neural networks (*Pasini* et al., 2001; *Costa* et al., 2006; *Bremnes and Michaelides*, 2007), decision trees (*Wantuch*, 2001) and regression (*Vislocky and Fritsch*, 1995; *Hilliker and Fritsch*, 1999). The statistical systems require information on the atmospheric profile, which is almost always extracted from a three-dimensional operational forecast model. The forecast variable depends on just this profile or both the profile and the latest surface observations. Apart from the input data from each forecast, historical data play a major role when establishing a statistical relationship. It is essential that the historical data and forecast properties of the operational model maintain a constant quality once the statistical relationship is defined. Due to the continuous improvement of the forecast models as well as the different measurement devices, this requirement remains difficult to fulfil. Statistic models will work well only if the type of event is well represented in the training data. Most systems appear to have used about three years of historical data. Dense fog events which form rarely in most locations are not sampled adequately in the learning phase which is too brief. The Austrian weather service has developed a Model Output Statistics (MOS) system based on ten years of historical data (*Golding*, 2002). Both statistical regression and neural networks need such a long historical data set. Moreover, multi-step processes, such as the Perfect-prog method (*Klein* et al., 1959) as well as the expert system, score table or decision tree approaches always demand a large historical data base, since each step in the process must be calibrated. Most statistical models are site-specific, implying that models developed for one location do not necessarily apply to another. A radical reconstruction of the model may be needed (*Mouskos*, 2007).

In spite of local fog forecasts, such restrictions inherent to statistical methods constitute a significant flexibility deficit in case of further model developments. Moreover, this cascade of statistical treatments disconnects the resulting forecasts from physical fog characteristics.

Physically modelling fog forecasts is a complex exercise. No actual fog forecast model is able to consider simultaneously all the requested factors for complete physical modelling. Interactions between thermodynamic, microphysical and dynamic processes have to be considered simultaneously. The proximity with the ground necessitates the consideration of high resolution local factors. Furthermore, The computing power limitation has usually led to neglect parts of the physical or dynamical processes. It appears that the numerical modelling quality and a reliable fog prediction depend on which fog type has to be forecasted. The complexity of various fog formation processes and the consequent inadequacy of simple forecast solutions motivate the engagement into the task of creating a fully physical fog forecast system.

1.4   Aim and outline

In this thesis, a new fog forecast model is developed to combine in one numerical approach all the physical processes to supply a complete fog forecast solution reproducing the miscellaneous fog properties. A new microphysical parametrisation, based on the one-dimensional fog forecast model, PAFOG (*Bott and Trautmann*, 2002), was implemented in the "Lokal Modell" (LM) (*Steppeler* et al., 2003), a nonhydrostatic operational mesoscale model of the German Meteorological Service. The flexibility of the LM's three-dimensional dynamical core allows numerical simulations in a high resolution grid. The detailed microphysics, PAFOG, offers an accurate computation of condensation/evaporation as well as sedimentation of cloud water which is a decisive factor in the evolution of a fog episode. The three-dimensional framework can resolve the accumulation of cold air and definitely solves the problem of advection forcing. LM-PAFOG is thus a new fog forecast method for simulating different kinds of fog, such as radiation fog, advection fog as well as orographic fog.

After an overview of the basic LM model frame, the low atmosphere parametrisation and cloud microphysics are detailed in Chapter 2. The requirements for the transformation of the LM into a fog forecast model and further implementations concerning the high grid resolution, the new PAFOG microphysics and visibility parametrisation are presented in detail in Chapter 3. A first assessment of the fog forecast model is made and the influence of the new microphysics scheme on fog formation is examined. In Chapter 4, the new forecast model performance is throughly analysed with validation studies and case studies.

A large part of the validation work was done in the framework of the COST 722 project. COST Action 722 is a consortium of scientists from fifteen countries. This cooperation gathers numerous fog forecast models among those: a MOS, a mesoscale model with physical parametrisation of visibility, a three-dimensional operational weather prediction model with post-processing methods and a three-dimensional model with high resolution and detailed microphysics. In Chapter 5, our new fog forecast model is directly confronted

with the performance of the other fog forecast methods in a common statistical evaluation and case studies on the area of Lindenberg (Germany). The potential and the limitations of different models are investigated.

The three-dimensional modelling approach used in our fog forecast model illustrates the limits of the actual measurements necessary for the model assessment. A new verification approach for the spatial extension of fog using satellite products for fog has been developed and tested on our new three-dimensional fog forecast model, LM-PAFOG. The results are presented in Chapter 6.

Finally, Chapter 7 presents the conclusions and outlook of this work.

Chapter 2

The "Lokal Modell"

Since December 1999, the Lokal Modell (LM) (*Steppeler* et al., 2003), is a part of the current numerical weather forecast system used by the German Meteorological Service (Deutscher Wetterdienst, DWD). In the last years, the LM has been continuously improved and was subjected to many modifications. Today, an international LM user group of six national meteorological services (Germany, Switzerland, Greece, Poland, Italy and Romania) coordinates the futher developments of the LM in the COnsortium for Small Scale MOdelling (COSMO). This chapter focuses on the LM version 3.19 used in this work. Further information about the next development can be found at http://www.cosmo-model.org.

2.1 Overview

2.1.1 Model grid

The LM is a nonhydrostatic limited-area numerical weather prediction model, designed to cover all horizontal resolutions from 50km to 50m. In its operational form, the LM uses a horizontal resolution of 7km. Since September 2005, its forecast area has been extended in order to cover all of Europe, yielding the Lokal Modell Europa (LME). The new vertical resolution is composed of 40 layers, the height of the lowest layer is 20 meters. The LM grid structure has been adapted to spherical coordinates so that the model domain is almost uniform and avoids regions with strong convergence of the meridians. The poles of the LM domain are defined so that the equator is located within the center of the model domain. Concerning the vertical grid structure, the LM uses generalised terrain-following coordinates with the highest vertical resolution close to the surface.
The discretisation of the prognostic variables is stored on an Arakawa-C-grid (*Arakawa*, 1966): thermodynamic quantities (pressure, specific humidity and temperature) are defined at the centre of a grid box whereas the dynamic variables (wind field, diffusion coefficients and turbulent kinetic energy) are located at the boundaries of the grid boxes.

2.1.2 Set of model equations

The LM is based on non-hydrostatic, fully compressible hydro-thermodynamical equations in a moist atmosphere without any scale approximation. The atmosphere is described

as an ideal mixture of dry air, water vapour, liquid water and water in solid state. The liquid and solid forms of water may be further subdivided into nonprecipitating categories of water such as cloud water and cloud ice with negligible sedimentation fluxes, and precipitating categories of water such as rain, snow and graupel with large sedimentation fluxes. The evolution of the nonhydrostatic compressible mean flow is based on the model equations detailed hereafter (*Doms and Schättler*, 2002). A complete description of the different variables is summarised in Appendix C.

$$\rho\frac{d\mathbf{v}}{dt} = -\nabla p + \rho\mathbf{g} - 2\mathbf{\Omega}\times(\rho\mathbf{v}) - \nabla\cdot(\underline{\mathbf{T}}) \tag{2.1}$$

$$\frac{dp}{dt} = -\frac{c_{pd}}{c_{vd}}p\nabla\cdot\mathbf{v} + (\frac{c_{pd}}{c_{vd}} - 1)Q_h \tag{2.2}$$

$$\rho c_{pd}\frac{dT}{dt} = \frac{dp}{dt} + Q_h \tag{2.3}$$

$$\rho\frac{dq_v}{dt} = -\nabla\cdot\mathbf{F}^v - (I^l + I^f) \tag{2.4}$$

$$\rho\frac{dq_{l,f}}{dt} = -\nabla\cdot(\mathbf{P}^{l,f} + \mathbf{F}^{l,f}) + I^{l,f} \tag{2.5}$$

$$\rho = p\{R_d(1 + (\frac{R_v}{R_d} - 1)q_v - q_l - q_f)T\}^{-1} \tag{2.6}$$

$$\tag{2.7}$$

Q_h represents the rate of diabatic heating/cooling and is given by

$$Q_h = L_v I^l + L_s I^f - \nabla\cdot(\mathbf{H} + \mathbf{R}) \tag{2.8}$$

In these chosen approach, the continuity equation, usually one of the primitive equations, has been replaced by a prognostic equation for the pressure. To allow a useful application of the linearisation assumptions related to the anelastic approximation, an hydrostatic reference state of the atmosphere is defined following the method of *Dudhia* (1993). By introducing the base state, any grid-scale thermodynamic variable ψ can be formally written as:

$$\psi(\lambda, \varphi, z, t) = \psi_0(z) + \psi'(\lambda, \varphi, z, t) \tag{2.9}$$

The prognostic equation for the pressure is thus the same for the pressure perturbations. The set of equations supplies a complete description of the state variable, where $\mathbf{v}$ is the barycentric velocity, T is the temperature, p is the pressure, ρ is the air density, q_v, q_l and q_f are the mass fraction of water vapour, liquid water and ice. To determine the variables of state, many terms concerning the subgrid-scale processes have to be known. These are the Reynolds stress tensor $\underline{\mathbf{T}}$, the turbulent flux of sensible heat $\mathbf{H}$, the turbulent fluxes of water vapour $\mathbf{F}^v$, liquid water $\mathbf{F}^l$ and ice $\mathbf{F}^f$. The knowledges of the precipitation fluxes of water and ice $\mathbf{P}^l$ and $\mathbf{P}^f$, the rates of phase changes of water and ice I^l and I^f, and the flux of solar and thermal electromagnetic radiation $\mathbf{R}$ are also required. The determination of these terms as functions of the model variables is done in adequate parametrisation schemes, as detailed in the following section.

2.1.3 Numerics

Based on this unfiltered equation system, the LM considers the processes of each scale, even the fast-moving sound waves. These acoustic fast waves, which are meteorologically unimportant, severely limit the time step of explicit time integration schemes. Very small time steps are necessary to fulfil numerical stability. In order to improve the numerical efficiency, the LM integration scheme uses the mode-splitting time integration method proposed by *Klemp and Wilhelmson* (1978). This technique separates the prognostic equations in terms of fast and slow modes. All terms which describe sound or gravity wave processes are integrated on a small time step. The other terms, which consider meteorological evolutions like advection and physical processes are calculated for longer time steps and stay constant during the integration of the small time step. By default, the numerical time integration scheme follows a Leapfrog scheme of second order accuracy. Alternatively, two other time integration schemes are implemented: a two time-level second order Runge-Kutta split explicit scheme (*Wicker and Skamarock*, 1998) and a three time-level semi-implicit scheme (*Thomas* et al., 2000). The LM numerical scheme also has to find a compromise for the ratio of horizontal grid spacing ($\sim$ 10 km) to vertical grid size ($\sim$ 100 m) and the numerical stability of the integration scheme needing a very small time step to consider the vertical sound propagating waves. In order to overcome this problem, horizontal advection of fast and slow modes are explicitly solved, whereas for stability reasons, vertical advection and vertical turbulent diffusion are treated implicitly by the Crank-Nicolson scheme (*Crank and Nicolson*, 1947).

2.1.4 Data assimilation

The data assimilation approach is based on a nudging method developed by *Schraff* (1997) and *Schraff and Hess* (2003). This technique corresponds to adjust the prognostic variables supplied by the model with the available observations.

$$\frac{\partial}{\partial t}\psi(x,t) = F_\psi(x,t) + G_\psi \cdot \sum_{k_{obs}}(W_k \cdot (\psi_k^{obs} - \psi(x_k,t))) \tag{2.10}$$

F_ψ denotes the physical parametrisations and model dynamics, ψ_k^{obs} is the kth observation influencing gridpoint x at time t, x_k is the position of the observation, G_ψ is a constant called nudging coefficient and W_k an observation-dependent weight, varying between 0 and 1. The timescale covering the relaxation process is controlled by the coefficient G_ψ. The deviation between the observed value and the model value reduces in about half an hour to $1/e$. In practical applications, the nudging term should remain smaller than the largest term of the dynamics or physics for not disturbing the equilibrium of the model. The variables being nudged are horizontal wind, temperature, and humidity at all levels, and pressure at the lowest model level. The analysis increments are adjusted hydrostatically to avoid uncontrolled sources in the vertical wind component. Concerning the soil water content, direct measurements are rarely available. A soil moisture analysis scheme has also been developed so that the 2-m temperature would correspond to the observed temperatures. This correction is done by minimising a cost function (*Hess*, 2001).

2.1.5   Initialisation and boundary conditions

The definition of the LM domain as a limited area requires lateral boundaries and their time evolution must be specified by an external data set. After the nudging operation, initial and hourly external boundary conditions are supplied by a coarse-grid model (GME[1], ECMWF[2], LM). In its operational form, the LM lateral boundary data are supplied by the operational hydrostatic model GME via a one-way interactive nesting using the relaxation scheme of *Davies* (1976). In a lateral boundary zone (about eight grid points wide), the prognostic values are gradually nudged in the model domain. This reduces the generation of numerical noise, which can propagate from the lateral boundaries inward to the center of the model domain. The top boundary condition is defined by a rigid lid and a Rayleigh damping layer in order to avoid a backscatter of waves at the upper boundary (*Doms and Schättler*, 2002).

2.1.6   Parametrisations

The subgrid scale processes such as turbulence, convection and radiation play a determinant role on the resolved scale. However, not all relevant physical atmospheric processes can be resolved by the model grid resolution. Physical parametrisations have to be included in order to consider the influence of sub-grid scale processes. The LM is based on a complete parametrisation set, considering all the relevant sub-grid scale processes.

The radiation scheme is based on a δ-two-stream version of the radiative transfer equation incorporating the effects of scattering, absorption and emission by cloud droplets, aerosols and gases in each part of the spectrum (*Ritter and Geleyn*, 1992). Sub-grid scale clouds are considered by an empirical function, depending on relative humidity, height and convective activity.

The cloud microphysics module uses a bulk microphysics parametrisation including water vapour, cloud water, ice, rain and snow. The precipitation can either be diagnosed or included in a three-dimensional prognostic precipitation transport scheme. Moist convection is parametrised by the mass flux convection scheme of *Tiedtke* (1989) with a closure based on moisture convergence.

Subgrid scale turbulence is parametrised with a diagnostic second order K-closure for the vertical fluxes. Optionally, a prognostic Turbulent Kinetic Energy (TKE) closure at level-2.5 closure developed by *Mellor and Yamada* (1982) can be used. The interaction between surface and atmosphere are parametrised with a stability-dependent drag-law formula of momentum, heat and moisture according to the Louis scheme (*Louis*, 1979).

This thesis focuses on the development of a fog forecast model based on the LM. The thermodynamic and dynamical processes taking place in the lowest atmosphere have a crucial impact on fog formation. Consequently, the actual parametrisation such as turbulence, heat and moisture transport at the surface and microphysics scheme are presented in more detail in the next two sections.

---

[1] The expression GME is a combination of its predecessors: GM, Global Model and EM. Europa Model

[2] European Centre for Medium-Range Weather Forecasting

2.2 Interaction soil/atmosphere

The boundary conditions at the surface play a decisive role because they correspond to source and sink term for the atmospheric heat and moisture. In the approach chosen in the LM, the coupling between atmosphere and the underlying surface is based on a stability and roughness-length dependent surface flux formulation which is based on a modified Businger relation (*Businger* et al., 1971). These surface fluxes constitute the lower boundary conditions for the atmospheric part of the model. In this drag-law formulation, the heat and moisture fluxes are defined in a linear relation.

The surface flux of sensible heat $\mathbf{F}^t$ is defined accordingly:

$$\mathbf{F}^t = -\rho K_h |v_h|(T_{atm} - T_{sfc}) \tag{2.11}$$

where ρ is the air density, K_h is the heat transfer coefficient, $|v_h|$ is the absolute wind speed in the lowest atmospheric layer, T_{atm} is the temperature of the lowest atmospheric layer and T_{sfc} is the temperature at the ground.

For the moisture flux, $\mathbf{F}^v_{sfc}$, at the surface, the parametrised relation is defined as:

$$\mathbf{F}^v_{sfc} = \rho K_h |v_h|(q^v_{atm} - q_{sfc}) \tag{2.12}$$

where q^v_{atm} is the specific humidity in the lowest atmospheric layer and q_{sfc} is a virtual specific humidity at the surface. The transfer coefficients are determined diagnostically as a function of the bulk Richardson number (see Section 2.3)

In this approach, the moisture flux is deduced by the balance involved by the evapotranspiration parametrisation while the temperature at the ground is obtained from a balance equation for the heat fluxes at the surface. The soil model TERRA provides the necessary thermal and hydrological processes in the soil, as well as the vegetation influence to complete the balance equation. Interception storage (e.g. lake, sea), snow and nine different soil types are considered. Depending on the season, the consideration of the soil surface diversity is completed with further parameters: roughness length, plant characteristics (plant cover, leaf area index, root depth). Each soil type is defined by different physical parameters, like pore volume and heat conductivity (*Doms* et al., 2005).

The interface soil/atmosphere is thus formulated by two coupled equations for the heat and moisture budget at the ground:

$$0 = F^t(T_{sfc}) + L_v(T_{sfc})F^v_{sfc}(\eta_g, T_{sfc}) + Q_{rad,net} + G_p + G_s + F_h(\eta_g, T_{sfc}) \tag{2.13}$$

$$(1 - f_i - f_s)(1 - f_{veg})E_b(T_{sfc}) + f_{veg}E_{trans}(T_{sfc}, \eta_g) + f_i E_i + f_s E_s = -F_v(q_{atm}) \tag{2.14}$$

In the heat budget equation (eq. 2.13), $Q_{rad,net}$ is the total radiation budget at the surface. F^t and F^v_{sfc} are the turbulent atmospheric fluxes of heat and water vapour at the ground (eq. 2.11 and 2.12). G_p and G_s account for the effects of freezing rain and melting snowfall, respectively, while F_h is the heat flux within the soil.

At the surface, rain and snow are partially captured by the interception store and the snow store. Both surface storages are continuously in interaction with the atmosphere

through evaporation and sublimation as well as dew and rime processes. The soil moisture storage is reduced by evaporation of bare soil and plant transpiration. The global evapotranspiration at the surface is detailed by the contributions of bare soil evaporation E_b, plant transpiration E_{trans}, evaporation of the interception store E_i and snow sublimation E_s depending on the fraction of surface covered by snow f_s, water f_i and plants f_{veg} .

Finally, T_{sfc} and η_g are respectively the temperature and the volumetric moisture content at the ground. These two parameters must still be determined in order to satisfy the heat and moisture budget (eq. 2.13 and 2.14) at the surface.

The heat soil flux F_h at the ground, necessary to complete the heat budget at the surface is assumed to be:

$$F_h(\eta_g, T_{sfc}) = \lambda \left. \frac{\partial T}{\partial z} \right|_{sfc} \tag{2.15}$$

where λ is the heat conductivity in the soil.

The vertical soil water flux F_η is described following the one-dimensional Darcy equation (see standard textbook, e.g. *Dingman*, 2002)

$$F_\eta = -\rho_w \left[-D(\eta) \frac{\partial \eta}{\partial z} + K(\eta) \right] \tag{2.16}$$

where $K(\eta)$ is the hydraulic conductivity and $D(\eta)$ is the hydraulic diffusivity. Both parameters depend on soil characteristics and on soil moisture according to *Rijtema* (1969):

$$D(\eta) = D_0 \exp\left[D_1 \frac{\eta_{PV} - \eta}{\eta_{PV} - \eta_{ADP}} \right] \tag{2.17}$$

$$K(\eta) = K_0 \exp\left[K_1 \frac{\eta_{PV} - \eta}{\eta_{PV} - \eta_{ADP}} \right] \tag{2.18}$$

The four constants K_0, K_1, D_0, D_1, as well as the pore volume η_{PV} and the soil moisture at air dryness point η_{ADP} depend on the soil type (*Doms* et al., 2005).

To solve the heat and moisture budget at the surface, the vertical profile of temperature T_{so} and moisture η in the soil have to be determined. The soil model TERRA can either solve the heat conduction equation and soil water transport in its two soil layers version through the extended force restore method (*Jacobsen and Heise*, 1982) or in its new operational multilayer version (*Schrodin and Heise*, 2001) by a direct numerical solution of the following equations.

$$\frac{\partial T_{so}}{\partial t} = \frac{1}{\rho c} \frac{\partial}{\partial z} \left(\lambda \frac{\partial T_{so}}{\partial z} \right) \tag{2.19}$$

$$\frac{\partial \eta}{\partial t} = \frac{\partial}{\partial z} \left(D(\eta) \frac{\partial \eta}{\partial z} + K(\eta) \right) \tag{2.20}$$

The volumetric heat capacity ρc is determined by taking the values for dry soil, water and ice into account. The parametrisation of the heat conductivity λ considers only the liquid water content of the soil. The soil moisture and soil temperature are thus prognostically determined. At each time step, T_g and η_g can be determined and the heat and moisture budget at the surface can be satisfied.

2.3 The Planetary Boundary Layer parametrisation

The Planetary Boundary Layer (PBL) is the lowest part of the atmosphere where the influence of the surface is present because of turbulent exchange of momentum, heat and moisture. Concerning these exchanges, the turbulent mixing is considered, based on a modified Louis scheme (*Louis*, 1979). The Monin-Obukhov similarity theory can be used to derive the bulk transfer coefficients for heat K_h and for momentum K_m at the surface (*Monin and Obukhov*, 1954). But the Monin-Obukhov length, necessary to determine the flux-profile depends itself on the fluxes. To avoid a costly computation of an iteration method, *Louis* (1979) proposed an analytic procedure using the bulk Richardson number, Ri_B, as a stability parameter.

$$Ri_B = \frac{g}{\theta_{sfc}} \frac{(\theta_{atm} - \theta_{sfc})(h - z_0)}{|v_h|^2} \tag{2.21}$$

where θ_{sfc} and θ_{atm} are the potential temperature respectively at the surface and in the lowest model atmospheric layer, z_0 is the roughness length and h corresponds to the Prandtl layer thickness. The lowest model layer (about 60 m thick) is assumed to be located within the Prandtl layer

Using the bulk Richardson number, the stability evolution at the surface can be simply determined by known temperature and wind profiles. The transfer coefficients are thus defined as follows:

$$K_m = \left(\frac{\kappa}{\ln(h/z_0)} \right)^2 f_m(Ri_B, h/z_0) \tag{2.22}$$

$$K_h = \frac{\kappa^2}{\ln(h/z_0) \ln(h/z_h)} f_h(Ri_B, h/z_0, h/z_h) \tag{2.23}$$

where κ is the von-Karman constant, z_h is the roughness length for heat exchange and f_m and f_h are stability functions in the constant flux layer. f_m and f_h are chosen to include the limiting cases of free convection and of laminar flow in a highly stable surface layer.

The influence of the surface through exchange of heat and moisture is not limited to the lowermost atmospheric layer of the model. In the lowest part of the atmosphere, the moisture and heat are transported mostly by turbulent processes. In the LM, where the horizontal grid scale is large compared to the vertical grid resolution, the vertical turbulent transport is considered to be dominating so that the horizontal turbulences are neglected. Turbulence can be parametrised by the K profile-theory which relates the subgrid scale flux to the vertical atmospheric gradient. For the momentum transport, the vertical turbulent flux is given by:

$$\overline{w'u'} = -K_m^v \frac{\partial \overline{u}}{\partial z}, \quad \overline{w'v'} = -K_m^v \frac{\partial \overline{v}}{\partial z} \tag{2.24}$$

The turbulent heat and moisture transports are expressed similarly:

$$\overline{w'\theta'} = -K_h^v \frac{\partial \overline{\theta}}{\partial z}, \quad \overline{w'q_v'} = -K_h^v \frac{\partial \overline{q_v}}{\partial z} \tag{2.25}$$

where u and v are the horizontal wind components, θ is the potential temperature, q_v is the mass fraction of water vapour, and K_m^v and K_h^v are the turbulent diffusion coefficients for momentum and heat.

To calculate the turbulent fluxes, the Louis scheme (*Louis*, 1979) is used again. As stability parameter, the Richardson number Ri is defined by a ratio involving the squared Brunt-Väisälä frequency, N^2, corresponding to the buoyancy influence and the influence of vertical wind shear, M^2:

$$Ri = \frac{N^2}{M^2} = \frac{\frac{g}{\theta_v}\frac{\partial \theta_v}{\partial z}}{\left(\frac{\partial u}{\partial z}\right)^2 + \left(\frac{\partial v}{\partial z}\right)^2} \tag{2.26}$$

The turbulent diffusion coefficients K_m^v and K_h^v are determined as:

$$K_m^v = l^2 S_m^{3/2}(Ri)\sqrt{M^2 - \alpha_n S_h(Ri)N^2} \tag{2.27}$$

$$K_h = \alpha_n S_h(Ri)K_m^v \tag{2.28}$$

where $S_m(Ri)$ and $S_h(Ri)$ are the stability functions for momentum and heat transport depending on the Richardson number. The turbulent length scale is parametrised according to *Blackadar* (1962):

$$l = \frac{\kappa z}{1 + \kappa z/l_\infty} \tag{2.29}$$

where z is the altitude. The turbulent length varies at low altitude before reaching its asymptotic value l_∞, set to 500m.

Although the Louis scheme provides an analytical solution to compute the turbulent mixing, this approach has to be completed in case of very stable stratification. The stability functions diverge from the physical solution when the Richardson number exceeds a critical value. For the case $Ri > Ri_c$, the diffusion coefficients are corrected as follows:

$$K_m^v = k_{m0}l^2 M^2 \tag{2.30}$$

$$K_h^v = \alpha_n k_{h0}l^2 M^2 \tag{2.31}$$

where the different constants are defined as $Ri_c = 0.38$, $k_{m0} = 0.010$, $k_{h0} = 0.007$, $\alpha_n = 1$.

2.4 Cloud microphysics scheme

The LM cloud microphysics are computed using a bulk microphysics parametrisation based on the Kessler scheme (*Kessler*, 1969). In its operational form, the LM runs with a two-category ice scheme, including five categories of water: water vapour, cloud water, ice, rain and snow. Water vapour, cloud water, as well as cloud ice represent the cloud phase and have a negligible fall velocity. Snow is considered as an aggregate of ice crystals having a non-negligible fall velocity. Rain and snow represent the precipitable phase. In order to describe adequately mixed phase clouds the condensation/evaporation processes of cloud water and depositional growth of cloud ice at temperature below the freezing point are considered as two distinct processes of the bulk microphysics scheme. The time

scale of the Bergeron-Findeisen process which defines the initial growth of ice particles confirms this hypothesis. It is generally much smaller than the characteristic dynamic time scale of stratiform clouds (*Bergeron*, 1935).

In a bulk scheme as used in LM, assumptions are made concerning the shape and the size distribution of the particles and microphysical processes have to be parametrised in terms of specific vapour, water and ice concentration. The depositional growth of cloud ice requires assumptions on shape, size and number density of crystal. Cloud ice is assumed to consist only of small hexagonal plates. The density of cloud ice particles is defined as a function of the ambient temperature based on the Fletcher-formula (*Fletcher*, 1962) and adapted with aircraft measurements of pristine crystals in stratiform clouds (*Hobbs and Rangno*, 1985; *Meyers* et al., 1992). The non-precipitating categories are assumed to be monodisperse whereas the precipitation particles follow an exponential size distribution with respect to particle diameter. For raindrops, it is based on a Marschall-Palmer distribution (*Marschall and Palmer*, 1948), while for snow the Gunn-Marshall distribution (*Gunn and Marshall*, 1958) is assumed.
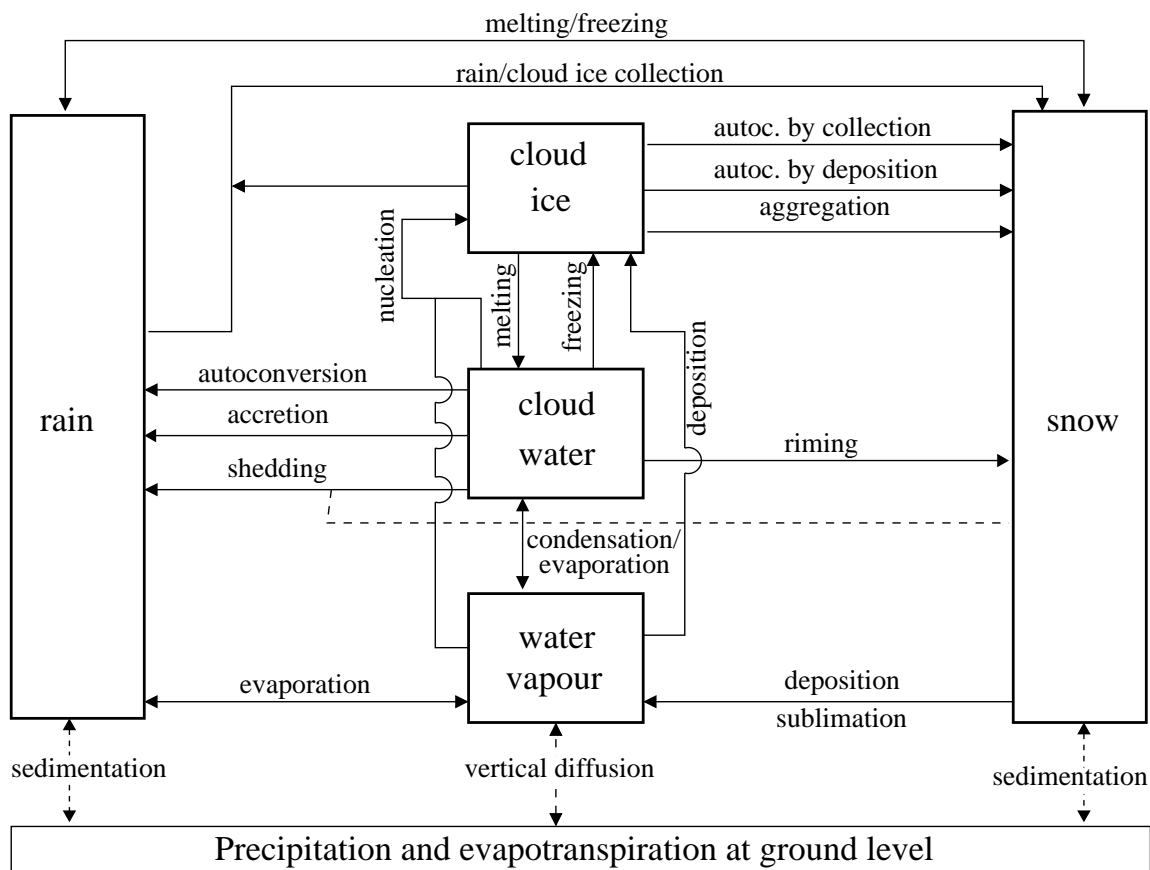
Figure 2.1: Cloud microphysic processes in LM: standard two-category ice scheme.

The different cloud microphysics processes of the two-categories ice scheme are illustrated in Figure 2.1. When a sufficient amount of cloud water or cloud ice is produced, the cloud water or ice particles are converted in raindrop or snow. By collision-coalescence processes the formation of raindrop is initiated (autoconversion). The rain or snow mass

fraction can be further increased by collection of others snowflakes, cloud droplets (accretion or aggregation). Depending on the temperature and humidity condition, the precipitation species may convert from rain to snow or vice versa and may also partially or completely evaporate before reaching the earth's surface.

To complete this microphysics scheme, the condensation/evaporation processes have to be parametrised. The calculation of condensation and evaporation rates, S_c, is based on an instantaneous saturation adjustment technique within clouds. If a grid box becomes supersaturated with respect to water during a time step, the temperature and concentration of water vapour, q_v and cloud water, q_c, are isobarically adjusted to a saturated state, taking latent heating into account. This phase transition is considered to be instantaneous. In this bulk approach, the nucleation process is strongly simplified. It is assumed that there is always a sufficient number of Cloud Condensed Nuclei (CCN) present to initiate the condensed water phase in case of supersaturation. As a closure for the saturation equilibrium, condensation/evaporation is treated as a quasi-reversible process with only two different thermodynamic states: saturated condition with $q_c > 0$ and subsaturated no-cloud case $q_c = 0$. Clouds always exist in case of water saturation and supersaturation situations are completely neglected.

Chapter 3

Implementation for three-dimensional fog modeling: LM-PAFOG

3.1 Requirements for three-dimensional fog forecasting

A three-dimensional fog model requires detailed cloud microphysics and should be able to run at spatial high resolutions. Horizontal resolution is an important factor when considering the different air flows and stagnant air pools induced by the topography. Moreover, the generation of a temperature inversion in the boundary layer is a determinant step in a potential formation of fog. The boundary layer also needs a very high vertical resolution. The dynamics core of the LM is a suitable tool for the fog forecast. The "Lokal Modell" is a fully compressible nonhydrostatic model, designed to cover various horizontal resolutions ranging from 50 km down to 50 m (*Doms and Schättler*, 2002). In the fog formation, the condensation/evaporation processes as well as the cloud droplet sedimentation are crucial. However, the operational use of the LM induces the presence of highly simplified parametrisation in order to restrain the computation time. In the LM, the condensation/evaporation is based on a bulk saturation adjustment scheme (Section 2.4). The driving scheme separates condensation from evaporation with a relative humidity threshold value (usually 100%). In case of coarse resolution, the relative humidity threshold is rarely reached: the large volume of the grid box is often filled with partial cloudiness. These clouds have to be correctly forecasted in order to represent the interactions with radiation, and thus with the energy balance. More sophisticated condensation/evaporation schemes are already available. In the formation of cloud droplets, the supersaturation conditions detailed by *Köhler* (1936), are conducted by the chemical composition and the size of the aerosols. Bigger aerosol particles and higher salt concentration decrease the critical point of supersaturation. For very small moist aerosol particles the contained salts allow the formation of droplets at relative humidity below 100%. Larger droplets grow when the smaller ones are already evaporated. To model these different processes, the droplet growth equation is solved for several droplet size bins as it was done in some one-dimensional models (*Brown*, 1980; *Flossmann* et al.,

1985; *Bott* et al., 1990) as well as in three-dimensional models (*Leporini*, 2005). However, the implementation of such microphysics schemes are computationally too expensive to be used for actual weather forecasting. The microphysics of our three-dimensional fog forecast model is an intermediate solution based on the Köhler theory so that only a total droplet number concentration has to be considered. The microphysics scheme still has a high degree of sophistication and the computation time is strongly reduced.

3.2 The microphysics parametrisation

The microphysics parametrisation is based on the one-dimensional fog forecast model, PAFOG (*Bott and Trautmann*, 2002). This parametrisation scheme introduces the cloud droplet concentration, N_c as prognostic variable. The cloud liquid water content in the lower part of the model atmosphere is thus controlled by this new variable, N_c, and the specific cloud water content, q_c. The prognostic equations for these variables are given by:

$$\frac{\partial N_c}{\partial t} = \mathbf{v} \cdot \nabla N_c + \frac{\partial}{\partial z}\left(K_h^v \frac{\partial N_c}{\partial z}\right) + \left(\frac{\partial N_c}{\partial t}\right)_{PAFOG} \tag{3.1}$$

$$\frac{\partial q_c}{\partial t} = \mathbf{v} \cdot \nabla q_c + \frac{\partial}{\partial z}\left(K_h^v \frac{\partial q_c}{\partial z}\right) + \left(\frac{\partial q_c}{\partial t}\right)_{PAFOG} \tag{3.2}$$

The first two terms on the right hand side describe advection and turbulent mixing processes, computed by the dynamic core of the LM. The third term gathers the influences of the the PAFOG microphysic processes, i.e. sedimentation of cloud droplets as well as the source and sink caused by the phase changes between the gaseous and liquid phase. Before defining the different processes of the parametrisation, an assumption on the droplet size distribution has to be made. In PAFOG, this is described by a log-normal function.

$$dN_c = \frac{N_c}{\sqrt{2\pi}\sigma_c D} exp\left[-\frac{1}{2\sigma_c^2} ln^2\left(\frac{D}{D_0}\right)\right] dD \tag{3.3}$$

where D is the droplet diameter, D_0 is the mean value of D and σ_c is the standard deviation of the given droplet size distribution. According to *Chaumerliac* et al. (1987), this quantity may be chosen as function of the particular aerosol type (maritime: $\sigma_c = 0.28$, continental: $\sigma_c = 0.15$). In our microphysics scheme, a constant value of $\sigma_c = 0.2$ is used. Only by the computation of the mean diameter, the microphysics scheme is able to consider the variation of the cloud droplet concentration. The selected distribution shape corresponds to the generally computed spectral distribution (*Bott*, 1991) or measurements (*Colomb* et al., 2007).
In this fixed microphysics framework, the following two prognostic equations are solved

with the PAFOG microphysics core.

$$\left(\frac{\partial N_c}{\partial t}\right)_{PAFOG} = \left(\frac{\partial N_c}{\partial t}\right)_{act} + \Delta(\overline{S})\left(\frac{\partial N_c}{\partial t}\right)_{eva} + \left(\frac{\partial N_c}{\partial t}\right)_{sed} \tag{3.4}$$

$$\left(\frac{\partial q_c}{\partial t}\right)_{PAFOG} = \left(\frac{\partial q_c}{\partial t}\right)_{con/eva} + \left(\frac{\partial q_c}{\partial t}\right)_{sed} \tag{3.5}$$

$$\Delta(\overline{S}) = \begin{cases} 1, & \text{for } \overline{S} < 0 \\ 0, & \text{for } \overline{S} > 0 \end{cases} \tag{3.6}$$

$$S = \frac{q_v}{q_{sat}^v} - 1 \tag{3.7}$$

sedimentation of cloud droplets and the source-sink terms $\sigma(N_c)$ and $\sigma(q_c)$ describe phase changes between the gaseous and liquid phase. where $\overline{S}$ is the mean supersaturation, q_v is the specific humidity and q_{sat}^v is the specific humidity value at saturation. We note that with the $\Delta(\overline{S})$ mechanism, the evaporation modifies N_c only if the air is unsaturated.

With the introduction of N_c as a new prognostic variable, the parametrisation of the cloud evolution is significantly improved. Contrary to the original mesoscale microphysics scheme, the cloud liquid water content is defined as a concentration of water droplets, giving more information about the microphysic structure of the cloud. The interactions between N_c and liquid water are quite complex: an increase in liquid water does not necessarily change the droplet number concentration. Existing droplets may grow without new droplets being formed. The cloud evolution is thus controlled by the evolution of N_c. The cloud formation is initiated by an activation process. The coupling between the $\Delta(\overline{S})$ mechanism and the one moment droplet size distribution is able to consider first the evaporation of the smallest cloud droplets. Also the sedimentation can increase or decrease N_c and cloud water, depending on the size of the settling droplets. At the ground, liquid water is treated like precipitation and droplets disappear due to deposition. The three parts of the PAFOG microphysics, activation, condensation/evaporation and sedimentation, are detailed hereafter.

3.2.1 Activation

The PAFOG microphysics needs an assumption about the number of activated cloud condensed nuclei when supersaturation is reached. Different authors (*Squires*, 1958; *Twomey*, 1959) have developed parametrisation of the nucleation process in order to avoid a difficult supersaturation forecast as well as a fine physical and chemical property description of the studied air parcel. Therefore, for a supersaturation S, the number of activated cloud droplets, N_{act} is calculated according to Twomey's relation (*Twomey*, 1959):

$$N_{act} = N_a S^k \tag{3.8}$$

where N_a is the Cloud Condensed Nuclei (CCN) concentration, and k are empirical constants which depend on the environment (maritime: $N_a = 100\ cm^{-3}$, $k = 0.7$, continental: $N_a = 3500\ cm^{-3}$, $k = 0.9$). In the present version, the aerosol concentration values were set constant in space and in time. For our study in Germany, we chose $N_a = 10000\ cm^{-3}$ as in *Bott and Trautmann* (2002) corresponding to a rural area.

The increase in total concentration of cloud droplets during a time step Δt represents the first term of (3.5), $\left(\frac{\partial N_c}{\partial t}\right)_{act}$ and with Twomey's relation is written as:

$$N_c(t + \Delta t) = N_c(t) + max(N_{act} - N_c(t), 0) \tag{3.9}$$

With the maximum operator, N_c only increases in case of a positive tendency in the supersaturation. Therefore if the supersaturation remains unchanged or decreases no new droplets are activated and the already existing droplets grow.

3.2.2 Condensation/evaporation

The parametrisation for the condensation and evaporation of cloud droplets is based on the works of *Nickerson* et al. (1986) and *Chaumerliac* et al. (1987).
After the activation process the time evolution of the cloud is controlled by the time rate of change for the cloud droplet diameter D due to condensation or evaporation (*Pruppacher and Klett*, 1997) and is expressed as:

$$\frac{dD}{dt} = G\overline{f}\frac{S}{D} \tag{3.10}$$

where S is the supersaturation (see eq. 3.7). The ventilation coefficient is, $\overline{f} = -4.33 \cdot 10^5 D^2 + 5.31 \cdot 10^3 D + 0.572$ (*Pruppacher and Rasmussen*, 1979) and G, the following thermodynamic function:

$$G = \frac{1}{\frac{L_v \rho_w}{KT}\left(\frac{L_v}{R_w T} - 1\right) + \frac{\rho_w R_w T}{e_{sat}^v(T)D_v}} \tag{3.11}$$

where e_{sat}^v is the saturation vapour pressure over a plane water surface, R_w the specific gas constant for moist air, D_v the water vapour diffusivity and K the thermal conductivity. The time evolution of the specific cloud water due to condensation or evaporation processes is then defined as:

$$\left(\frac{\partial q_c}{\partial t}\right)_{con/eva} = \frac{\rho_w}{\rho}\int_0^\infty \frac{\pi}{2}D^2\frac{dD}{dt}\frac{dN_c(D)}{dD}dD \tag{3.12}$$

Replacing $\frac{dD}{dt}$ by (3.10) and introducing the log-normal distribution for the cloud droplets concentration, we find:

$$\left(\frac{\partial q_c}{\partial t}\right)_{con/eva} = \frac{\rho_w}{\rho}\frac{\pi}{2}GSN_cD_0 exp\left(\frac{\sigma_c^2}{2}\right) \tag{3.13}$$

In case of evaporation, the smallest droplets disappear first and N_c decreases. From (3.10), we can deduce the critical droplet diameter, $D_{c,eva}$ of the biggest droplets still evaporated in a time step:

$$\int_{D_{c,eva}}^0 DdD = \int_t^{t+\Delta t} GSdt \tag{3.14}$$

Considering G and S constant over the time step, we finally have:

$$D_{c,eva} = \sqrt{-2GS\Delta t} \tag{3.15}$$

Integrating from the smallest droplet to the critical diameter, we obtain:

$$N_c|_{eva} = \int\limits_{0}^{D_{c,eva}} N_c(D)dD \tag{3.16}$$

Therefore the loss in droplet number concentration due to evaporation, $\left(\frac{\partial N_c}{\partial t}\right)_{eva}$ can be integrated on a time step Δt as

$$N_c(t + \Delta t)|_{eva} = N_c(t) - N_c|_{eva} \tag{3.17}$$

During the condensation/evaporation processes, the supersaturation S has to be known. Because of the discrepancy between the supersaturation time constant and a reasonable model time step integration, it is not possible to calculate S exactly. However, *Sakakibara* (1979) proposes a solution corresponding to the supersaturation mean value on the integration time step. Moreover, the solution is numerically stable for any time step values and for any cloud droplet concentration values. Finally, the precision of the solution increases with the decrease of the time step. The analytical solution is based on the macroscopic prognostic equation for supersaturation:

$$\frac{dS}{dt} = \left(\frac{S+1}{p} - \frac{0.623(S+1)}{RT^2}\frac{L_v}{\rho_a c_{pd}}\right)\frac{dp}{dt} + \left(\frac{1}{q_{sat}^v} + \frac{0.623(S+1)L_v^2}{RT^2 c_{pd}}\right)\frac{\partial q_v}{\partial t} \tag{3.18}$$

with

$$\frac{dp}{dt} = -\rho_a g w \tag{3.19}$$

$$\frac{\partial q_v}{\partial t} = -\frac{\partial q_c}{\partial t}|_{con/eva} \tag{3.20}$$

where P, T and w are pressure, temperature and vertical velocity respectively; q_{sat}^v is the specific humidity value at saturation, L_v is the latent heat of vaporisation, g is the acceleration of gravity and c_{pd} is the heat capacity for dry air at constant pressure. Introducing the results of the equation (3.13), the time dependence of the supersaturation S is given by:

$$\frac{dS}{dt} = (c_1 + c_2 + c_3)S + c_3 \tag{3.21}$$

where

$$c_1 = -\frac{1}{q_{sat}^v}\frac{\rho_w}{\rho}\frac{\pi}{2}G\Sigma_c \tag{3.22}$$

$$c_2 = -\frac{L_v^2}{RT^2 c_{pd}}\frac{\rho_w}{\rho}\frac{\pi}{2}G\Sigma_c \tag{3.23}$$

$$c_3 = \left(\frac{1}{p} - \frac{L_v}{RT^2\rho c_{pd}}\right)\frac{dp}{dt} \tag{3.24}$$

$$\Sigma_c = N_c D_0 exp\left(\frac{\sigma_c^2}{2}\right) \tag{3.25}$$

By solving the previous equation, a mean value for the supersaturation, $\overline{S}$, over the time step Δt is then deduced:

$$\overline{S} = -\frac{c_3}{c} - \left(S(t) + \frac{c_3}{c}\right)\left(\frac{1 - e^{c\Delta t}}{c\Delta t}\right) \tag{3.26}$$

where $S(t)$ is the supersaturation at the beginning of the time step Δt and $c = c_1 + c_2 + c_3$. Knowing the supersaturation, we can quantify the influence of the phase changes on the liquid water content, the specific humidity and the temperature:

$$\frac{\partial q_c}{\partial t}_{con/eva} = \frac{\rho_w}{\rho}\frac{\pi}{2}G\overline{S}\Sigma_c \tag{3.27}$$

$$\frac{\partial q_v}{\partial t}_{con/eva} = -\frac{\rho_w}{\rho}\frac{\pi}{2}G\overline{S}\Sigma_c \tag{3.28}$$

$$\frac{\partial T}{\partial t}_{con/eva} = -\frac{L_v}{c_{pd}}\frac{\partial q_v}{\partial t}|_{con/eva} \tag{3.29}$$

$$\tag{3.30}$$

3.2.3 Sedimentation

Fog events are linked with calm synoptic situations, where the vertical wind velocity is very weak. The sedimentation of cloud droplets has to be considered. Thus, the sedimentation tendencies for cloud water and condensation nuclei are defined as:

$$\left(\frac{\partial N_c}{\partial t}\right)_{sed} = \frac{\partial S_{n,c}}{\partial z} - \frac{\partial(wN_c)}{\partial z} \tag{3.31}$$

$$\left(\frac{\partial q_c}{\partial t}\right)_{sed} = \frac{\partial S_{q,c}}{\partial z} - \frac{\partial(wq_c)}{\partial z} \tag{3.32}$$

where $S_{n,c}$ and $S_{q,c}$ are the sedimentation terms for cloud droplet concentration and liquid water content (see eq. 3.36 & 3.35).
The formulation of *Berry and Pranger* (1974) expresses the settling velocity as a function of droplet diameter and the Reynolds number Re

$$v(D) = \frac{\eta Re}{D\rho} \tag{3.33}$$

where η the coefficient of dynamic viscosity in air, is given as:

$$\eta = 1.496286 \times 10^{-6}\frac{T^{3/2}}{T + 120} \tag{3.34}$$

With the equation (3.33), the sedimentation terms can then be evaluated:

$$S_{n,c} = \int\limits_0^\infty N_c(D)v(D)dD = \frac{N_c v(D_0)}{\sqrt{2}\sigma_c\xi}exp\left(\frac{(k_2 - 1)^2}{4\xi^2}\right) \tag{3.35}$$

$$S_{q,c} = \frac{1}{\rho} \int_0^\infty m(D) N_c(D) v(D) dD = \frac{N_c m(D_0) v(D_0)}{\sqrt{2}\sigma_c \xi \rho} exp\left(\frac{(k_2+2)^2}{4\xi^2}\right) \qquad (3.36)$$

using $a_2 = 1.01338$, $a_3 = -0.0191182$ and the following parameters

$$\xi = \sqrt{\frac{1}{2\sigma_c^2} - 9a_3} \qquad (3.37)$$

$$k_2 = 3a_2 + 6a_3 ln(aD_0^3) \qquad (3.38)$$

$$a = \frac{4\rho\rho_w g}{3\eta^2} \qquad (3.39)$$

$$m(D_{c,0}) = \frac{\pi}{6}\rho_w D_0^3 \qquad (3.40)$$

For the numerical solution of sedimentation, the positive definite advection scheme of *Bott* (1989) is used. Since the size distribution of the droplets is known, the sedimentation of the droplets can be computed accurately.

3.3   Microphysics implementation

The PAFOG microphysics, detailed in Section 3.2, was implemented in the "Lokal Modell". The condensation/evaporation parametrisation, based on a saturation adjustment scheme, was substituted by a detailed microphysics (Figure 3.1). PAFOG microphysics is limited to the lowest part of the atmosphere, currently below 2000 meters (Figure 3.2). In this domain, where fog and low stratus clouds form, the condensation and evaporation processes as well as the sedimentation of cloud droplets are modeled with the PAFOG cloud microphysics. Precipitation, autoconversion, accretion, evaporation of precipitation and processes including the ice phase stay unchanged and are forecasted by the original LM microphysics in the whole atmosphere. Thus, the implementation of the PAFOG microphysics into the LM does not interfere with the already existing cloud and precipitation microphysics scheme of the LM. Liquid water content already is a prognostic variable in the LM. Once formed, this quantity is transported by advection and turbulence. The implementation of the PAFOG microphysics introduces the total droplet number concentration, N_c, as a new prognostic variable into the dynamic core of the LM needing horizontal and vertical advection as well as the turbulent transport of N_c. The three-dimensional link between liquid water and N_c is hereby ensured.

3.4   Spatial discretisation

The fog is strongly dependent on the boundary layer processes such as radiative cooling at the surface and heat and humidity transport at the interface soil/atmosphere. The fog forms close to the surface and grows steadily upwards. The modelling of such processes requires a high vertical resolution. In the actual operational weather forecast models, the lowest layer in the atmosphere is about 20 m thick in the LM. With this coarse grid the fog formation cannot be described.
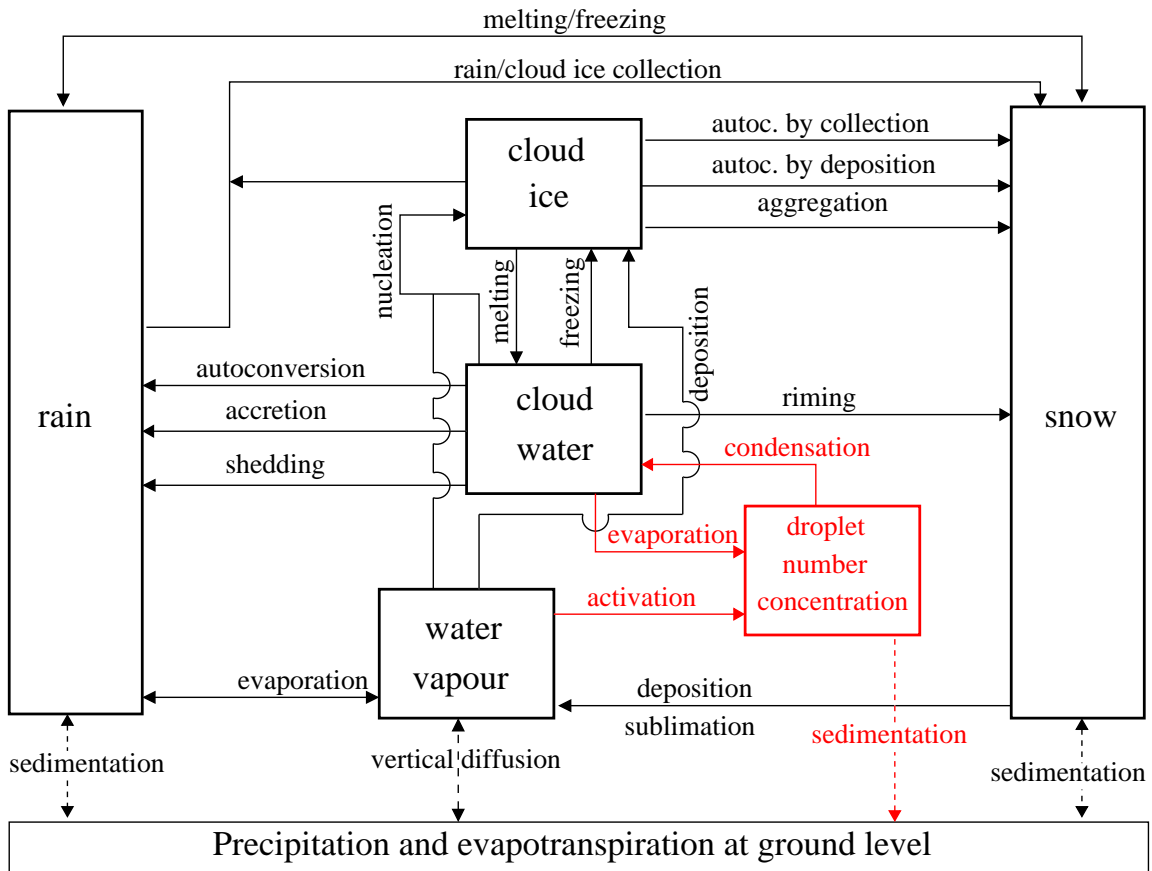
Figure 3.1: Cloud microphysic processes in LM-PAFOG: standard LM two-category ice scheme (black part), PAFOG microphysics (red part).
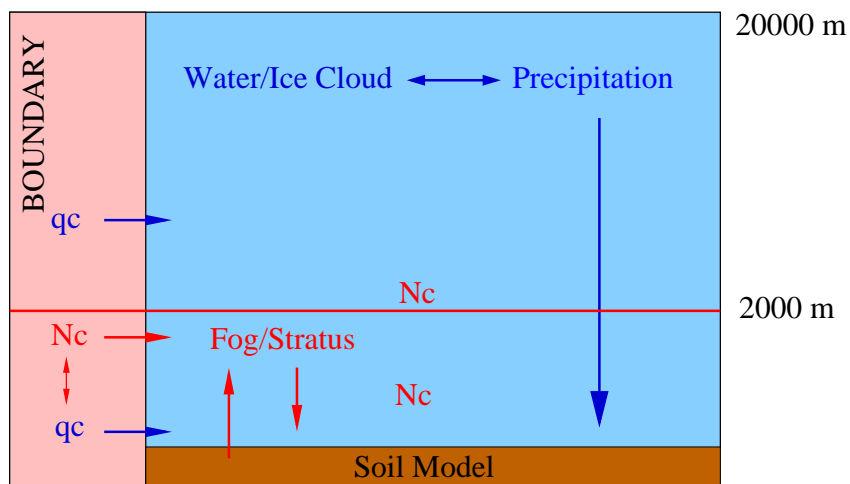
Figure 3.2: Cross Section of LM-PAFOG domain.

The determinant evolution for the formation of radiation fog occurs close to the surface. The modelling of the boundary processes can only succeed with a high vertical resolution. In case of a radiative fog event, the surface cooling causes the formation of large temperature and humidity gradients in the lowest meter of the atmosphere. From this thin saturated atmospheric layer, the fog grows steadily upward. In our three-dimensional fog forecast model, LM-PAFOG, the high vertical resolution is thus concentrated near the ground: 25 of 40 levels are located in the first 2000 meters and ten layers of 4 meters offer a fine detection of fog formation at the ground. The horizontal resolution should also be rather high to consider the variation of the surface parameters (orography, soil types). A resolution of 2.8 km is presently used and the different air flows and stagnant air pools induced by the topography are thus better modelled.

3.5   Boundary conditions for N_c

The structure of PAFOG microphysics is based on a new prognostic variable, N_c, the droplet number concentration. The main goal is to define a clear link between N_c and the liquid water content q_c. The cloud formation processes -activation, condensation/evaporation and sedimentation- allow a more precise modelling of the cloud water concentration. But the PAFOG microphysics core experiences difficulties when forecasting cloud cover evolution, if a cloud is transported into the PAFOG domain. In this case, the cloud is only defined by its liquid water content and the PAFOG microphysics is unable to evaporate or sediment this cloud water because there is no correspondence with a droplet concentration. Therefore, liquid water accumulates in an environment that might have a relative humidity far below the saturation and finally may form precipitation. This invisible cloud water results from the initialisation of cloud cover at forecast start and from the advection or turbulent diffusion through the lateral boundaries as well as the advection through the top boundary, since PAFOG is restricted to the lowest 2000 meters of the atmosphere. In order to optimise the relation between N_c and liquid water content, a boundary condition for N_c has to be formulated.

A possible solution is to relate liquid water content at the boundary directly to N_c assuming a lognormal droplet size distribution. We can solve equation (3) of *Chaumerliac* et al. (1987) for N_c and thus use it at the boundaries.

$$q_c = \frac{N_c}{\rho}(\frac{\pi}{6}D_0^3\rho_w)exp(\frac{9}{2}\sigma_c^2) \tag{3.41}$$

$$N_c = \rho q_c(\frac{1}{\frac{\pi}{6}D_0^3\rho_w})exp(-\frac{9}{2}\sigma_c^2) \tag{3.42}$$

The credibility of the N_c boundary values depends on the choice of the mean diameter and the standard deviation defining the lognormal distribution. These parameters values are based on the work of *Miles* et al. (2000), who summarises the N_c measurement campaigns in marine and continental environments for low-level stratiform clouds. The N_c boundary parametrisation detailed hereafter was developed for a continental environment. The N_c lognormal distribution at the boundary is parametrised with a fixed mean diameter of 10 μm and a variable standard deviation. The value of the standard deviation σ_c changes with the height:

- between 0 and 1000 meters, σ_c has a constant value of 0.2.

- At the top of the PAFOG domain, σ_c reaches its maximun value of 0.35.

- The standard deviation σ_c is linearly interpolated between 0.2 at 1000m and 0.35 at the top of the PAFOG domain.

This N_c boundary parametrisation is added to the lateral boundaries as well as to the three layers above the top of the PAFOG domain in order to attribute a droplet number concentration value to each cloud coming into the PAFOG domain due to advection or turbulent diffusion. Moreover, this boundary condition is applied at initialisation when liquid water is present in the studied area.

With this procedure every cloud entering in the forecast area is also considered as a prescribed size distribution of droplets. Thus, growth and dissipation of fog and very low clouds can be ensured by the PAFOG microphysics.

3.6   Visibility parametrisation

The PAFOG microphysic introduces the total droplet number concentration as prognostic quantity. With this new variable, the influence of light scattering induced by the cloud droplets and aerosol particles can be considered for our visibility calculation. The visibility, *VIS*, is expressed in meter and is calculated following the Koschmieder's parametrisation (*Koschmieder*, 1924):

$$VIS = \frac{3.912}{\beta_{ext}} \tag{3.43}$$

The extinction coefficient, β_{ext}, is expressed in terms of the aerosol extinction coefficient, $\beta_{ext,A}$, and the scattering influence of the air molecules $\beta_R = 1.227 \times 10^{-5} m^{-1}$:

$$\beta_{ext} = \beta_{ext,A}(RH) + \beta_R \tag{3.44}$$

The humidity dependence on the aerosol extinction coefficient follows *Shettle and Fenn* (1979):

$$\beta_{ext,A}(RH) = N_a \cdot \sigma_{ext,A}(RH, A) \tag{3.45}$$

where N_a is the total aerosol concentration and $\sigma_{ext,A}$ is the extinction cross section. The values of $\sigma_{ext,A}$ are computed in "look up" tables for 8 relative humidity values ($RH = 0, 0.5, 0.7, 0.8, 0.9, 0.95, 0.98, 0.99$) and 3 aerosol concentrations (N_a types: rural, urban, maritime) following the work of *Shettle and Fenn* (1979). Thus, $\sigma_{ext,A}$ are linearly interpolated depending on the humidity conditions.

In presence of fog, the extinction coefficient, β_{ext}, is completed by adding a term for the scattering influence of cloud droplets. Following *Johnson* (1954), the scattering coefficient for the fog droplets is defined as:

$$\beta_{scat,D} = \pi \sum_i N_i r_i^2 \tag{3.46}$$

Considering the total cloud droplet distribution as a log-normal size distribution (see eq. 3.3), $\beta_{scat,D}$ becomes:

$$\beta_{scat,D} = Q_{av} N_c \frac{\pi}{4} \left(\frac{6}{\pi} \frac{LWC}{\rho_w N_c} \right)^{\frac{2}{3}} exp(-\sigma_c^2) \qquad (3.47)$$

where Q_{av} is the scattering efficiency of a droplet, deduced from the Mie theory ($Q_{av} = 2$) and LWC is the liquid water content in $g.m^{-3}$. Thus, the visibility values can be deduced with the following parametrisation:

$$VIS = \frac{3.912}{\beta_{ext} + \beta_{scat,D}} \qquad (3.48)$$

With the implementation of detailed microphysics a very sensitive visibility parametrisation can be deduced. The visibility decrease is thus influenced by the aerosol concentration present in the forecast area, the concentration of cloud droplet and their respective size distribution as well as the liquid water content. With these four different parameters, the influence on the visibility decrease can be considered for the numerous variation of the microphysics structure of fog.

3.7   Influence of the microphysics

The influence of the new PAFOG microphysics can be identified by studying of vertical cross section and time evolution of liquid water content column (Figure 3.3). The new microphysics PAFOG strongly modifies the cloud formation in the lowest atmosphere. Clouds are not parametrised as a simple liquid water distribution, but as a distribution of water droplets (Figure 3.3-a). The spatial distribution of droplet number concentration drives the distribution of liquid water content. A good coherence between the high droplet number concentration and the high values of liquid water content can be generally identified and thus suggests the formation of small droplets (Figures 3.3 c & d). With the PAFOG microphysics, the vertical structure has a heterogeneous distribution with a clustering of the highest liquid water content nearest the ground. The vertical structure is controlled by the sedimentation scheme present in the PAFOG microphysics: knowing the droplet sizes, their fall velocity can be simply deduced.

In the standard case, the liquid water is uniformly distributed in the cloud with the smallest values close to the ground (Figures 3.3 d & e). Generally, the sedimentation occurs if a critical liquid water concentration is exceeded, the decrease of the water content is uniformly applied due to the lack of information concerning the droplet size.

On a single point comparison, the time evolution of liquid water content highlights the role of our new fog microphysics scheme (Figures 3.3 d & f). The PAFOG microphysics confirms its significant influence on the fog structure and on the fog duration. The PAFOG microphysics implies the formation of dense fog close to the ground, while in the standard approach the liquid water maximum gathers at the cloud top. The introduction of the cloud droplet concentration as a new prognostic variable gives a more precise and more realistic description of the cloud water content.
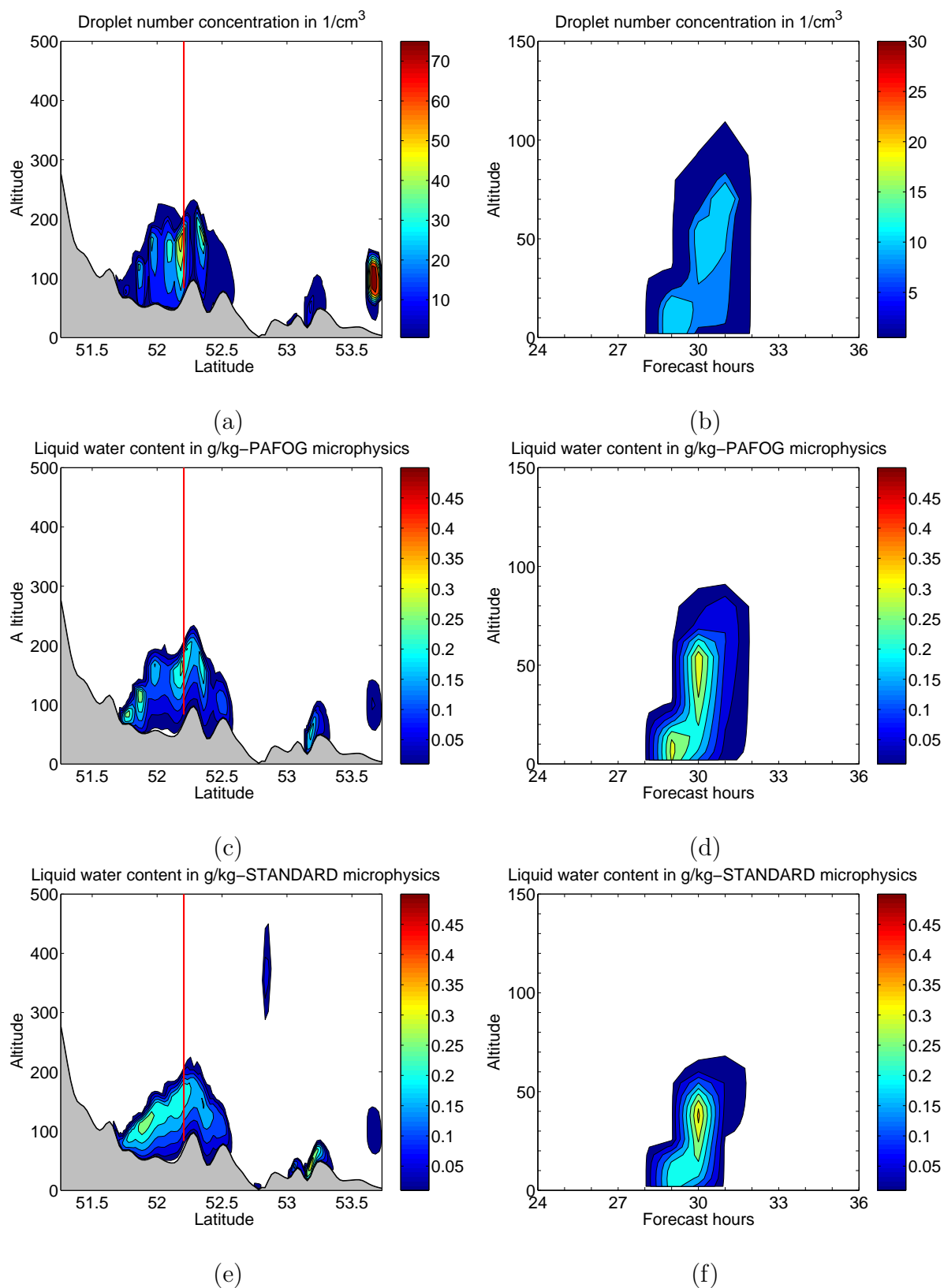
Figure 3.3: Cross section and vertical profile time evolution of droplet concentration number (fig. a & b), liquid water content computed with the PAFOG microphysics (fig. c & d) and liquid water content computed with the standard microphysics (fig. e & f) for a fog event at the Lindenberg Observatory (red line), 27 September 2005 at 02 UTC

The visibility value can be modified by the variation of the cloud droplet number and the liquid water concentration. The variation of liquid water content close to the ground also has a decisive influence on the visibility values. For a same fog event, both microphysic schemes propose two different scenarios. With its detailed description, the PAFOG microphysics forms a dense fog event, especially in the first hours, with a liquid water content around 0.3 g/kg, while the standard approach reaches a value of 0.2 g/kg. Moreover, the fog cloud disperses one hour later than the forecast carried out by the standard microphysics scheme.

An adequate parametrisation of the cloud sedimentation and a fine description of the cloud in terms of cloud droplets have a decisive impact on the fog forecast quality. However, the processes involved in the fog formation is based on a complex and non linear fashion. The microphysics scheme is only one of the influent parameter. The combination of a fine grid resolution and a detailled microphysics has to agree with the dynamic core of the model. To assess the qualities of our new fog forecast model, a complete analysis is presented in the next chapter.

Chapter 4

Evaluation of LM-PAFOG fog forecasts

4.1 Approach

In order to quantify the performance of the LM-PAFOG forecasts, an extensive validation study has been conducted. In the framework of the COST722 "Short range forecasting of fog, visibility and low clouds", LM-PAFOG has participated in a large intercomparison campaign of European fog forecast models. The campaign was divided into two types of evaluations:

- A statistical study of the fog forecasts in terms of visibility for a continuous four month period.

- Analysis of selected events, underlining the strengths and weaknesses of the fog model parametrisations and thus contributing to the understanding of the comprehensive results.

First, the evaluation methodology and the selected data are discussed. Then, the presentation of the LM-PAFOG performances in the statistical evaluation as well as in the selected scenes are presented in more detail. Finally, the LM-PAFOG results have been confronted with the other four model forecasts participating in this intercomparison study. These results will be presented in Chapter 5.

4.2 Aims and framework

The evaluation of the model aims to assess the forecast quality of our new model, i.e. its agreement with actual occurrences. In the case of a fog forecast model evaluation, the study has to verify spatial extension, time evolution and physical parameters involved in fog formation and evolution. In terms of quality, such considerations can be translated into two questions:

- Is the forecasted fog cloud at the right place and at the right time ?

- How well does the fog forecast model consider the physical processes involved in formation, evolution and dissipation ?

Such an approach requires a large set of measurements with a fine temporal resolution to follow in detail the evolution of the different fog episodes. Ideally, visibility and detailed measurements close to the surface such as thermodynamic and dynamic profiles as well as radiative fluxes, would be decisive information to capture the evolution of the fog events.

4.2.1   Forecast area and available measurements

Only few places are equipped with the measurement networks able to follow the processes occurring close to the ground. On the flat terrain of our research area, the meteorological observatory of Lindenberg delivers the largest set of measurements in Germany (Figure 4.1). In a cooperation with the German Meteorological Service, the observatory supplied a detailed set of measurements for the four month period of the intercomparison campaign (September, 1st-December, 31st 2005) including the following parameters:

- horizontal visibility at 2m,

- cloud cover,

- sensible and latent heat fluxes, incoming and outgoing short wave and long wave fluxes, measured at the surface

- 10m-mast with observations of humidity, temperature and wind (level of measurements, for humidity and temperature: 1, 2, 4 and 10m; wind speed and wind direction: 10 m),

- 100m-mast with observations of humidity, temperature and wind (level of measurements, for humidity and temperature: 10, 20, 30, 40, 60, 80 and 98 m; wind speed and wind direction: 40 and 98 m),

- standard radiosonding profiles, supplying vertical profiles of temperature, humidity and wind at 00, 06, 12 and 18 UTC.

To evaluate the spatial evolution of our three dimensional forecast, further measurements have been extracted from the SYNOP database (surface SYNOPtic observations), which gathers the standard measurements on the globe. In the studied area, 28 SYNOP-stations complete the point data measurements of the Lindenberg observatory (Figure 4.2). These stations supply only surface measurements: visibility, temperature, relative humidity at 2m and wind speed at 10m. The time resolution of the SYNOP data is strongly dependent on each individual weather station. The measurements are delivered with an interval of one, three or six hours. Unfortunately, the SYNOP data available for this study are limited to the time period of the three selected fog events.
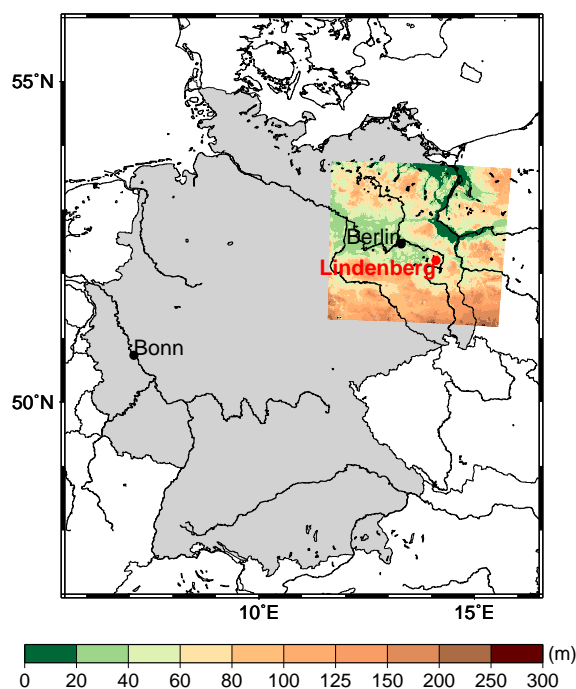
Figure 4.1: Forecast domain of LM-PAFOG. The colour scale from green to brown represents the topography in the Lindenberg area.
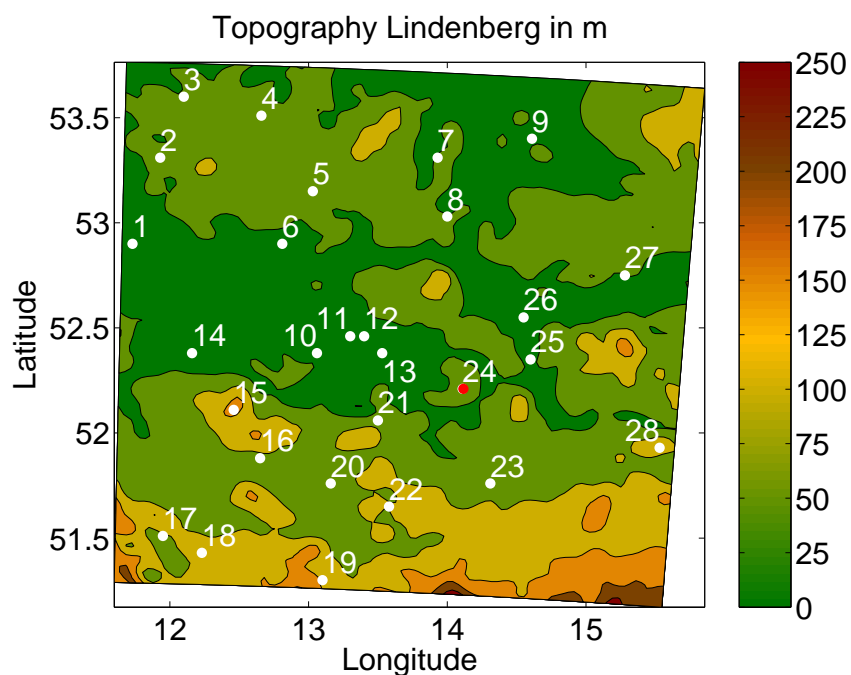
Figure 4.2: SYNOP stations in the Lindenberg area. The red point represents the Lindenberg observatory of the DWD. The stations 11, 12 and 13 are situated in the urban area of Berlin. The colour scale from green to brown represents the topography in the Lindenberg area.

4.2.2 Occurrence of fog events

During the last quarter of 2005, the visibility measurements identified 36 fog events. A detailed study concerning the fog occurrence for different visibility thresholds is presented in Table 4.1. For the studied period the supplied observations underline the very low frequency of fog events: Fog appears in 2% of the period with a visibility below 600 m, 4% with a visibility below 1000 m and 6% below 1500 m. Moreover, the low occurrence of fog events is confirmed if we study the frequency of fog per forecast hour (Figure 4.3). In a statistical study, such a low occurence may have some influence on the statistical results even if the forecast model is not modified as the accuracy of the different statistical scores is strongly influenced by the very low number of fog events. A single correct or false forecast has a large weight in the statistic approach. Some statistical tools can quantify the model results and confine the influence of low occurence. However, to improve the accuracy of our statistical study, the only solution would be to extend the period of the comparison to a significantly larger time period. In the following discussions, the potential influence of the low fog occurence has to be considered.

Table 4.1: Number of hourly observations with a visibility below 350, 600, 1000, 1500 and 3000 m in the Lindenberg area during the last quarter of 2005.

Visibility (in m)	350	600	1000	1500	3000	Total hours
Lindenberg	61	76	116	181	356	2928
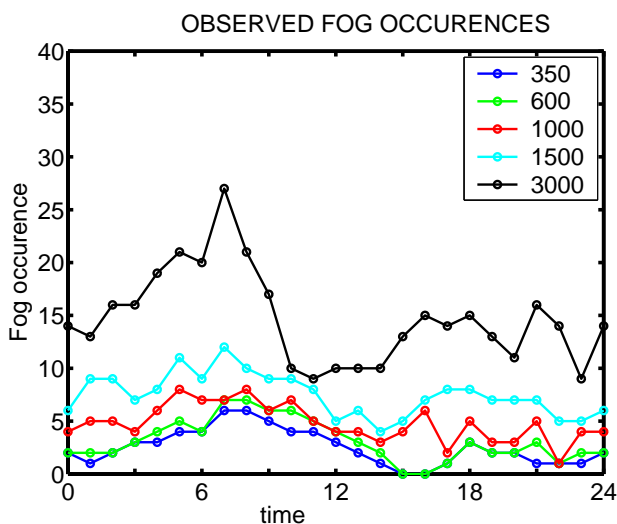
Figure 4.3: Time distribution of fog event occurrence per time of the day and per visibility threshold (350, 600, 1000, 1500 and 3000 m).

4.2.3 Model configuration

In this study, LM-PAFOG has been used in a semi-operational version. During the four month period of the intercomparison study, 48 hours of simulation were computed daily for an area around Berlin and Lindenberg (Figure 4.1). This experiment uses a model domain of 100 by 100 grid points at a gridspacing resolution of 2.8 km and a time step of 10 seconds. This configuration requires about 60 minutes for a 48 hour simulation if 16 processors of the supercomputer of the German Meteorological Service are used. With a 280 by 280 km limited forecast area, the model needs a nesting in a larger domain. LM-PAFOG is initialised with three-dimensional assimilation data based on observation nudging issued from the coarse LM grid runs (7x7 km). The boundary conditions are renewed each hour by a 1-way nesting.

4.3 Statistical evaluation approach

4.3.1 Method

Fog has been simplified in a simple binary event, it does or does not occur. Based on this simple consideration, the forecast performance is evaluated by a study of forecast visibility. In our case, the chosen statistical approach focuses on a four month period, in which the 2m-visibility outputs of LM-PAFOG are compared with the measurements supplied by the Lindenberg observatory.

LM-PAFOG delivered continuous hourly forecasts during the entire period: the model was initialised each day at 00 UTC for 48 forecast hours, which corresponds to 6000 consecutive forecast hours. The influence of the forecast duration on the forecast quality can be thus accurately defined. For each hour of this period, the model supplied two forecasts: one with a run initialised at 00 UTC, and one with a run initialised at 00 UTC the day before.

Moreover, to test the variation of the forecast performance in terms of fog intensity, the different forecasts have been categorised in five levels, corresponding to the fog events with a visibility below 350, 600, 1000, 1500 and 3000 m.

The evaluation of LM-PAFOG is included in a comparison campaign between different fog forecast methods. To obtain a common evaluation scheme independent of the used forecast method, the validation of the spatial extent has been neglected. The single point of the forecast area corresponding to the Lindenberg observatory has been extracted for the comparison.

4.3.2 Verification methods for deterministic forecasts

The quantitative skill assessment for such dichotomous classifications is a common task in the analysis of model forecasts. In our case, the different forecasts can be split into "fog" or "no fog", and threshold values for visibility have to be used to define a fog event. In the climatological and meteorological domains, the use of contingency table-based statistics has a long tradition and is still widely recognised as the most appropriate approach to product validation. Several scalar indicators have been proposed, applied and evaluated. A selection of these indicators was chosen based on their specific information content and

their successful application in similar studies (*Brooks and Doswell*, 1996; *Doswell* et al., 1990; *Marzban*, 1998; *Murphy*, 1993; *Stephenson*, 2000; *Thornes and Stephenson*, 2001; *Wilson and Burrows*, 2004; *Zhang and Casey*, 2000). These statistical tools are detailed in the next paragraphs.

The basis of all indicators is a 2 by 2 contingency table showing agreement and disagreement between the dichotomous classification to be tested and the reference data set (table 4.2).

Table 4.2: Contingency table for categorical forecasts of a binary event. The numbers of observations in each category are denoted by a, b, c and d, respectively.

	Observation yes	Observation no	Total
Forecast yes	a (Hit)	b (False)	$a + b$
Forecast no	c (Miss)	d (Correct Rejection)	$c + d$
Total	$a + c$	$b + d$	$a + b + c + d$

Several types of forecast performances can be defined based on the contingency table (Table 4.3). In this table, "a" gives the number of correctly forecasted events, "b" the false alarms (forecasted but not observed), "c" the misses (observed but not forecasted) and "d" the correct negatives. For each comparison data set, a table of this kind is computed. The statistical indicators are calculated based on the values "a" to "d".

The **Accuracy, ACC** (*Finley*, 1884), is the most intuitive score to quantify the overall forecast quality, corresponding to the ratio of correct predictions and the sample size. Nevertheless the evolution of this score cannot identify the difference between a correct detection of fog ("a") or a correct negative fog event ("d"). In case of very high or very low frequency of the studied properties, it can produce misleading information.

The **Hit Rate, HR** (*Swets*, 1986), or probability of detection, is the proportion of occurrences that are forecasted correctly. The hit rate only considers the detection skill in fog situations. To quantify the forecast skill, the description of the forecast qualities has to balance the number of hits with the false alarms.

In analogy to the hit rate, the **False Alarm Rate, FAR** (*Swets*, 1986), expresses the proportion of false alarms in all non-event forecast.

The **False alarm ratio, F** (*Donaldson* et al., 1975), corresponds to the proportion of false alarms in the positive forecast events.

The **Bias score, B** (*Donaldson* et al., 1975), is a ratio of the frequency of forecasted events to the frequency of observed events and can be interpreted as a measure of overestimation ($B > 1$) or underestimation ($B < 1$). Finally, to quantify the forecast accuracy, forecast skill is defined as a skill score, which is interpreted as a percentage

Table 4.3: Statistical indicators used in this study, with computation, theoretical range of values and best values for a maximum skill prediction.

Name	Equation	Range	Best
Accuracy	$ACC = \frac{a+d}{a+b+c+d}$	0...1	1
Hit Rate	$HR = \frac{a}{a+c}$	0...1	1
False Alarm Rate	$FAR = \frac{b}{b+d}$	0...1	0
False alarm ratio	$F = \frac{b}{a+b}$	0...1	0
Bias score	$B = \frac{a+b}{a+c}$	$0...\infty$	1
Equitable Threat Score	$ETS = \frac{a-h_{random}}{a+b+c-h_{random}}$ with $h_{random} = \frac{(a+c)(a+d)}{a+b+c+d}$	$-1/3...1$	1

of improvement over the reference forecasts. Common choices for the reference forecasts are persistence, climatological values or random forecasts. The skill score for forecast is generally expressed by

$$S_{forecast} = \frac{S - S_{ref}}{S_{perf} - S_{ref}} \tag{4.1}$$

where S characterises a particular measure of accuracy, S_{ref} is the accuracy of a reference forecast and S_{perf} is the value of the accuracy measure in case of a perfect forecast.

With the use of skill scores the forecast performance of a model in different situations or the performance of different models can be easily compared due to the use of the same reference in the comparison.

The **Equitable Threat Score, ETS**, or Gilbert Skill Score (*Gilbert*, 1884; *Schaefer*, 1990) measures the fraction of observed and forecasted events that were correctly predicted, adjusted for hits associated with random chance, h_{random}. It is usually used for the forecast verifications of rare events, because this score reduces the influence of the correct negative forecast, which have no skill in case of fog forecasting. The forecast skill focuses thus on the performance to correctly detect the fog events.

Each of these indicators underlines an appointed strength or weakness of the forecast system, so that for each step of the evaluation all values are detailed and interpreted as appropriate. The combination of the different statistical scores constitutes a good characterisation scheme for the classification results.

The Relative Operational Characteristic, ROC, diagrams (*Marzban*, 2004; *Mason*, 1980, 1982, 1989; *Wilson and Burrows*, 2004) generally facilitate to identify the situations

in which the model produces its best forecasts. By confrontation of Hit Rate, HR, and False Alarm Rate, FAR, the ROC diagram balances the positive influence of correct forecasts in foggy situations with the undesirable false alarms in "no fog" situations.

To evaluate the detection skill of a forecast system, the pseudo-ROC diagram, PSROC, combines the hit rate influence with the False alarm ratio, F, corresponding to the false alarms produced in case of a forecast of a fog event.

The proximity of the upper left hand corner of the plot in ROC and PSROC underlines increasing skill of the forecast system.

4.3.3 Verification results

In this section the results of the verification study will be detailed and interpreted. The verification will address the evolution of the forecast performances in terms of forecast duration and in terms of fog intensity. The results of each statistical score have been sorted by visibility threshold and by forecast hour. Therefore, the model sensitivity to detect a fog event can be studied and the model quality at different times of day can be differentiated.

The purpose of such a statistical approach is to summarise the results of the forecast appraisal in order to highlight in a comprehensible way the strengths and weaknesses of the model. Based on the accuracy score, the global quality of the model forecast is determined by a very pragmatic approach (Figure 4.4-a). The accuracy Figures point out that between 80% and 95% of the studied situations were correctly predicted depending on the forecast time and the studied visibility threshold. Such satisfying values have to be put in perspective to the low frequency of fog events in the Lindenberg area. If a forecast system is not able to forecast any presence of a fog event, the accuracy value would still deliver high score values in spite of no valuable forecast information. As already mentioned before, fog is a rare event and the determinant factor to consider a forecast model as valuable is primarily conditioned by its ability to detect a fog event. In our case, the accuracy values are not essential, because the successful forecasts cannot be differentiated in terms "fog" or "no fog" event. However, its evolution is an interesting information to point out the model properties. Aside from this mentioned limitation, these score variations reveal a very high correspondence between the fog climatology in the Lindenberg area and the model forecasts. Regarding the fog occurences (Figure 4.3), the oscillations seem to follow the day/night time evolution. A relation can be detailed so that the increase of fog occurence involves a decrease of the accuracy values.

To understand the causes of these variations, the bias score, which is able to differentiate the sources of forecast errors, has been analysed. The bias underlines a bivalent time evolution in the LM-PAFOG forecast qualities and a day/night oscillation is also identified (Figure 4.4-b). Each night, between the 18th and 36th forecast hour and after the 42nd hour, the model shows a tendency to overestimate the number of fog events. On the other side, LM-PAFOG systematically underestimates the number of fog events in the afternoon with a value clearly below the equilibrium value of 1. However, the results cannot be characterised so simply. In the first six forecast hours, corresponding to night time, the bias points out a significant underestimation trend. Such a tendency can be

influenced by the "spin up" phase of the forecast. In the first forecast hours, the model needs a few hours to incorporate the forcing due to the initialisation. This assumption can be confirmed by the successive increases of the bias score between the first night periods. However, the tendencies, highlighted by the bias score, have to be balanced with the low number of fog events. The lower the visibility threshold is, the higher the influence of a fog event is in the score equation. Considering the different visibility thresholds, this consequence is clearly identified in case of overestimation. The model behaviour in phases of overestimation thus shows exaggerated variations due to the shortness of our studied period.

(a)   (b)
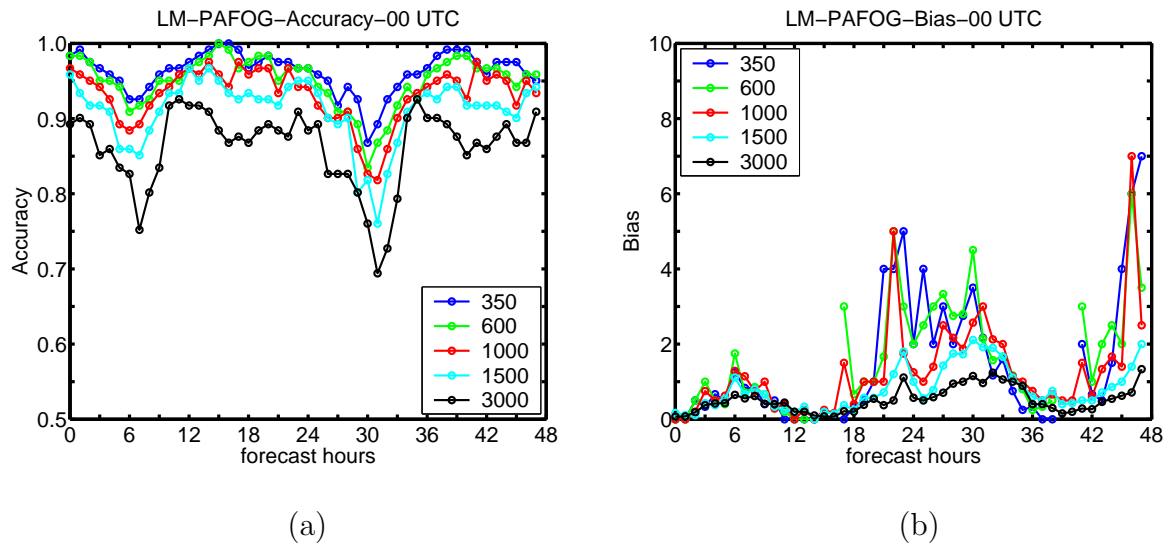
Figure 4.4: Time evolution of accuracy (fig. a) and bias (fig. b) per forecast hours and for five different visibility thresholds (350, 600, 1000, 1500 and 3000 m) based on the LM-PAFOG forecasts initialised at 00 UTC .

The first results have already identified a large fluctuation in time of the forecast performances. However, the skill measures cannot perform an identification of the origin of forecast properties in an individual score evaluation. Based on the contingency table results, a common tool called Relative Operating Characteristic (ROC) helps to identify the detection quality of the model by consideration of hit rate and false alarm rate in the same plot. This score combination gives a complete description of the forecast skill. The hit rate measures the forecast correctness in a foggy situation and the false alarm rate penalises the surplus of fog forecasts in the case of "no fog" situations. A good skill in a ROC diagram means a significant improvement of the forecasts. Generally, proximity to the upper left hand corner of the plot in ROC indicates increasing skill of the forecasts.

Before presenting the results, note that the ROC diagrams used here are applied for the evaluation of deterministic forecasts. Originally, the ROC approach is used for the treatment of probabilistic results. Due to the continuous structure of the probability value, a curve normally results, corresponding to the discrimination capacity of the forecast system for each probability. In our approach, for each forecast situation (a chosen forecast hour and a chosen visibility threshold) the statistical results can only correspond to a probability of 100%. Illustrated in Figures 4.5 (a)-(c), the forecast scores have been

computed per visibility threshold and per forecast hour in ROC diagrams. The splitting of the forecast hours into 6 hour intervals gives a comprehensive time evolution of the forecast skill. To identify the conditions in which LM-PAFOG delivers the best forecast, the forecast skills of all 48 forecast hours have been summarized in these Figures.

In a first overview, the ROC diagrams show a large diffusion in the performance of the model forecast, depending on the forecast time and the visibility thresholds. Focusing on the visibility thresholds, LM-PAFOG can reach very good performance for the lowest values of the visibility threshold (350m): the hit rate can reach 80% and more and the false alarm rate stays below 10%. However, the forecast skills deteriorate strongly with higher visibility thresholds. For a visibility threshold of 3000m, the hit rate maximum reaches 40 % and the false alarm rate can reach 20% (Figure 4.5-c). In this analysis, the results still have to be balanced with the low number of encountered fog events during the four month period. The best forecast skill in case of dense fog event cannot be concluded clearly. The low occurence of dense fog events during the studied period can influence strongly the statistical results. If the chosen visibility threshold is reduced, the sample of considered fog events decreases dramatically. For a visibility threshold restraining to the dense fog events (350m), the hit rate value can thus more easily reach high values due to the lack of resolution in the statistic study.

Besides the difficulty to point out the effect of fog intensity on the forecast performance, the quality fluctuation in terms of forecast duration can be identified. For the lowest visibility thresholds, the LM-PAFOG performances report a "spin up" effect: in the first forecast hours, the model has to assimilate the initialisation forcing. In the first 6 hours, LM-PAFOG is not able to produce any dense fog cloud ($HR = 0\%$). Only for a threshold of 3000 m, the hit rate increases around 10-20%. As already mentioned in this section, the forecast performances are independent of the forecast duration. The performances are not significantly deteriorated with prediction duration. However, the results are correlated with the period of the day, which is currently forecasted. The statistical appraisals, corresponding to the same period of the day (i.e the same colour of the marker), deliver values close to each other. However, for each period, the model qualities are strongly different. In the morning (red) and in the evening (green), the hit rate values vary between 20 and 50%. LM-PAFOG does not produce any fog cloud during the afternoon (13-18 hours and 37-42 hours intervals): the hit rate stays on the 0% mark. Such score variations highlight an obvious difficulty of the model parameterization to forecast fog in the afternoon.

The statistical assessment of the LM-PAFOG forecast can be partially summarised by the time evolution of the Equitable Threat Score, ETS (Figure 4.6). As a skill score, its values measure the improvement of the forecast system, compared to a random forecast, and the results of the different visibility thresholds can be compared to each other.
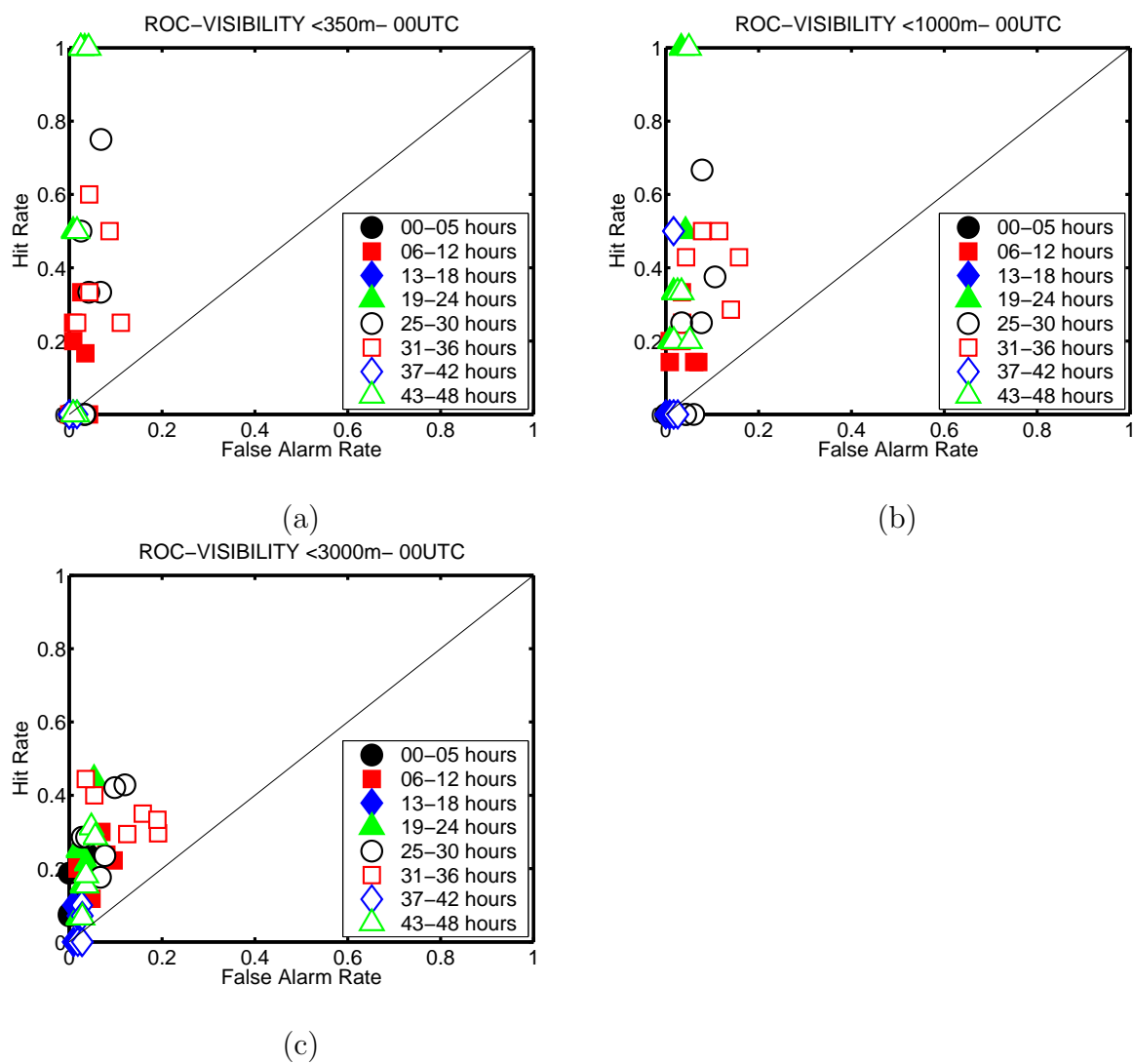
Figure 4.5: ROC per forecast hours and for three different visibility thresholds 350 m (a), 1000 m (b), 3000 m (c) based on the LM-PAFOG forecasts initialised at 00 UTC. The diagonal line represents a hypothetical forecast with no skill.

The time evolution of the ETS confirms the bivalent forecast quality by day and by night. In the afternoon, the ETS also underlines the difficulty of the model. In the remainder of the day, the ETS values detail that of the fog events that were forecasted, around 20% were correctly forecasted. Moreover, the fog density does not have a significant influence on the model performance with values varying around 10-30%. However these moderate ETS values highlight the necessity of further developments. First of all, the forecast quality has to be equivalent and consistent during the entire forecast duration.
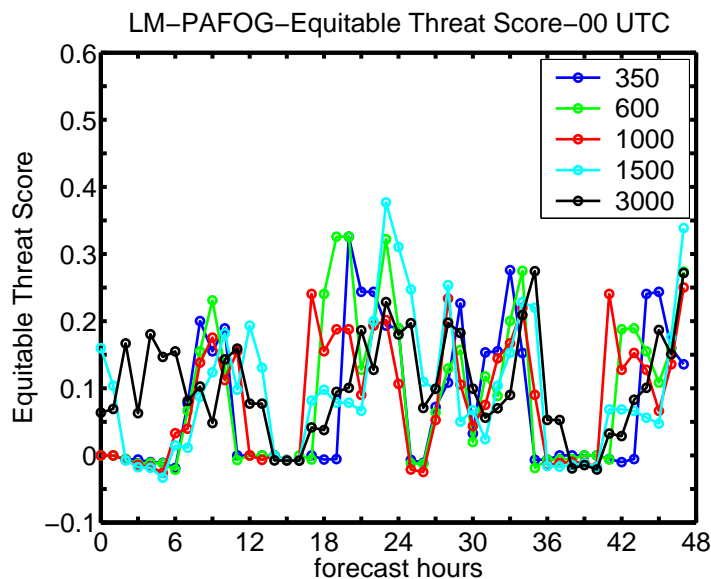
Figure 4.6: Time evolution of the Equitable Threat Score per forecast hour and for five different visibility thresholds (350, 600, 1000, 1500 and 3000 m) based on the LM-PAFOG forecasts initialised at 00 UTC .

4.3.4 Conclusions

The statistical study allowed a complete diagnostic of LM-PAFOG forecast performances. In a systematic comparison of the 2m-visibility forecasts with the corresponding measurements during four months, the forecast performances of LM-PAFOG have been highlighted and sorted by different visibility thresholds and by forecast hour. The results suggest that the forecast duration does not have a significant influence on the forecast skills. The model performances behave differently whether it is day or night and the model qualities show a pronounced diurnal cycle. LM-PAFOG clearly has some difficulty to detect fog in the afternoon, while the model can identify the fog events in the remainder of the day and those independently of the fog density.

However, the chosen approach for this statistical study was a severe constraint in the evaluation of the model performances. Only one measurement point supplied regularly measurements of 2m-visibility during the complete 4 month period. A comparison of a single point of the forecasted area with the corresponding measurement can bias the performances of different forecast systems. For the evaluation of a three-dimensional fog forecast model, the focus on a single point of the forecast area is a very challenging exercise.

The incertitudes concerning the spatial component are not incorporated in the results. A small variation in time or in space can cause a false forecast. Unfortunately, the choice of a single point involved a very low occurrence of fog events in spite of the four month study. The few number of fog events has shown a significant influence on the accuracy of each statistic score. Further study comparing 3x3 and 5x5 grid points area centred on the measurement point have been performed (results not shown). Nevertheless, due to the low occurrence of fog event, no significant differences between the several statistical results can be recognised.

The statistical approach in a restricted environment has already detected strengths and weaknesses of the forecast system in terms of time of day and in terms of fog intensity. Nevertheless, the evaluation study has to be extended and will focus on the parametrisations of the model in order to understand the cause of such a forecast performances. In the next section (Section 4.4), the LM-PAFOG forecast quality will be detailed in the study of three fog events. A detailed analysis of the dynamics and thermodynamics evolution of LM-PAFOG as well as a study of the spatial extension of the fog parcel should help to identify the responsible processes.

4.4   Detailed analysis of LM-PAFOG forecasts of selected fog episodes

4.4.1   Method

To complete the evaluation of our model, the parametrisations of the physical processes involved in the fog formation also have to be evaluated. Such evaluations reveal the complexity of the fog formation. Three primary processes can be identified for the formation of fog. Cooling, moistening or turbulent mixing processes at the surface can create a saturation situation resulting in fog appearance. The thermodynamic and dynamical parameters interact together for the formation or dissipation of fog. *Duynkerke* (1991) identified the most important parameters involved in the three mechanisms:

- cooling of moist air by radiative flux divergence,

- vertical mixing of heat and moisture,

- vegetation,

- horizontal and vertical wind,

- heat and moisture transport in soil,

- advection,

- topographic effects.

Moreover, each parameter is dependent on the actual synoptic situation, the season and the localisation. In complex topography the advection initiated by the katabatic and anabatic flows controls the cold air pooling and outflows in the valley. The cloud cover

can also strongly modify the energetic balance at the surface. The presence of clouds can increase the incoming longwave radiation and limit the longwave radiative cooling. Once the fog has formed, the fog development may be further influenced by

- longwave radiative cooling,

- gravitational droplet settling,

- fog microphysics,

- shortwave radiation.

In order to evaluate the parametrisation, the fog to be analysed has to be selected respecting the dependencies. Three different fog periods have been selected:

- Episode 1— October 6th and 7th, 2005: Under the influence of a dominating high pressure system an absolutely clear sky supplied the necessary conditions for a radiative fog formation at sunrise. The only clouds forming in the forecast area are exclusively fog. The results are independent of the cloud cover. The influence of radiative cooling processes can be isolated.

- Episode 2— September 26th to 27th, 2005: After a rain episode advecting a warm and humid airmass, the Lindenberg area stays under the influence of a strong high pressure system. During the night, the radiative cooling induced the formation of a dense fog system in spite of the presence of a mid-altitude cloud cover (4/8). In this second step, the capacity to forecast fog in cloudy situations can be evaluated.

- Episode 3— December 6th to 7th, 2005: With the residual cloud cover of a cold front, a stable and moist boundary layer is present in the Lindenberg area and induces a reduced visibility as well as the formation of low stratus and fog during the night. In a weather situation close to saturation, the accuracy of the condensation process can be evaluated. A light cooling of the atmosphere or a light turbulent mixing in the boundary layer can modify the time evolution of fog.

The model forecasts of these three selected fog periods have been compared with the SYNOP measurements at the Lindenberg observatory (Figure 4.2). The consistency of the fog forecast will be evaluated considering the spatial component of the forecasts. A comparison of 2m-visibility, 2m-relative humidity and 10m-wind speed at different locations in the Lindenberg area has been carried out. Moreover, the single point corresponding to the Lindenberg observatory location has been compared with the set of boundary layer measurements in situ (vertical profile of wind, temperature, relative humidity as well as radiative fluxes at the surface). With theses successive steps, the comparison approach will highlight the advantages and shortcomings of LM-PAFOG modelling to deliver a successful fog forecast.

Note that there are different types of visibility observations. Visibility observations are still performed manually at some stations. All horizontal directions are taken into account when reporting the minimum visibility. Other stations uses automatic visiometers. These measure the visibility over a 2 litre volume and return a value at one point. The horizontal

inhomogeneities in the visibility, which is apparent to a manual observer, cannot be taken into account. Nevertheless, it is probably appropriate to consider visibility as a point value if the minimum visibility is less than the numerical grid length.

4.4.2 Episode 1, October 6-7th, 2005: Radiative fog without cloud cover

Description of the fog period

The situation over central Europe and the Lindenberg area is dominated by high pressure with an inflow of relative dry air from an easterly direction (Figure 4.7). In the following days the high pressure moves slowly towards the East. The dominating high pressure system ensures a clear sky. During the night, the radiative cooling and turbulent mixing initiate the first formation of fog. By sunrise, the temperature inversion is maintained but in the morning the lower atmosphere is gradually heated: the inversion and the condition of supersaturation near the ground slowly disappear.

In the Lindenberg area two radiative fogs were observed in the southern part of the studied domain. During the early morning of October 6th, the fog grew at the western part of the domain and stretched out until it covered the southern half of the domain. Only at 12 UTC, the last fog disappeared. During the night to October 7th from 21 UTC to 09 UTC, the fog developed at the west and east of the domain and extended to fill a second time the south half of the studied area. In both fog periods visibilities of 300m or less were reported at several sites (Figure 4.9).
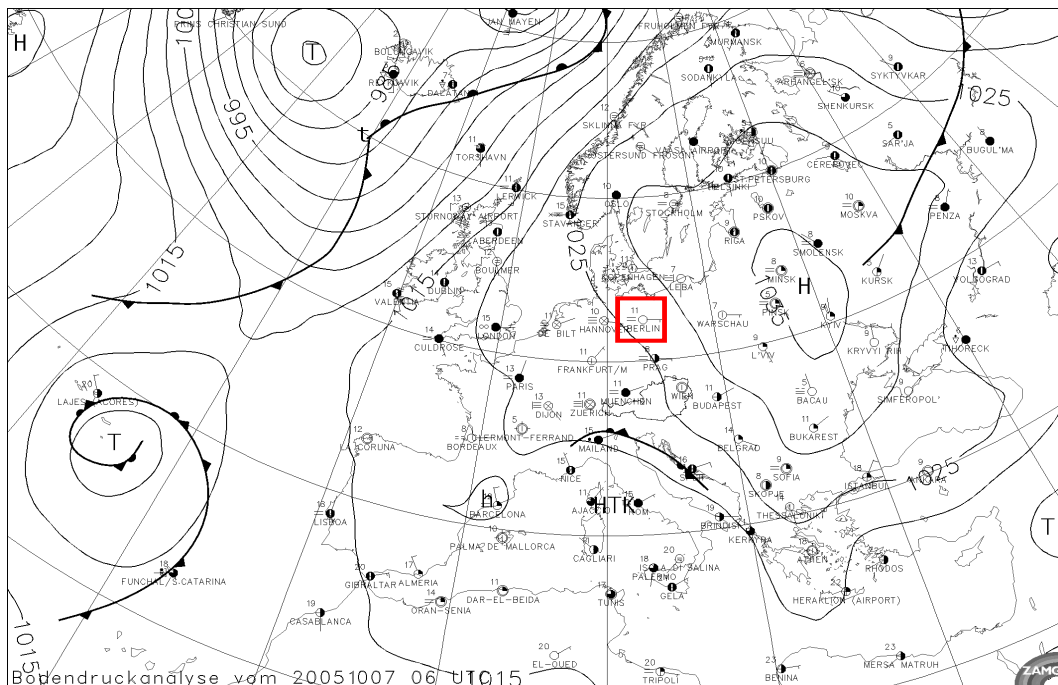
Figure 4.7: Surface pressure analysis on October 7th, 2005 at 06 UTC, supplied by the Central Institute for Meteorology and Geodynamics (ZAMG), Vienna, Austria. The red frame delimits the forecast area.
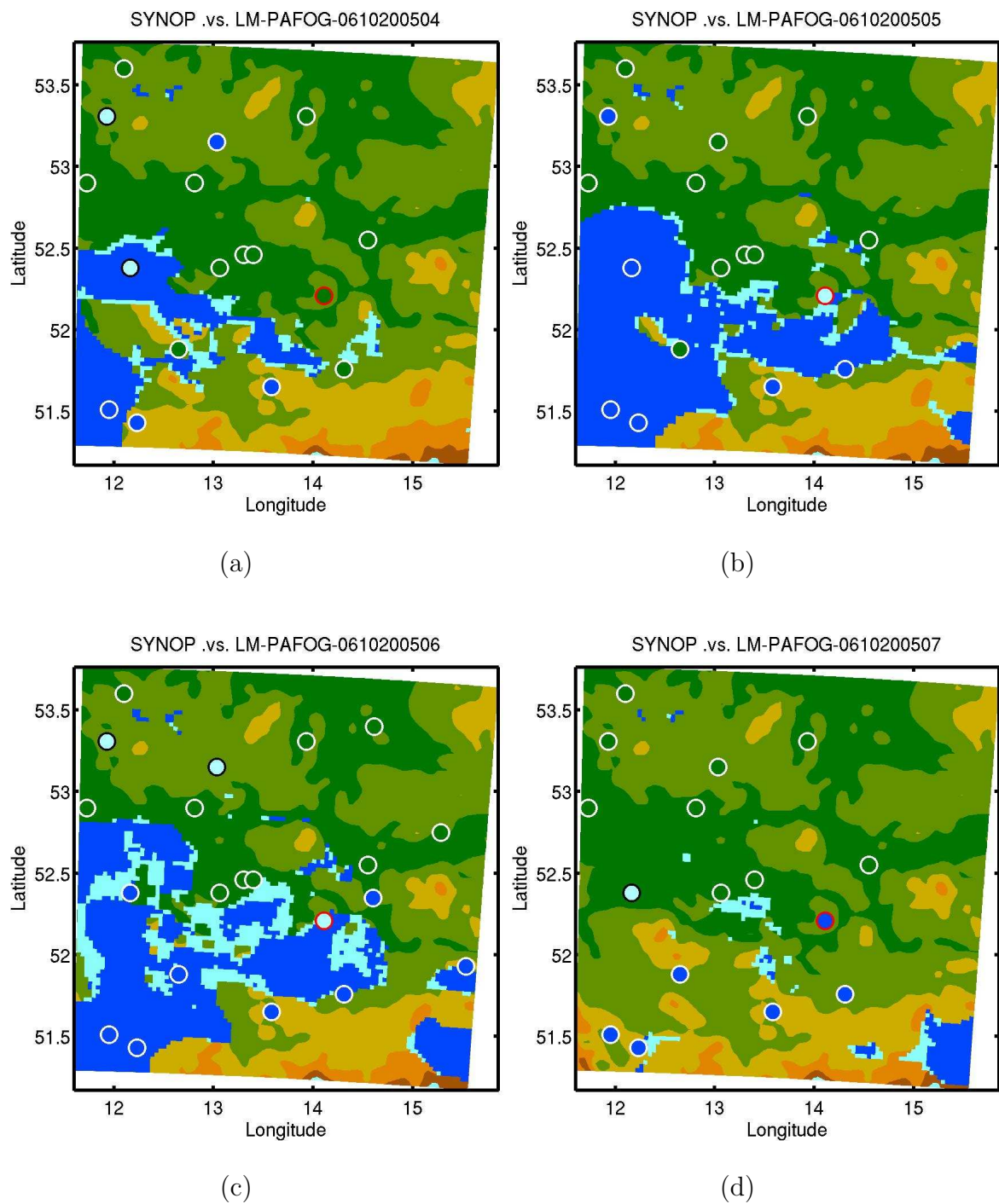
Figure 4.8: Horizontal cross-section of 2m-visibility in the Lindenberg area at October 6th, 2005 04-07 UTC. The surface corresponds to the 2m-visibility forecasts. The circle markers correspond to the position of the visibility measurements. The red circle corresponds to the Lindenberg observatory. The visibility values have been separated in three categories. **Deep blue** corresponds to fog with a visibility below 1000m. **Cyan** represents fog with a visibility between 1000 and 3000m. **Green** and brown areas denote areas without fog (visibility exceeding 3000m).

Appraisal of the forecasted fog area

In a first step, the fog forecasts are evaluated only considering the presence of fog or not at different locations in the domain. A comparison of the fog spatial distribution between the 2m visibility between LM-PAFOG forecast and the visibility measurements supplied by the SYNOP network is done. The large influence of local parameters in the fog formation as well as the type of measurement systems strongly restrain the comparison. Only the grid points of the forecast domain corresponding to the locations of SYNOP stations (Figure 4.2) were extracted from the forecast and compared with the measurements in contingency tables in terms of visibility events for each forecast hour (Figure 4.8). Two visibility thresholds have been chosen: 1000m and 3000m.

The appraisal of the visibility forecasts has been summarised in Figures 4.9 a & b in a very pragmatic approach. The number of stations observing a fog (blue line) and the number of extracted grid points forecasting fog (red line) have been identified for each forecast hour. The proportion of agreements (type "fog-fog") between observed and forecasted fog periods has thus been deduced (green line). Regarding the time evolution, LM-PAFOG forecasts are able to reproduce in good agreement the formation and evolution of the fog area. In this case the forecasted fog occurs generally at the right time and at the right place (red and green curves sticking together). Nevertheless, the model tends to underestimate the fog areas. The fog appears with a delay of a few hours and no fog is still present in the Lindenberg area after 06 UTC.

Different hypotheses can explain this underestimation tendency. The chosen approach restrains the comparison to 28 of 10000 grid points to estimate the spatial extension of a fog episode. The fog episode can be forecasted at the right time, however if it does not occur exactly at the location of a station, the value of the forecast cannot be positively confirmed. Figure 4.8 points out this typical situation. The stations surrounding the forecasted area have detected a fog episode but it is not formed by the model at these places. Moreover, the fog could have been formed in upper layers up to the 2m level. And, in this study the vertical component is not considered.

Another factor could be the visibility parametrisation. The presence of fog is not directly deduced from the presence of liquid water close to the ground, but it is defined by the concept of visibility which has to be below 1000m in case of fog. As already mentioned in section 3.6, the visibility parametrisations are generally empirical relations deduced from microphysic and optical measurements in situ. Several studies have pointed out the importance of the microphysics parameter variations for the different types of fog (*Colomb* et al., 2007; *Gultepe* et al., 2006b). In LM-PAFOG, the influence of aerosol concentration, CCN concentration and liquid water content is considered to determine the visibility forecasts. Note that between the results for the 1000 and 3000m thresholds the areas of the forecasted fog show significant differences in their extension. In our case the visibility parametrisation may still need to be further calibrated and thus adapted to the special environment of the Lindenberg domain. The forecasted fog extension can be improved through the visibility parametrisation, however the single visibility parametrisation cannot explain the limited time periods of fog.
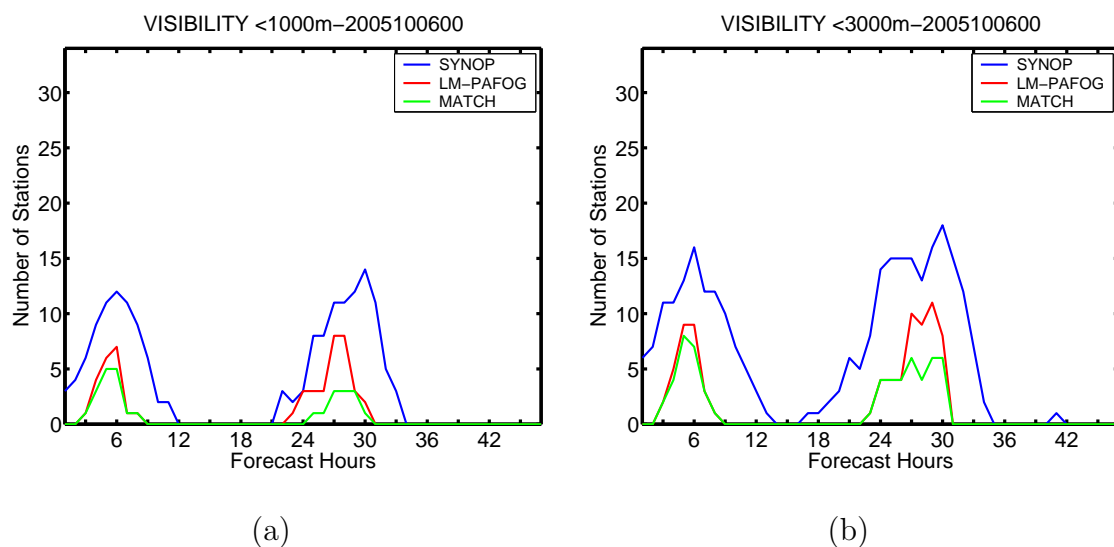
Figure 4.9: Comparison of the time evolution of LM-PAFOG fog spatial distribution forecast with the 2m-visibility measurements extracted from the SYNOP data network on the Lindenberg area at October 06-07th, 2005 for a visibility threshold of 1000 m (a) and 3000 m (b).
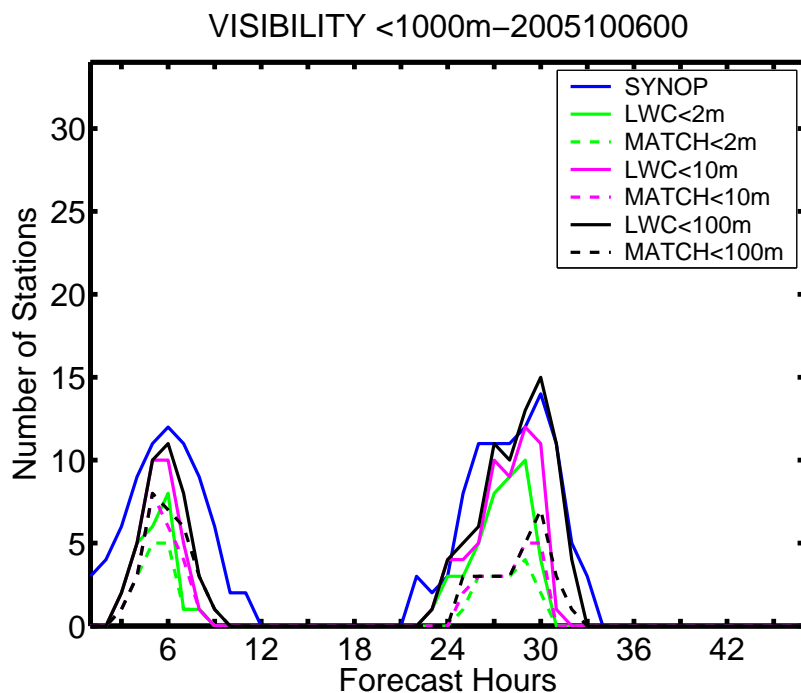
Figure 4.10: Comparison of the time evolution of LM-PAFOG fog spatial distribution forecast in terms of liquid water content with the 2m-visibility measurements extracted from the SYNOP data network (full line) in the Lindenberg area at October 06-07th, 2005 for a visibility threshold of 1000 m. Dashed lines correspond to number of agreements between measurements and forecasts.

Therefore, a last study concerning the spatial extension of the forecasted fog area has been carried out avoiding any considerations about visibility and considering the vertical distribution of fog.

For this comparison the forecasted fog is thus considered as a presence of specific water content exceeding a value of 0.01 g/kg. Such threshold values have been deduced from fog measurement campaigns (*Kunkel*, 1984; *Gultepe* et al., 2006a) and corresponds to an earliest or latest state of fog presence, i.e. a visibility value of roughly 3000m depending on the microphysical structure of the cloud.

The evaluation of the fog spatial extension consists in comparing the 2m visibility measurements with the presence of forecasted liquid water content in the first 2, 20 and 100m above the ground. The liquid water content in the model column was integrated from the ground to the defined altitude. With the same modality as in Figure 4.9, the number of SYNOP stations detecting fog (blue line) and the number of extracted grid points forecasting fog in the first 2, 10 and 100 m (respectively green, magenta and black lines) has been sorted per forecast hour. The agreements between measurements and fog forecasts are pointed out (dashed lines) in Figure 4.10. With this analysis we note that the forecasted fog area increases significantly if the fog, present in the first 10m, is considered even if they do not have a contact with the ground. Extending the comparison to the first 100m the increase of the forecasted fog area is minor. However, the number of agreements between measurements and forecasted fog is not improved in the same proportions in spite of the larger fog area. Moreover, this new consideration of the fog area has not explained the difficulty of LM-PAFOG to correctly describe the duration of the fog. The duration of the forecasted fog has not been improved.

This analysis highlights the difficulties to evaluate the fog forecast quality produced by a three-dimensional model. The localised formation of fog does not allow us to compare the local measurements with a large model area. Nevertheless, considering the 28 grid points corresponding to the SYNOP station location, LM-PAFOG depicts the time evolution of fog in good agreement. However, the model shows some difficulties to form a fog area with a large sufficiently contact area with the ground. This aspect of the forecasted fog has a decisive influence on the performance of LM-PAFOG, i.e. delay in the time evolution of the fog episode. In this case, such limitations may highlight the weaknesses of the parametrisation in the lowest atmosphere.

Analysis of thermodynamic and dynamic parameters close to the ground

After a spatial analysis of the fog distribution based on the sparse location of the SYNOP stations, a detailed comparison has been conducted based on the large set of available measurements supplied by the meteorological observatory of Lindenberg. This study only focuses on the grid points of the forecast domain corresponding to the locations of the measurements.

The selected fog episode corresponds to a pure radiative fog forming at sunrise. The influence of the radiative cooling during the night as well as the heat and moisture turbulent mixing has to be accurately identified by the model to obtain a successful forecast. A light wind field ensures the necessary vertical mixing.

In a first step, the time evolutions of 2m visibility, 2m temperature, 2m relative humidity and 10m wind speed fields have been examined separately for each SYNOP station

location and compared with the measurements. The results are presented in Figures 4.11, 4.12, 4.13 and 4.14. The numbering of the stations has been defined so that the following numbers are close to the adjacent point in the forecast domain (Figure 4.2). The trend of the thermodynamic and dynamic parameters can thus identify the potential geographical patterns in the results. For our analysis, the forecast domain has been sorted in three areas showing different evolutions of the boundary layer parameters.

The first region, corresponding to the north-north west part of the domain, is described by the grid points 1 to 9. LM-PAFOG shows some difficulties to correctly forecast both fog periods in the region. Only the grid points 1 and 6 have forecasted a short fog period with a visibility between 1000 and 3000m (Figure 4.11). In this region, the forecasted relative humidity is underestimated for the entire simulations. For one part, the low relative humidity value can be explained by the initialisation of the model in this area. The temperature values have been overestimated by more than 2 degrees in the first forecast hours. The first fog period thus cannot be correctly forecasted. In a second part, the wind field is clearly overestimated with a bias usually higher than 2 ms^{-1}. The large mixing occurring in the lowest part of the atmosphere keeps the relative humidity values away from the saturation condition. The moist air close to the ground is continuously mixed with the dryer upper layer of the atmosphere. Therefore, even if temperature and humidity are periodically forecasted correctly, the wind bias forbids any fog formation in this region. The proximity of the domain's lateral boundaries could explain this regional forecast. The lateral boundary values are interpolated in a nesting process using the forecast of the operational LM version. The coarser grid resolution of the LM is not able to differentiate the fine variations taking place close to the ground contrary to the high vertical resolution of LM-PAFOG. Some inaccuracies can be induced by these lateral boundary values.

The second area is described by grid points 10 to 13 and corresponds to the urban area of Berlin. The evolution of fog in cities is difficult to forecast. Urban surfaces exhibit unique exchange processes leading to heat and moisture fluxes that are typically not well represented in the land surface schemes used in mesoscale weather forecast models. Although LM-PAFOG has a land-surface parametrisation considering the urban area, the influence of buildings in the atmospheric boundary layer is strongly simplified. Only roughness length value and evapotranspiration fluxes are adapted. Nevertheless an urban island has a significant impact on low level wind and temperature fields. The traditional land-surface scheme is not able to capture the heat loading and release of the building as well as other heat sources present in an urban area. Such aspects are decisive in this case for a successful fog forecast in the city area of Berlin. Regarding the 2m temperature bias (Figure 4.12), the temperature values are slightly underestimated during the night (22-28 hours). Although no fog was observed in the city, this variation can be responsible for the formation of fog in the model forecasts.
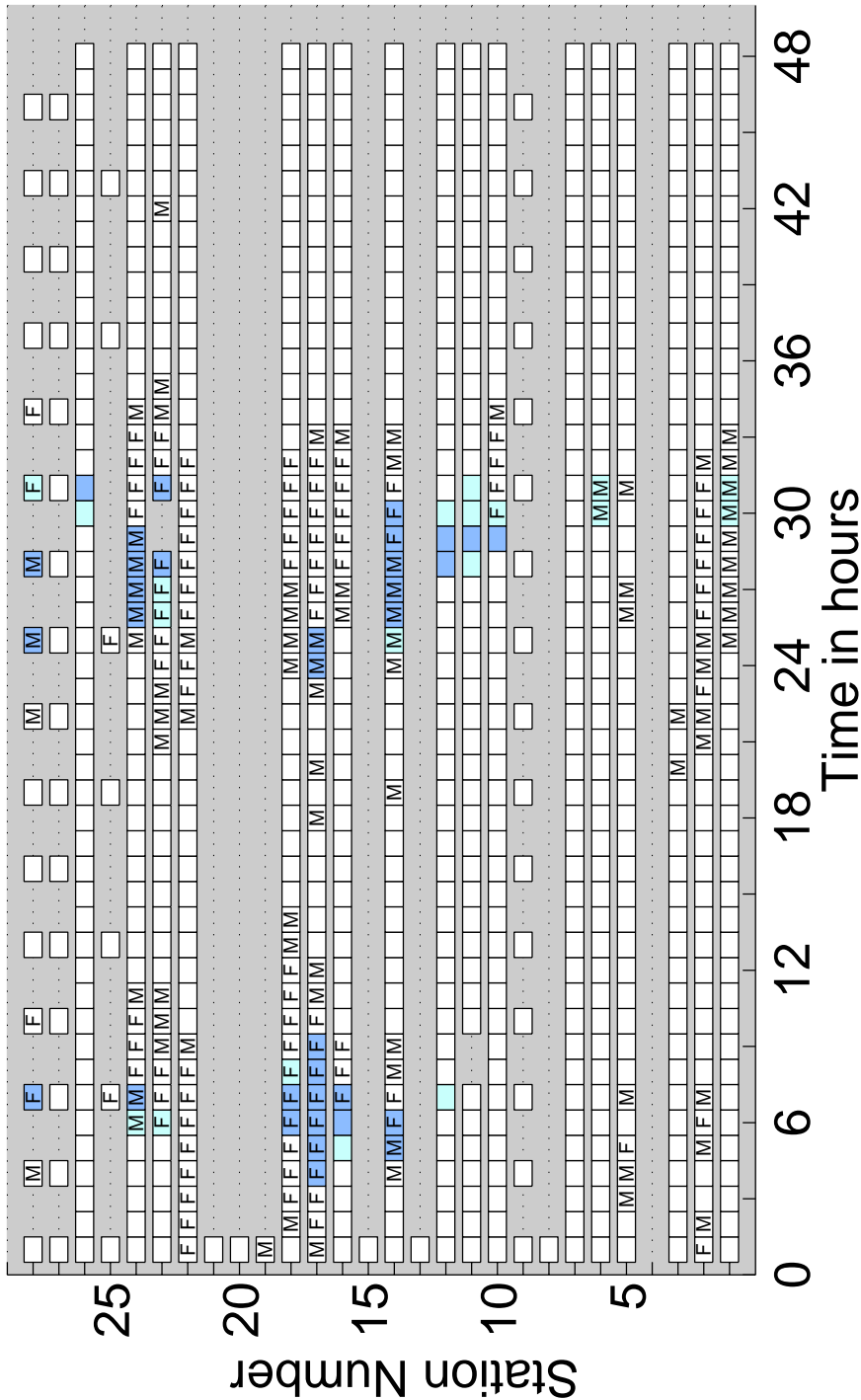
Figure 4.11: Comparison of forecasted 2m-visibility with each SYNOP station in the Lindenberg area at October 6-7th, 2005. Capital letters notify the presence of fog reported from each SYNOP station: **F** corresponds to a fog with a visibility below 1000m; **M** marks a mist with a visibility between 1000 and 3000 m. The colour scale points out the presence of fog issued from the LM-PAFOG forecasts: **deep blue** corresponds to a fog with a visibility below 1000m; **cyan** represents a mist with a visibility between 1000 and 3000m; **white** is the period without fog, i.e. visibility higher than 3000m. Boxes are only plotted where measurements were available. Initialisation: October 6th, 2005 at 00UTC.

Figure 4.12: Comparison of forecasted 2m-temperature with each SYNOP station in the Lindenberg area at October 6-7th, 2005. The colour scale sorts the bias in 5 categories: **deep red** corresponds to an overestimation of the model, with a bias larger than 2°C; **red** corresponds to an overestimation of the model, with a bias between 0.5°C and 2°C; **white** marks the agreement between measurements and forecasts, with a bias between 0.5°C and -0.5°C; **cyan** corresponds to an underestimation of the model, with a bias between -0.5°C and -2°C; **deep blue** corresponds to an underestimation of the model, with a bias lower than -2°C. Boxes are only plotted where measurements were available. Initialisation: October 6th, 2005 at 00UTC.

Figure 4.13: Comparison of forecasted 2m-relative humidity for each SYNOP station in the Lindenberg area at October 6–7th, 2005. The colour scale sorts the bias in 5 categories: **deep red** corresponds to an overestimation of the model, with a bias larger than 5%; **red** corresponds to an overestimation of the model, with a bias between 1% and 5%; **white** marks the agreement between measurements and forecasts, with a bias between 1% and -1%; **cyan** corresponds to an underestimation of the model, with a bias between -1% and -5%; **deep blue** corresponds to an underestimation of the model, with a bias lower than -5%. Boxes are only plotted where measurements were available. Initialisation: October 6th, 2005 at 00UTC.

Figure 4.14: Comparison of forecasted 10m-wind for each SYNOP station in the Lindenberg area at 2005 October, 6-7th. The colour scale sorts the bias in 5 categories: **deep red** corresponds to an overestimation of the model, with a bias larger than 2 m.s^{-1}; **red** corresponds to an overestimation of the model, with a bias between 0.5 m.s^{-1} and 2 m.s^{-1}; **white** marks the agreement between measurements and forecasts, with a bias between 0.5 m.s^{-1} and -0.5 m.s^{-1}; **cyan** corresponds to an underestimation of the model, with a bias between -0.5 m.s^{-1} and -2 m.s^{-1}; **deep blue** corresponds to an underestimation of the model, with a bias lower than -2 m.s^{-1}. Boxes are only plotted where measurements were available. Initialisation: October 6th, 2005 at 00UTC.

The third region, considering the south half part of the domain, is depicted by the grid points 14 to 28. In this area, most fog has been referenced. LM-PAFOG has clearly forecasted both fog periods with a good agreement. The forecasted fog occurs at the correct place. Nevertheless, the duration of the fog periods is underestimated. If the model forms fog, the forecasted areas partially cover the observed period. LM-PAFOG well identifies the first hours of fog periods, however after 8 UTC no fog is further forecasted (Figure 4.11). This trend to early fog forecast can be explained by the evolution of the 2m temperature and 2m relative humidity bias (Figures 4.12 and 4.13). Between the 9th and 15th forecast hours as well as between the 31th and 40th hours, the 2m relative humidity value are strongly underestimated with differences exceeding 5%. Such biases thus strongly restrain the formation of fog in the morning. The low relative humidity values can be partially explained by an overestimation of the 2m temperature during the same period. However, the overestimation pattern in the 2m temperature bias does not correspond exactly to the same underestimation period of the relative humidity values. The retroaction between relative humidity and temperature cannot be the only reason for the early fog formation.

To better understand the processes responsible for this fog formation delay, the analysis focuses particularly on the grid point of the Lindenberg observatory. The larger set of measurements available at this location supplies complementary information. In case of a radiative fog by a preceding clear sky, the fog formation is controlled by the radiative cooling at the surface as well as heat and moisture turbulent fluxes between soil and atmosphere. The observed radiative fluxes at the surface are compared with the model values in Figure 4.15. The radiative balance is well reproduced by the model. The short wave (SW) as well as long wave (LW) fluxes at the ground are easily evaluated in this clear sky situation. Note that the influence of the fog presence can be recognised. In a clear sky, the only influence on the radiative fluxes balance comes from fog. The increase in the LW flux balance points out the presence of fog. Excepting the influence of the fog formation delay, the SW and LW fluxes balance agree very well with the measurements.

Some difficulties concerning the latent and sensible heat flux parametrisation are highlighted. LM-PAFOG forecasts exhibit two distinct performances between day and night time. Before 6 UTC and between 17 and 30 UTC, the sensible and latent fluxes agree well with the observations. Their negative values around -20 Wm^{-2} confirm the cooling of the ground and a slight increase in surface humidity. However, between 6 and 17 UTC and 30 and 40 UTC, the fluxes disagree strongly with the local observations. The sensible flux is overestimated with a bias reaching 100 Wm^{-2} at 12 UTC. The latent flux continuously stays close to the 0 Wm^{-2} mark. With such a behaviour a larger heating due to the sensible turbulent fluxes and a restrained moisture turbulent flux close to the ground are diagnosed for this selected fog episode. The vertical profiles of specific humidity and temperature, presented in Figure 4.16 a & d, confirms such an evolution of the turbulent flux parametrisation. Until 6 UTC, the temperature inversion caused by the radiative cooling at the ground agrees well with the observations, and the specific humidity is similar to the measurements. However, at sunrise the forecasted specific humidity does not increase anymore and stagnates around a value of 7.4 g/kg, while the measurements reach values up to 8.5 g/kg. Moreover, the release of the temperature inversion occurs faster than in the in-situ observations.
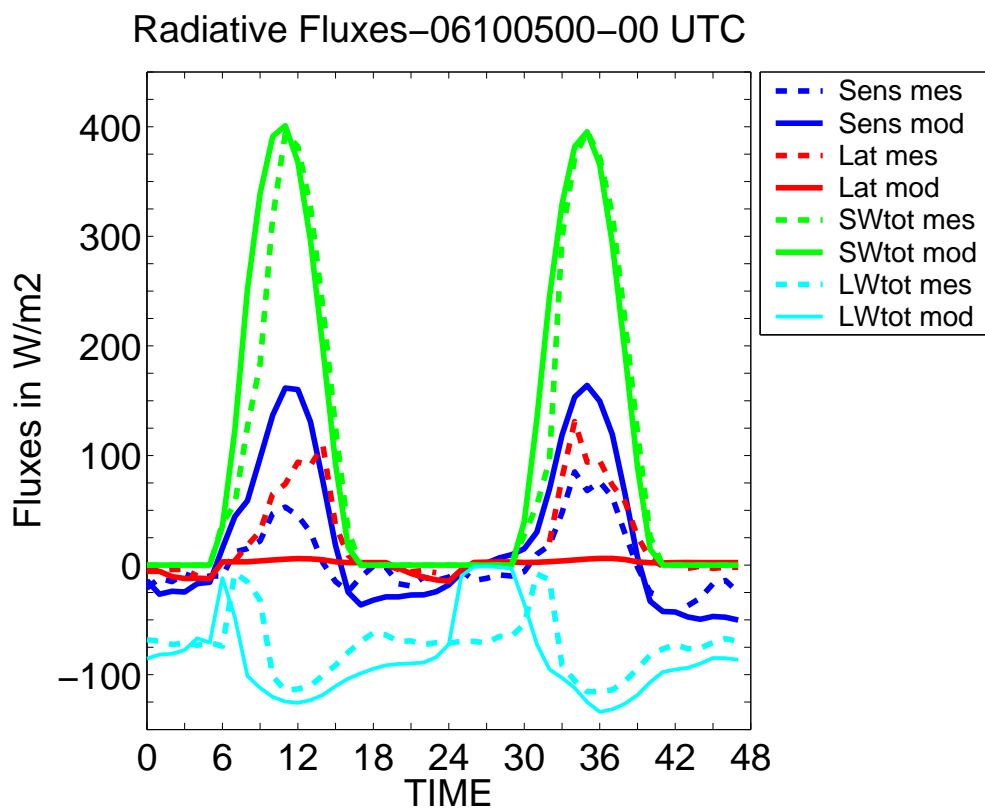
Figure 4.15: Time evolution of radiative fluxes at the ground, forecasted by LM-PAFOG. Initialisation: October 6th, 2005 at 00 UTC.
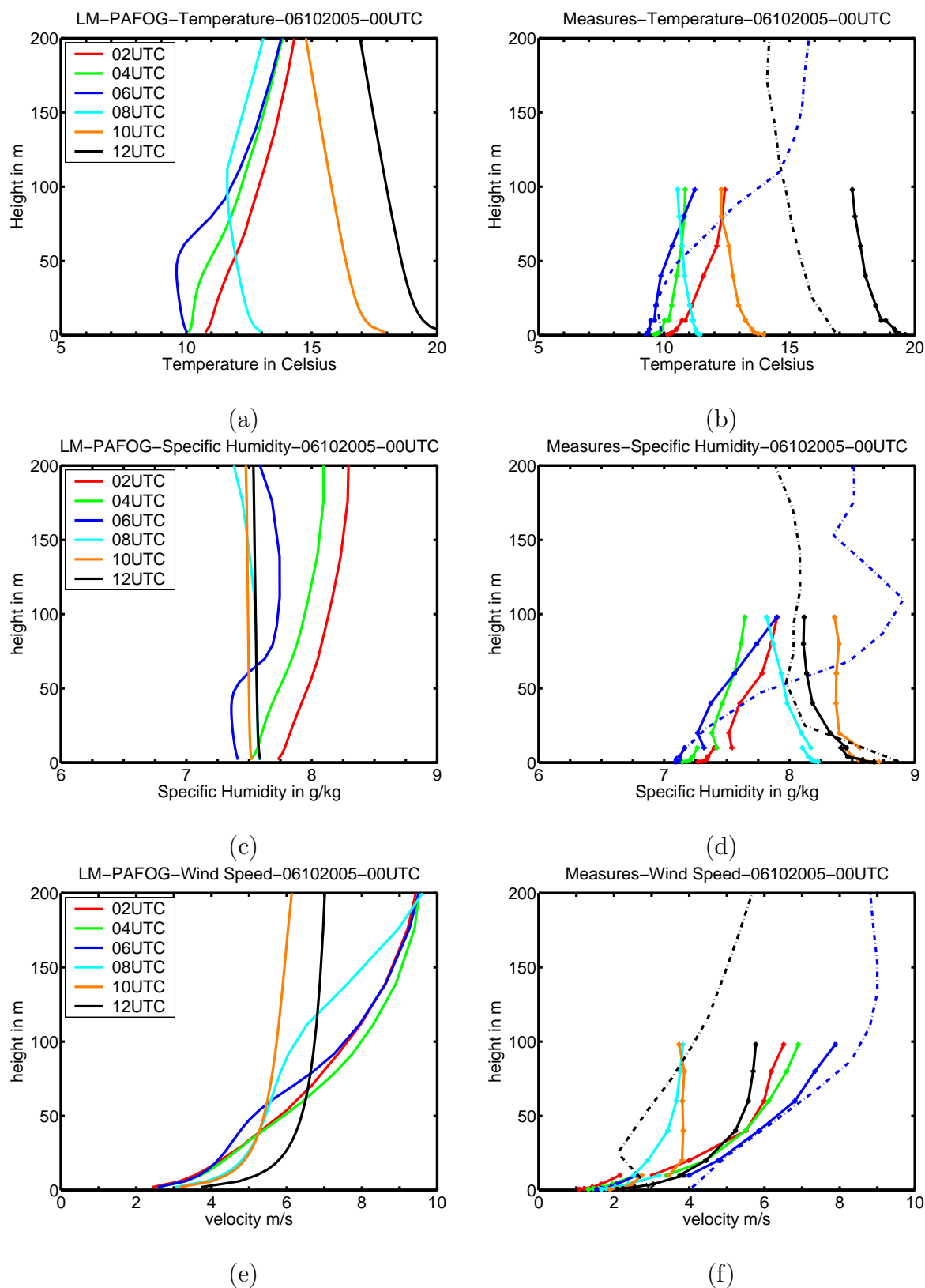
Figure 4.16: Vertical profiles of temperature, specific humidity and wind speed, forecasted by LM-PAFOG and reported from the measurements at the Lindenberg observatory. October 6th, 2005 02-12 UTC. Full lines correspond to the mast measurements and the dashed lines represent the radiosounding profiles.

The condition of saturation at the ground cannot be filled much longer. Regarding the wind profiles (Figures 4.16 e & f), the vertical profiles match with the observations despite of a light overestimation in the first meters. The wind field forecast cannot be responsible for such a deterioration of the fog forecast performances. The turbulent mixing parametrisation seems to play an important role in the deterioration of the fog forecast quality.

Conclusions

This selected fog period supplies the necessary conditions for a radiative fog formation. A strong radiative cooling during the night as well as the heat and moisture turbulent mixing at the ground have been observed. Under these conditions, LM-PAFOG is able to combine these different ingredients involved in the fog formation. Both fog periods have been forecasted. However, the spatial extension and duration of the fog episode have been underestimated by the model. The performances of the LM-PAFOG forecasts are controlled by the contribution of the parametrisation influences at the interface soil-atmosphere. The radiative cooling and the heat transport at the ground are forecasted well, which generally ensures an accurate temperature forecast at the ground. Nevertheless, the forecast performances have pointed out strong variations of forecast performances between day and night time caused by the turbulent mixing parametrisation. In a calm and stable boundary during the night, LM-PAFOG delivers accurate fog forecasts in accordance with the spatial distribution and time period of fog. However, when the turbulent mixing becomes more pronounced due to the sun radiative warming, the forecasted moisture turbulent fluxes between soil and atmosphere do not follow a similar increase. The presence of fog at sunrise cannot be ensured involving a underestimation of the forecasted fog period.

Moreover, the local formation of such a radiative fog is sensitive to any spatial variation of its environment. An inaccurate initialisation of the lateral boundary of the forecast domain or an unadapted parametrisation of the soil properties (urban island) are sufficient to deteriorate the fog forecast.

4.4.3 Episode 2, September, 27th 2005: Radiative fog after a rain event

Synoptic situation

During September 26th and 27th, the situation over central Europe and the Lindenberg area is dominated by high pressure with weak wind and pressure gradients. A low pressure system south of Island (Figure 4.17) moving to the east is slowly approaching bringing in colder and windier weather during the next coming days. In front of the system flows a relative warm and humid air mass from south/southwest over Central Europe. After a rain episode the day before, a residual cloud cover is sparsely present in the Lindenberg area and a moist environment is observed at the surface. In several places, radiative cooling during night time causes radiation fog in cloud free areas. In the Lindenberg area radiative fog periods were observed in the night to the 27th September from 19 UTC until 08 UTC of the following day (Figure 4.18). Localised formations of fog have been observed in the north, east and south west part of the forecast area. Visibilities of 200 m and below have been reported at several sites.
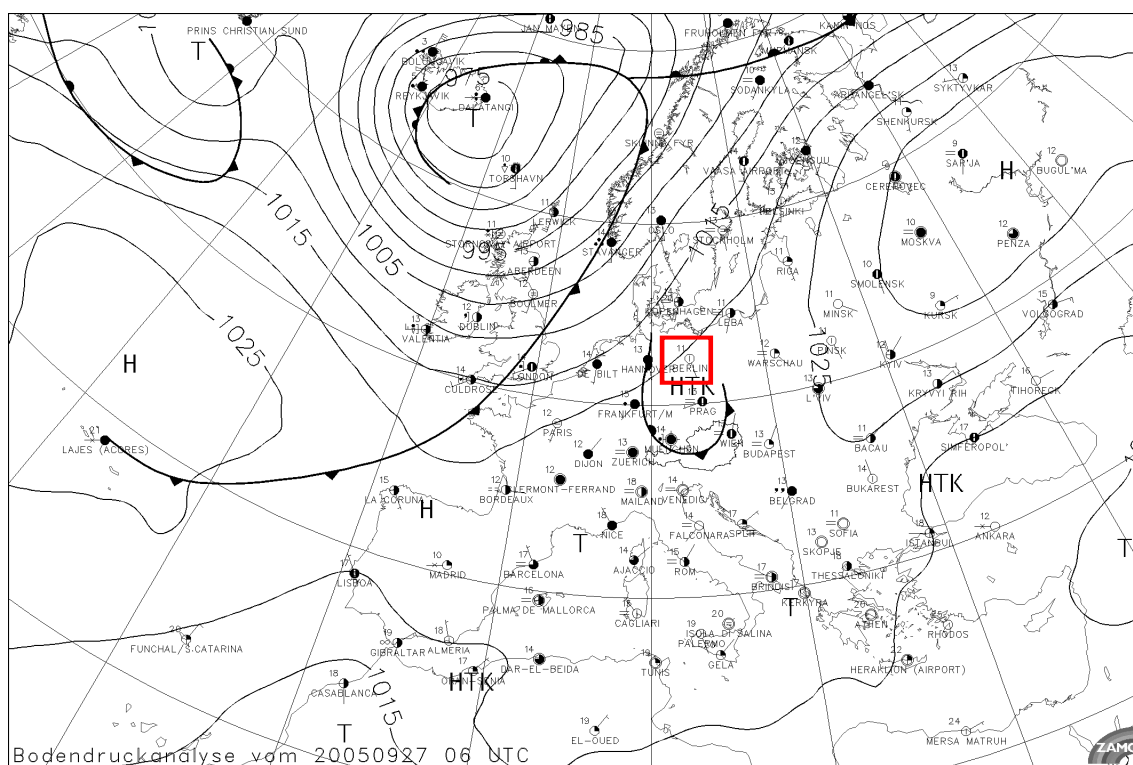
Figure 4.17: Surface pressure analysis on September, 27th 2005 at 06 UTC, supplied by the Central Institute for Meteorology and Geodynamics (ZAMG), Vienna, Austria. The red frame delimits the forecast area.
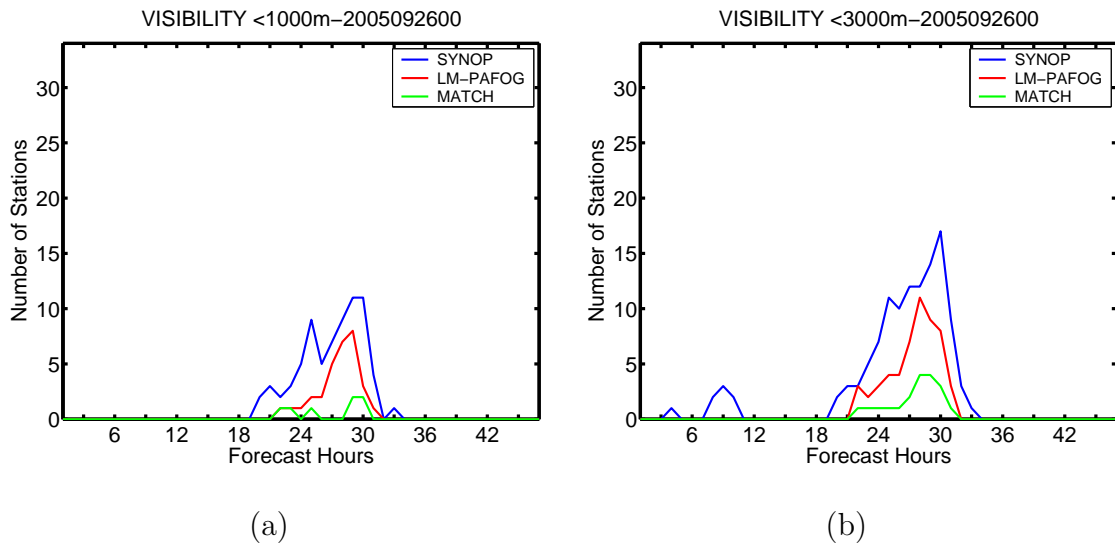
Figure 4.18: Comparison of the time evolution of LM-PAFOG fog spatial distribution forecast with the 2m-visibility measurements extracted from the SYNOP data network in the Lindenberg area at September 26-27th, 2005 for a visibility threshold of 1000 m (a) and 3000 m (b).
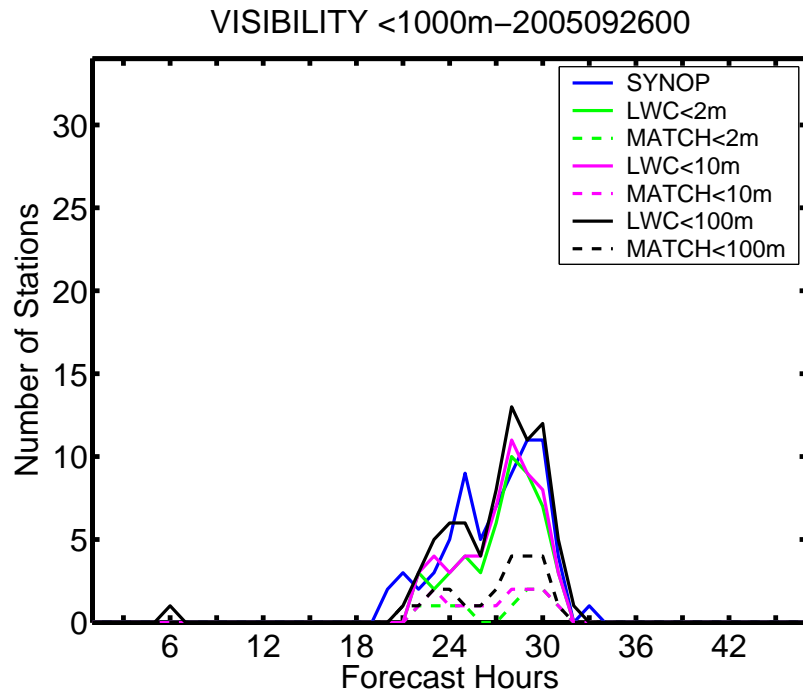
Figure 4.19: Comparison of the time evolution of LM-PAFOG fog spatial distribution forecast in terms of liquid water content with the 2m-visibility measurements extracted from the SYNOP data network in the Lindenberg area at September 26-27th, 2005 for a visibility threshold of 1000 m. Dashed lines correspond to number of agreements between measurements and forecasts.

Appraisal of the fog forecast

As in the last selected fog episode study, the spatial extension of forecasted fog and the influence of thermodynamic and dynamic parameter involved in the fog formation have been analysed successively.

The forecast performances of LM-PAFOG were analysed first in a comparison of the forecasted fog spatial distribution and the 2m visibility measurement network, present in the Lindenberg area. The comparison has been conducted for two different visibility thresholds: 1000 and 3000 m. The results are presented in Figures 4.9 a & b. Regarding the time evolution of the fog episode we note that LM-PAFOG fog forecasts occur during the corresponding observed fog period. Moreover, the extension of fog is equivalent to the observed surface. A slight underestimation trend of the fog spatial extension can be identified. Such conclusions have to be considered carefully due to the large variability of the SYNOP observation density in the Lindenberg area. The formation of fog in an area of high measurement density thus has a larger influence in this analysis approach. Nevertheless, this comparison is sufficient to analysis the spatial inaccuracy of the fog forecasts in this case. The number of agreements between forecasts and observations (green curve) stays very low. No more than two grid points correspond to the 2m-visibility measurements: the fog does not form in the correct place.

In a second step the fog spatial extension is again considered as the presence of the liquid water content in the first 2, 10 and 100 m of the atmosphere and is compared to the visibility measurements (Figure 4.19). The influence of the visibility parametrisation on this analysis can be avoided and the fog area, which has no contact with the ground, is considered. Nevertheless the analysis of the liquid water spatial distribution does not indicate the proximity of additional fog area without ground contact. The number of agreements between forecasts and observations does not increase even if the fog in the first 10 or 100 m is included in the comparison. During this night fog, the clouds touch the ground and the forecasted 2m-visibility is reduced as predicted. However, the necessary conditions for a fog formation is not given by the model for the correct areas.

During this fog period the influence of a residual cloud cover play an important role in the accuracy of the fog forecast. Figure 4.20 points out the time evolution of the radiative fluxes at the Lindenberg observatory. Between the 6th and 15th forecast hours the surface radiative balance shows a disagreement with the measurements. The lack of cloud cover over Lindenberg has an identified influence: the short wave fluxes are strongly overestimated, sensible and latent fluxes do not correspond with the supplied measurements. Only from the 18th forecast hour, the cloud cover appears above Lindenberg. Then, the radiative balance at the surface follows the time evolution of the measurements. The unbalanced radiative fluxes cannot be compensated and the fog formation at the Lindenberg observatory is strongly affected. In Figures 4.21 a & d, the influence of the cloud cover is demonstrated. The late presence of a cloud above Lindenberg has strongly favoured the warming of the low atmosphere. The 2m-temperature is clearly overestimated. Moreover, by night, no radiative cooling at the surface can adjust the overestimated temperature (Figure 4.21-c). The 2m-relative humidity thus cannot reach supersaturation (Figure 4.21-b). The formation of fog becomes impossible (Figure 4.21-a) in spite of a good accuracy of the 10m wind speed ensuring a calm and stable atmosphere for the fog formation during night (Figure 4.21-d).

The difficulties occurring at Lindenberg are not a localised problem. The other stations of the studied area register similar results (Appendix A). The forecast domain has been initialised with a 2m-temperature bias exceeding 2°C, which restrains the maximum values of the relative humidity at the ground. Nevertheless the only inaccuracy of the cloud cover spatial extension is responsible for this mismatched forecast. The forecast of radiative fog in presence of sparse cloud cover stays a challenging exercise in spite of a three-dimensional modelling approach able to consider a dynamic cloud cover evolution.
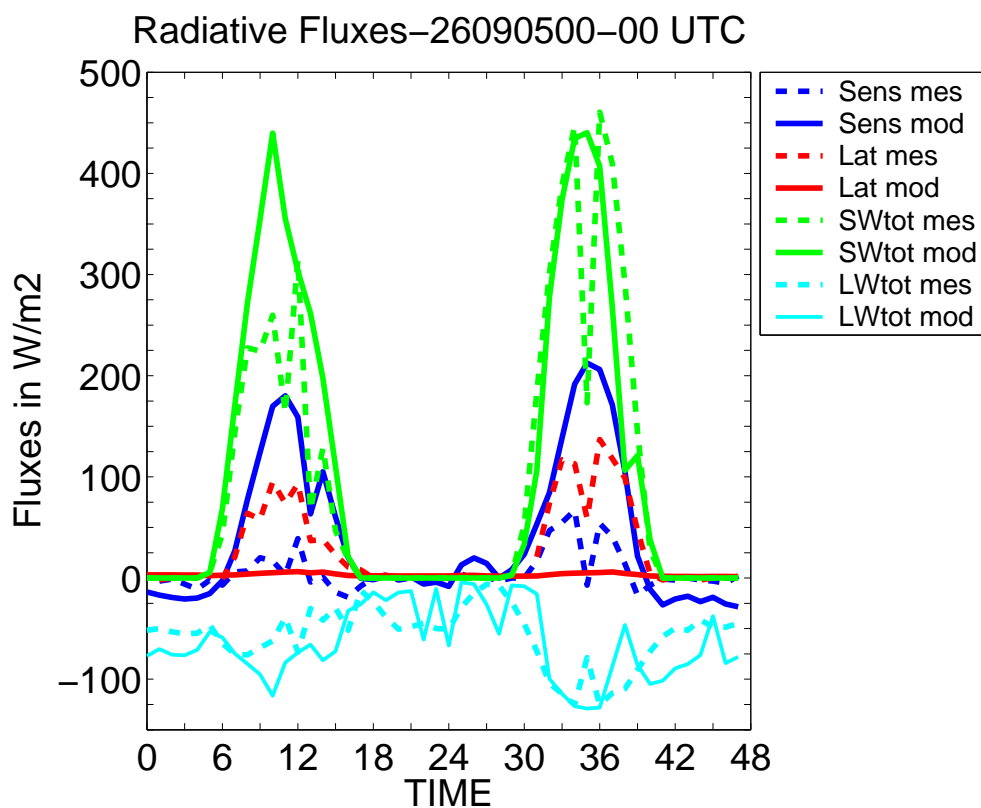
Figure 4.20: Time evolution of radiative fluxes at the ground, forecasted by LM-PAFOG. Initialisation: September 26th, 2005 at 00 UTC.
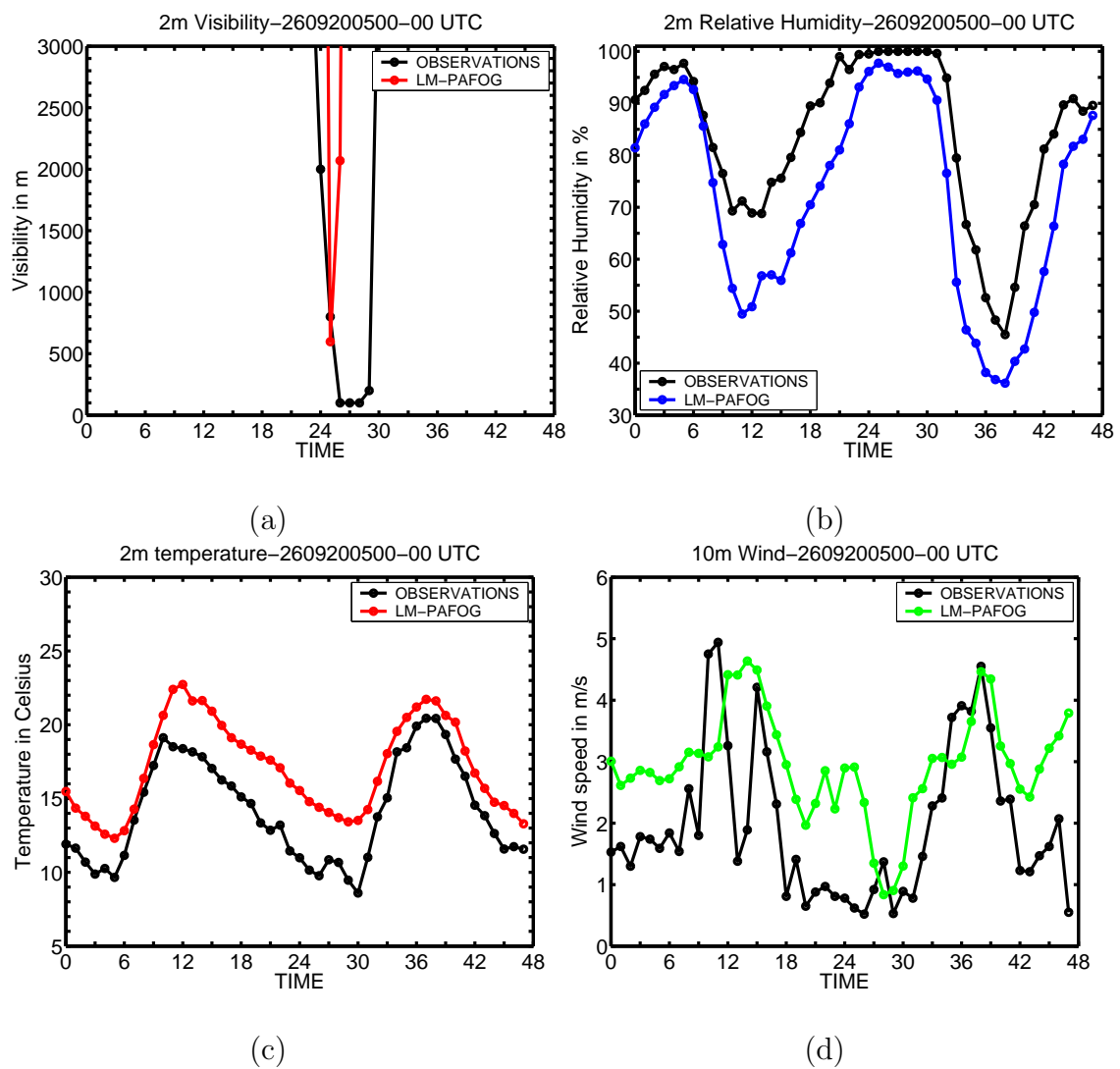
Figure 4.21: Time evolution of 2m visibility (a), 2m relative humidity (b), 2m temperature (c) and 10m wind speed (d), forecasted by LM-PAFOG. Initialisation: September 26th, 2005 at 00 UTC.

4.4.4 Episode 3, December 6-7th, 2005: fog influenced by a low stratus

Synoptic situation

A trough is placed over central Europe with a weak low pressure system located east of Lindenberg moving slowly northwards (Figure 4.22). The boundary layer is dominated by a weak wind and a thin stable moist layer with a tendency to light rain east of Lindenberg. The cloud cover is increasing near Lindenberg as the low pressure system moves northward. In general the visibility is reduced to below 10 km most of the time. Fog and low stratus formed during the night to 7th December especially where the cloud cover is sparse.

On the Lindenberg area a long fog period was observed. The visibility is reduced in the morning of the 6th December and the fog extends during the next days (Figure 4.23). Localised formations of fog have been observed in the north and east part of the forecast area. Visibilities of 100 m and below have been reported at several sites.
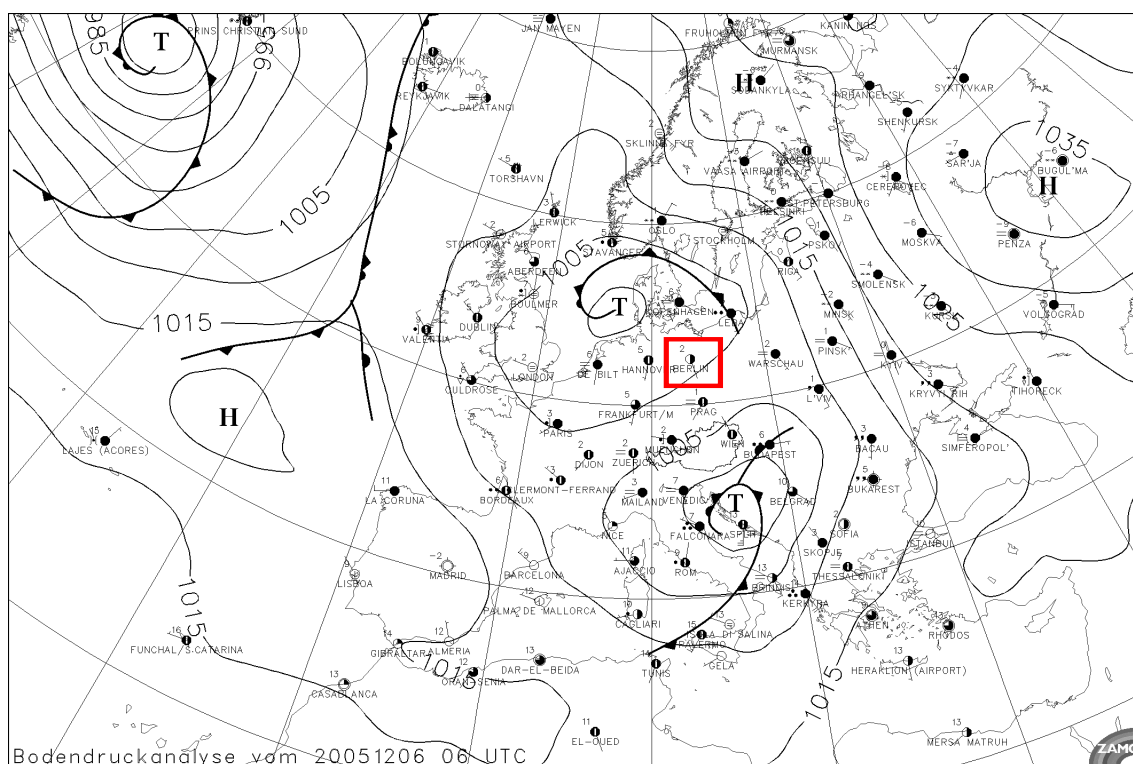
Figure 4.22: Surface pressure analysis on December 6th, 2005 at 06 UTC, supplied by the Central Institute for Meteorology and Geodynamics (ZAMG), Vienna, Austria. The red frame delimits the forecast area.
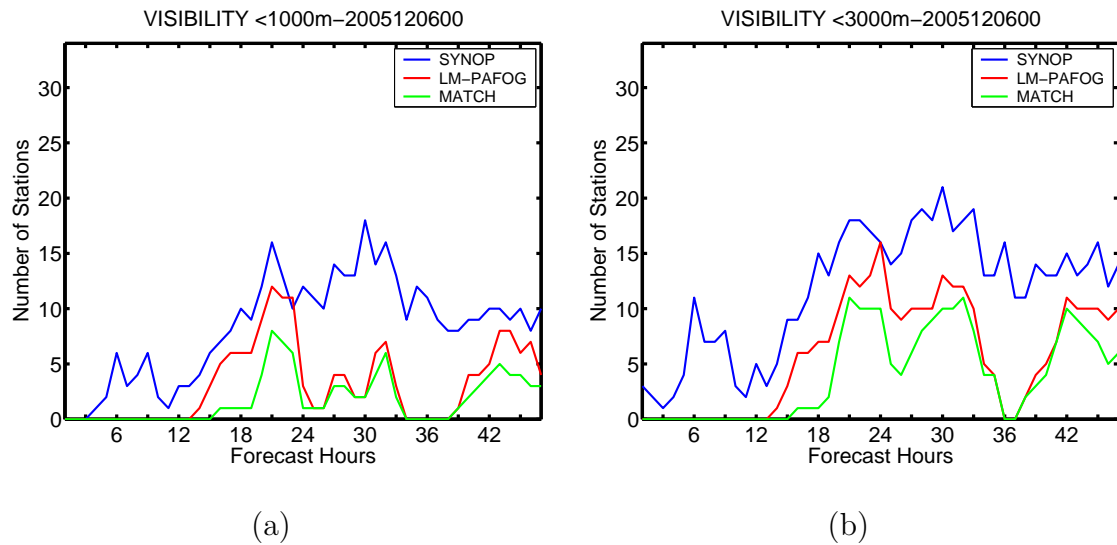
Figure 4.23: Comparison of the time evolution of LM-PAFOG fog spatial distribution forecast with the 2m-visibility measurements extracted from the SYNOP data network on the Lindenberg area at December 06-07th, 2005 for a visibility threshold of 1000 m (Fig-a) and 3000 m (Fig-b).
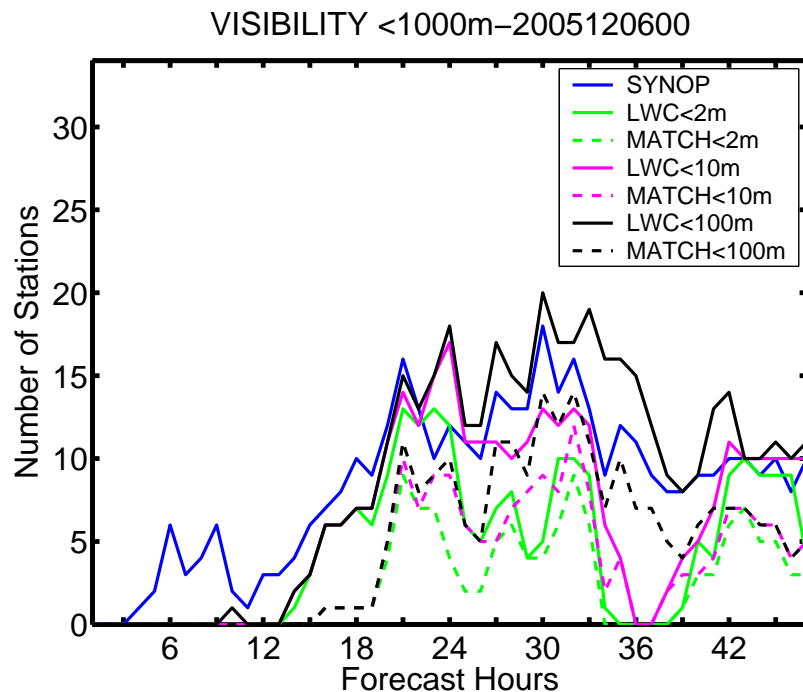
Figure 4.24: Comparison of the time evolution of LM-PAFOG fog spatial distribution forecast in terms of liquid water content mask with the 2m-visibility measurements extracted from the SYNOP data network on the Lindenberg area at December 06-07th, 2005 for a visibility threshold of 1000 m. Dashed lines correspond to number of agreements between measurements and forecasts.

Appraisal of the fog forecast

This last selected fog period provides an interesting case to understand the time evolution of the model performance. The exceptional long fog episode ensures the presence of fog during the entire forecasted period. To evaluate the development, the forecast has been compared first with the 2m-visibility measurements supplied by the SYNOP network. The evaluation has been conducted for two visibility thresholds: 1000 m and 3000 m (Figure 4.23 a & b). A large variability of the model performance can be identified. In the first 12 forecast hours, LM-PAFOG has some difficulties to forecast fog in the area. Between the 12th and the 24th forecast hours the forecasted spatial distribution coincides very well with the observed fog. From the 24th hour the forecast quality deteriorates progressively. The fog density changes abruptly. Regarding the results for both visibility thresholds, we note that most of the forecasted fog area cannot reproduce visibility values below 1000m as observed. However, the forecasted visibility values are in a range between 1000 and 3000m. The dissipation process is strongly amplified between the 33th and 39th forecast hours until the fog disappears completely. And finally, in the last forecast hours, forecasted fog is formed again and the spatial distribution shows a good agreement in this period beginning with sunset.

As in the two other case studies, the liquid water spatial distribution, present below a certain altitude (2 m, 10 m and 100 m), has been compared with the SYNOP visibility measurements (Figure 4.24). Considering the three-dimensional distribution of the fog area we note that LM-PAFOG always has more difficulty to form fog at the ground. Regarding the first 10 m of the atmosphere, the liquid water spatial distribution (magenta lines) shows a better agreement with the visibility measurement than the 2 m fog layer (green lines). Moreover, between the 33th and 39th forecast hours LM-PAFOG forecasts very low stratus, but no clouds are present in the first 10 m. The equivalent area corresponding to the liquid water spatial distribution in the first 100 m gives the best agreement with the visibility measurements. Nevertheless, in this case LM-PAFOG does not fill the necessary conditions for the fog formation in the low atmosphere.

The first conclusions concerning the fog forecast performance in this case agree with the results of the statistical study presented in section 4.3, i.e. bivalent behaviour of LM-PAFOG performance between well-according night forecasts and missing fog episode occurring by day. In this case, further studies focusing on the Lindenberg observatory have been completed to identify the reasons of these forecast quality variations.

In a first step, the radiative balance at the ground has been analysed (Figure 4.25). Despite an underestimation of the short wave fluxes between the 6th and 18th hour forecast, the radiative balance is well considered. The sensible and latent heat fluxes show a good agreement with the measured fluxes. The long wave fluxes agreement confirms a good representation of the cloud cover thickness.

Moreover, in Figures 4.26 a & d, a comparison with the detailed set of measurements supplied by the Lindenberg observatory demonstrates the behaviour of LM-PAFOG in the boundary layer. The time evolution of the 2m-visibility confirms the difficulties of LM-PAFOG to forecast fog between the 33th and 39th forecast hours. The 2m temperature
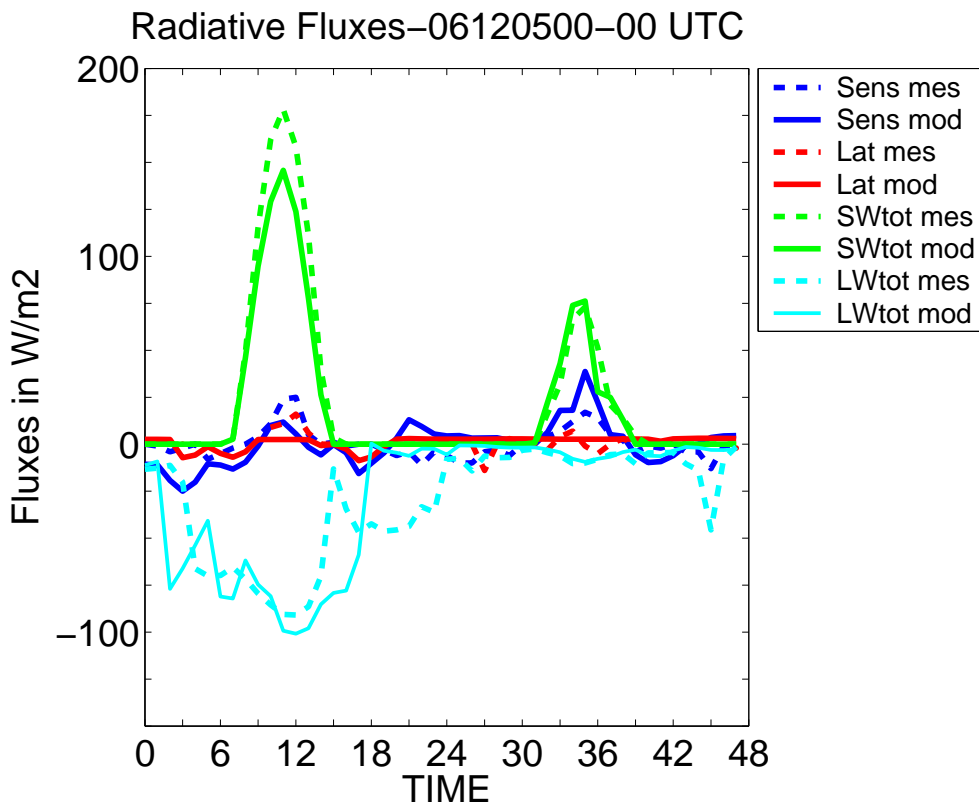
Figure 4.25: Time evolution of radiative fluxes at the ground, forecasted by LM-PAFOG. Initialisation: December 6th, 2005 at 00 UTC.

time evolution highlights a constant colder tendency than the Lindenberg measurements. From the 30th forecast hour, a significant temperature increase occurs until forecast and measurements agree. The 10m wind speed shows a very good accordance with the measurements. The 2m relative humidity time evolution explains the difficulty to predict the fog formation. In this case, LM-PAFOG is initialised with a too dry atmosphere. Despite low humidity values close to the ground, LM-PAFOG is able to adapt its 2m relative humidity forecasts to the Lindenberg measurements relatively well. Finally, the decrease between the 33th and 39th forecast hour is the only significant disagreement of the LM-PAFOG forecast with the measurement.

The vertical profiles of temperature and relative humidity (Figure 4.27) highlight an accurate forecast. In this case the model reproduces the formation of the temperature inversion at the ground very well (green curve). Nevertheless, the weakness of the humidity transport at the interface soil/atmosphere is confirmed. At 12 UTC (orange curve), the relative humidity values point out a drying in the first meter above the ground, which forbids further presence of fog in the area. Moreover, the comparison with the other SYNOP stations localised in the forecast area deliver similar results (Appendix B). For each location registering a fog presence by day a successful fog forecast did not occur due to a rapid decrease of the 2 m relative humidity.

This last selected fog episode underlines the potential of our new three-dimensional fog forecast model. The initialisation of the forecast area as well as the evolution of the cloud cover supplied the necessary accuracy for a successful fog forecast. Nevertheless, the weak moistening in the lowermost atmospheric layers at midday has been observed again. Due to the sparse information about the humidity spatial distribution around Lindenberg, the influence of the turbulence parametrisation on this humidity decrease can only be speculated and can thus explain the difference between the day and night forecast performances.

(a)   (b)

(c)   (d)
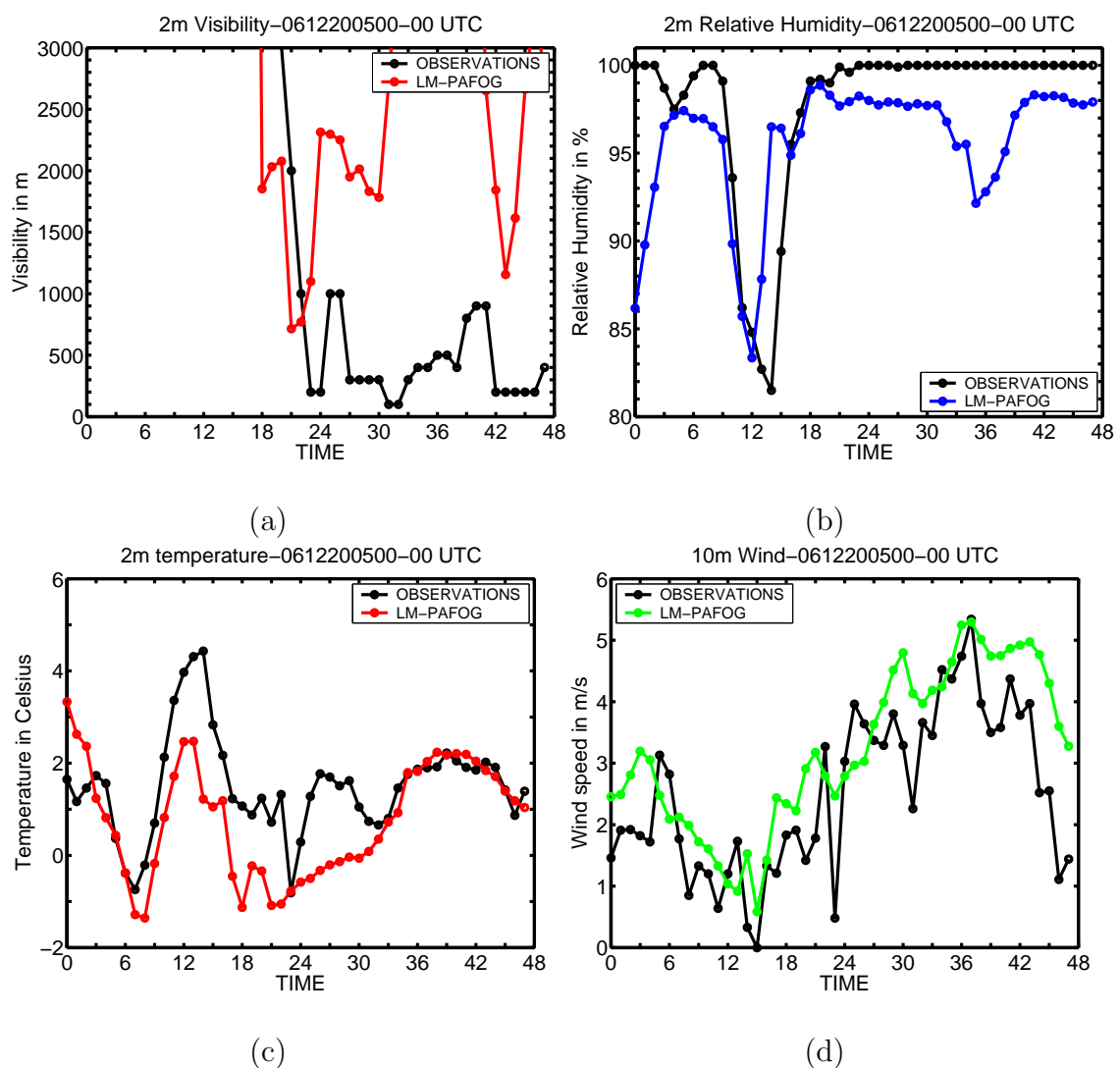
Figure 4.26: Time evolution of 2m visibility (a), 2m relative humidity (b), 2m temperature (c) and 10m wind speed (d), forecasted by LM-PAFOG. Initialisation: December 6th, 2005 at 00 UTC.

(a)   (b)

(c)   (d)
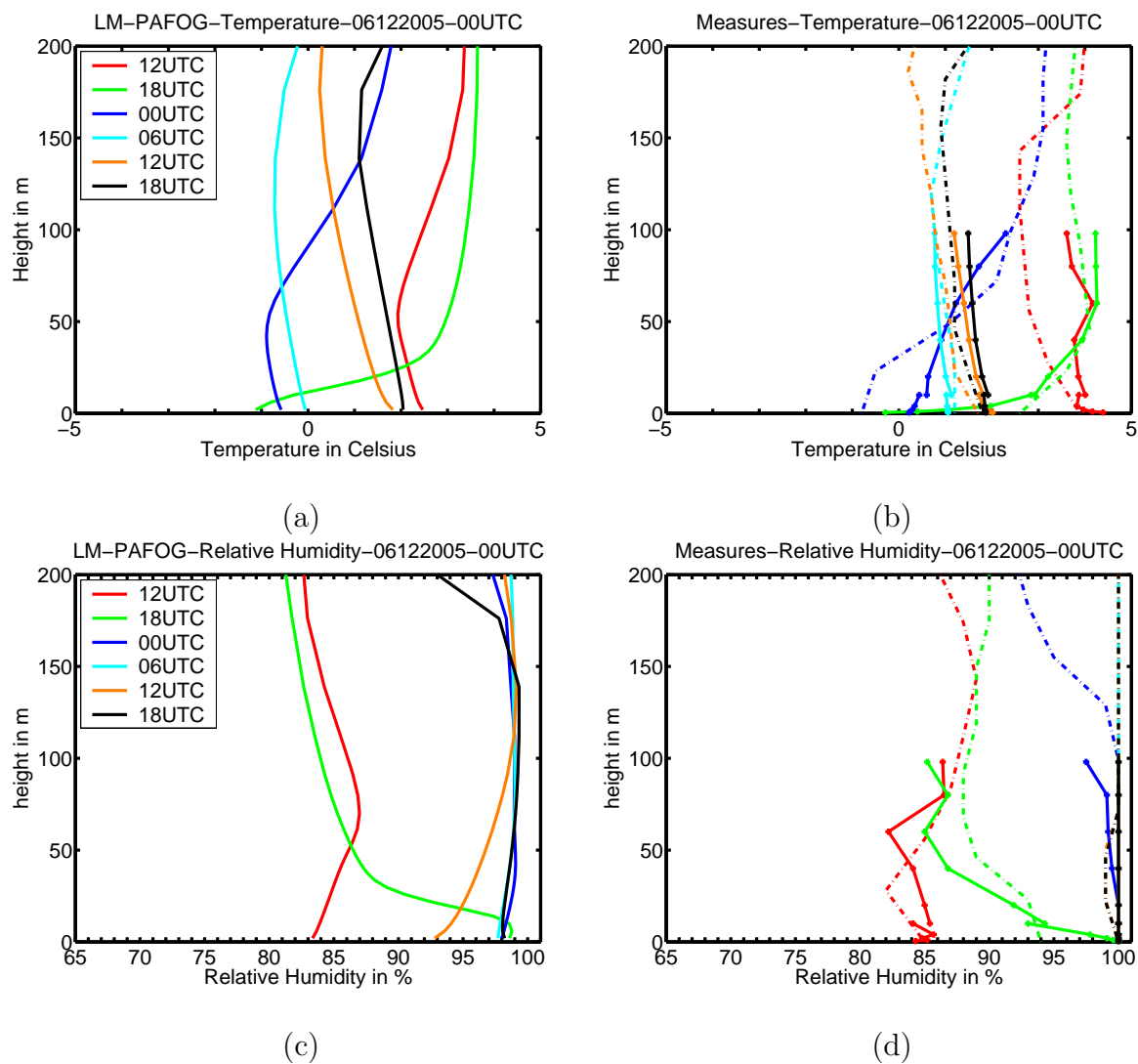
Figure 4.27: Vertical profiles of temperature, relative humidity and wind speed, forecasted by LM-PAFOG and reported from the measurements at the Lindenberg observatory. Period: December 6th, 2005 12 UTC -December 7th, 2005 18 UTC. Full lines correspond to the mast measurements and the dashed lines represent the radiosounding profiles.

4.5   Limits of the soil/atmosphere transfer scheme

For an accurate fog forecast a high vertical resolution is necessary. Therefore, the original turbulence mixing parametrisation has been adapted to this new grid structure. With ten layers of 4 m in the lowest atmosphere, LM-PAFOG has to be very sensitive to the variations of turbulent mixing occurring by fog formation contrary to the operational LM version with a coarse grid resolution of 20 m at the ground. Few modifications have been made in the turbulence scheme. The minimun values of turbulent exchange coefficient, K_m^v and K_h^v have been reduced from 1 to 0.001 m^2s^{-1}, which corresponds to more realistic values in case of fog formation in stable atmosphere (*Bott*, 1992). Such an adjustment is a necessary correction of the scheme to allow the formation of fog during the night. The two states of turbulent mixing occurring in the formation, persistence and dissipation of fog are thus considered.

Nevertheless, the already mentioned low moistening at the surface mentioned above points out the difficulties to accurately adjust the turbulence mixing parametrisation. For the same radiative fog, Figures 4.28 a & d show, vertical profiles of the exchange coefficients for matter and heat calculated at different times delivered by the original LM version with vertical coarse grid and the LM-PAFOG model version with high vertical resolution. The turbulent exchange coefficients are not a measurable parameter, but the differences between both model versions clearly highlight the weaknesses of the turbulence scheme of LM which is also used in LM-PAFOG.

Regarding Figures 4.28 a & c, we note that the LM-PAFOG parametrisation develops stronger mixing processes than the original LM. The low moistening at the surface can thus be explained by an excessive vertical turbulent mixing. From 6 UTC, the gradients of K_m^v in the first meters, produced by LM-PAFOG, are more pronounced than those produced by LM forecasts. The humidity supplied by the soil is immediately mixed with the dry upper layer of the atmosphere until an altitude of 500m in this example. The condition of saturation at the surface cannot occur during the day. The dissipation of fog thus starts earlier than generally observed.

Regarding Figures 4.28 b & d, we note that a direct comparison is not appropriate. The original LM as a mesoscale forecast model is not developed to consider a detailed evolution of the atmospheric boundary layer: the vertical profiles are rapidly set to their minimum value $K_m^v = 1m^2.s^{-1}$ in stable nocturnal conditions. With its fine vertical resolution and the modification of the turbulence scheme, LM-PAFOG is able to reproduce a vertical profile of the turbulent exchange coefficients in a calm atmosphere. A slight turbulent mixing is ensured in the first 20m in a stable atmospheric structure. However, the numeric stability of the turbulent scheme is not ensured. The presence of such overshooting in the vertical profiles points out the limits of LM turbulence scheme (*Louis*, 1979) in case of fine vertical grid resolution. The necessary modifications for an accurate turbulent mixing parametrisation should involve the definition of a new empirical stability function adapted to our fine resolution. To avoid such complex and time-consuming solutions, alternative turbulence schemes implemented in the LM have also been tested. However, further numerical instabilities have been registered.

Until now, no turbulent mixing parametrisation adapted to the fine vertical grid of LM-PAFOG has been found. Further researches and test phases are currently in progress.

(a) LM by day

(b)LM by night

(c) LM-PAFOG by day

(d) LM-PAFOG by night
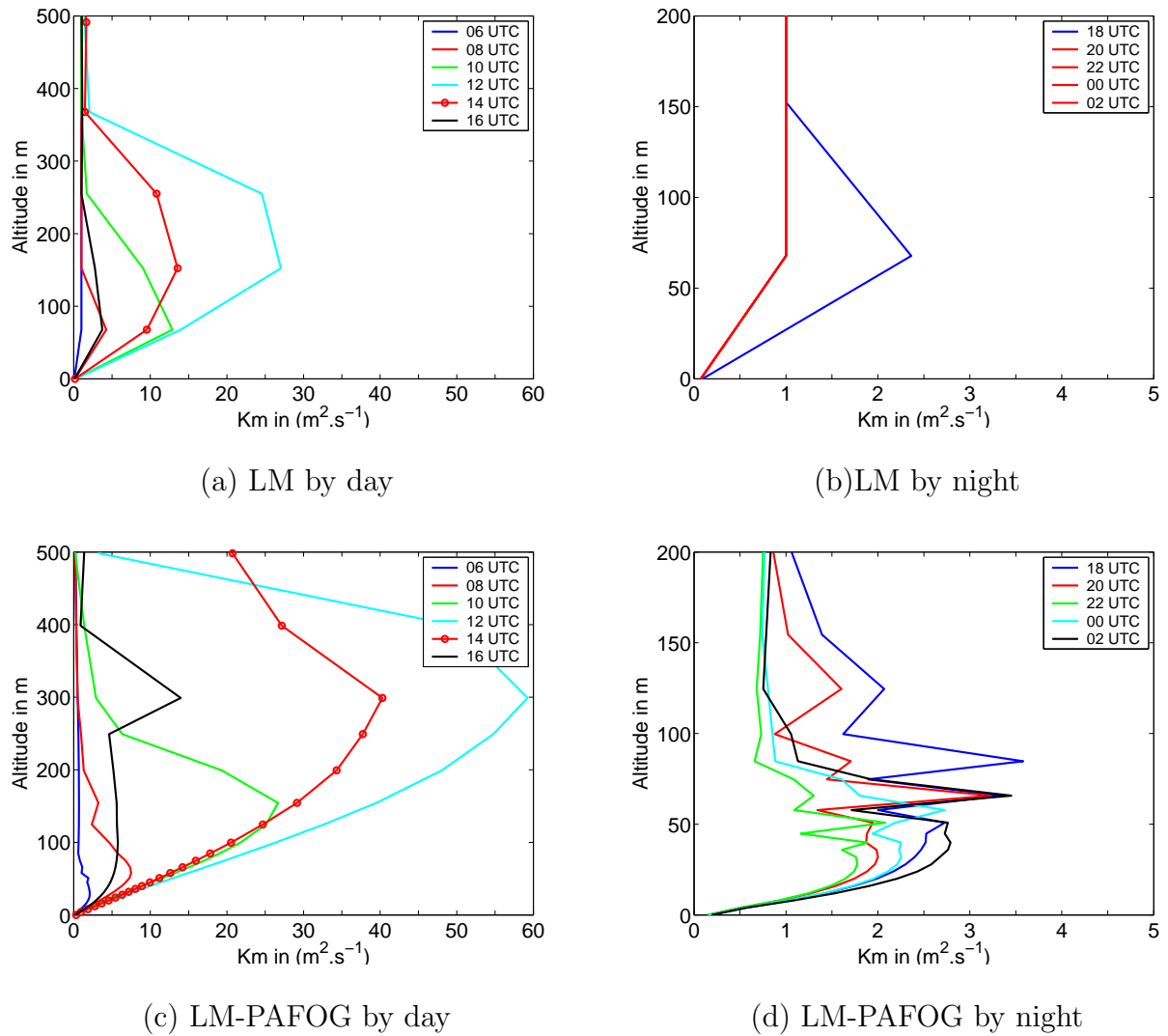
Figure 4.28: Vertical profiles of turbulence exchange coefficients for LM (original version) and LM-PAFOG.

4.6   Conclusions

Based on the framework of the COST 722 model intercomparison in the Lindenberg area, the reliability of the LM-PAFOG forecasts has been evaluated in a statistical study analysing a continuous four month period and in a second step, detailed studies of three selected fog episodes have pointed out the qualities of the model parametrisations.

These two complementary approaches clearly identify the influence of the diurnal cycle on the LM-PAFOG forecast performances. LM-PAFOG obviously has some difficulties to form fog in the afternoon, while its does well forecast the observed fog episodes in the calm nocturnal atmosphere. In a calm atmosphere, the three-dimensional forecast system captures the radiative fog formation occurring in the studied area. With the fine vertical grid resolution, the radiative cooling is generally well parametrised and ensures an accurate energy balance at the surface. The wind field is also well reproduced by the dynamic core. Nevertheless, the coupling of cooling, moistening and mixing processes necessary for the fog formation in the low part of the atmosphere only occurs sporadically. The different factors explaining these performances have been identified. Due to the small number of stations present in the studied area, the evaluation of a three-dimensional fog forecast remains a complex exercise. The very localised formation of fog restrains our study to comparisons between single grid points and station observations. The spatial distribution of fog can only be partially considered with the sparse stations present in the studied area. Moreover, the local comparisons point out the influence of several parameters responsible for the inaccurate fog forecast. The nesting approach for the initialisation of the forecasted area does not systematically ensure the necessary accuracy, especially in the lowest part of the atmosphere. The simple parametrisation of the soil surface seems to be insufficient for an accurate fog forecast, especially when considering correctly the influence of the urban environment on the surface energy balance. The turbulent mixing parametrisation chosen in this evaluation is not compatible with the fine vertical grid resolution. It has been clearly identified as responsible for the no-fog formation during the afternoon. The turbulent mixing is a cornerstone of the fog formation. Without an accurate turbulent mixing parametrisation, any other improvements cannot be quantified.

Chapter 5

Model intercomparison in the Lindenberg area

5.1 Introduction

A large variety of fog models exists at the European national weather services. Each of these models has its own characteristics and in particular, shortcomings or strengths. The COST-722 action "Short-Range Forecasting Methods of fog, visibility and low clouds", a project supported by the European science foundation, offered an excellent platform in the domain of fog forecasts for effective co-operations, successful use of research and integration of results into the national weather services. In this framework, an inter-comparison campaign of European fog forecast models has been conducted involving: Austria, Denmark, France, Germany and Switzerland (*Masbou* et al., 2007). A statistical forecast system, MOS-ARPEGE, as well as three-dimensional models such as: ALADIN-AUSTRIA, DMI-HIRLAM, NMM-PAFOG and LM-PAFOG are involved in this model comparison.

The evaluation of LM-PAFOG, presented in Chapter 4, is based on the model results in the COST-722 intercomparison. Therefore, the performances of LM-PAFOG are not restrained to the comparison with station measurements. Our model can be directly compared to the results with other fog forecast systems. The performances of different models under the same forecast conditions give an interesting overview of European fog forecast quality and underline the strengths and shortcomings of the different forecast methods.

First, the intercomparison methodology is discussed. Then, the models involved in the study are shortly introduced. Finally, the performances of each model have been confronted in a statistical evaluation as well as in selected fog scenes. Further steps concerning the fog forecast improvements have been highlighted.

5.2   Intercomparison approach and its limits

To offer the largest comparison possibilities between different fog forecast systems, the evaluation can only occur in restrained conditions. Statistical models, which give their forecasts in terms of probability of fog occurrence, have to be compared with deterministic forecast system. Local forecasts, produced by a statistical scheme or a one-dimensional fog forecast model, can be confronted with the predictions of three-dimensional fog forecast models.

The study thus focused only on a single point of comparison corresponding to the Lindenberg observatory of the German Meteorological Service during the last quarter of 2005 (September-December 2005). To facilitate the participation of various models in this study, the time initialisation scheme and the frequency of the forecast outputs have not be imposed.

As presented in detail in Section 4.1, the campaign was divided into two phases. First, the forecast performances were analysed in a statistical framework in order to underline the reliability of fog predictions for a four month period study. The forecasts have been compared to a set of visibility measurements, based on the Lindenberg area in Germany.

In the second part, the comparison focused more specifically on the different model parametrisations. The analysis concentrated on a set of chosen fog events, which are described by a detailed set of measurements, supplied by the Lindenberg observatory of the German Meteorological Service (DWD). The evolution of the boundary layer, as rendered by each method, was studied in details.

5.3   Description of the participating models

Five different models were included in the intercomparison. The participants involve universities and weather services. Different forecast approaches are represented in the comparison campaign: one statistical model, MOS-ARPEGE, and four deterministic fog forecast models. Among the deterministic fog forecast models, two of them run for operational forecasts: ALADIN-AUSTRIA and DMI-HIRLAM. The others are research models: NMM-PAFOG and LM-PAFOG.

5.3.1   A probabilistic approach to fog forecasts: MOS-ARPEGE (France)

As with any statistical model, a prognostic relationship is determined from a learning data set and defines the dependence of the predictand (element to be forecasted) on the predictors (input data necessary to produce a forecasts). The statistical model used is a Model Output Statistics application (MOS) (*Glahn and Lowry*, 1972).

The predictors of the statistical model either come from forecast fields of the numerical weather prediction model ARPEGE (*Courtier and Geleyn*, 1988) or from recent observations of the Lindenberg synoptic station. The predictand for the statistical model is the observed categorised visibility: visibility measures (distances) are converted into two categories, 0 or 1, whether they are greater or lower than a given threshold. The

intercomparison involves a set of 5 visibility thresholds: 350, 600, 1000, 1500 and 3000 meters.

Using a Linear Discriminant Analysis, LDA (*Fischer*, 1936), the prognostic relationship has been adjusted during the learning phase. Training data, composed of forecast and observation data of the Lindenberg area from September 2001 to April 2005, have been used to select the predictors and to compute the coefficients of the statistical equations. Due to the restrained ARPEGE operational archive, soil wetness, radiation fluxes or turbulent fields values are not available. In linear models, like LDA, the coefficients are the solution of a linear system of a matricial equation. The predictors, necessary to compute the models, have been selected as (*Petithomme*, 2007):

- pressure at ground level

- averaged total cloud cover

- averaged 10m wind speed

- 2m temperature using a mixing ratio conservation formula

- 2m relative humidity using a mixing ratio conservation formula

- vertical gradient of temperature (between 2m and 20m and between 2m and 50m)

- vertical gradient of relative humidity (between 2m and 20m and between 2m and 50m)

Vertical gradients are assumed to be constant and thus only depend on fields at top and bottom of the layer. After the learning phase, MOS-ARPEGE is thus calibrated to supply visibility forecast on the single area of the Lindenberg observatory.

5.3.2 The deterministic models

In the four deterministic models, different approaches to fog forecasting are proposed. The models differ in the computation of radiation, microphysics, turbulence processes as well as the Soil-Vegetation-Atmosphere Transfer (SVAT) scheme. Moreover, the initialisation of the models is not imposed: each model can use its own initialisation processes (nesting or data assimilation). Two different fog modelling approach are proposed. The nonhydrostatic model, NMM-PAFOG and LM-PAFOG, compute the fog evolution with a parametrised fog microphysics in a high resolution horizontal and vertical grid box structure. While the hydrostatic operational model, ALADIN-AUSTRIA and DMI-HIRLAM, are based on a lower resolution vertical and horizontal grid box structure, which forces an adhoc treatment of cloud water parametrisation close to the surface. A brief description of the involved models follows. The main characteristics are summarised in Table 5.1.

ALADIN-AUSTRIA

ALADIN-AUSTRIA (*Wang* et al., 2006) is the three-dimensional operational model of the Central Institute for Meteorology and Geodynamics in Vienna, Austria (ZAMG). The initialisation is based on the combination of a three-dimensional variational data

	ALADIN-AUSTRIA	DMI-HIRLAM	NMM-PAFOG	LM-PAFOG
Scientists	H. Seidl & A. Kann	C. Petersen & N.W. Nielsen	M.D. Müller	M. Masbou & A. Bott
Institute	ZAMG, Austria	DMI, Denmark	University of Basel, Switzerland	University of Bonn, Germany
time step	415 s	450 s	4 s	10 s
Hz resolution no. of pixels	300 x 270	610 x 568	160 x 160	100 x 100
Δxy	9.6 km	16 km	2 km	2.8 km
Vert. resolution no. of levels	45	40	45	40
< 200 m	3	3	14	20
< 2000 m	13	13	30	25
Δz_{min}	30 m	30 m	4 m	4 m
soil model	ISBA (*Noilhan and Planton*, 1989)	modified ISBA (*Noilhan and Planton*, 1989)	*Chen and Dudhia* (2001)	TERRA (*Schrodin and Heise*, 2001)
no. levels	3	3	4	7
Model equations	Hydrostatic	Hydrostatic	Nonhydrostatic	Nonhydrostatic
Turbulence scheme	*Louis* (1979) scheme	prognostic TKE *Cuxart* et al. (2000)	prognostic TKE *Janjic* (1990, 1996, 2002)	*Louis* (1979) scheme
initialisation	ARPEGE/IFS	Assimilation	GFS	LM 7km *Steppeler* et al. (2003)
Lateral boundary conditions	every 3 hours	every 3 hours	every hour (NMM 12km)	every hour
Microphysics	*Kessler* (1969)	*Sundqvist* (1988)	*Ferrier* (2002) & PAFOG ($<1500m$)	*Kessler* (1969) & PAFOG ($<2000m$)
Visibility	*Seidl* et al. (2007) (statistics) & *Gultepe* et al. (2006a) (case study)	*Petersen and Nielsen* (2000)	Complex relation of moist parameters (personal communication, M.D. Müller)	*Koschmieder* (1924)

Table 5.1: Summary of main properties of the four deterministic fog forecast models involved in the Lindenberg model intercomparison.

assimilation (*Fisher*, 2002) and the interpolation of the global model ARPEGE analysis data in the forecast area. The lateral boundary conditions are defined by the French global model ARPEGE (*Courtier and Geleyn*, 1988) with a coupling frequency of 3 hours. The vertical grid is composed of 45 levels, the lowest level is approximately 30 m above the ground. The forecast area is centered on Austria, covering a large part of Eastern Europe with a horizontal resolution of about 10 km (Figure 5.1).
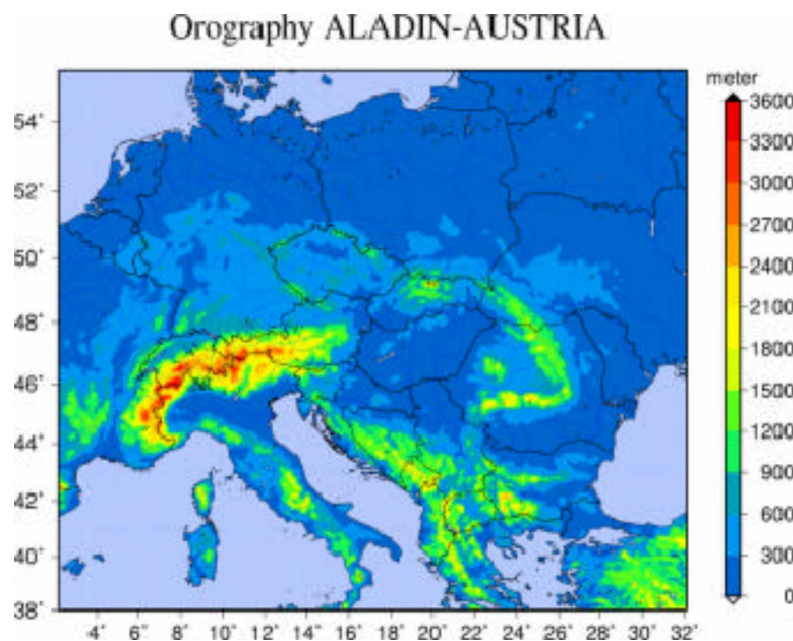
Figure 5.1: Forecast domain of ALADIN-AUSTRIA (Source: *Wang* et al. (2006)).

The radiation scheme is based on the δ-two-stream approximation of the radiative transfer equation incorporating effects of scattering, absorption and emission by cloud droplets, aerosols and gases in each part of the radiative spectrum (*Ritter and Geleyn*, 1992; *Geleyn and Hollingsworth*, 1979). Both emission and absorption of radiation are handled through bulk values across the entire short wave and long wave spectrum.

Turbulent fluxes of momentum, heat and water vapour are modelled considering the Louis scheme (*Louis*, 1979).

The ISBA (Interactions Sol Biosphere Atmosphere) scheme elaborated by *Noilhan and Planton* (1989) parametrises heat, mass and momentum exchanges between the surface and the overlying atmosphere. The influence of the vegetation fraction and different soil types on the soil thermo-hydrous properties are included in the scheme. The thermal inertia of the vegetation and its ability to immediately re-evaporate the dew are considered to determine the soil surface evaporation.

A revised form of the bulk microphysics *Kessler* (1969) scheme computes condensation rates at each level contributing directly to the precipitation flux. Sub-cloud evaporation, melting and freezing are taken into account additionally.

For this study, the operational version has been modified to better consider the specificity of fog forecasts. In order to improve the capability of the model to handle lifted inversions connected with low stratus/stratocumulus, a new sub-inversion cloudiness scheme

has been introduced (*Seidl and Kann*, 2002). This scheme has been implemented into both ALADIN versions used in this study .

In the statistical study, the current operational version used a diagnostic cloudiness scheme. Explicitly resolved cloudiness and cloud water content are determined simply as a function of humidity and temperature.

In the case studies, the operational version uses the Lopez microphysical parametrisation, which allow cloud water and cloud ice to be treated more explicitly (*Lopez*, 2002).

The modifications in the microphysics processes caused the use of two different approaches to derive realistic values of fog density and hence visibility.

The operational version of ALADIN-AUSTRIA does not compute visibility at all. Reasonable empirical criteria were set in order to distinguish different thresholds of visibility. A version of the sub-inversion cloudiness scheme with an identical parameter setting as the operational scheme computes sub-inversion cloudiness. Surface humidity and the presence of sub-inversions were used for further distinction of visibility classes (*Seidl* et al., 2007).

For the second phase of the intercomparison, the case study has been rerun with ALADIN-AUSTRIA including prognostic cloud liquid water. Visibility is computed from the mean liquid water content of the two models closest to the ground, following *Gultepe* et al. (2006a).

DMI-HIRLAM (Denmark)

DMI-HIRLAM, the three-dimensional operational forecast model used at the Danish Meteorological Institute (DMI), is a slightly revised version of the numerical weather prediction model and data assimilation system developed by the HIRLAM cooperation (*Unden* et al., 2002). The model is initialised by the combined analysis from a three-dimensional variational data-assimilation, soil analysis data and background from the previous run and analysis from the European Centre for Medium-Range Weather Forecasting, ECMWF. The lateral boundary conditions are updated every 3 hours with ECMWF analysis data. The vertical grid is composed of 40 levels. The lowest level is situated about 30m high. The forecast area is centered on Denmark, covering a large part of Northern Europe with a horizontal resolution of about 16 km (Figure 5.2).

The vertical diffusion scheme is detailed by a prognostic equation for Turbulent Kinetic Energy (TKE) following a modified Cuxart-Bourgeault-Redelsberger (CBR) parametrisation (*Cuxart* et al., 2000).

The radiation processes consider the particularity of long wave and short wave calculation separately. For each spectral domain, the influence of aerosols, O_2, ozone, CO_2, water vapour and cloud water are included in the computation in a simple way (*Savijäri*, 1990).

The microphysics scheme is based on the bulk parametrisation including water vapour, cloud water, rain and snow (*Sundqvist*, 1988; *Sundqvist* et al., 1989; *Sundqvist*, 1993). The conversion of cloud water to rain or snow is computed without a prognostic equation for precipitable water or snow. The Soft TRAnsition COndensation (STRACO) scheme has been additionally implemented to ensure a gradual transition from convective to stratiform precipitation (*Sass*, 1997).
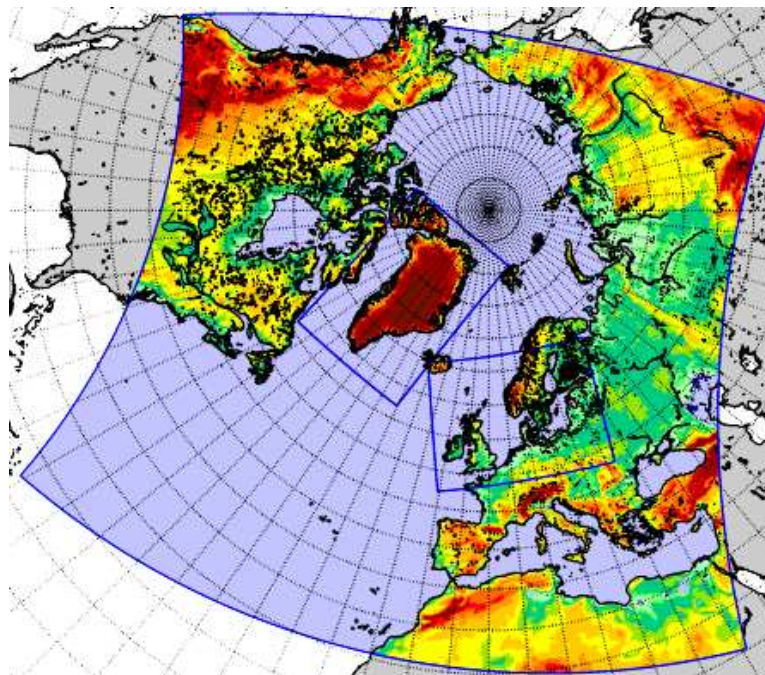
Figure 5.2: Forecast domain of DMI-HIRLAM (Source: website of the Danish meteorological institute, http://www.dmi.dk).

The moisture and heat exchanges at the surface are considered in a land surface scheme based on the ISBA (*Noilhan and Planton*, 1989) model. These interactions are balanced by the presence of five different soil types (sea, sea ice, forest, low vegetation and bare), which influence the thermal and hydrous soil evolution.

In DMI-HIRLAM, the 2m-visibility forecast is based on the diagnostic parametrisation of *Petersen and Nielsen* (2000). An empirical relation depending on the solar zenith, cloud cover, wind velocity, temperature, specific humidity at the lowest model level as well as the precipitation impact has been implemented using a statistical analysis of SYNOP reports from 30 Danish stations. The coarse vertical resolution close to the ground has not allowed a prognostic evaluation of 2m-visibility depending on the cloud water output of the model.

NMM-PAFOG (Switzerland)

NMM-PAFOG is a three-dimensional mesoscale model based on the Nonhydrostatic Mesoscale Model (NMM) of NOAA[1]-NCEP[2] with sophisticated cloud microphysics (*Müller*, 2006). The model domain is initialised with 1° resolution Global Forecasting System (GFS) data. Boundary conditions are updated hourly from a 13 km resolution NMM simulation, which is also initialised with 1° resolution of the Global Forecasting System (GFS). The model uses hybrid sigma-pressure coordinates (sigma in the lower part, pressure in the upper part). The current setup uses 45 vertical layers, where the vertical resolution in the planetary boundary layer is very high, starting with a thickness of 4 m for the first level and

---

[1]National Oceanic and Atmospheric Administration
[2]National Center for Environmental Prediction

a total of 27 layers in the lowest 1000 m above ground. In the horizontal a domain of 160 x 160 grid points with a resolution of 2 km centered on Lindenberg Observatory is used (Figure 5.3).
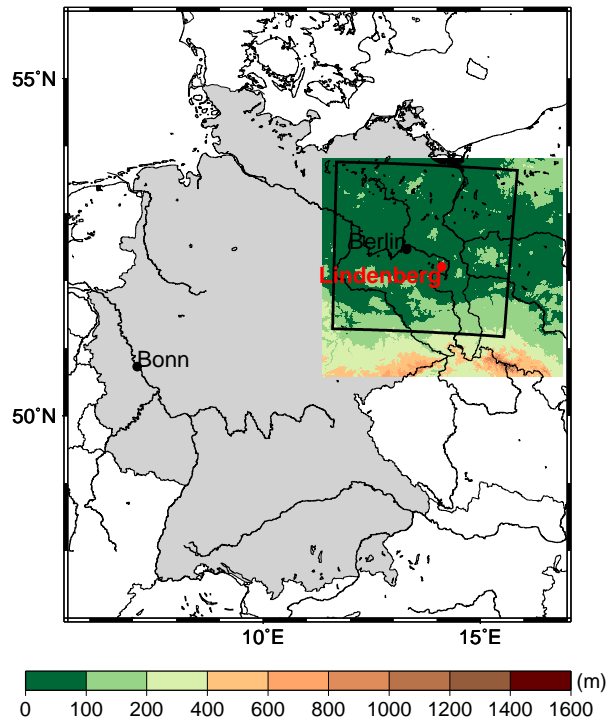
Figure 5.3: Forecast domain of NMM-PAFOG. The colour scale from green to brown represents the topography in the Lindenberg area. The black square denotes the limits of the LM-PAFOG forecast domain.

The radiation parametrisation is based on the scheme developed at the Geophysical Fluid Dynamics Laboratory. The long wave radiation scheme follows the simplified exchange method of *Fels and Schwarzkopf* (1975) and *Schwarzkopf and Fels* (1991), based on a calculation over spectral bands associated with carbon dioxide, water vapour and ozone. The short wave radiation scheme follows the *Lacis and Hansen* (1974) parametrisation.

The surface scheme, based on the NOAA land surface model (*Chen and Dudhia*, 2001), is a 4-layer soil temperature and moisture model with canopy moisture and snow cover prediction.

The boundary layer scheme (Mellor-Yamada-Janjic scheme, *Janjic* (1996, 2002)) represents a non-singular implementation of the Mellor-Yamada level 2.5 turbulence closure model (*Mellor and Yamada*, 1982) through the full range of atmospheric turbulent regimes.

The microphysics calculations have been improved to better consider the formation of fog. The fog microphysic has been extracted from the one-dimensional fog forecast model PAFOG (*Bott and Trautmann*, 2002). The PAFOG microphysics introduce Cloud Condensation Nuclei (CCN) as a new prognostic variable. This more detailed microphysics scheme is active in the lower 1500 m above ground and there replaces the condensation

algorithm of the Ferrier microphysics (*Ferrier*, 2002). Precipitation and ice physics are also computed with Ferrier microphysics in the lowest 1500 m. The visibility parametrisation is based on a relation involving precipitation rate and type, humidity, liquid water content and aerosol concentration (personal communication M.D. Müller).

LM-PAFOG (Germany)

The main characteristics of LM-PAFOG were already summarised. For further details, a comprehensive description is presented in the Chapters 2 and 3.

5.4   Statistical study

The model comparison campaign gathers fog forecast systems issued from different methods. Two different forecast philosophies are represented by the French statistical approach, which predicts the probability of a fog event occurrence, and the four deterministic models, which determine the formation of a fog episode with a parametrisation getting close to the physical and dynamic behaviours observed in the atmosphere. The only similarity between the different forecast methods can be found in the final forecast product: the presence or not of fog.

To quantify the fog forecast quality of each forecast system, a common statistical study scheme has been used. The outputs of the models have been homogenised around the same definition of a "fog event": for each forecast, a "fog event" is obtained when the forecasted visibility is equal, or is lower than, a certain threshold. Comparing the 2m-visibility value of each deterministic model with the chosen threshold, the forecast results can be translated into binary probability values, where the value is set to "1" in case of fog. For the statistical model, the forecast output already delivers a probability of the "fog event" ranging continuously from 0 to 1 for a chosen visibility threshold. For each forecasted probability, the results are split into "fog" or "no fog" categories.

Sorted into binary events, the forecasts of each participating model have been thus analysed using contingency-table-based statistics and the derived indicators as already used in the statistical evaluation of LM-PAFOG (section 4.3). The influence of the fog intensity on the forecast has been tested by ranging the visibility forecasts in five levels: 350, 600, 1000, 1500 and 3000m.

The statistical evaluation focused on a four month period (September-December 2005), in which each participating model independently delivered its continuous fog forecasts for the Lindenberg area. Neither the initialisation times, nor the duration of a forecast run were harmonised.

The set of data, supplied by each participant in terms of initialising time and forecast frequency are presented in Table 5.2. Note that only MOS-ARPEGE, ALADIN-AUSTRIA, DMI-HIRLAM and LM-PAFOG participated in this statistical comparison. NMM-PAFOG delivered its forecasts exclusively for the selected fog events.

Due to the large set of forecasts and the variability of the models results, some limitations have been applied for a consistent statistical analysis. The forecast comparison only

Table 5.2: Initialisation and forecast occurrence of the four models, participating in the statistical study of the intercomparison.

Forecast models	Initialisation time	Forecast time
Denmark-HIRLAM	00, 06, 12, 18 UTC	24 hourly forecasts
Austria-ALADIN	00, 12 UTC	48 hourly forecasts
Germany-LM-PAFOG	00 UTC	48 hourly forecasts
France-MOS-ARPEGE	00, 12 UTC	00 + 21, 24 , 27, 30 hours 12 + 09, 12, 15, 18 hours

focuses on the model runs initialised at 00UTC. Moreover, an ensemble model, taking into account the value of each model forecast, has been developed in order to identify a global fog forecast quality among the several approaches. The time evolutions of the forecast quality as well as the influence of the fog density can be evaluated in the best conditions.

After an introduction of the new ensemble model, the influence of the visibility parametrisation on the forecast quality of all four models has been analysed focusing on the 24 [th] forecast hour. Then, the time evolution of the participating models has been examined for the 1000m visibility threshold corresponding to the official limit between fog and no fog forecast.

5.4.1 A new model: the ensemble forecast

The atmosphere can never be described perfectly, either in terms of spatial coverage or accurate measurements. The uncertain initial state of the model is one reason for the stochastic nature of the weather forecasts. Moreover, the single models have their own initialisation scheme and their own parametrisation in our study. Such differences can be responsible for large discrepancy between the model forecasts. Each model supplies its "best forecasts" in different situations. The definition of a basic quality of the European fog forecast can become difficult. To overcome these problems, the ensemble mean is used generally to outperform the forecasts of single models.

In order to analyse the basic quality of the European fog forecast, an ensemble forecast has been calculated using single realisations of the four models under consideration. The ensemble forecasts are based on the mean of the fog probabilities, computed by the models. The ensemble forecast is produced, if at least three of four models have an output at the same forecast time. The fog event probability of the ensemble, P_{ens}, is thus defined for a forecast time:

$$P_{ens} = \frac{1}{n} \sum_{i=1}^{n} P_i \qquad (5.1)$$

where P_i is the fog event probability of the ith model and n is the quantity of available forecasts at this time. P_i can be either, 0 or 1 for the deterministic models, or between 0 and 1 for statistic models. The ensemble forecasts have been computed with the set of model outputs initialised at 00 UTC.

5.4.2   Fog intensity and forecast skill

In a first analysis, the performances of each model for different fog intensities have been examined. To isolate the influence of the visibility parametrisation on the forecast quality, the comparison focuses only on the 24th forecast hour.

For each model, Relative Operative Characteristic (ROC) and PSeudo Relative Operative Characteristic (PSROC) diagrams underline the forecast performances for the five chosen visibility thresholds (Figures 5.4 and 5.5). Note that the deterministic model results deliver only a single point corresponding to a probability of 100% for each visibility threshold, while the probabilistic model, MOS-ARPEGE, produces a curve corresponding to the probability value ranging between 0 and 100%.

With these two diagram types, the notion of "best forecast" can be defined with two different points of view. A forecaster will base his decision on the results shown in a ROC curve, because the positive or negative influences of a fog forecast are balanced with the number of observations, i.e. the fog climatology in the studied area. To improve the quality of the fog detection, the developer of a fog forecast system will base his decision on the PSROC curve results, because the influence of a false alarm is balanced with the number of forecasted fog events. The proximity of the left hand corner of the plot in ROC and PSROC underlines increasing skill of the forecast system. The consideration of five visibility thresholds points out an evident dependency of the forecast quality with the density of the fog events.

ALADIN-AUSTRIA (Figures 5.4-a & 5.5-a) shows a good forecast skill for the visibility thresholds higher than 1000 meters. The model detects more than 70% of the fog events and the false alarm rate represents 20%. However, for the low visibility thresholds (350 m and 600 m), its detection scheme has a significantly lower detection rate. Furthermore, the detection skill, detailed in the PSROC, underlines a low reliability, especially for the dense fog events. For the 350 and 600 m visibility thresholds, the proportion of false alarms in the forecasted fog events reaches 90%.

For DMI-HIRLAM results (Figures 5.4-b & 5.5-b), the definition of a best forecast skill is a difficult exercise. The detection quality increases significantly when the visibility threshold considers the light fog events (3000 m). However, the increase of the hit rate also initiates the increase of the false alarm numbers, and thus larger false alarm rate values. The low reliability of the fog detection scheme is confirmed in the PSROC diagram and is independent of the visibility threshold. The false alarm ratio stays close to the 80% value for each of the five visibility thresholds.

The results of LM-PAFOG (Figures 5.4-c & 5.5-c) underline a very strong influence of the model with the visibility thresholds. LM-PAFOG shows very good performances for the lowest values of the visibility threshold (600 m), but the hit rate values deteriorate strongly with higher visibility thresholds. And although the hit rate decreases, the false alarm rate stays constant.
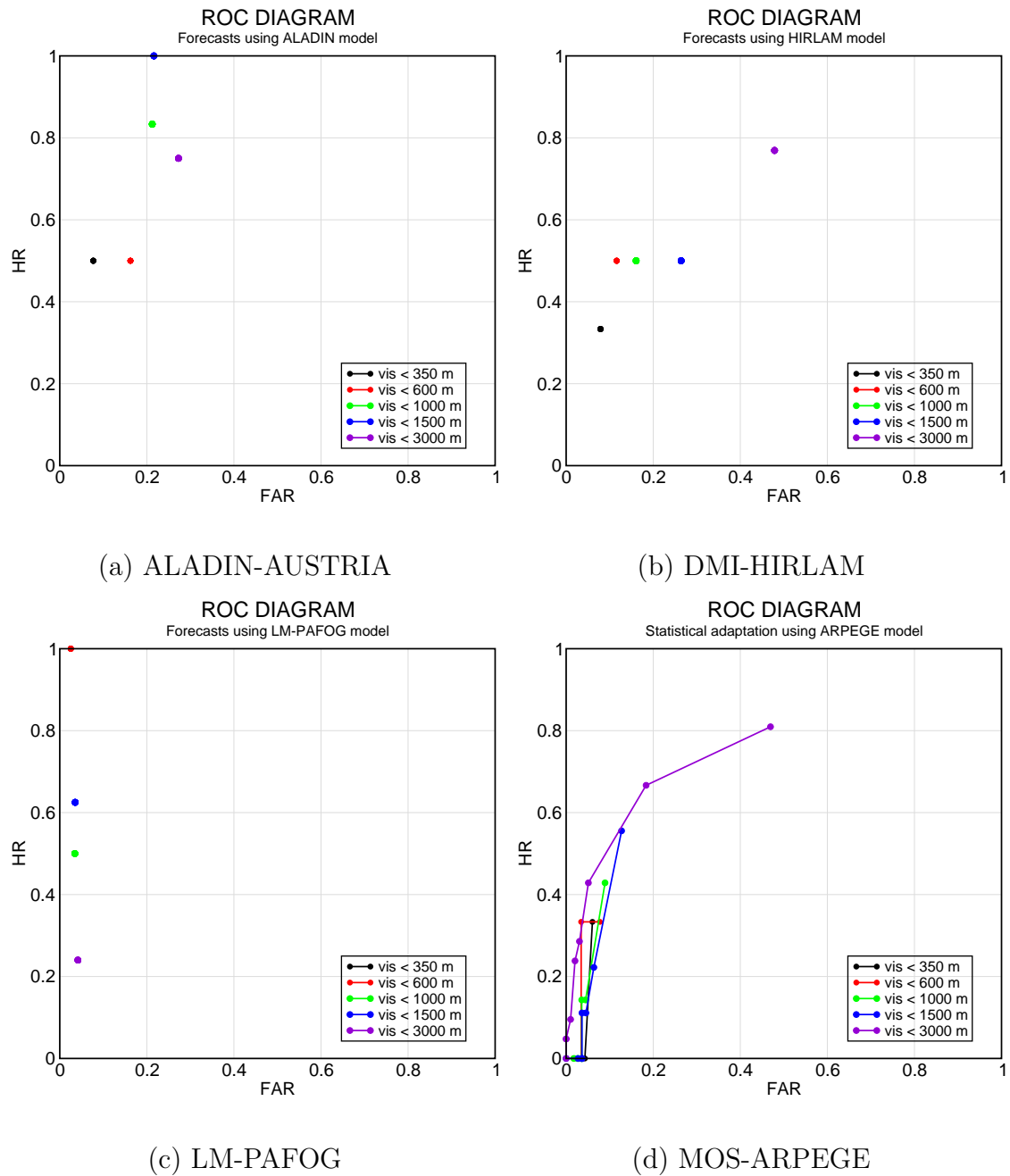
Figure 5.4: ROC curves based on the model forecast of ALADIN-AUSTRIA (a), DMI-HIRLAM (b), LM-PAFOG (c) and MOS-ARPEGE (d) at 00 UTC+24.

(a) ALADIN-AUSTRIA

(b) DMI-HIRLAM

(c) LM-PAFOG
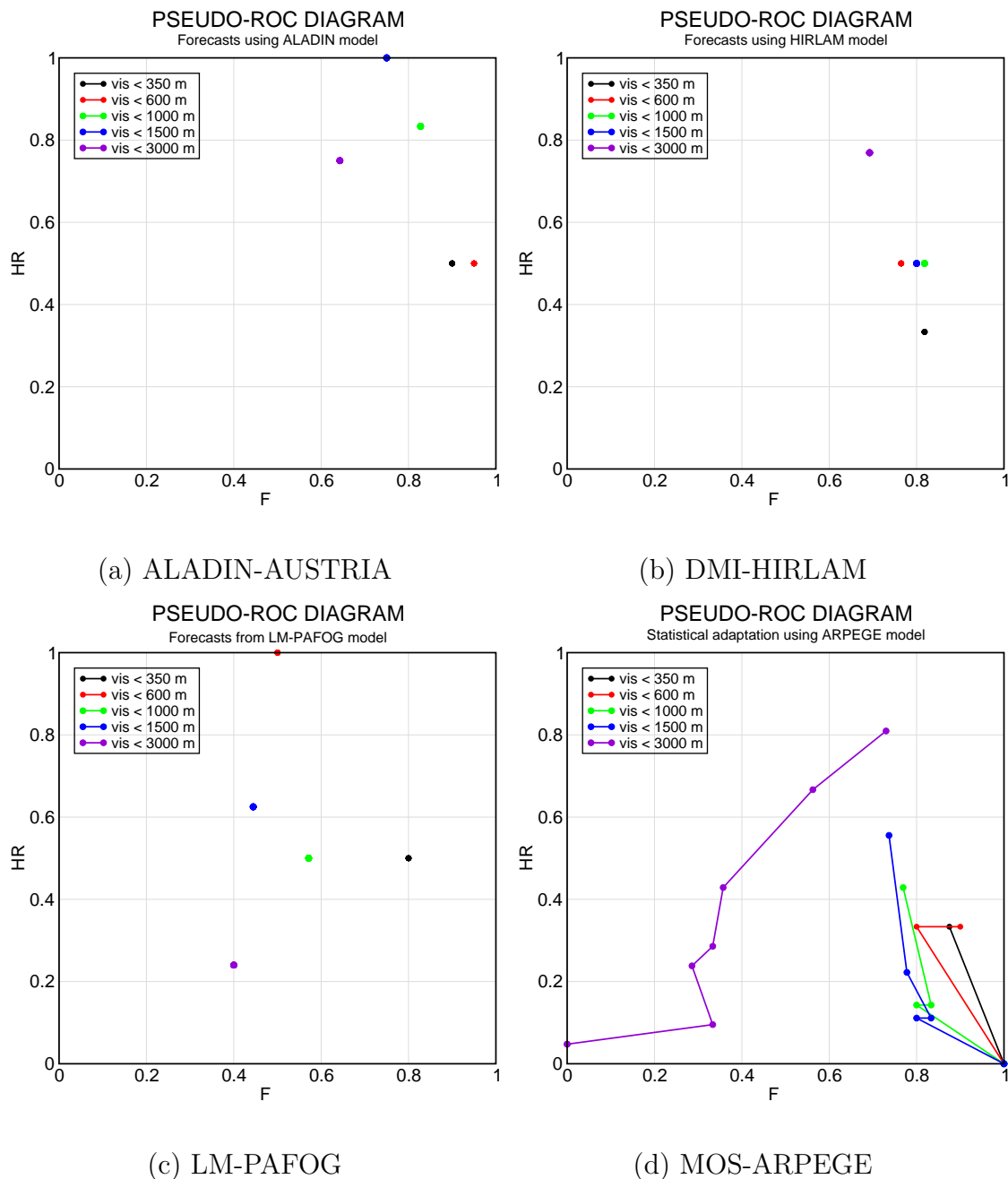
(d) MOS-ARPEGE

Figure 5.5: PSROC curves based on the model forecast of ALADIN-AUSTRIA (a), DMI-HIRLAM (b), LM-PAFOG (c) and MOS-ARPEGE (d) at 00 UTC+24.

Obviously, the visibility parametrisation used by LM-PAFOG is designed to forecast fog events involving low visibility conditions. Furthermore, the detection skill confirms the good reliability of the fog forecast in case of dense fog episodes. The false alarm ratio value stays close to the 50% mark, which is significantly lower than the performances of the other forecast systems.

MOS-ARPEGE (Figures 5.4-d & 5.5-d), as a statistical model, sorted its results per visibility thresholds and per probability thresholds. Lower probability thresholds result in both high hit rates and high false alarms rates. In the ROC diagram, these points are located in the upper right corner. MOS-ARPEGE has some difficulties to detect the different fog events. Generally, the hit rates do not exceed 60%. Furthermore, the detection skill, detailled in Figure 5.5-d, underlines very low forecast reliabilty. The only conclusion concerning these results is that the forecast skill of this model increases with the visibility threshold value. These variations point out a strong dependence of the statistical model results with the fog climatology encountered during our study.

As already mentioned in Section 4.2.2, the fog occurrence is very rare in the chosen four month period of our intercomparison campaign. Depending on the visibility threshold, the number of fog events ranges between 2 and 14 episodes during the 24th forecast hour. The different scores thus have a coarse variation: for a resolution of 1%, the hit rates need at least the forecast of 100 fog events. Such a score variation can be a limitation to draw valuable conclusions concerning each model. However, each model is confronted to the same fog climatology limitation. Each model result is influenced in the same way, the strengths and weaknesses of each model concerning their visibility parameterization are appraisable.

The results of the four models do not point out a "best model". The ROC curves of each model show a good capacity to distinguish fog events. ALADIN-AUSTRIA and DMI-HIRLAM have a high detection rate of fog events, especially for those with visibility values higher than 1000 m. LM-PAFOG shows a good capacity to forecast dense fog events and has some difficulties to identify fog events of a lower intensity. Concerning the results of probabilistic models, the forecast quality of MOS-ARPEGE is difficult to quantify due to the very low occurrence of fog events during the four month period. However, for the 3000 m visibility threshold, MOS-ARPEGE gives very good reliability scores and a promising discrimination skill (Figures 5.4-d & 5.5-d).

Finally, regarding the performance of the ensemble forecast (Figures 5.6 a & b), the overall fog forecast quality can be deduced. The ensemble outputs are close to the best model results for each visibility threshold. In Figure 5.6-a, the ROC diagram shows good forecast skills for each visibility threshold, and the improvements of forecast quality have not deteriorated the reliability compared to the four single models. Nevertheless, the pseudo-ROC curves (Figure 5.6-b) confirm the general tendency to overestimate the fog occurrence: the false alarm ratio values stay close to 70%.

These results point out a very large spread of the forecast qualities for various thresholds. To refine the comparison between the models, the study will now examine the influence of the forecast duration on their respective performances.
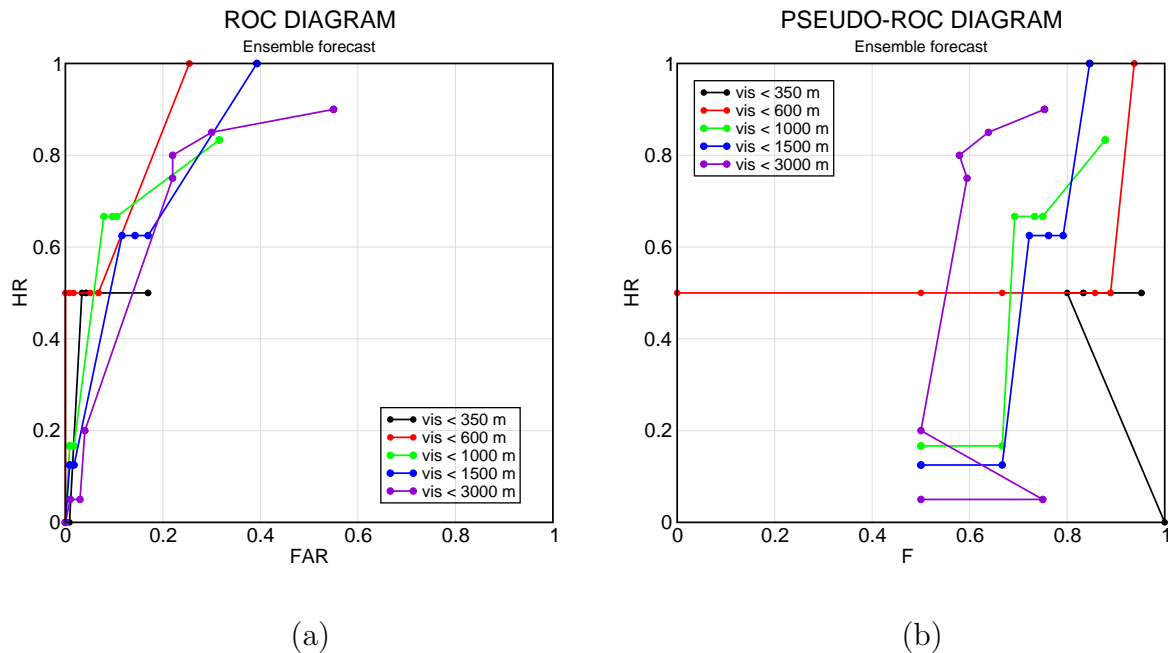
Figure 5.6: ROC diagram (a) and Pseudo-ROC diagram (b) based on the ensemble forecast at 00UTC+24.

5.4.3 Time evolution of fog forecast performances for a visibility threshold of 1000 m

In this second part, the forecast performances of the different participating models will be given as a function of forecast duration. Only the single visibility threshold of 1000m, which correspond to the limit used by the WMO [3] distinguishing "fog and "no fog" period, has been chosen for reasons of concision. Some arrangements were necessary to compare the model outputs issued from the deterministic and statistical forecast systems in a common approach. The ensemble and MOS-ARPEGE deliver a fog forecast with probability levels ranging between 0 and 1, while the deterministic models consider the presence of fog as a binary event. The probability of 0.3, corresponding to the best forecast skill of the models, has been chosen for this evaluation (personal communication H. Petithomme).

In Figures 5.7 a & e, the different statistical scores, resulting from the participating models and the ensemble highlight once again the large discrepancy of the different forecast qualities.

The ensemble forecast quality shows a clear dependence on the diurnal cycle. The ensemble shows a better capacity to forecast fog by night than by day. The Hit Rate, HR, shows a frequent detection of night fog events (HR > 70%) and significantly lower values during the day (HR between 20 and 50%). However the numerous detections induce many false alarms as well. During the night, the False Alarm Rates, FAR, vary between 20 and 40%. By day, FAR stays around 5%. The simultaneous increases of hit and false

---

[3]World Meteorological Organisation
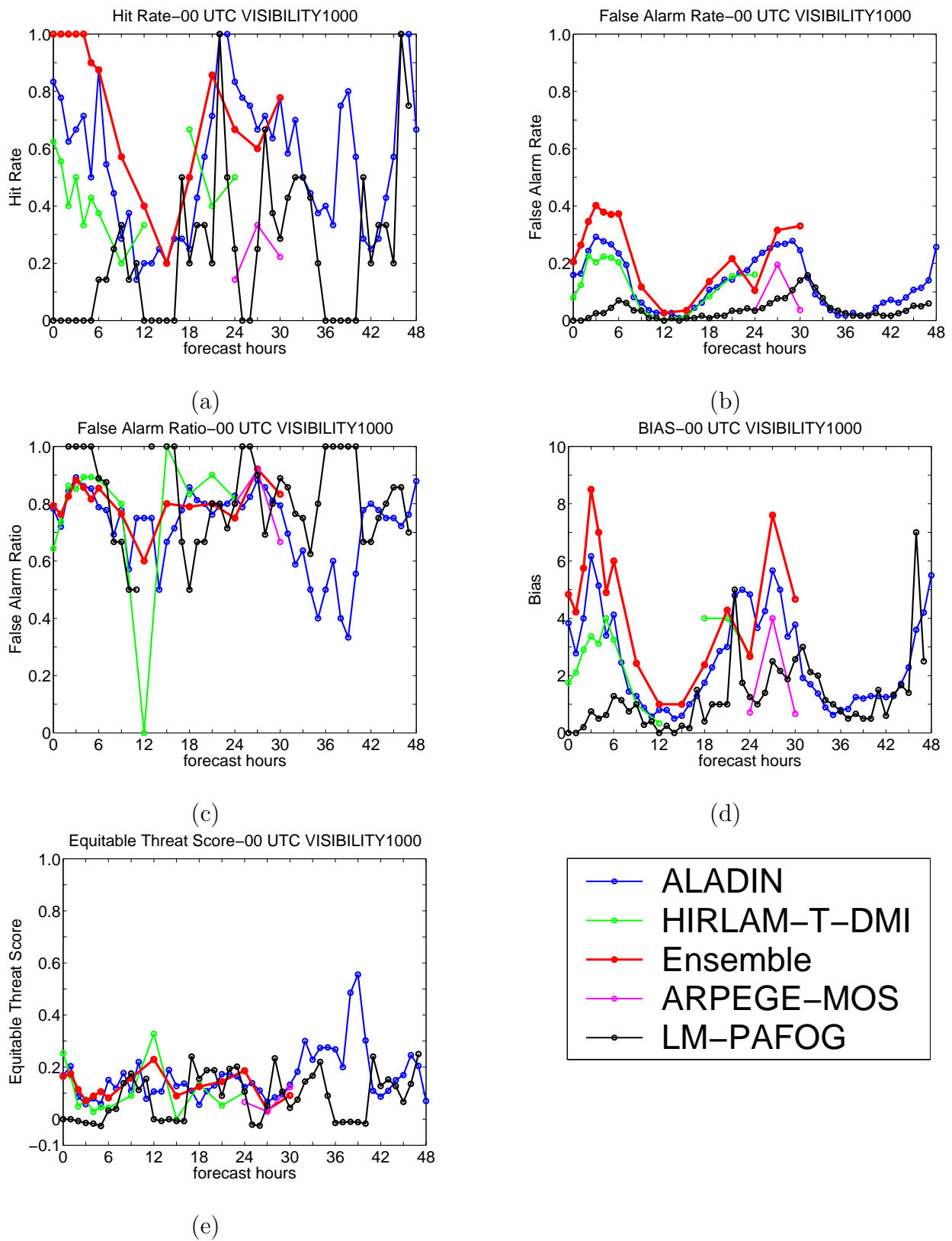
Figure 5.7: Time evolution of hit rate (a), false alarm rate (b), false alarm ratio (c), bias (d) and equitable threat score (e) per forecast hours for a visibility threshold of 1000 m based on the forecasts initialised at 00 UTC.

alarm scores reveal a large tendency for overestimating the number of fog events: the bias score varies between 2 and 8 (Figure 5.7-d). The skill scores of the ensemble underline a constant low reliability of the model. The false alarm ratio, F, is almost constantly larger than 70 %. In other terms: only 30% of the forecasted fog events really occur (Figure 5.7-c).

The time evolution of the ensemble forecast quality has underlined the general characteristis of the involved fog models. the model insufficiencies have a negative impact on the correct rendition of the mean diurnal cycle of fog.

ALADIN-AUSTRIA and DMI HIRLAM contribute to the properties of the ensemble forecast. ALADIN-AUSTRIA shows large HR and FAR values compared to the other members. By night, HR lies between 60 and 80% and FAR values are around 20% (Figure 5.7-a). This model shows a good capacity to distinguish fog and no-fog events. Moreover, the forecast quality increases during the simulation. The false alarm ratio is significantly lower for the second night than for the first one. F decreases from 70% to 40%. DMI-HIRLAM also has a good fog forecast skill. HR fluctuates between 40 and 60% by night and FAR stays very close to the 20% value. Its false alarm ratio evolution fluctuates around 80%.

Both operational models are already used to produce official fog forecasts. These models are thus adjusted to reduce the potential human risk involved in a foggy situation. Despite the coarse grid resolution, a detailed visibility parametrisation compensates the lack of resolution in the lowest part of the atmosphere. The overestimation may thus be a chosen property of the fog forecasts, controlled by the visibility parametrisation.

As already detailed in section 4.3, LM-PAFOG also shows a similar dependence with respect to the diurnal cycle. Its statistical results present a moderate detection skill compared to the other models (HR between 20 and 60%). However, its forecasts produce only few false alarm situations: FAR values stay below 20%. Compared to the other deterministic models, the initial forcing of LM-PAFOG and the afternoon fog forecasts are the major weaknesses of our model. Apart from these shortcomings, LM-PAFOG proposes a forecast relevance equivalent to the other participants which benefit from an adjusted assimilation scheme and larger experience with their model.

As the only statistical model, MOS-ARPEGE shows significant differences related to its forecast philosophy. The French model shows low hit rate values (HR between 10 and 30%) but also low false alarm values (FAR between 5 and 20%). However, its reliability score is equivalent to the ensemble forecast (Figure 5.7-e). The low occurence of fog events limits the resolution of MOS-ARPEGE forecasts. Moreover, the probabilistic model is strongly dependent on its training period. The very rare fog events are obviously underrepresented in the learning phase of the statistical model, especially the dense episodes. This could explain its difficulties to correctly predict a fog event.

A direct comparison of the overall forecast quality of each model can be done using the Equitable Threat Score, ETS, since it highlights neither detection nor false alarms. In spite of the different fog forecast approaches and identified time variations, the different

ETS (Figure 5.7) stay low, close to the 20% value. Finally, the ETS time evolution does not allow a ranking in model quality. The model performances change nearly every time step.

5.4.4   Conclusions

With the statistical study the fog forecast qualities of three deterministic models (ALADIN-AUSTRIA, DMI-HIRLAM and LM-PAFOG) and one statistical model (MOS-ARPEGE) were analysed. In this first phase, the model results have been compared to each other in a probabilistic approach. Although the study was based on a four month forecast period, the results suffer from the low occurrence of fog events during this period. The forecast quality scores are strongly influenced by the chosen visibility threshold. The sample size was not sufficient to include enough rare fog types and thus sharp score variations clouded the results.

The statistical study was not able to determine a clear overall model quality ranking, due to erratic ETS values. The performance of each model fluctuates in time and the choice of "a best model" depends on the need of each user. The ensemble forecast combines the qualities of each involved model and therefore compensated for the weakness of individual models. In the framework of this ensemble forecast, the common characteristics of the involved fog forecast model have been studied. They show significant difficulties to forecast low visibility fog events with a good accuracy. The statistical study points out a lack of reliability for each of the four involved models. Only 30% of fog events are forecasted at the right time and the right place. Nevertheless it has to be noted that the score values result from a automatical comparison scheme focusing only on single point forecasts and the in-situ 2m-visibility measurements. If the results were subjectively evaluated by a forecaster, better skills could be deduced.

Concerning LM-PAFOG, the accuracy of its fog forecasts is already similar to the concurrent fog forecast systems. However, this four month comparison period highlighted some necessary adjustments of several parametrisations. The actual visibility parametrisation, focusing on the detection of the dense fog episodes, should be adjusted to enhance the sensitivity of the model. Compared to the other models, the first forecast hours of LM-PAFOG highlighted the inaccurate initialisation of LM-PAFOG. An initialisation scheme, adjusted to the particularity of LM-PAFOG, would also be a significant improvement.

To identify the potential of LM-PAFOG and its advantages, the comparison with the other models has been further extended in the analysis of selected fog events, considering the differences of the various thermodynamic and dynamic parametrisations.

5.5   Comparison for selected fog episodes

After the statistical evaluation of general fog forecast performance, the four deterministic fog forecast model were tested for three selected fog scenes. As in the evaluation of LM-PAFOG (section 4.4), radiative fog episodes, influenced by different cloud cover structures and occurring at different periods of the day have been selected:

- Episode 1- October 6th and 7th, 2005: in a clear sky situation, a radiative fog event was observed around sunrise on both days.

- Episode 2- September 26th to 27th, 2005: under the influence of a sparse cloud cover, the formation of radiative fog was observed during the night, followed by a rapid increase in visibility above 20 km.

- Episode 3- December 6th to 8th, 2005: a stable and moist boundary layer ensured the presence of low stratus and fog during two entire days.

The variations between the different fog events should point out the shortcomings and the advantages of the different parametrisation involved in the fog formations for each forecast system. The statistical model, MOS-ARPEGE, could not participate in these furthers evaluations due to its non-deterministic outputs.

To quantify the model performance and compare them to each others, the forecast for the single grid point corresponding to the meteorological observatory of Lindenberg was the only available information supplied by each model. Although each forecast system is based on a three-dimensional forecast environment, the framework of the intercomparison campaign was not conceptualised for considering the evolution of the fog's spatial distribution. Nevertheless, the comparison between single column forecasts and boundary layer measurements remains a sufficient evaluation to test the consistency of the fog forecast systems.

5.5.1   Episode 1 - October 6-7th, 2005: Radiative fog event without cloud cover

In a clear sky, two radiative fog episodes have been observed by sunrise on the October 6th and October 7th, 2005 (Figure 5.8). Visibility lower than 300 m was reported for both fog formations. The formation of fog was controlled by radiative cooling, as well as by turbulent heat and moisture mixing at the surface.

Regarding the time evolution of the 2m-visibility forecasts (Figure 5.8), the different behaviours of each model can be highlighted. ALADIN-AUSTRIA and LM-PAFOG clearly identified both fog formations of few hours, but only LM-PAFOG reproduced the fog density as a visibility below 400 m. HIRLAM-DMI and NMM-PAFOG seemed to have more difficulties to clearly identify the fog events. Their visibility forecasts never decrease below the 1000 m threshold corresponding the presence of fog. The visibility forecasts of NMM-PAFOG vary between 1500 and 3000 m between the 18th and 42nd forecast hours. Concerning HIRLAM-DMI, the model forecast is only sensitive to the second fog event. Between the 24th and 33rd forecast hours, the 2m-visibility values decrease to a minimum of 2500 m.
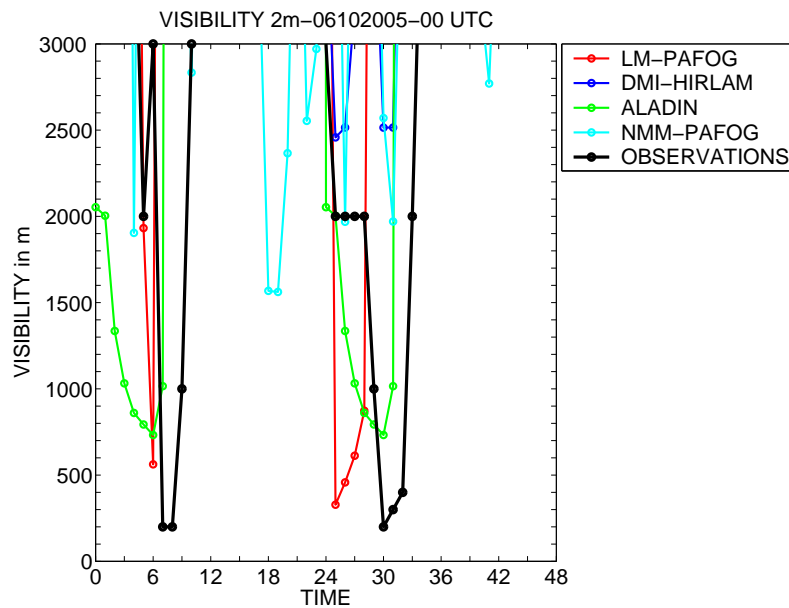
Figure 5.8: Time evolution of the visibility forecast at the Lindenberg. Initialisation: October 6th, 2005 at 00 UTC.

The large discrepancy between the models' forecasts has to be considered carefully. Delays of the fog formation or large fluctuations of the density of fog forecasts can be caused by small spatial inaccuracy of the three-dimensional models. Therefore, a completed evaluation of the forecast quality cannot occurred in a single point comparison. The influence of radiative cooling on the boundary layer evolution and its consequences on the temperature and humidity profiles must be taken into account. The influence of the boundary layer wind profile has been also assessed. The formation of radiative fog can only occur in a very weak wind field conditions.

In such a radiation fog event, the accuracy of the energy balance at the surface is decisive for a successful fog forecast. The radiative fluxes at the surface are compared with the different model values in Figure 5.9.

In these clear sky situations, the short wave as well as the long wave fluxes at the ground are well quantified by the different models. Note that the influence of the fog formation can be easily identified, since the only anomalies in the radiative flux balance are caused by fog. In Figure 5.9-b the increase of long wave flux corresponds exactly to the fog period shown in Figure 5.8. Although each model reported the presence of fog, the consequences on the long wave flux balance are very different. Only the DMI-HIRLAM and LM-PAFOG long wave flux balances reflect the fog or low cloud presence in the Lindenberg area. The forecasted long wave fluxes of ALADIN-AUSTRIA and NMM-PAFOG appear to be insensitive to the formation of fog, while their respective visibility forecasts warns the users of both fog events. With this basic comparison the decisive role of the visibility parametrisation can be highlighted. The presence of fog is not exclusively limited to a cloud disturbing the radiative fluxes at the surface. An adequate calibration of the visibility parametrisation can compensate the limitations of physical parametrisations involved in the fog formation.
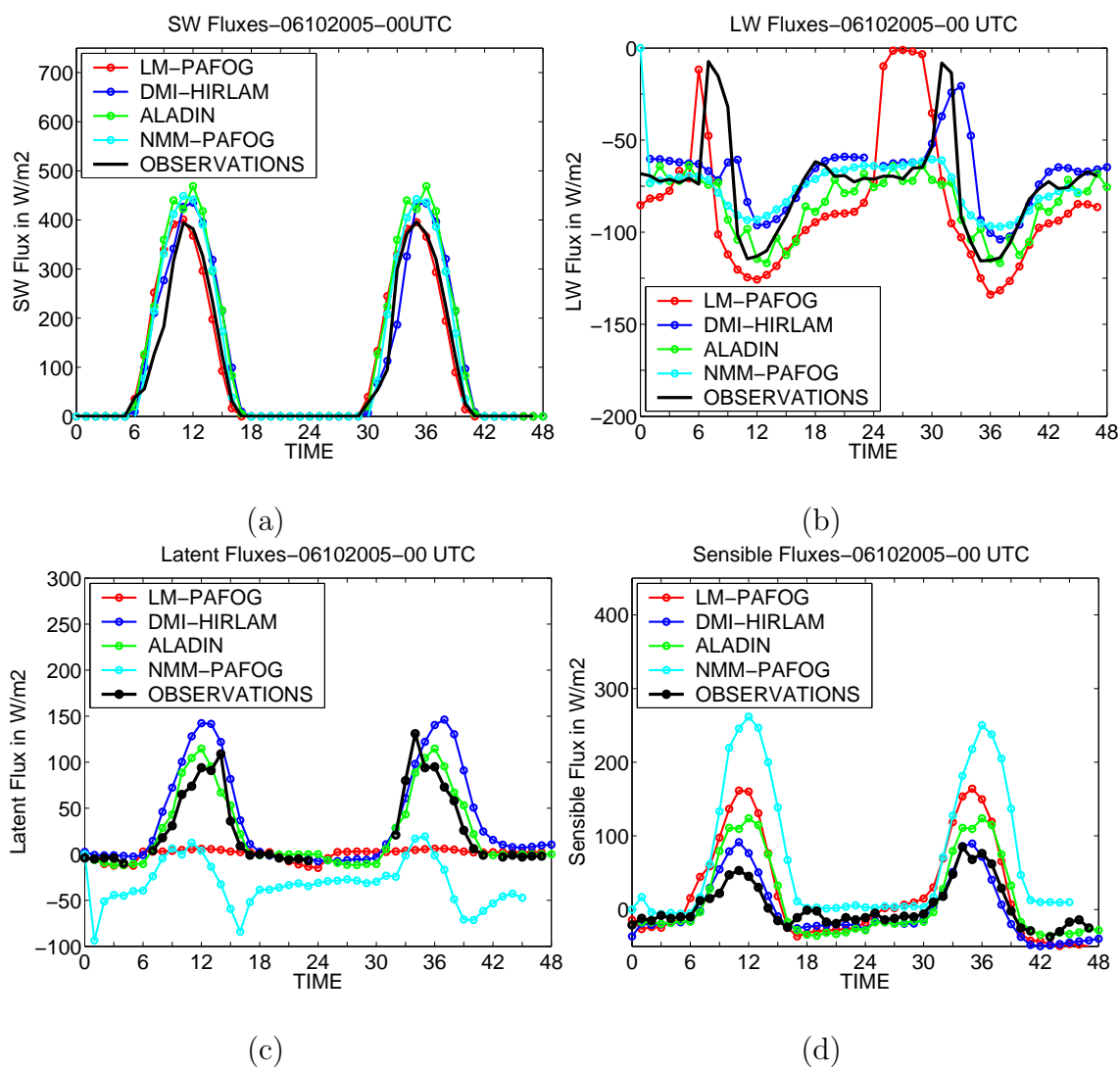
Figure 5.9: Time series of short wave fluxes (a), long wave fluxes (b), latent heat fluxes (c) and sensible heat fluxes (d), forecasted by ALADIN-AUSTRIA, DMI-HIRLAM, NMM-PAFOG and LM-PAFOG. Initialisation: October 6th, 2005 at 00 UTC.
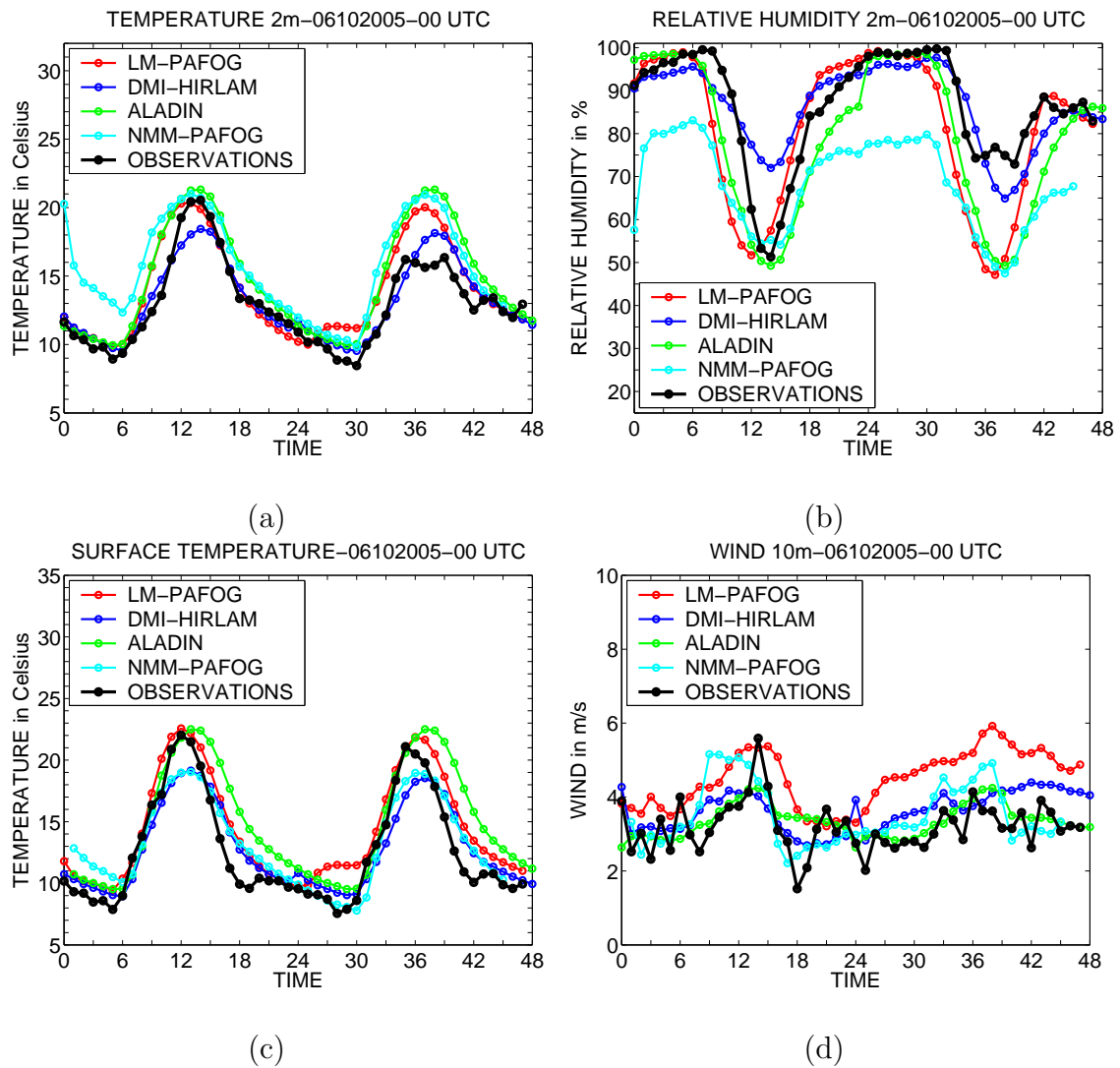
Figure 5.10: Time series of 2 m temperature (a), 2 m relative humidity (b), surface temperature (c) and 10 m wind speed (d), forecasted by ALADIN-AUSTRIA, DMI-HIRLAM, NMM-PAFOG and LM-PAFOG. Initialisation: October 6th, 2005 at 00 UTC.

The latent heat and sensible heat fluxes at the surface are presented in Figure 5.9 c & d. The time evolutions of these fluxes are well reproduced by the two operational models, DMI-HIRLAM and ALADIN-AUSTRIA, while obvious errors are visible in the forecasts of NMM-PAFOG and LM-PAFOG.

LM-PAFOG forecasts point out two distinct behaviours during day and night time. By night the sensible heat and latent heat fluxes agree well with the observations. The cooling of the ground and the increase of surface humidity are confirmed. However, between 6th and 17th forecast hours and between 30th and 40th forecast hours, the latent heat flux is very weak with values close to $0\ Wm^{-2}$ and the sensible heat flux is overestimated with a bias reaching $100\ Wm^{-2}$ at 12 UTC. With such heat and moisture turbulent fluxes at the surface a drying of the lowermost atmosphere is awaited.

The latent heat fluxes of NMM-PAFOG do not agree at all with the observations. The negative values between -100 and $0\ Wm^{-2}$ point out a continuous moistening of the soil. The moisture present in the atmosphere is transferred to the soil and the lowermost atmospheric layer of the model is dried progressively. The sensible heat flux of NMM-PAFOG exhibit two distinct performance between day and night time. Before 6 UTC and between 18th and 30th forecast hours, the forecasted values agree well with the observations. However, between 6 and 18 UTC as well as between the 30th and 42th forecast hours, the sensible heat flux is overestimated with a bias exceeding $200\ Wm^{-2}$. A larger heating of the lowermost atmosphere is expected by day due to the behaviour of the sensible heat turbulent flux.

The time evolution of the surface temperature as well as the relative humidity and temperature at 2 m (Figure 5.10) confirm the decisive role of the turbulent fluxes.

The 2m-temperature as well as surface temperature forecasts of ALADIN-AUSTRIA and DMI-HIRLAM agree well with the observations. Despite the overestimation of the sensible heat fluxes, NMM-PAFOG and LM-PAFOG also deliver accurate temperature forecasts. Only NMM-PAFOG forecasts show some difficulties with the temperature initialisation in the first hours.

Regarding the 2m-relative humidity evolution, DMI-HIRLAM, ALADIN-AUSTRIA and LM-PAFOG forecasts closely follow the observed values. Nevertheless, the early dissipation of the forecasted fog in ALADIN-AUSTRIA and LM-PAFOG can be identified in the decrease of relative humidity between 6th and 9th forecast hours and between 30th and 33th forecast hours.

Concerning NMM-PAFOG forecasts, the 2m-relative humidity values differ from the measurements due to an initialisation with a very dry atmosphere. Moreover, the maximum values, which are reached during the night, decreases from the first forecasted day to the next one. Before 6 UTC the relative humidity forecasts exceed 80 %, then between 18th and 30th forecast hour the values stay around 75 % and after the 39th forecast hour the 2m-relative humidity is below 70 %. During both night periods, the forecasted 2m-temperature was roughly the same. A clear drying of the lowermost atmosphere, which was expected while the time evolution of the latent heat fluxes, is confirmed. Therefore, fog formation is inhibitted.
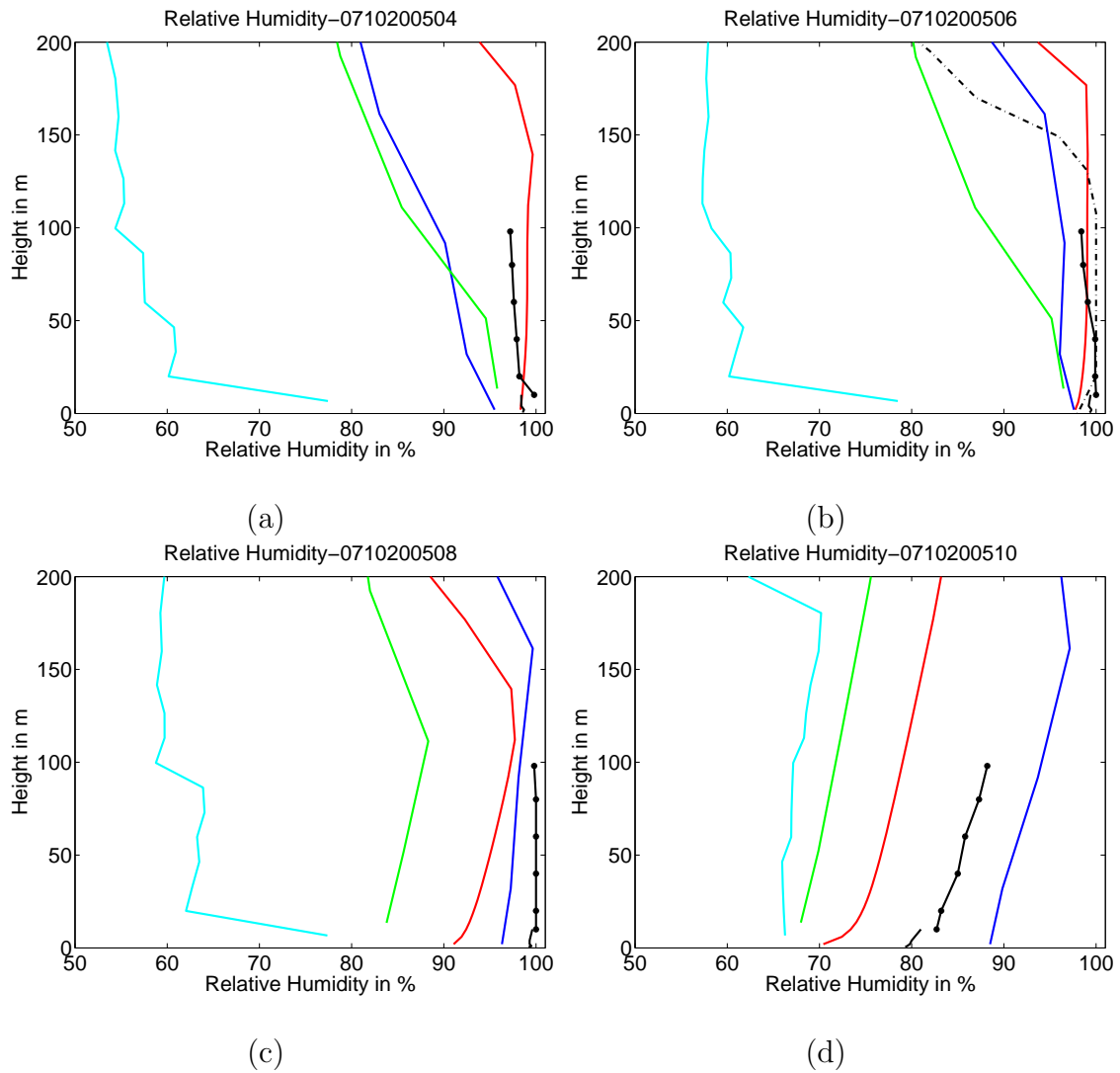
Figure 5.11: Vertical profile of relative humidity at Lindenberg from radiosounding (black dashed line), 10 m and 100 m masts (black line), ALADIN-AUSTRIA forecasts (green line), DMI-HIRLAM forecasts (blue line), NMM-PAFOG forecasts (cyan line) and LM-PAFOG forecasts (red line) on October 7th, 2005 at 04 UTC (a), at 06 UTC (b), at 08 UTC (c) and 10 UTC (d).
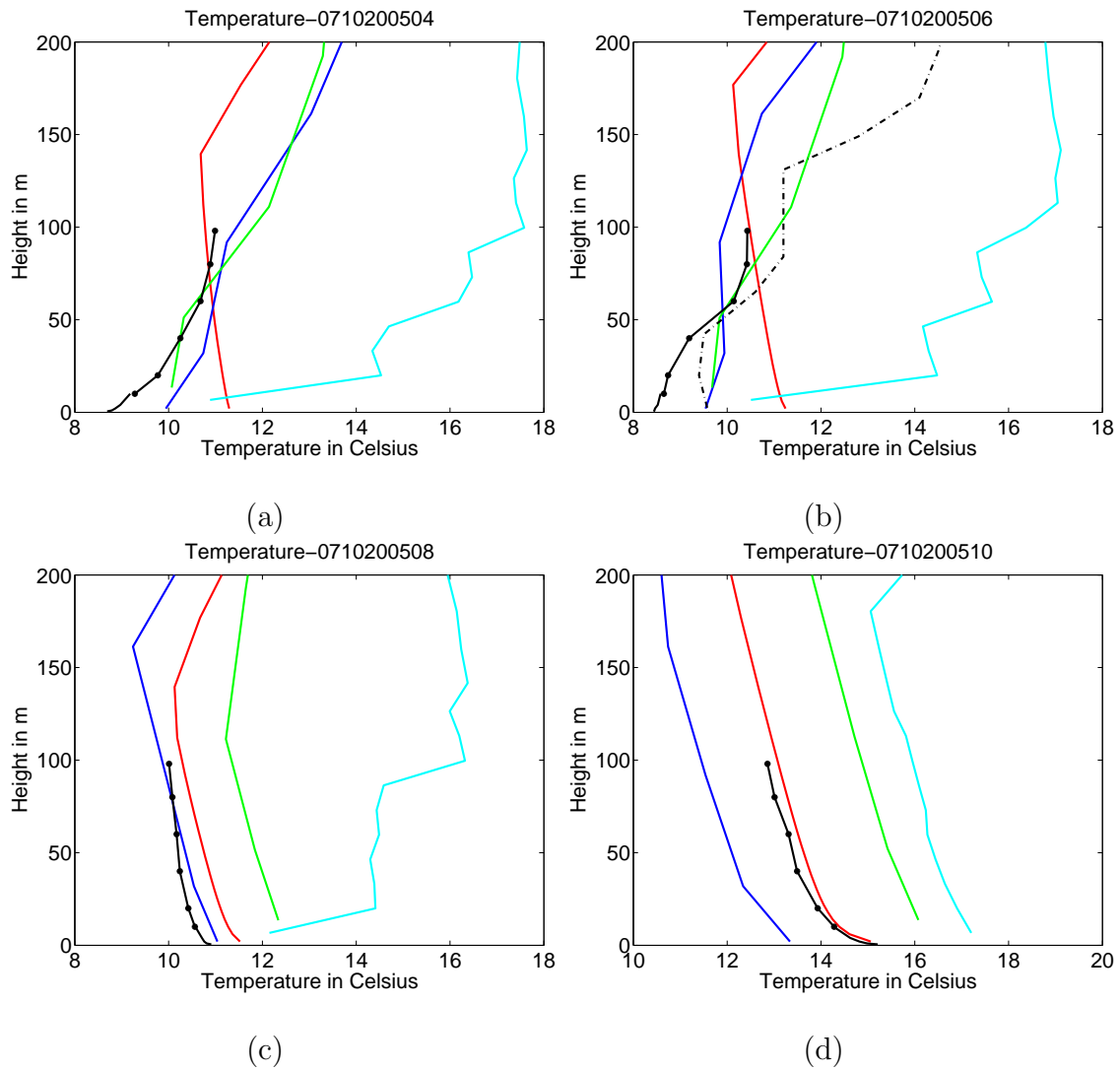
Figure 5.12: Vertical profile of temperature at Lindenberg from radiosounding (black dashed line), 10 m and 100 m masts (black line), ALADIN-AUSTRIA forecasts (green line), DMI-HIRLAM forecasts (blue line), NMM-PAFOG forecasts (cyan line) and LM-PAFOG forecasts (red line) on October 7th, 2005 at 04 UTC (a), at 06 UTC (b), at 08 UTC (c) and 10 UTC (d).
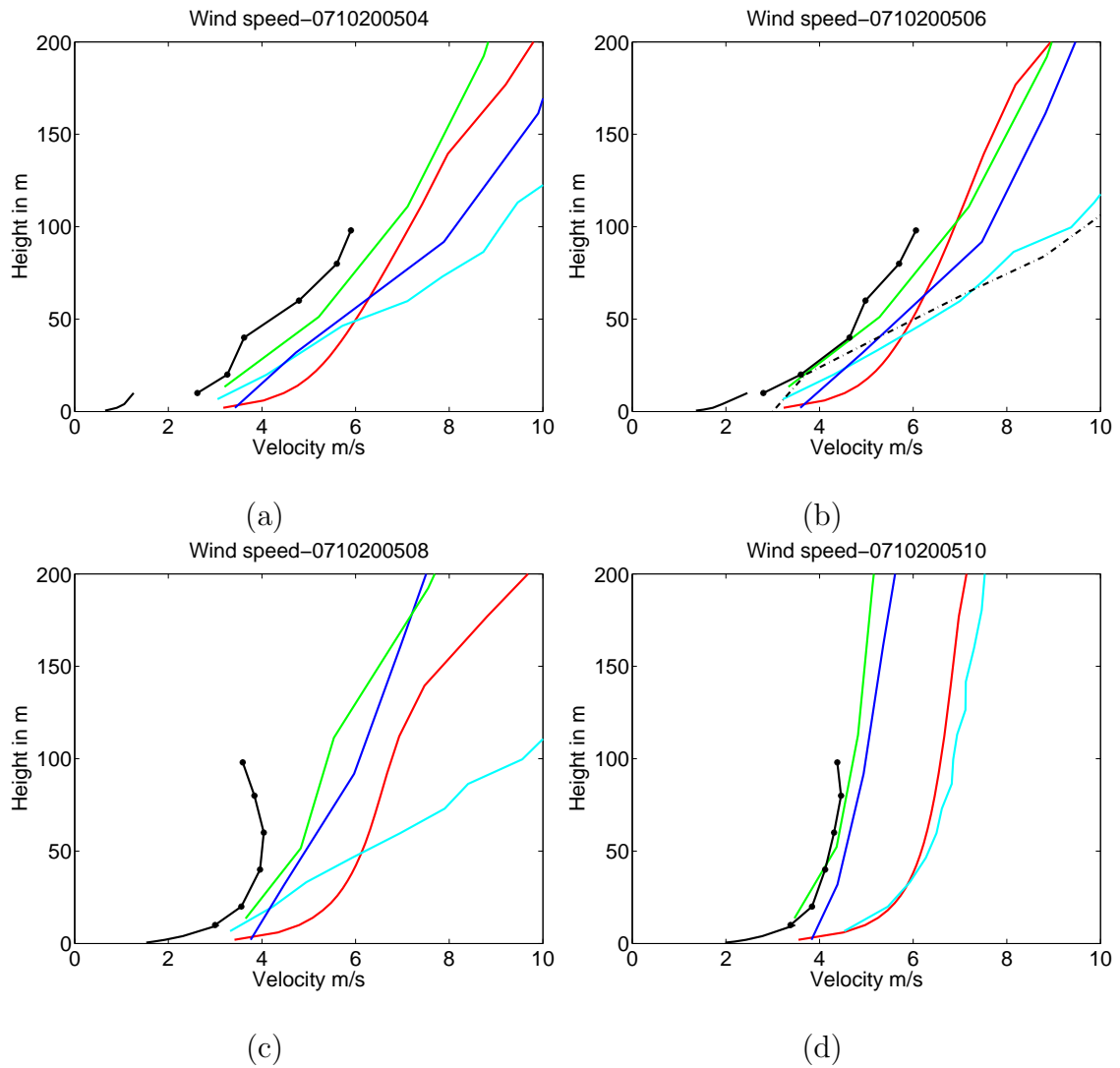
Figure 5.13: Vertical profile of wind speed at Lindenberg from radiosounding (black dashed line), 10 m and 100 m masts (black line), ALADIN-AUSTRIA forecasts (green line), DMI-HIRLAM forecasts (blue line), NMM-PAFOG forecasts (cyan line) and LM-PAFOG forecasts (red line) on October 7th, 2005 at 04 UTC (a), at 06 UTC (b), at 08 UTC (c) and 10 UTC (d).

Regarding the vertical profiles of temperature and relative humidity, differences between the four model performance can be distinguished (Figures 5.11 and 5.12).

The NMM-PAFOG forecasts disagree with the meteorological mast measurements. The temperature is strongly overestimated through the profile with a bias exceeding 4°C, which causes a large underestimation of the relative humidity values, with a bias reaching -30%. Generally, the evolution of NMM-PAFOG forecasts points out the weakness of the NMM-PAFOG initialization. For the initialization of the NMM-PAFOG forecast domain the global model analysis data with a horizontal resolution of 40 km are interpolated to the NMM-PAFOG grid with a horizontal resolution of 2 km. Such an approach can introduce large inaccuracies. The coarse grid of the global model does not contain enough information for an adapted intialization of NMM-PAFOG. At 00 UTC the 2m-temperature is forced with a bias of 8 °C (Figure 5.10-b). The initialiazation of the soil properties with very low soil moisture values could explain the inverted behaviour of the latent heat fluxes forecasted by NMM-PAFOG as well as the drying of the lowermost atmosphere.

The temperature and humidity forecast of ALADIN-AUSTRIA, DMI-HIRLAM are in agreement with the structure of the vertical profiles. ALADIN-AUSTRIA and DMI-HIRLAM reproduce with a good precision the temperature inversion caused by the warming of the upper atmosphere. However, the saturation at the ground is not reached by the model forecast at Lindenberg. These models supply forecasts which coincide well with all the available measurements.

The vertical profiles of temperature and humidity forecasted by LM-PAFOG agree also with the mast measurements. Nevertheless, the limitations of the turbulence scheme are responsible for the early dissipation of fog. The temperature inversion already disappears at 04 UTC (Figure 5.12-a) and a drying of the lowest part of the atmosphere is identified at 08 UTC (Figure 5.11-c).

To finalise the evaluation of the four model forecasts the influence of the wind field in the boundary layer has been examined in Figures 5.10-d and 5.13. In this case, all four models deliver an accurate forecast of the wind speed. The vertical profiles as well as the time evolution during the entire forecasted period agree well with the observations.

After these comparisons in the case of a radiative fog event, it can be only concluded that no fog forecast can reproduced all physical processes involved in the fog formation with the necessary accuracy.

The evaluation of the NMM-PAFOG forecast is strongly limited by its faulty initialisation scheme. In this case, the forecast domain was initialised with a dry atmosphere and a dry soil. A fog formation cannot be expected.

LM-PAFOG has shown its capability to form a radiative fog event. Nevertheless, the adaptation of the turbulence scheme on the high vertical resolution of model grid points out some difficulties to describe this vertical transport accurately.

ALADIN-AUSTRIA and DMI-HIRLAM forecasts agree well with the complete set of measurements. The parametrisation of radiative fluxes at the ground and the thermodynamic and dynamic processes react well to the different variations.
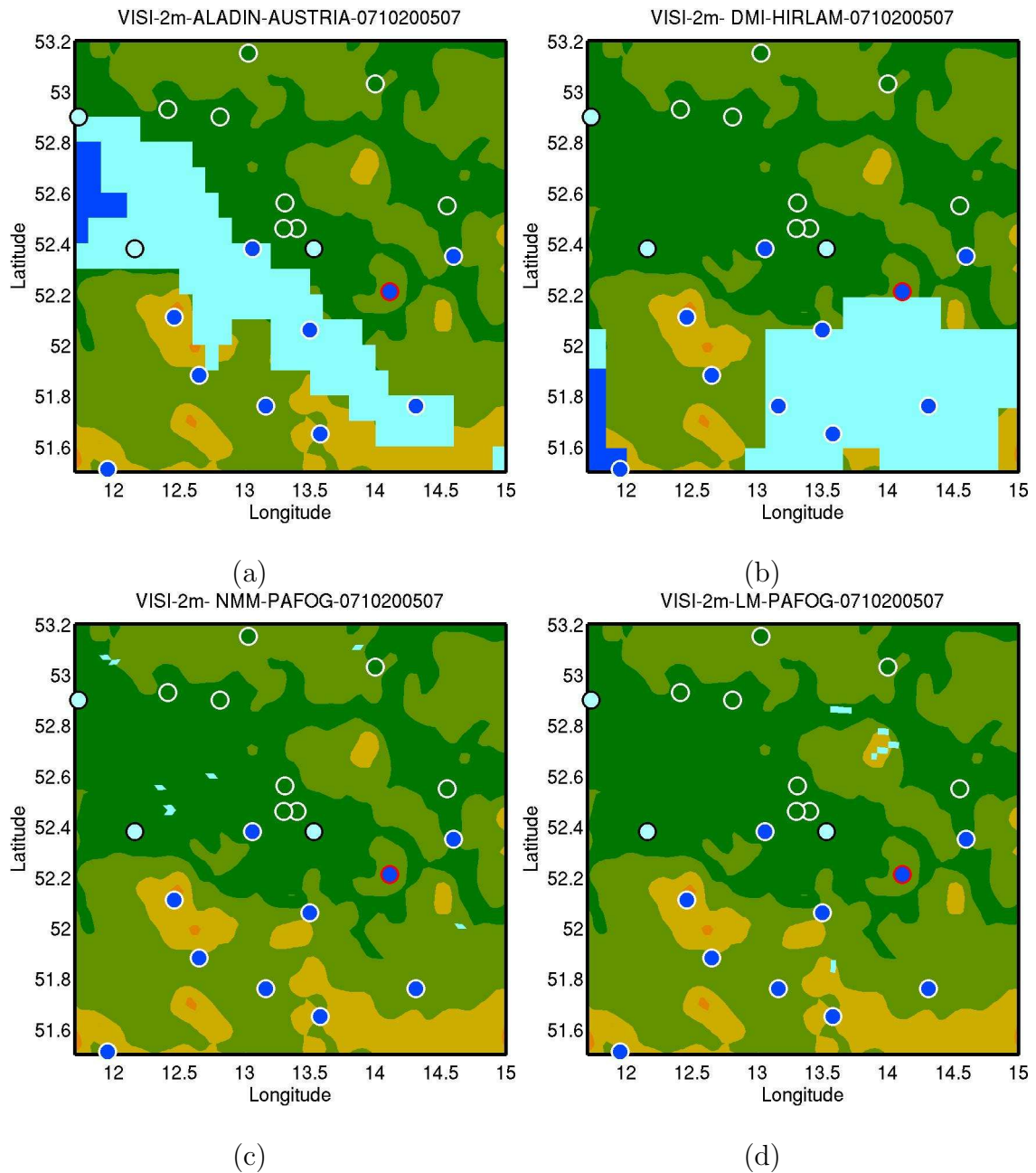
Figure 5.14: Spatial distribution of 2m visibility in the Lindenberg area on October 7th, 2005 at 07 UTC based on ALADIN-AUSTRIA forecasts (a), DMI-HIRLAM forecasts (b), NMM-PAFOG forecasts (c) and LM-PAFOG forecasts (d). The circle markers correspond to the position of the visibility measurements. The red circle corresponds to the Lindenberg observatory. The visibility values have been separated in three categories. **Deep blue** corresponds to a fog event with a visibility below 1000 m. **Cyan** represents a fog event with a visibility between 1000 and 3000 m. **Green** and brown areas denotes areas without fog (visibility exceeding 3000m).

However, due to the large vertical grid resolution (60 m thick close to the ground) the saturation condition close to the ground does not occur and the visibility parametrisations have to be adjusted to correct this lack of information in the boundary layer evolution.

Finally, the horizontal cross section comparing 2m-visibility forecast with the corresponding SYNOP measurement present in the Lindenberg area (Figure 5.14), point out the difficulty to compare four three-dimensional fog forecast models. The analysis of the single point corresponding to the Lindenberg observatory (red circle) does not take into account the horizontal spatial component of the forecast. In this case, both operational models, ALADIN-AUSTRIA and DMI-HIRLAM, reproduce the formation of the radiative fog event well in spite of the inaccuracy of the fog's spatial extension. The research fog forecast models, NMM-PAFOG and LM-PAFOG, cannot emphasise the advantage of the high vertical grid resolution and the fog microphysics due to the encountered difficulties in the initialisation and turbulence parametrisation.

5.5.2 Episode 2 - September 27th, 2005: Radiative fog event after a rain event

Under the influence of a residual cloud cover present in the Lindenberg area radiative cooling during the night from 26th to 27th September 2005 causes radiation fog in cloud free areas (Figure 5.15). Visibilities lower than 200 m were reported for this fog episode.

Note that the initialisation time of each model is different in this case study. The forecasts giving the best results have been sorted. LM-PAFOG is initialised the 26th September at 00UTC in order to avoid its spin up effect in the first 6 forecast hours. DMI-HIRLAM is initialised the 26th September at 12 UTC and finally, ALADIN-AUSTRIA and NMM-PAFOG are initialised the 27th September at 00 UTC.
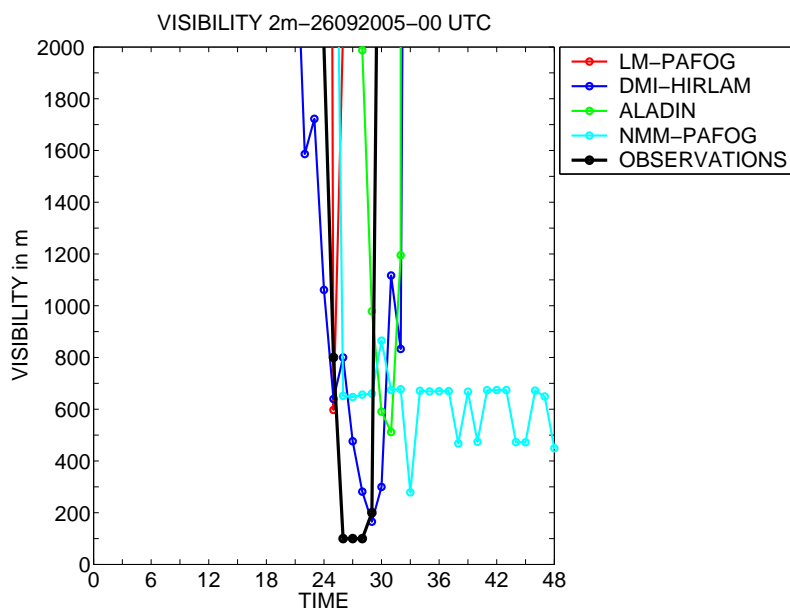
Figure 5.15: Time evolution of the visibility forecast at Lindenberg. Initialisation: September 26th, 2005 at 00 UTC.

Analysing the time evolution of the 2m-visibility forecast (Figure 5.15) the successful fog forecasts by each of the four models are highlighted. DMI-HIRLAM forecasts follow almost exactly the time evolution of the visibility measurements and the density of fog is also accurately reported with a lowest value of 200 m. LM-PAFOG detects the first hour of the fog period, but the forecasted fog is already dissipated after one hour. NMM-PAFOG forecasts reproduce the fog episode with a lower intensity than the observations and with a long persistence. The forecasted visibility stays around 600 m until the end of the model run. ALADIN-AUSTRIA simulates the formation of the fog event 4 hours later.

As already mentioned in the previous section, the radiative flux balance at the surface controls the formation, persistence and dissipation of fog. The analysis of the radiative fluxes at the surface is presented in Figure 5.16. In a forecast area with broken cloud cover the forecasts of short wave and long wave fluxes yield accurate results (Figures 5.16 a & b). The influence of the cloud cover does not deteriorate the forecasted radiative flux values of the four models.
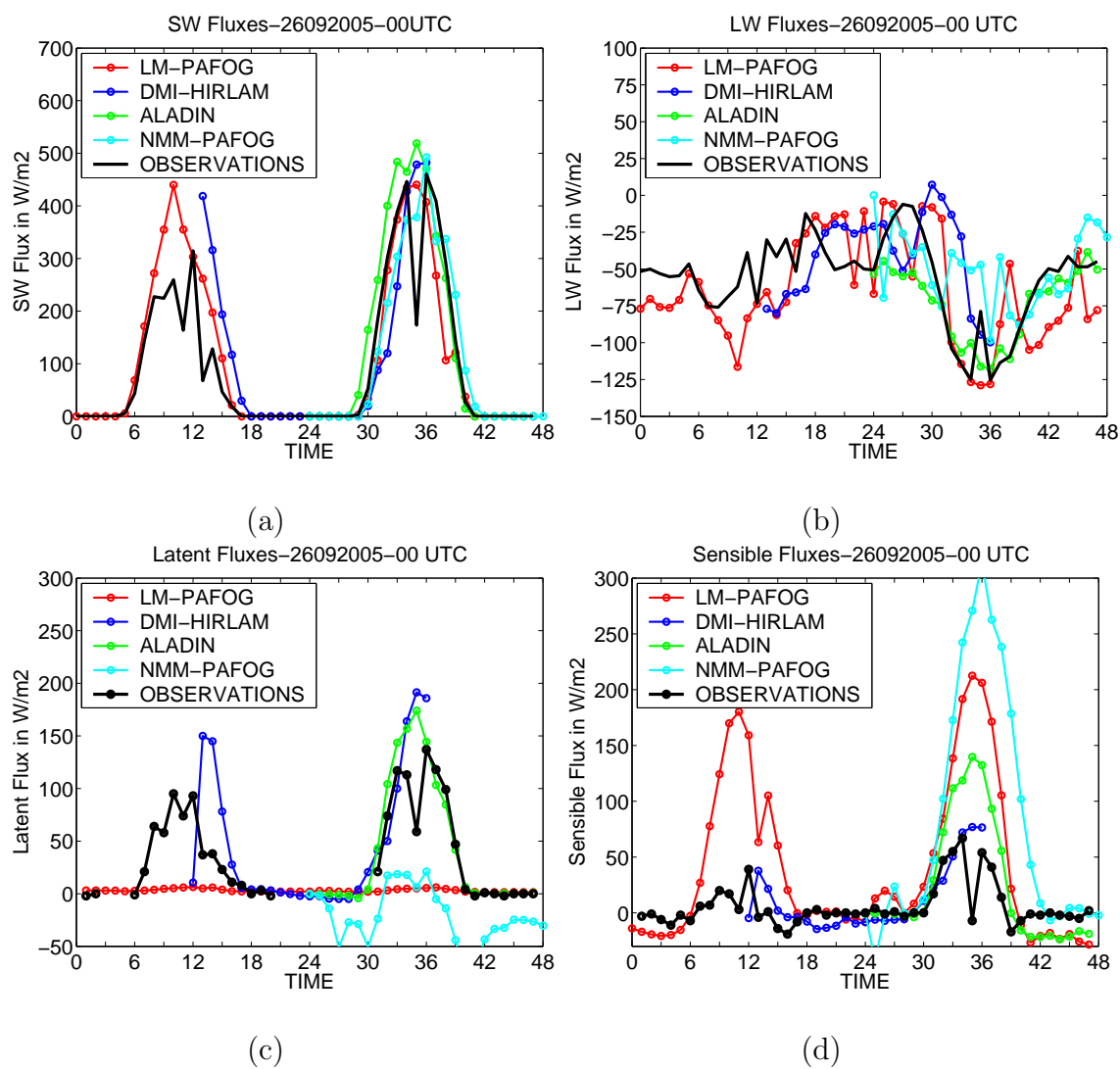
Figure 5.16: Time evolution of short wave fluxes (a), long wave fluxes (b), latent heat fluxes (c) and sensible heat fluxes (d), forecasted by ALADIN-AUSTRIA, DMI-HIRLAM, NMM-PAFOG and LM-PAFOG. Initialisation: September 26th, 2005 at 00 UTC.
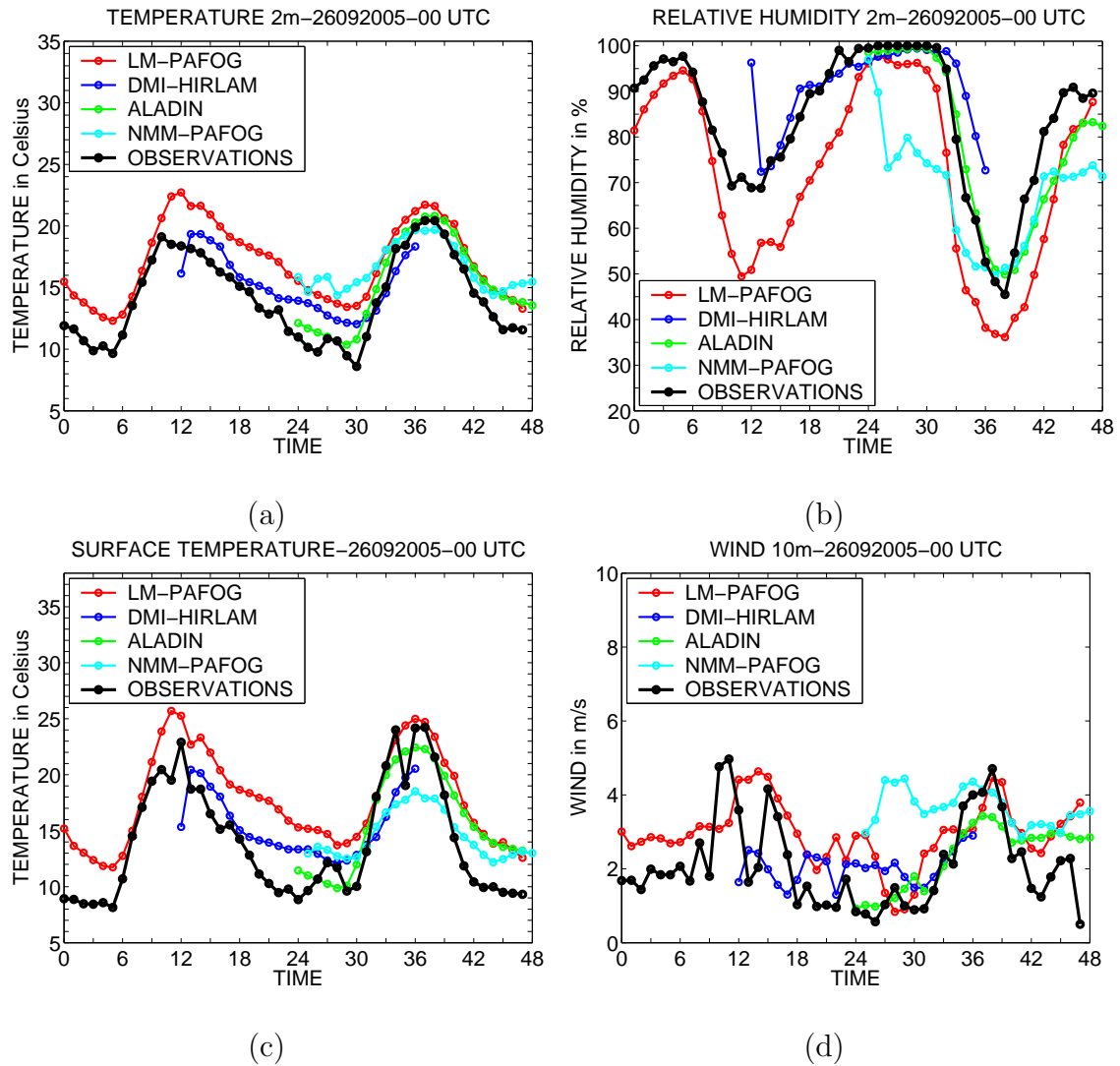
Figure 5.17: Time evolution of 2m temperature (a), 2m relative humidity (b), surface temperature (c) and 10m wind speed (d), forecasted by ALADIN-AUSTRIA, DMI-HIRLAM, NMM-PAFOG and LM-PAFOG. Initialisation: September 26th, 2005 at 00 UTC.

Nevertheless, obvious differences concerning the forecasted sensible heat and latent heat fluxes have been detected again (Figures 5.16 c & d). ALADIN-AUSTRIA and DMI-HIRLAM deliver accurate forecasts. Some difficulties, similar to the first case study, are identified in the NMM-PAFOG and LM-PAFOG results.   The chosen turbulence parametrisations of both research models disagree with the variation of the boundary layer mixing between day and night time. Obvious differences of the forecast performance between day and night time are identified. By night the forecasted fluxes agree relatively well with the observation, while an overestimation of the sensible heat flux and a very weak latent heat flux are present during the day time. An excessive warming and drying of the lowermost atmosphere is expected during the day, considering the latent heat and sensible heat flux forecasts of NMM-PAFOG and LM-PAFOG.

Based on accurate radiative fluxes at the surface, the forecasts of ALADIN-AUSTRIA and DMI-HIRLAM confirm the agreement of temperature and humidity variables with the 2m-measurements (Figures 5.17-a, b & c). In fact, the temperature time evolution coming from ALADIN-AUSTRIA and HIRLAM-DMI forecasts follow with a bias lower than 2 °C the Lindenberg observations. The 2m relative humidity forecasts show a good agreement as well (Figure 5.17-b).

NMM-PAFOG and LM-PAFOG, which are already limited by their turbulent flux parametrisations, are also handicapped by a misleading initialisation of their respective forecast domain. The NMM-PAFOG initialisation fields, which are based on the data of the global model GFS, are again a large source of inaccuracies. The 2m-temperature is forced with a bias of 5 °C. The wind profile is clearly overestimated with a bias of 2 m/s (Figure 5.17-d). Despite the accurate humidity initialisation values, the "spin up" of the model causes a sharp decrease of the relative humidity in the first forecast hours (Figure 5.17-b). Such behaviour can explain the unexpected latent heat fluxes at the ground (Figure 5.16-c). The inaccurate initialisation of the LM-PAFOG temperature field irreversibly deteriorate the forecast performance. The surface temperature values have been overestimated with a bias exceeding 3°C. The 2m-relative humidity values cannot reach saturation and no fog can be formed at this place. Despite these limitations, the time evolution of the temperature, humidity and wind field agree well with the observations (Figure 5.17).

To clearly identify the qualities of each forecast model, the atmospheric structure in the boundary layer has been compared with the temperature and humidity of 100m-mast and radiosonde measurements(Figures 5.18 and 5.19). The difficulties of NMM-PAFOG and LM-PAFOG are again identified. The temperature and relative humidity profiles stay close to the mast and radiosonde profiles. The temperature inversion is well defined in the lowest 100 meters (Figure 5.19 a & c). Nevertheless, even if ALADIN-AUSTRIA and DMI-HIRLAM have reproduced the fog event, the 50m-thickness of the fog event (Figures 5.18 b & c) and the sharp temperature gradient in the first 10m (Figures 5.19 a & c) which is caused by the radiative cooling at surface cannot be reproduced due to their coarse vertical resolutions. Empirical visibility parametrisations are developed to correct the lack of information and introduce some inaccuracies.
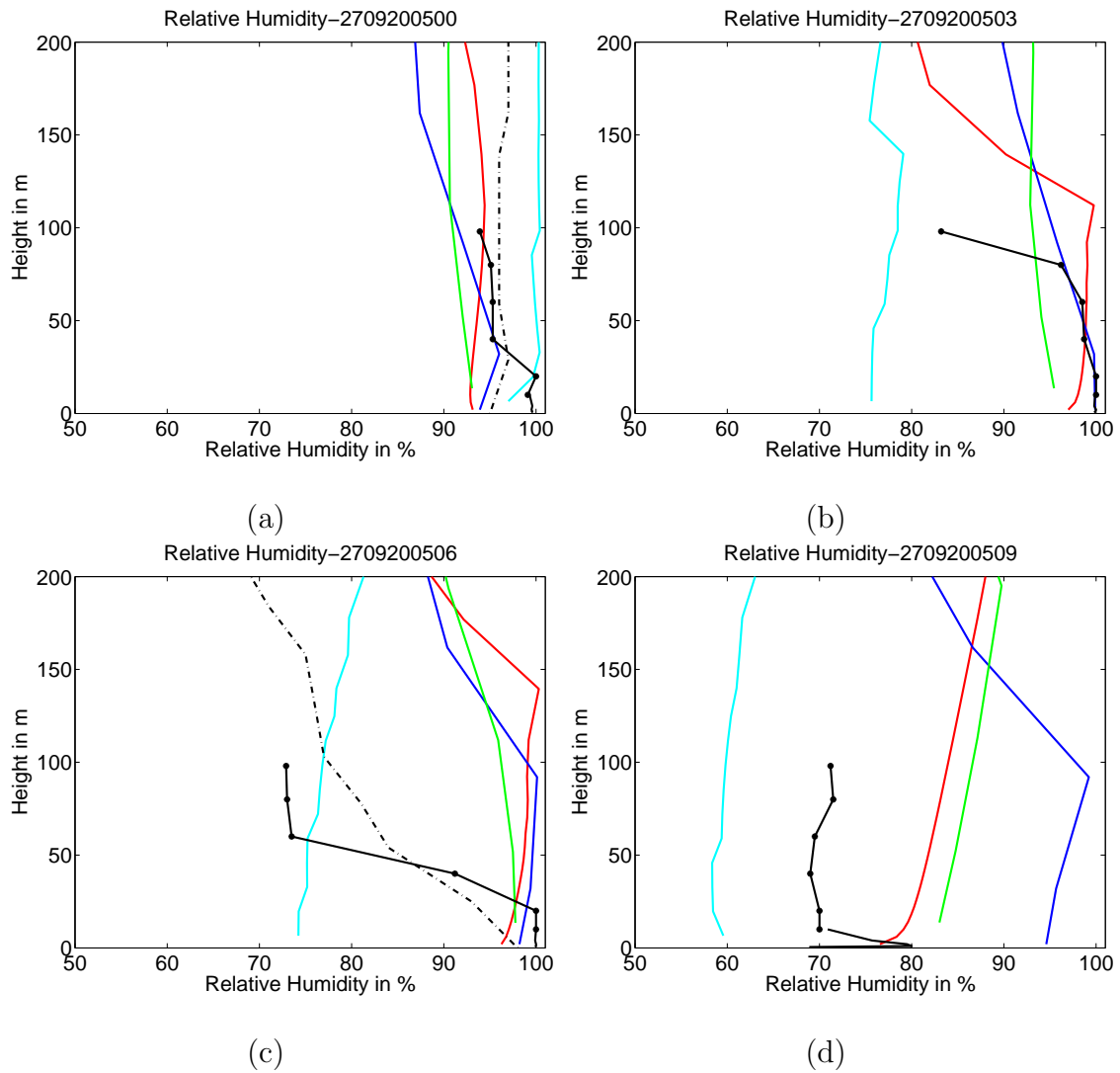
Figure 5.18: Vertical profile of relative humidity at Lindenberg from radiosounding (black dashed line), 10 m and 100 m masts (black line), ALADIN-AUSTRIA forecasts (green line), DMI-HIRLAM forecasts (blue line), NMM-PAFOG forecasts (cyan line) and LM-PAFOG forecasts (red line) on September 27th, 2005 at 00 UTC (a), at 03 UTC (b), at 06 UTC (c) and 09 UTC (d).
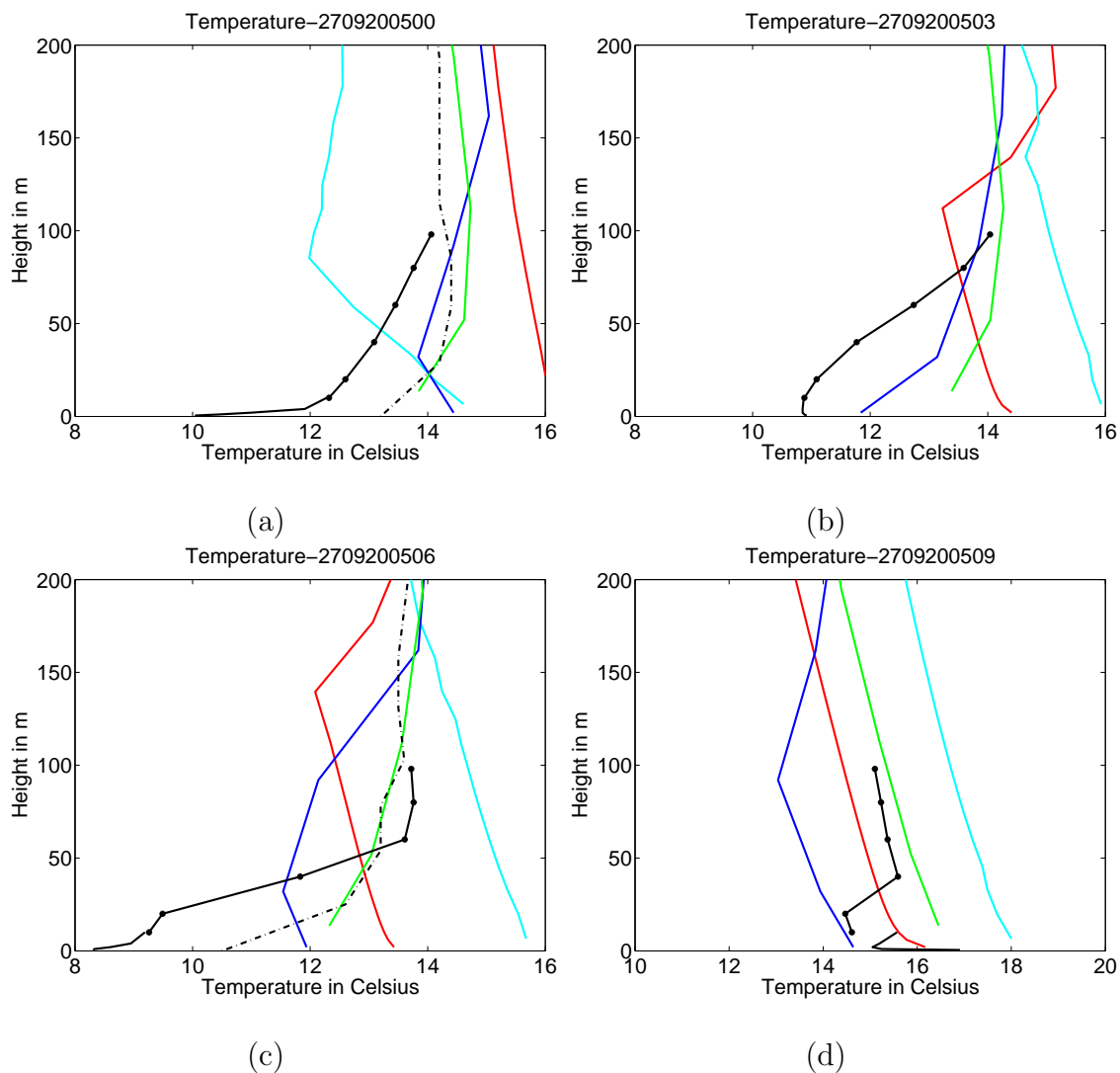
**Figure 5.19:** Vertical profile of temperature at Lindenberg from radiosounding (black dashed line), 10 m and 100 m masts (black line), ALADIN-AUSTRIA forecasts (green line), DMI-HIRLAM forecasts (blue line), NMM-PAFOG forecasts (cyan line) and LM-PAFOG forecasts (red line) on September 27th, 2005 at 00 UTC (a), at 03 UTC (b), at 06 UTC (c) and 09 UTC (d).

In order to understand the results of these three-dimensional fog forecast models, the comparisons at one point (Lindenberg observatory) have been completed with an analysis based on a larger area. In a comparison of the different model forecasts with 2m-visibility measurements close to Lindenberg, the role of the spatial distribution of fog in the quality of three-dimensional fog forecast can be evaluated (Figure 5.20). The particularity of the localised fog formation and the influence of the visibility parametrisation are highlighted.

The four models predict fog at Lindenberg (red marker) or close to the observatory, but each fog forecast delivers a different spatial distribution of fog in the Lindenberg area. The delay in the fog formation observed in the single point comparison of the visibility forecasts (Figure 5.15) may be linked to the spatial distribution inaccuracy of the model. ALADIN-AUSTRIA forms fog north and east of the Lindenberg observation site in spite of its accurate forecasts in temperature and humidity. DMI-HIRLAM forecasts cover the entire area. Such visibility forecasts ensure a detection of the fog event, but other locations without fog are affected by the large spatial extention. Regarding the NMM-PAFOG and LM-PAFOG results, the limitation caused by the initialisation process seems to be only a localised problem. West of the Lindenberg observatory the NMM-PAFOG forecast has a significant decrease of the visibility and its forecasted fog area covers almost the entire domain. The fog area forecasted by LM-PAFOG surrounds the observatory of Lindenberg.

In a comparison of the spatial distribution of liquid water content present in the lower-most atmosphere (Figure 5.21) with the corresponding 2m-visibility forecast, the results have been sorted in two categories. ALADIN-AUSTRIA and LM-PAFOG forecasts of liquid water content and visibility fields have an identical spatial distribution. A successful fog forecast is only possible if the saturation condition is reached at the surface. Due to the local variation of the thermodynamic parameter at the surface, this approach usually caused an underestimation of the forecasted fog area and is strongly dependant of the parametrisation accuracy. Regarding DMI-HIRLAM and NMM-PAFOG results, the spatial distribution of 2m liquid water content and 2m visibility have a significant dispersion. Both models compensate their spatial distribution inaccuracies with the visibility parametrisation. Such an approach generally caused an overestimation of the fog area's extent.

Finally, the visibility measurements around Lindenberg confirm the presence of fog in the northern and eastern part of the studied area (visibility < 1000 m). However, the comparison with the model output underlines the difficulty of the four models to forecast the fog at the right place. For this case study (Figure 5.20), each forecast has a satisfying spatial distribution of fog, but the forecasted visibility does not show the same spatial variation as in the measurements.
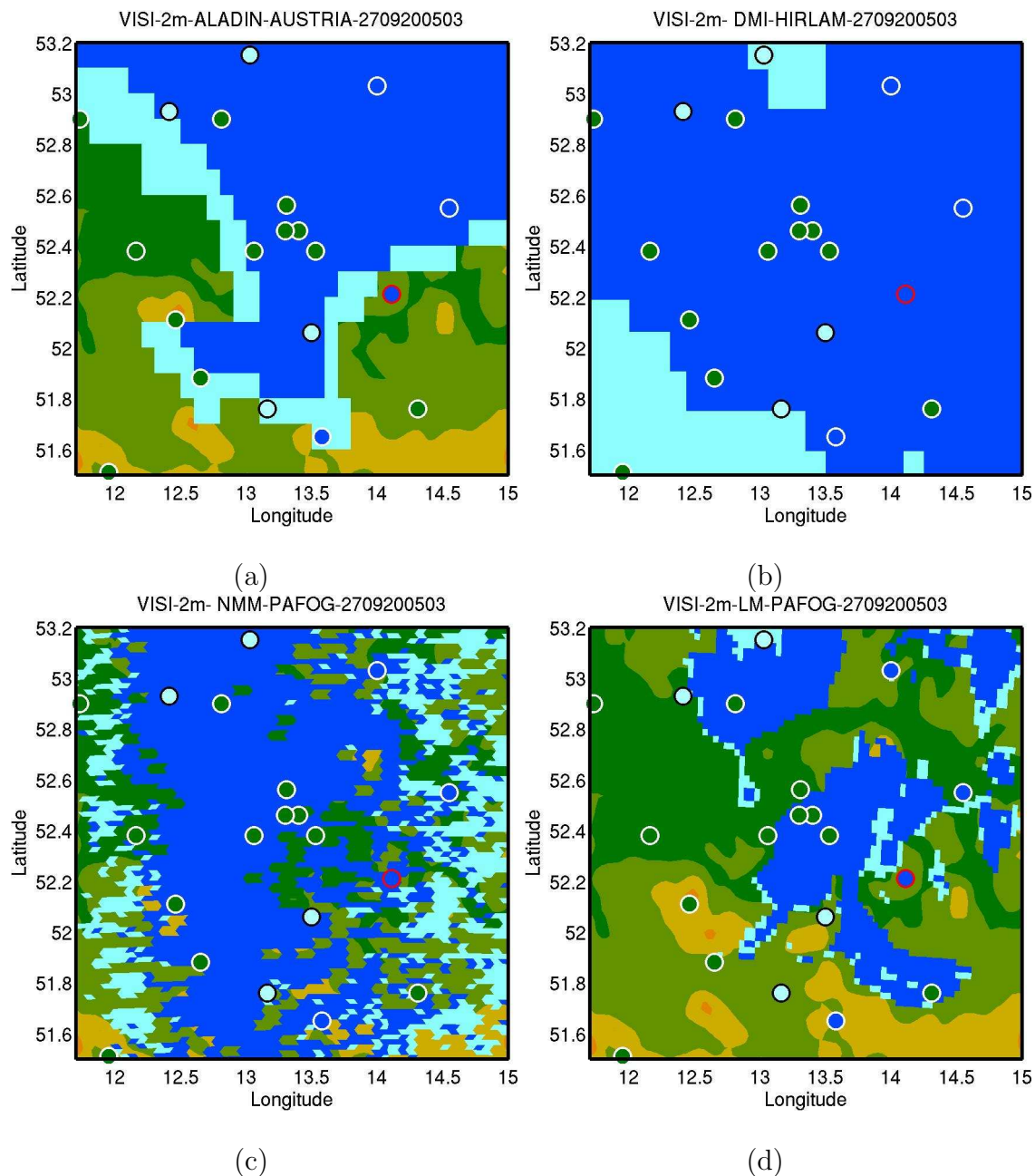
Figure 5.20: Spatial distribution of 2m visibility in the Lindenberg area on September 27th, 2005 at 03 UTC based on ALADIN-AUSTRIA forecasts (a), DMI-HIRLAM forecasts (b), NMM-PAFOG forecasts (c) and LM-PAFOG forecasts (d). The circle markers correspond to the position of the visibility measurements. The red circle corresponds to the Lindenberg observatory. The visibility values have been separated in three categories. **Deep blue** corresponds to a fog event with a visibility below 1000m. **Cyan** represents a fog event with a visibility between 1000 and 3000m. **Green** and brown areas denote areas without fog (visibility exceeding 3000m).
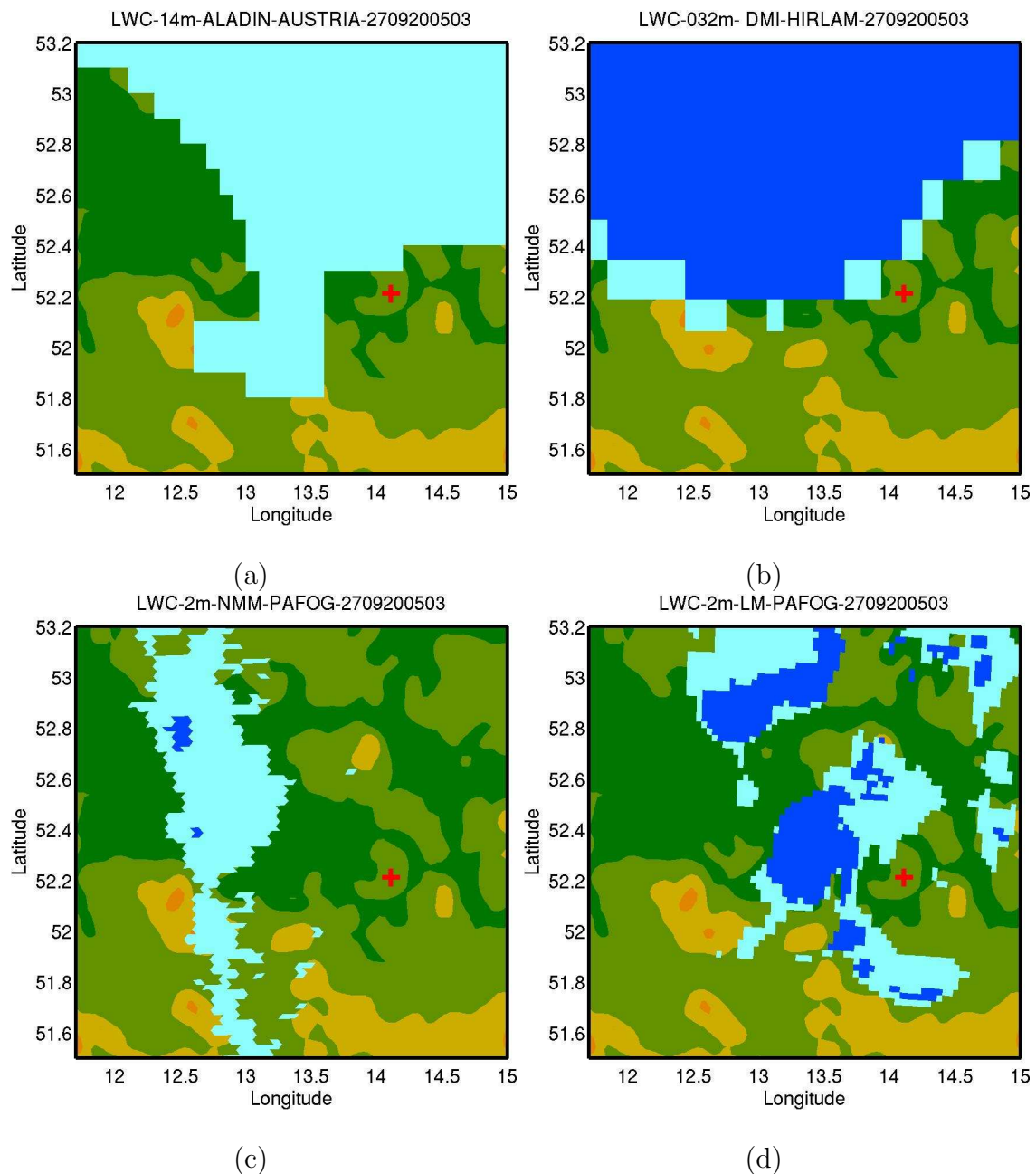
Figure 5.21: Spatial distribution of liquid water content for the lowest layer of the model in the Lindenberg area on September 27th, 2005 at 03 UTC based on ALADIN-AUSTRIA forecasts (a), DMI-HIRLAM forecasts (b), NMM-PAFOG forecasts (c) and LM-PAFOG forecasts (d). **Deep blue** corresponds to a fog event with a liquid water content up to 0.1 g/kg. **Cyan** represents a fog event with a liquid water content below 0.1 g/kg. Green and brown areas denote areas without fog. The red cross corresponds to the Lindenberg observatory.

5.5.3 Episode 3 - December 6-7th, 2005: fog event influenced by very low stratus

From the 6th of December sunset until the 8th December 2005, a stable and moist boundary layer present in the Lindenberg area supplies the necessary conditions for a formation of fog and low stratus during both days. Visibility observations lower than 200 m were reported. During this foggy period, the incoming radiative fluxes were strongly influenced by a large cloud cover.

The time evolution of the visibility forecasts at Lindenberg points out large differences between the models (Figure 5.22) and an obvious agreement with the observation cannot be recognised. NMM-PAFOG and DMI-HIRLAM forecast already in the first hours a sharp visibility decrease despite the lack of fog in the area. From the 21th forecast hour, which corresponds to the beginning of the fog period, each of the four models recognise the formation of fog at Lindenberg. The NMM-PAFOG visibility value decreases sharply to reach a value of 500 m. The forecasted values of ALADIN-AUSTRIA, DMI-HIRLAM and LM-PAFOG oscillate strongly. Between the 18th and 30th forecast hours and after the 36th hour, the lowest visibility values are prognosticated with values reaching 200 m for DMI-HIRLAM, 600 m for ALADIN-AUSTRIA and 900 m for LM-PAFOG. During day time, between the 30th and 40th forecast hours, these three model forecasts show a common dissipation of fog. Regarding the results of the previous case study, the variability of these different results may depend on the spatial distribution of fog as well as the chosen visibility parametrisation.
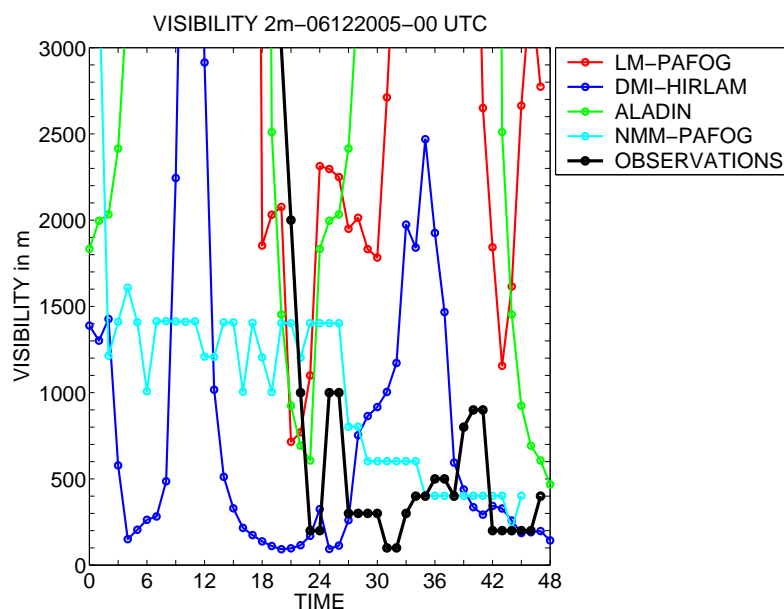
Figure 5.22: Time evolution of the visibility forecast at Lindenberg. Initialisation: December 6th, 2005 at 00 UTC.

Futher investigations concerning the energy balance at the surface as well as the evolution of dynamics and thermodynamics in the boundary layer are necessary to understand the variability between forecasts.

During the presence of a large cloud cover the potential variation of radiative fluxes has a decisive role in the localised formation of fog (Figure 5.23). Regarding the time evolution of short wave and long wave fluxes (Figures 5.23 a & b), a large discrepancy between the model forecasts and the observations is apparent. Both research models, NMM-PAFOG and LM-PAFOG, agree well with the measurements. Regarding the forecats of ALADIN-AUSTRIA, an underestimation of the cloud cover in the last 24 forecast hours involves a bias of 100 Wm^{-2} in the time evolutions of short wave and long wave fluxes. DMI-HIRLAM results underline the presence of a constant cloud cover over the Lindenberg area. This early formation of clouds can be identified in the radiative fluxes. In the first 24 forecast hours, a bias value of 100 Wm^{-2} can be measured. As soon as the observed and forecasted cloud cover agree, the bias value converges to 0 Wm^{-2}.

During the entire two forecasted days, a stable and moist boundary layer is responsible for this long fog period. Contrary to both previous case studies, two distinct turbulent regimes between mixed boundary layer during the day and a stable atmosphere in nocturnal time do not occur. Regarding the time evolution of latent heat and sensible heat fluxes at the surface (Figures 5.23 c & d), the behaviour of each model forecast agree well with the observation. In this case, LM-PAFOG and NMM-PAFOG are not disadvantaged by the time evolution of their radiative balance at the surface. Nevertheless, the latent heat fluxes forecasted by NMM-PAFOG differ more and more from the observation in the last forecast hours. This tendency points out one more time a continuous drying of the lowermost atmosphere in NMM-PAFOG forecast domain.

The influence of the radiative fluxes can be observed in the time evolution of temperature and relative humidity at the surface (Figure 5.24 a, b & c). Moreover, the weak mixing of the boundary layer can be cross-checked with the time evolution of the 10m-wind (Figure 5.24-d). In spite of an accurate initialisation in temperature, humidity and wind speed at 00 UTC, NMM-PAFOG forecasts disagree progressively with the measurements. The 2m-temperature forecasts have a bias reaching $4°C$ in the last forecast hours. Its 2m-relative values drop abruptly after one forecast hour, the drying of the lowermost atmosphere is responsible for a growing bias value, which can reach -20 %. Regarding the other models, ALADIN-AUSTRIA, DMI-HIRLAM and LM-PAFOG, the influence of the cloud cover induce small bias in the time evolutions of temperature. Relative humidity and wind speed agree well with the observations.

The vertical profiles of temperature and relative humidity are presented in Figures 5.25 & 5.26. In Figure 5.26, the radiosonding as well as the mast profile measurements show a small displacement of the temperature inversion in the altitude (around 150 m). The fog becomes a very low stratus and the proximity of the cloud near the surface causes high humidity value in the low atmosphere.

(a)

(b)

(c)

(d)
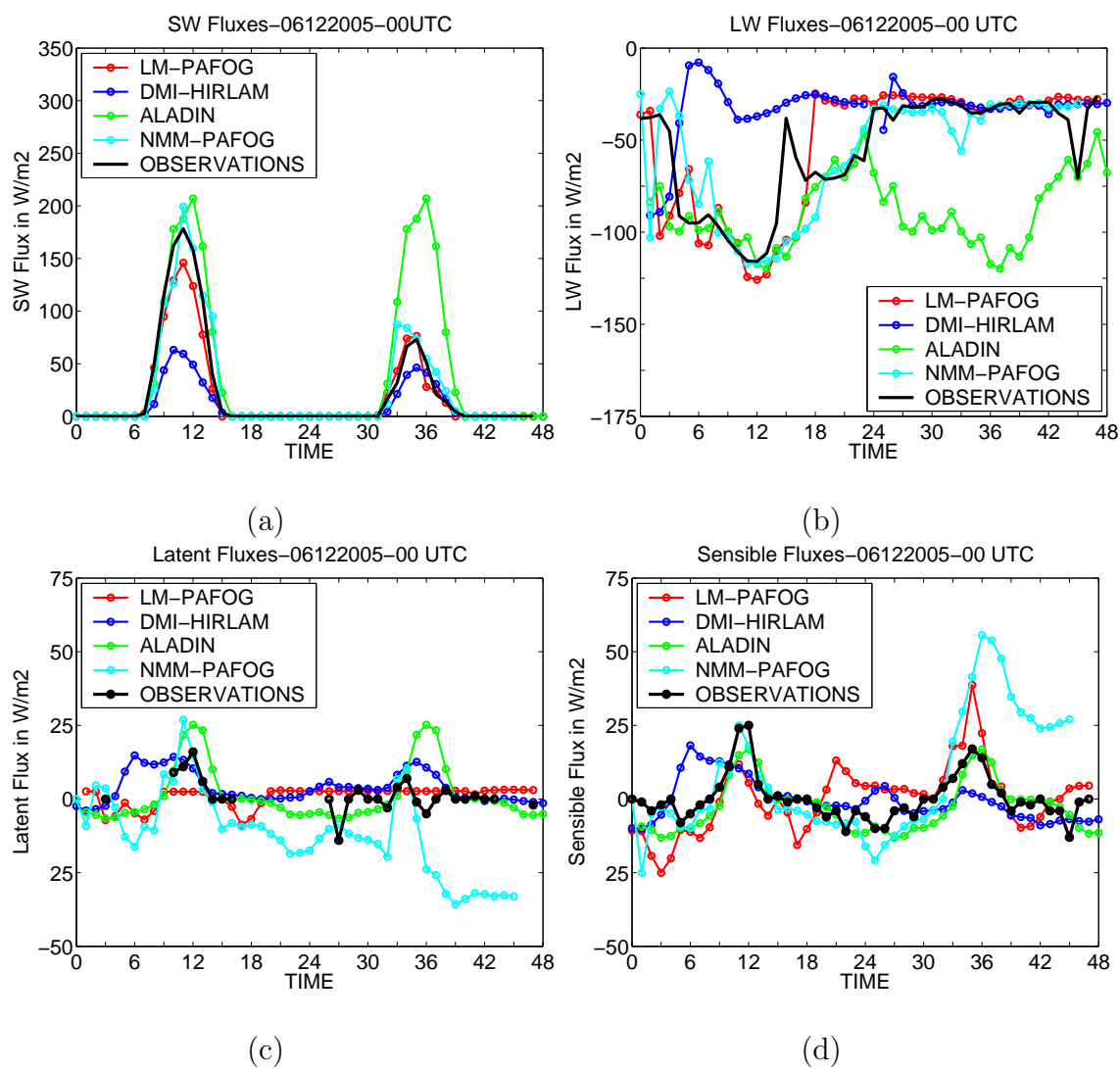
Figure 5.23: Time evolution of short wave fluxes (a), long wave fluxes (b), latent heat fluxes (c) and sensible heat fluxes (d), forecasted by ALADIN-AUSTRIA, DMI-HIRLAM, NMM-PAFOG and LM-PAFOG. Initialisation: December 6th, 2005 at 00 UTC.
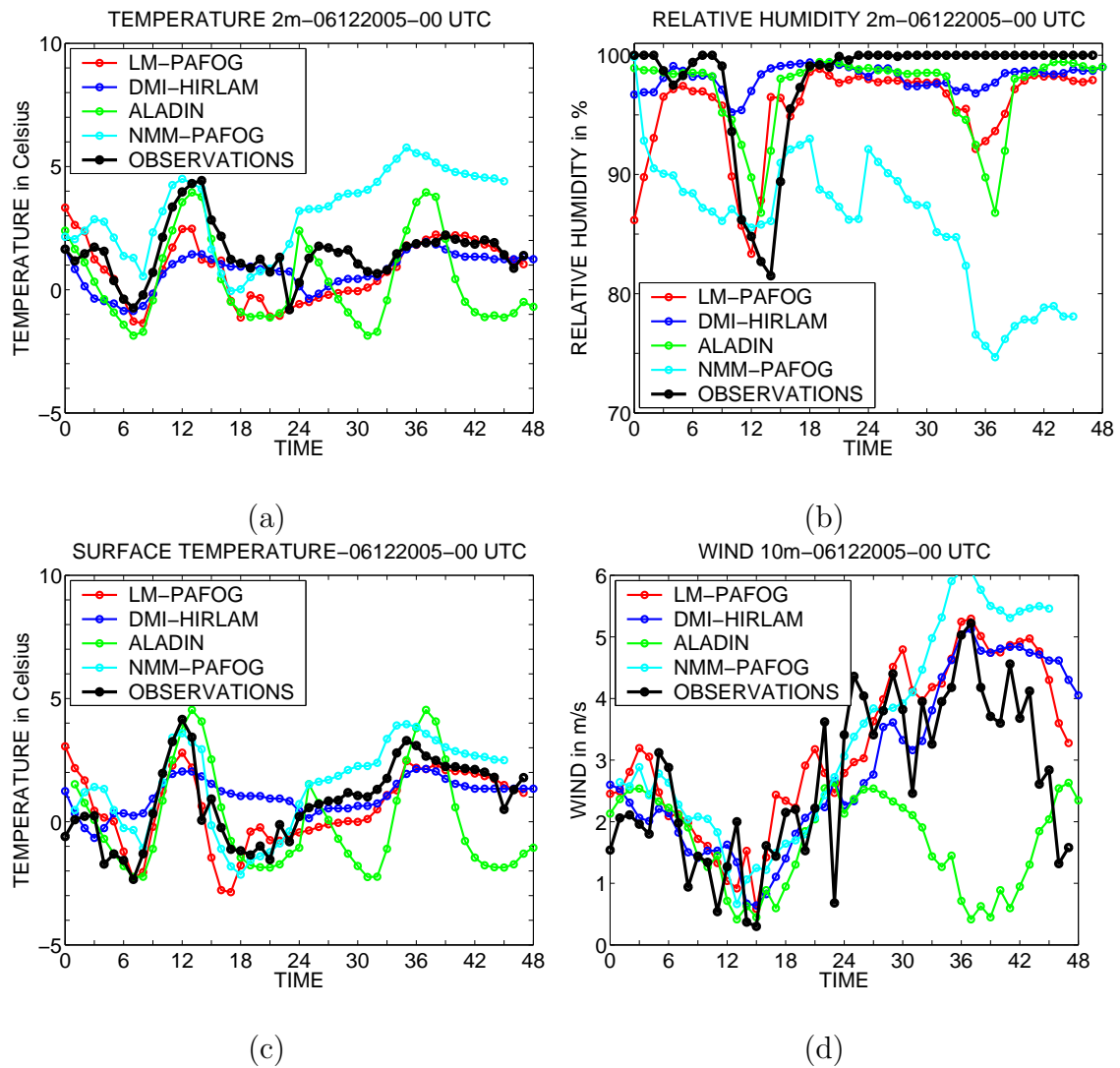
Figure 5.24: Time evolution of 2m temperature (a), 2m relative humidity (b), surface temperature (c) and 10m wind speed (d), forecasted by ALADIN-AUSTRIA, DMI-HIRLAM, NMM-PAFOG and LM-PAFOG. Initialisation: December 6th, 2005 at 00 UTC.

DMI-HIRLAM and LM-PAFOG have temperature and relative humidity profiles which coincide well with the mast measurements. The temperature inversion is very well captured by both models. However, the saturation is reached in the low atmosphere (around 50 m) and relative humidity at the surface stays below 100% (around 98 %).

ALADIN-AUSTRIA is confronted to its low cloudiness problems (*Seidl and Kann*, 2002). Through the assimilation process, inversions are filtered and thus the formation of stratus cannot occur. The relative humidity profiles of ALADIN-AUSTRIA have values around 95% and the temperature profile shows an inversion. However, the model is not able to reach the saturation and the cloud cover remains at very low values. The SK-scheme (*Seidl* et al., 2007), normally able to solve this problem, is unsuccessful for this case study at Lindenberg. The large difference of the radiative balance at the surface can not be adjusted (Figure 5.23-b).

The large different between the NMM-PAFOG forecasts and the observations can be clearly identified regarding the vertical profiles. The temperature bias oscillates between $2°$ to $4°C$ and the relative humidity has a bias up to 30 %. In spite of these large differences, an inversion of temperature is present in the vertical profile (Figure 5.26) and the visibility values are close to the Lindenberg measurements (Figure 5.22).

Despite a similar difficulty to reach the saturation at the ground, the comparison of 2m-visibility forecasts with SYNOP measurements in the Lindenberg delivers very different results (Figure 5.27). The horizontal cross section of the forecasted liquid water in the lowermost atmosphere (Figure 5.28) and for an altitude of 200 m (Figure 5.29) is also supplied in order to separate the influence of the visibility parametrisation from the influence of the condensation parametrisation.

ALADIN-AUSTRIA forecasts fog in the north of the Lindenberg area (Figure 5.29-a). This fog distribution agrees with the 2m-visibility measurements, but it is still underestimated. The analysis of the liquid water fields for the altitude of 14 m and 200 m shows that the cloud cover is distributed around the Lindenberg observatory (Figure 5.28-a & 5.29-a). A direct relation between the liquid water content and the 2m-visibility is again pointed out.

DMI-HIRLAM forecasts very well reproduce the spatial distribution of fog as well as the intensity of this episode (Figure 5.27-b). Moreover, its two-dimensional fields of liquid water content (Figure 5.28-b and 5.29-b) agree with the forecasted 2 m visibility field. In this situation, the visibility parametrisation has clearly identified the fog extension.

Regarding the LM-PAFOG forecasts, the analyses of liquid water content at 2 m as well as its spatial distribution of 2m visibility confirm the difficulties of LM-PAFOG to maintain saturation at the surface (Figure 5.27-d & 5.28-d). LM-PAFOG cannot form fog at the ground due to the drying of the lowest part of the atmosphere. In this case, the visibility parametrisation of LM-PAFOG shows its limits. The visibility does not decrease in the case of very high relative humidity values without saturation.

Despite very low relative humidity values, the spatial extension of fog forecasted by NMM-PAFOG covers the entire area (Figure 5.27-c). This large overestimation of fog extension can be explained by the visibility parametrisation. Regarding the 2m-liquid water content extension, no correspondence between visibility and cloud water can be found (Figure 5.28-c).
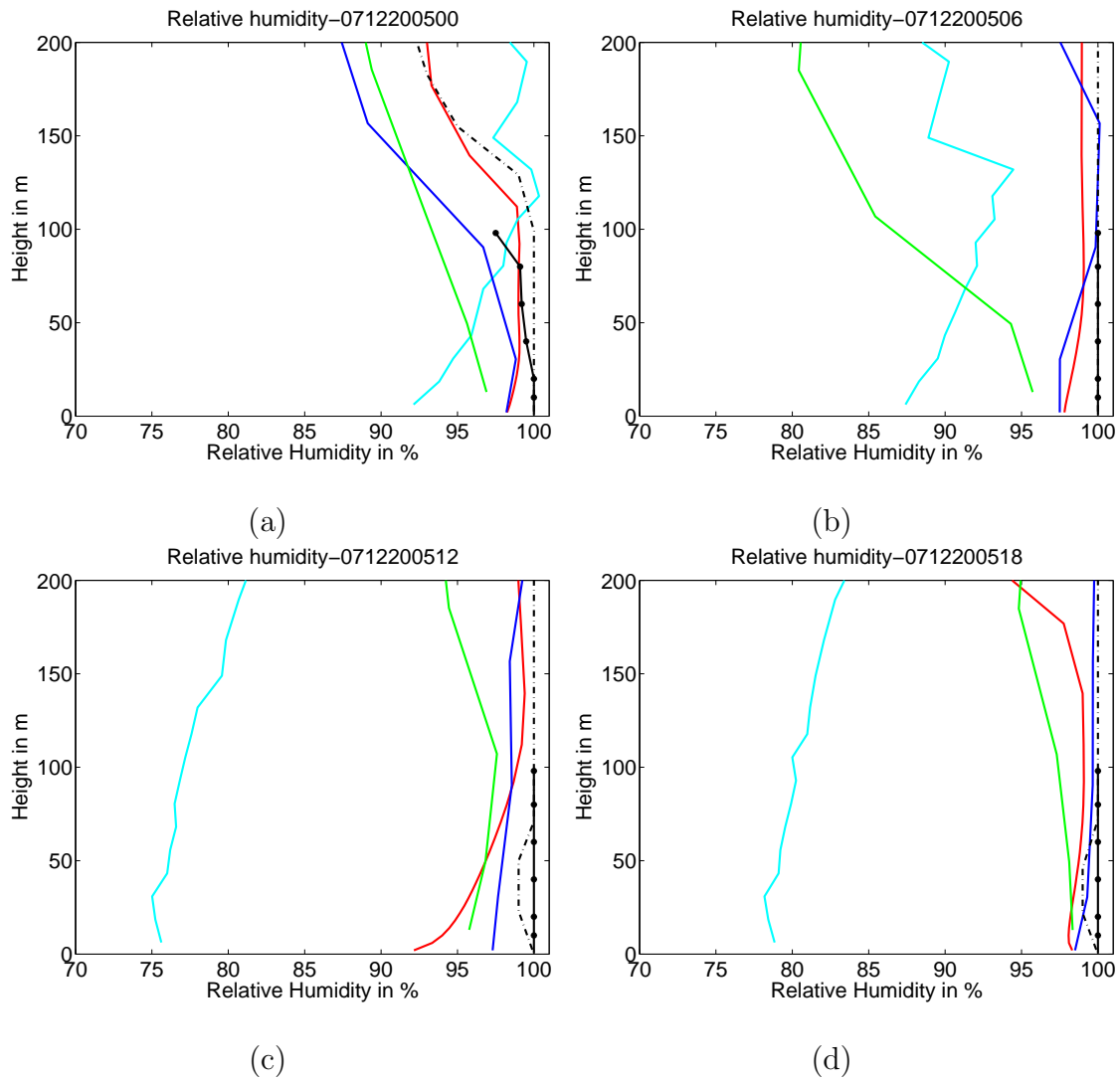
Figure 5.25: Vertical profile of relative humidity at Lindenberg from radiosounding (black dashed line), 10 m and 100 m masts (black line), ALADIN-AUSTRIA forecasts (green line), DMI-HIRLAM forecasts (blue line), NMM-PAFOG forecasts (cyan line) and LM-PAFOG forecasts (red line) on December 7th, 2005 at 00 UTC (a), at 06 UTC (b), at 12 UTC (c) and 18UTC (d).
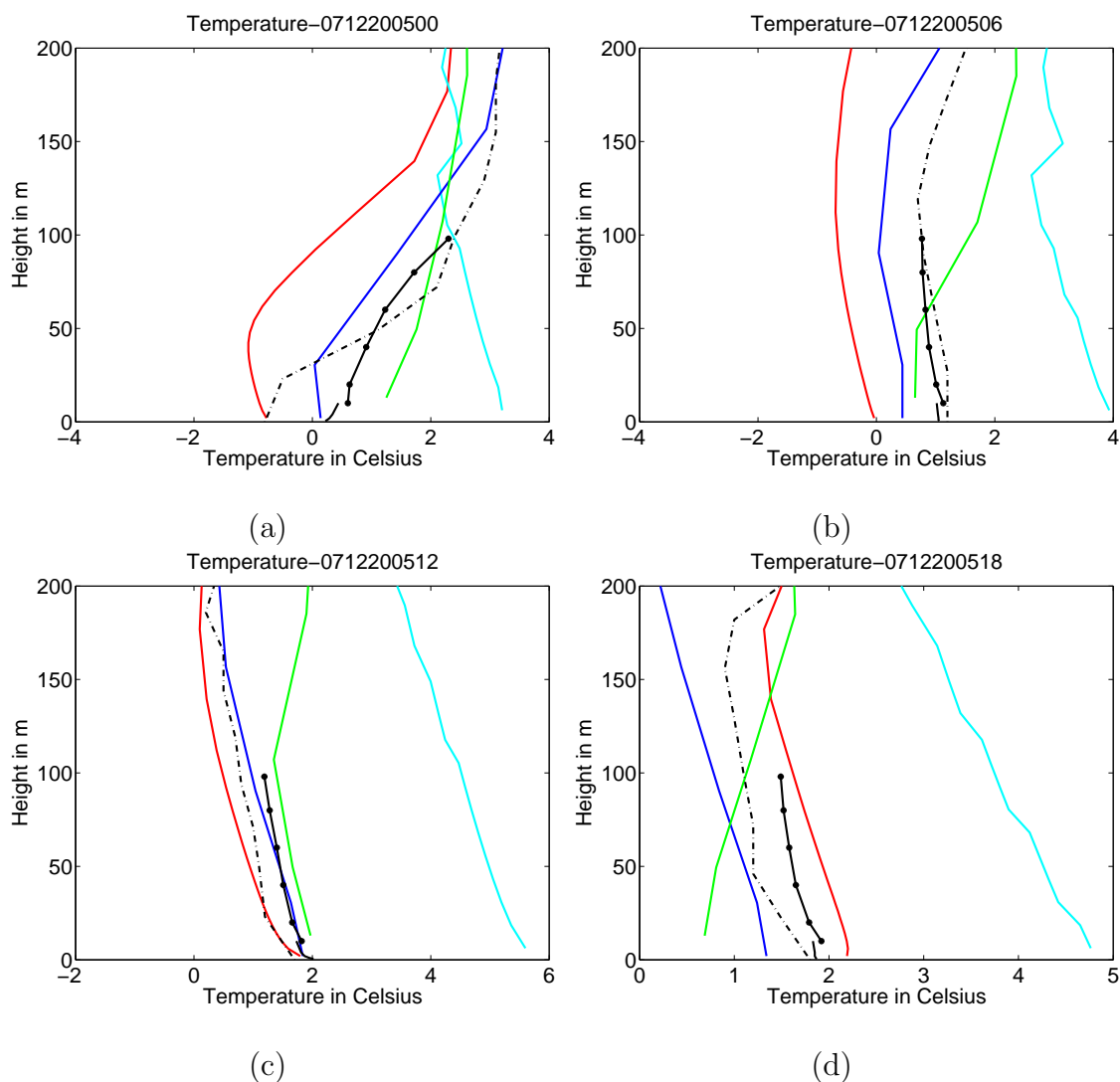
Figure 5.26: Vertical profile of temperature at Lindenberg from radiosounding (black dashed line), 10 m and 100 m masts (black line), ALADIN-AUSTRIA forecasts (green line), DMI-HIRLAM forecasts (blue line), NMM-PAFOG forecasts (cyan line) and LM-PAFOG forecasts (red line) on December 7th, 2005 at 00 UTC (a), at 06 UTC (b), at 12 UTC (c) and 18 UTC (d).

The four models show the presence of fog or very low stratus. DMI-HIRLAM has a very good accordance with the measurement in the one pixel study as well as in the spatial distribution study. NMM-PAFOG gives a good forecast of fog in spite of strong differences in temperature and relative humidity profiles. ALADIN-AUSTRIA is confronted to its weakness of cloud cover forecast in the Lindenberg: in spite of the good agreement of temperature, relative humidity and wind profiles, it is not able to induce a formation of fog. However, the spatial distribution of fog has a lower extension but a good correspondence with the 2m visibility measurements. LM-PAFOG forecasts are very similar to the Lindenberg measurements, but the humidity transport at the soil/atmosphere involves the formation of very low cloud on the domain but no fog.
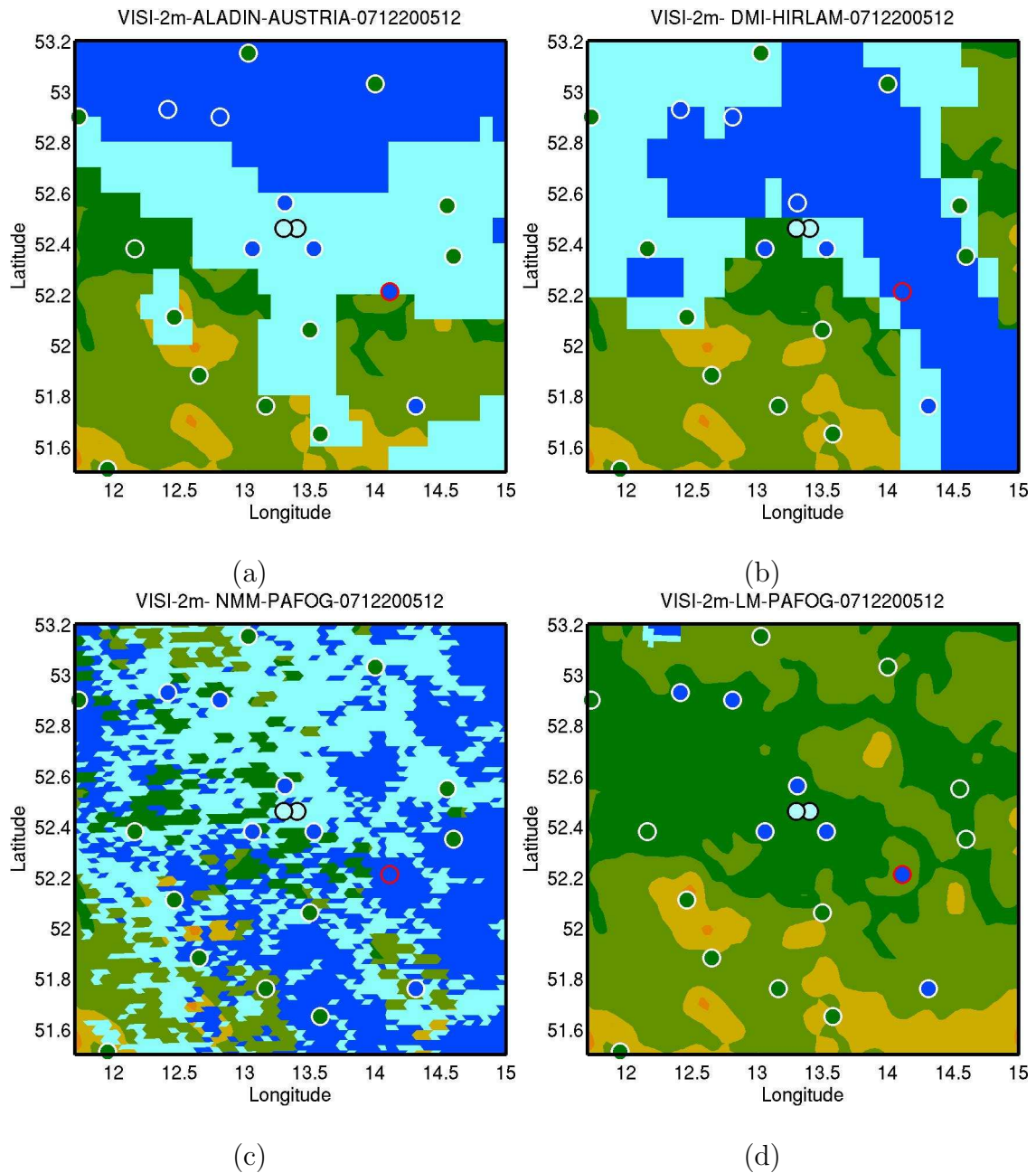
Figure 5.27: Spatial distribution of 2m visibility in the Lindenberg area on December 7th, 2005 at 12 UTC based on ALADIN-AUSTRIA forecasts (a), DMI-HIRLAM forecasts (b), NMM-PAFOG forecasts (c) and LM-PAFOG forecasts (d). The circle markers correspond to the position of the visibility measurements. The red circle corresponds to the Lindenberg observatory. The visibility values have been separated in three categories. **Deep blue** corresponds to a fog event with a visibility below 1000 m. **Cyan** represents a fog event with a visibility between 1000 and 3000 m. **Green** and brown areas denote areas without fog (visibility exceeding 3000m).
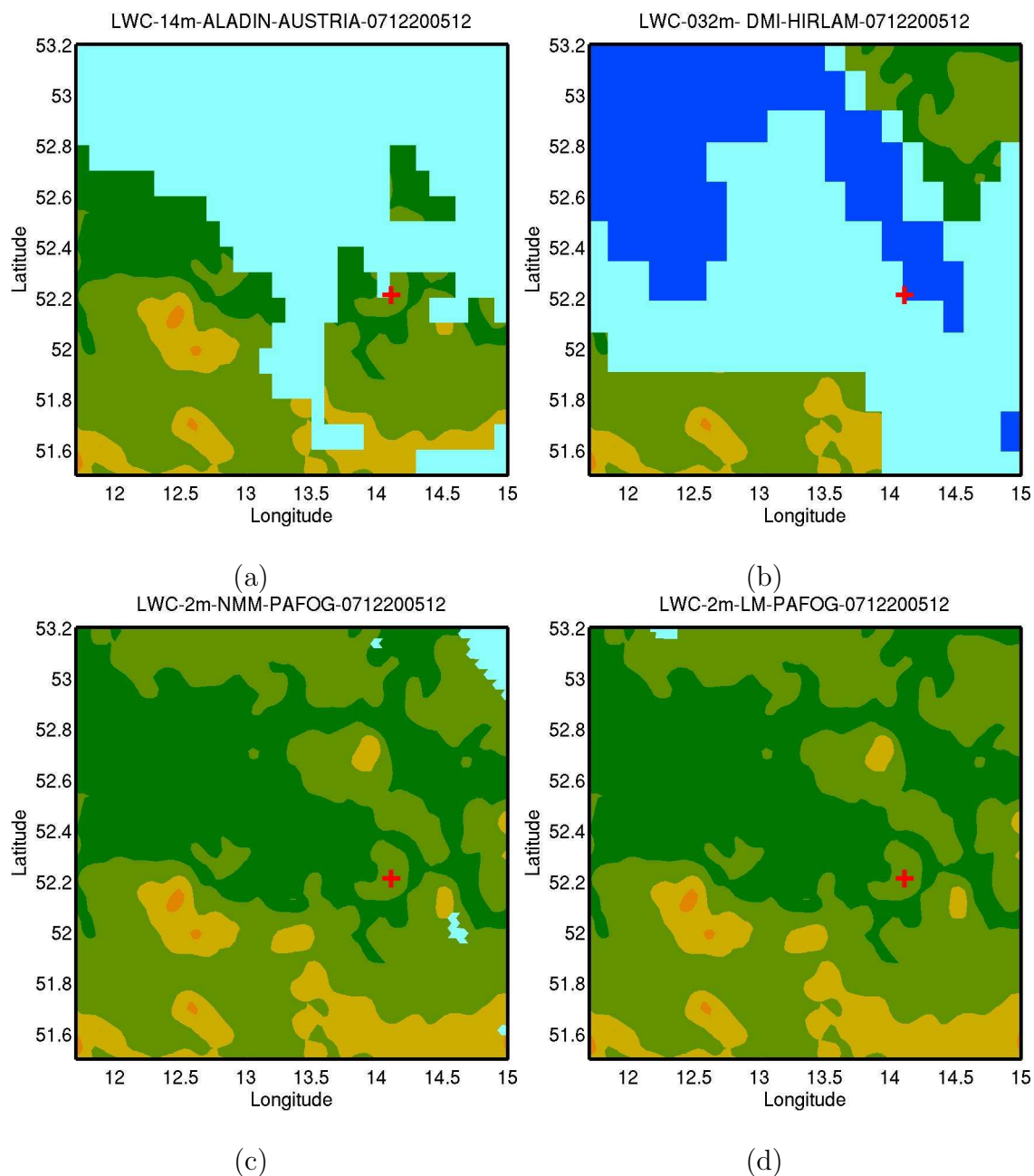
Figure 5.28: Spatial distribution of liquid water content for the lowest layer of the model in the Lindenberg area on December 7th, 2005 at 12 UTC based on ALADIN-AUSTRIA forecasts (a), DMI-HIRLAM forecasts (b), NMM-PAFOG forecasts (c) and LM-PAFOG (d). **Deep blue** corresponds to a fog event with a liquid water content up to 0.1 g/kg. **Cyan** represents a fog event with a liquid water content below 0.1 g/kg. Green and brown areas denote areas without fog. The red cross corresponds to the Lindenberg observatory.

(a)

(b)

(c)

(d)
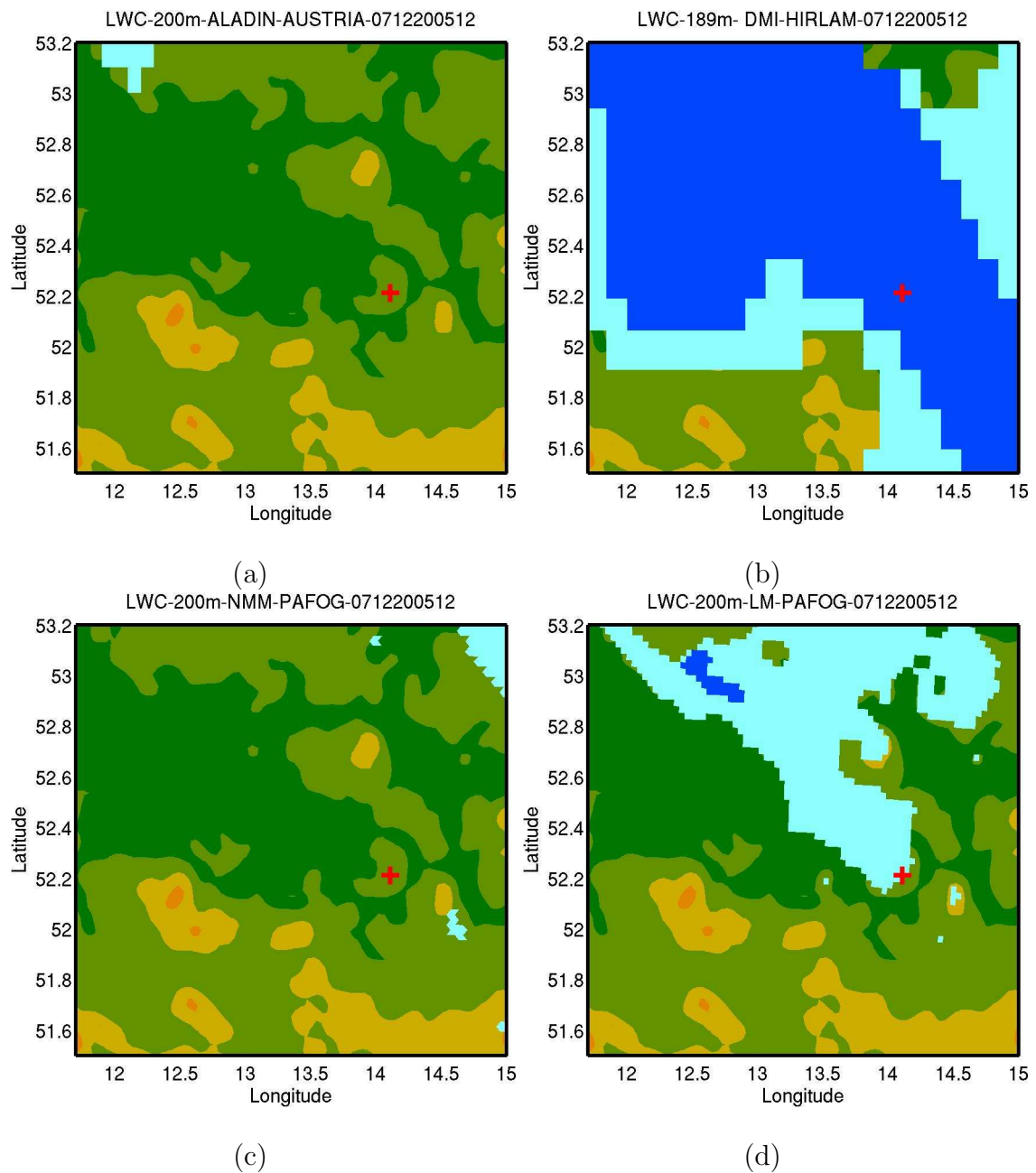
Figure 5.29: spatial distribution of liquid water content for an altitude around 200m in the Lindenberg area on December 7th, 2005 at 12 UTC based on ALADIN-AUSTRIA forecasts (a), DMI-HIRLAM forecasts (b), NMM-PAFOG forecasts (c) and LM-PAFOG forecasts (d). **Deep blue** corresponds to a fog event with a liquid water content up to 0.1 g/kg. **Cyan** represents a fog event with a liquid water content below 0.1 g/kg. Green and brown areas denote areas without fog. The red cross corresponds to the Lindenberg observatory.

5.6   Conclusions

The COST 722 model intercomparison gives a large overview of the actual European fog forecast possibilities. In the first phase, four different models have been compared with visibility measurements from the Lindenberg observatory in a statistical framework for a 4 months period (September-December 2005). From this part of the study, two different behaviours can be identified: ALADIN-AUSTRIA and DMI-HIRLAM have very good discrimination scores, but a tendency to "overforecast". MOS-ARPEGE and LM-PAFOG detect less fog events but have a significant lower tendency to produce false alarms. The statistical study was not able to identify a "best model". But, from the four available models, ensemble forecasts have been set up. The ensemble highlights the qualities of each involved model and avoids strong forecast errors. However, the statistical study points out the lack of reliability for each of the four involved models. In spite of a good capacity to discriminate fog events, only 30 % of fog forecasts are in the right time and in the right place.

Considering the difficulties to produce a good fog forecast the intercomparison focused in a second part on three case studies in order to determine the assets and shortcomings of the different parametrisations used by the involved models. These comparisons have shown the parametrisation weakness at the soil/atmosphere interface. The models with a coarse vertical resolution have a lack of information for the 2 m values. Their forecasts at the surface are corrected by an empirical parametrisation of the visibility. The models with a fine vertical resolution are able to define the lowest atmosphere with a good precision, nevertheless the determination of turbulence transports and surface fluxes stays complex. A single reason of errors in fog forecasting can not be identified. Detailed parametrisation of the microphysics involved of fog formation and dissipation as well as high-resolution non-hydrostatic models may help to simulate the processes more realistically. However, these models are still under development. Accurate data assimilation and initialisation schemes adapted to small-scale features have to be improved. Still existing operational models have considerable errors on larger scales. But the experience of their data assimilation scheme can limit these errors and thus still favour large scale models with simple parametrisation compared to the new three-dimensional fog forecast systems.

The results presented in this study are based on a single point comparison. In order to quantify the influence of each parameter, the study should be extended to a comparison based on the spatial distribution of fog.

Chapter 6

Satellite products for fog and three-dimensional fog forecasts

The quality of three-dimensional fog forecasts is rather difficult to assess with the currently available station measurements. The network of 2m visibility measurements reduces the fog spatial distribution verification to only a few points. In our studied area (280 km x 280 km) around the Lindenberg Observatory only 35 stations are available. A better resolution of the fog spatial distribution is needed. Therefore, a verification method has been developed based on a comparison with satellite products for fog and very low stratus.

6.1 Description of the satellite products

In order to assess the spatial accuracy of the fog forecast obtained in three-dimensional modelling, a comparison with satellite data was performed. The satellite products used here are derived from Meteosat 8 SEVIRI (Spinning-Enhanced Visible and InfraRed Imager) data (*Cermak*, 2006; *Cermak* et al., 2006; *Cermak and Bendix*, 2008). To ensure a clean delineation and the exclusion of all unwanted surfaces, the satellite product development is based on a series of tests. Each of these tests explicitly or implicitly addresses a property assumed for fog:

- Fog is a *cloud*

- in a *water* phase

- composed of *small droplets*

- *low* above the ground and

- with a *stratiform surface.*

These properties are tested with individual spectral and spatial tests, with procedures differing according to the time of the day. In addition and as a constant assessment independent of the time of day, a confidence level is computed based on channels at infrared wavelengths only. It is implemented as a blackbody temperature difference between the 12.0 μm and the 8.7 μm channels. This temperature difference $\Delta T = T_{12.0} - T_{8.7}$ is

compared to a threshold B found in radiative transfer calculations to derive a water cloud confidence level P_c:

$$P_c(a) = \frac{B - \Delta T(a) - CCR}{-2CCR} \tag{6.1}$$

with $P_c(a)$ the confidence level at pixel a, $0 \leq P_c \leq 1$, t the threshold value and CCR the cloud confidence range.

The cloud confidence range is the range between the threshold and a certain clear or a certain cloudy pixel. All values in the center of the clear peak are to be assigned a confidence level of 0, those in the center of the cloudy peak of 1. To accommodate the average gap between the two peaks, CCR is set to 2 K. A value $\Delta T(a) = t$ is thus assigned a P_c of 0.5.

With this first test, the selected clouds are considered only as low clouds. However, the main challenge of the fog detection with satellite data is the determination of cloud geometrical properties: top and base of the stratiform cloud. For each low cloud entity, the stratiform cloud structure is identified with the standard deviation of the black body temperature in the thermal infrared channel at 10.8 μm. Where it falls below a certain threshold (2K), the entity is identified as a stratus patch. If a temperature lapse rate of 0.7K/100m is assumed, a threshold of 2 K roughly corresponds to a height difference of 290 m.

Finally, the group of very low clouds is subdivided into areas with and without ground contact. Firstly, the cloud top is determined by the coupling of the 10.8 μm blackbody temperature with the altitude supplied by a Digital Elevation Model (DEM). The 10.8 μm blackbody temperature of every fringe pixel of a given entity is compared to that of any and all bordering clear pixels. Using the blackbody temperature difference, the ground elevation for both the cloudy and the clear pixel and an assumed atmospheric temperature lapse rate (Γ =0.7K/100 m), the cloud top altitude, $z_t(c,r)$ for each pixel is defined as follows:

$$z_t(c,r) = z_s(c,r) + \frac{T_t(c,r) - T_s(c,r)}{\Gamma} \tag{6.2}$$

with $T_t(c,r)$ the temperature of the cloud top, $T_s(c,r)$ the surface temperature and Γ the environmental temperature lapse rate.

Satellites observe clouds from above. Liquid water path and the cloud top height are known for a given pixel. The information concerning the cloud base can only be deduced by making assumptions concerning the liquid water cloud structure. The satellite products for fog and very low stratus described here used a new method to parametrise a liquid water path in the cloud. The modeled cloud is considered as consisting of three layers with different water mixing β:

- On the assumption that moisture feeds into the cloud from below, β is smaller in the lower part of the cloud and gradually increases towards the central region.

- In the central region of the cloud (between base and top layers) β is constant. Moreover, β is scaled depending on the top height.

- Near the cloud top, dry air entrainment quickly reduces ρ_c to zero. Thus, where the uppermost 50 m are reached, liquid water linearly drops to 0 up to the cloud top.

For each cloud layer, the adiabatic liquid water content is computed from an assumed cloud base to the known cloud top and then modified according to β assumed for the layer:

$$\rho_c(z) = (1 - \beta)\rho_a m_l(z) \tag{6.3}$$

with ρ_a the density of air and $m_l(z)$ liquid water mixing ratio at height z.

Using this new method, the cloud water distribution is simulated for clouds with the known cloud top height and assumed cloud base height. This procedure is repeated iteratively until the liquid water path of the modelled cloud agrees with the liquid water path retrieved from the satellite imagery. The corresponding cloud base height is accepted as the valid assumption for the given pixel.

The satellite products presented above are useful to determine the quality of the fog spatial distribution. The satellite data are obtained from Meteosat Second Generation (MSG) with a frequency of 15 minutes and a spatial resolution of about 3 km in Germany. However, in the prototype cloud classification developed by *Cermak and Bendix* (2008), the determination of the cloud base is severely influenced by the assumption of the liquid water distribution in the cloud, and due to the satellite position, the detection of low clouds is strongly limited in the presence of a multilayer cloud structure. In spite of these restriction, the satellite products supply large low stratus surfaces and not only sparse information of a few pixels. In the next section a comparison between these products and the 2m liquid water forecasted by LM-PAFOG for a few selected cases will be used to highlight the potential of this verification method.

6.2   Comparisons

The comparison between the satellite products and the fog forecasted by the LM-PAFOG is interesting because a quick estimate of area coincidence is possible. The satellite products are projected on the model grid. By this mapping process, both fog masks can be compared by visual inspection as well as by quantitative inspection based on a confidence table.

For this first analysis, we restrict ourselves to the three fog events previously discussed (section 4.4). These three fog events have different cloud cover time evolutions, which is particularly interesting for studying the possibilities and the qualities of this verification method:

- September 26th-27th, 2005: After a rainy spell the days before, cloud cover on the studied area oscillates from 0/8 to 4/8, due to the development of a high pressure domain over Europe.

- October 6th-7th, 2005: During the whole period, the cloud cover is only modified by the formation of radiative fog events in the Lindenberg area.

(a) 2005 September 26-27th-1000m

(b) 2005 September 26-27th-3000m

(c) 2005 October 6-7th-1000m

(d) 2005 October 6-7th-3000m

(e) 2005 December 6-7th-1000m

(f) 2005 December 6-7th-3000m
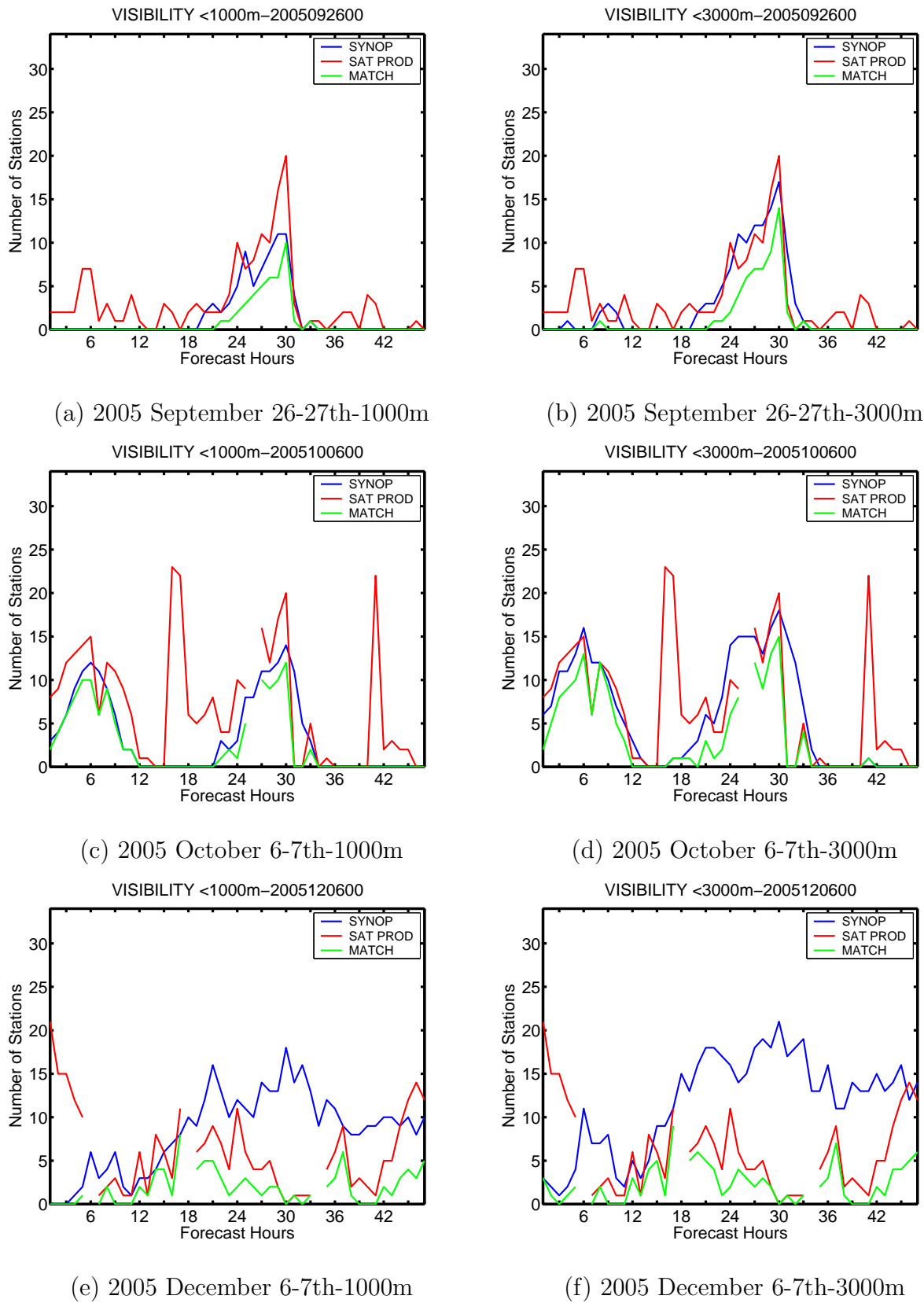
Figure 6.1: Time evolution of fog spatial distribution extracted from the Meteosat 8 satellite products and the 2m-visibility SYNOP measurements for a visibility threshold of 1000m and 3000m on the Lindenberg area at 2005 September, 26-27th (fig. a and b), at 2005 October, 6-7th (fig. c and d)and at 2005 December, 6-7th (fig. e and f).

- December 6-7th, 2005: In this case, cloud cover is fixed at 8/8 due to the presence of a large stratus. A dense fog event took place below.

6.2.1 Satellite products quality

Before comparing the satellite products with the model outputs, we analysed the reliability of the satellite data. The quality of fog/very low stratus products was already examined and validated in *Cermak* (2006) using ceiling measurements for all of Europe. However, in our study, ground clouds and very low stratus have to be clearly differentiated. We have assumed the satellite spatial distribution as an equivalent ground fog distribution. The supplied spatial repartition has been compared with 2m visibility measurements present in the Lindenberg area. The quality of the satellite products as a verification tool for fog spatial distribution can be simply deduced. However, we also have to consider that these comparisons are not exact: the satellite products can only identify liquid water distribution and do not give any information about the liquid water content. And, the decrease in visibility, parameter to identify fog presence, can be influenced by different parameters: one of them is the presence of cloud droplets. In spite of these restrictions the results were processed in contingency tables in terms of visibility events: for each hour a "yes" event is obtained when the forecasted visibility reaches or is lower than a given threshold. It was computed for two visibility thresholds: 1000 m and 3000 m. Only the pixel of the satellite products corresponding to the position of the 2m-visibility stations can be used in this comparison. And it was assumed that the fog derived from the satellite products always fulfills the condition of a visibility event.

Figures 6.1 summarise the satellite product quality. The limitations of the products as spatial fog distribution can be identify in Figures 6.1 (e) and (f). For the 6th-7th December case, the fog detection is penalised by the presence of low stratus multi-layers. Due to the lack of information in the lower atmosphere, the interferences between the different low cloud classes induce low hit quantity. A decoupling between the 2m-visibility measurements (SYNOP) and satellite spatial distribution is clearly identified in this case.

Considering the different assumptions in the satellite products induced by the satellite modus detection, a forecast verification method can be envisaged. The two other comparison cases reproduce very well the spatial and time evolution of the fog events (Figures 6.1 (a)-(d)). For the 26th-27th September case, the satellite observations have a tendency to overestimate the fog surface. During the "no fog" period, the satellite detects continuously a small residual cloud cover. Otherwise, the fog period is clearly identified as the 2m observations and satellite spatial distribution coincide very well. We note that the satellite products are not exactly calibrated for the visibility: the satellite distribution shows a better accordance for the visibility threshold of 3000 m than for the 1000 m threshold. However, in further comparisons with three-dimensional fog forecast model, the products should be compared with the liquid water distribution of the forecast model. The imprecision in visibility is not a potential error source for the verification method.

For the 6-7th October case (Figures 6.1 (c) and (d)), the satellite data also recognise the fog distribution. The identified fog surface is also in this case weak overestimated.

This could be caused by the choice of the visibility threshold or a bad estimation of the cloud base. In spite of the good quality of the products for weak cloud cover, some artefacts (forecast hours: 00UTC + 16 and 00UTC + 42) in satellite observations underline the reliability fluctuations of the data. The presence of such artefacts shows the difficulty to define the cloud base. A comparison with these satellite products have to be conducted very carefully.

To summarise this study, the satellite products for fog and very low stratus can not be used in a systematic verification process for the spatial distribution of fog. The limitation of satellite observations, induced by the downward looking position of the satellite instrumentation, reduces strongly the use of these products. The satellite data can be used as verification tool in case of fog events with very weak cloud cover. In this framework, the spatial structure of fog can be clearly identified and analysed on the whole forecast area.

6.2.2   Results of the verification method

In order to improve the LM-PAFOG forecasts, the September and the October cases have been exhaustively investigated in a comparison between the satellite products and the spatial distribution of 2m-liquid water content, forecasted by LM-PAFOG. The forecasted liquid water surface considered as fog corresponds to the domain defined by the pixels with a liquid water content higher than 0.01 g/kg in the lowest level (2 m). An outlook of the fog events can be done by mapping of the fog surfaces on correctly geo-referenced coordinates. The results of both cases are presented in Figures 6.3 and 6.2. Black shaded areas indicate fog occurrence as detected by the satellite and colour shadding shows the modeled liquid water content cover in the lowest layer. For the 2005 October 7th, the results look very promising in terms of spatial distribution as well as temporal evolution. Especially in the first hours (Figures 6.2 (a) and (b)), the very small and sparse fog domains coincide. Later, the extensive band of fog is also identify. The forecast accuracy of fog spatial distribution underlines similar qualities as in the comparison with the SYNOP station network: LM-PAFOG fog cover is systematically underestimated.

Concerning the 2005 September 26-27th case, the forecasted fog surface has more difficulties to coincide with the satellite data (Figure 6.3). The forecasted fog surface grows for a large part to the west of the satellite observations. But, the fog patches formed in the north part of the studied area agree partially with the satellite data. In this case, the fog cover is not underestimated, but the spatial distribution of fog has a bad position. The quality of the satellite products to determine the fog spatial extention have been demonstrated in the last section (see section 6.2.1). In both cases, the satellite data supply very interesting information about the structure of the very low clouds. The comparison with LM-PAFOG underlines the model capacities to describe the evolution of the smallest fog patches. But the imprecision about the cloud base height restricts the conclusion about the comparison results. A systematic verification of the satellite data is necessary before their implementation in a verification process.
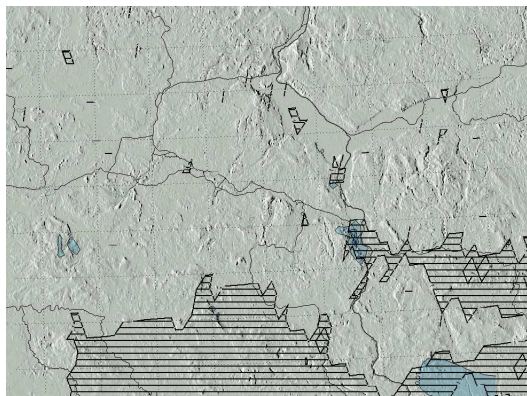
(a) 2005 October 6th-23 UTC
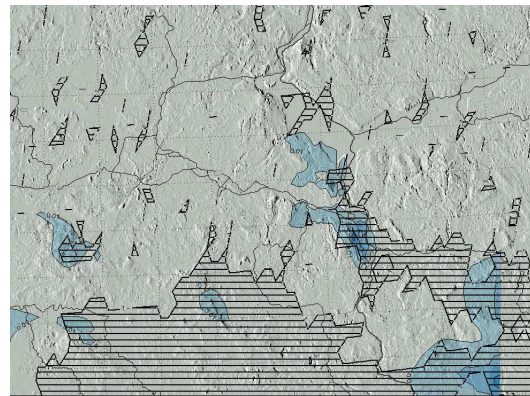
(b) 2005 October 7th-00 UTC
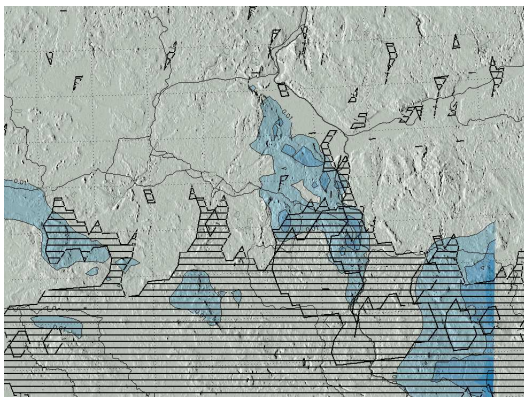
(c) 2005 October 7th-01 UTC
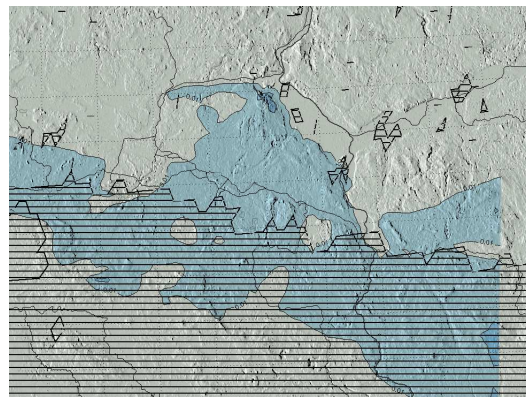
(d) 2005 October 7th-03 UTC
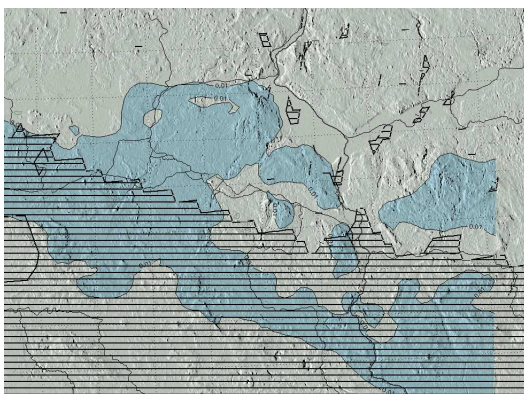
(e) 2005 October 7th-04 UTC
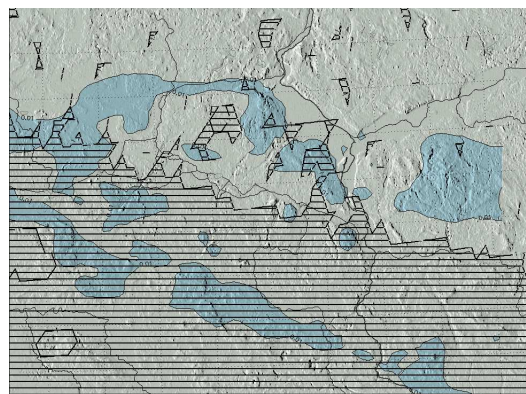
(f) 2005 October 7th-05 UTC

Figure 6.2: Spatial distribution of fog on the Lindenberg area on 2005 October 7th during the fog event (03-06 UTC) as seen by satellite (black shaded areas) and liquid water content simulated by LM-PAFOG (blue areas).
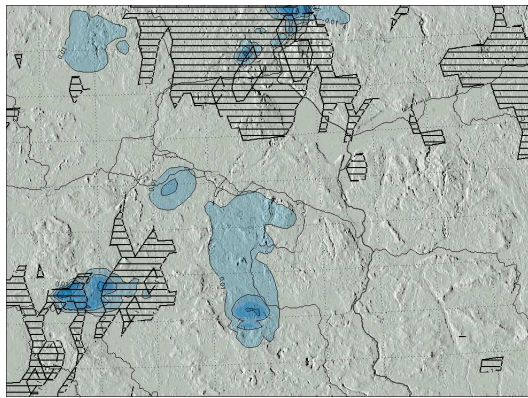
(a) 2005 September 27th-01 UTC
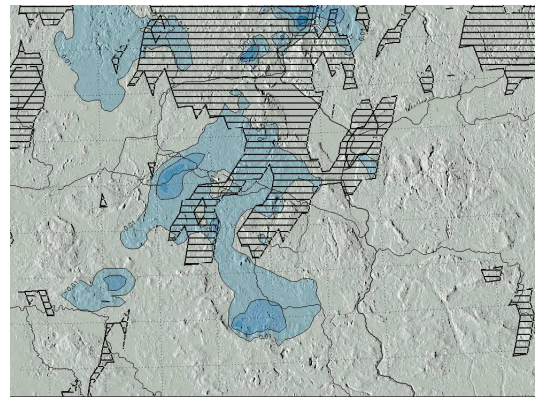
(b) 2005 September 27th-02 UTC
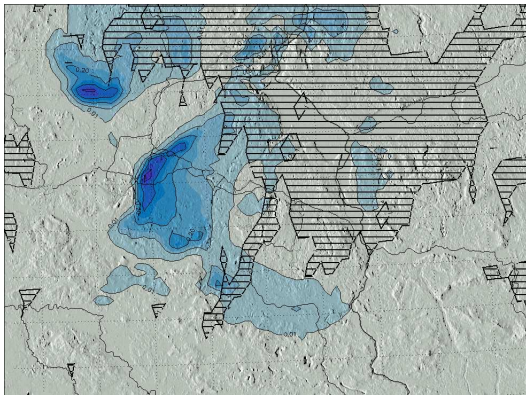
(c) 2005 September 27th-03 UTC
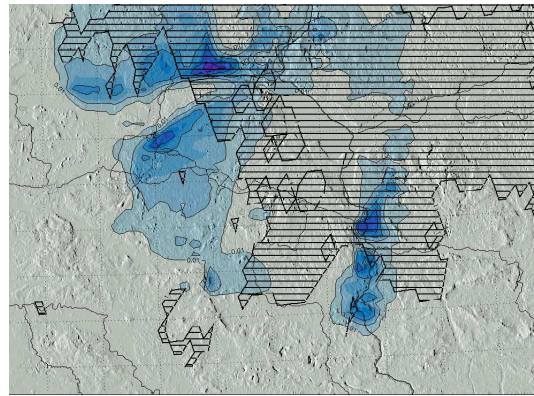
(d) 2005 September 27th-04 UTC
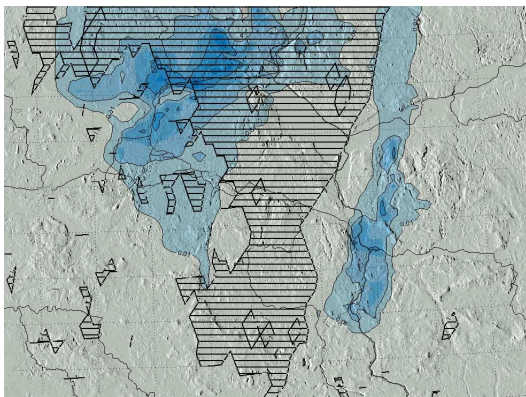
(e) 2005 September 27th-05 UTC
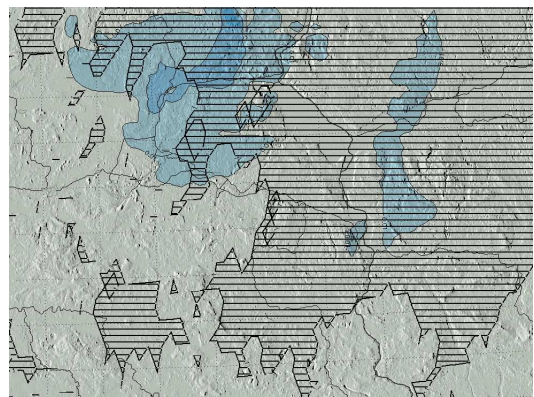
(f) 2005 September 27th-06 UTC

Figure 6.3: Spatial distribution of fog on the Lindenberg area on 2005 September 27th during the fog event (01-06 UTC) as seen by satellite (black shaded areas) and liquid water content simulated by LM-PAFOG (blue areas).
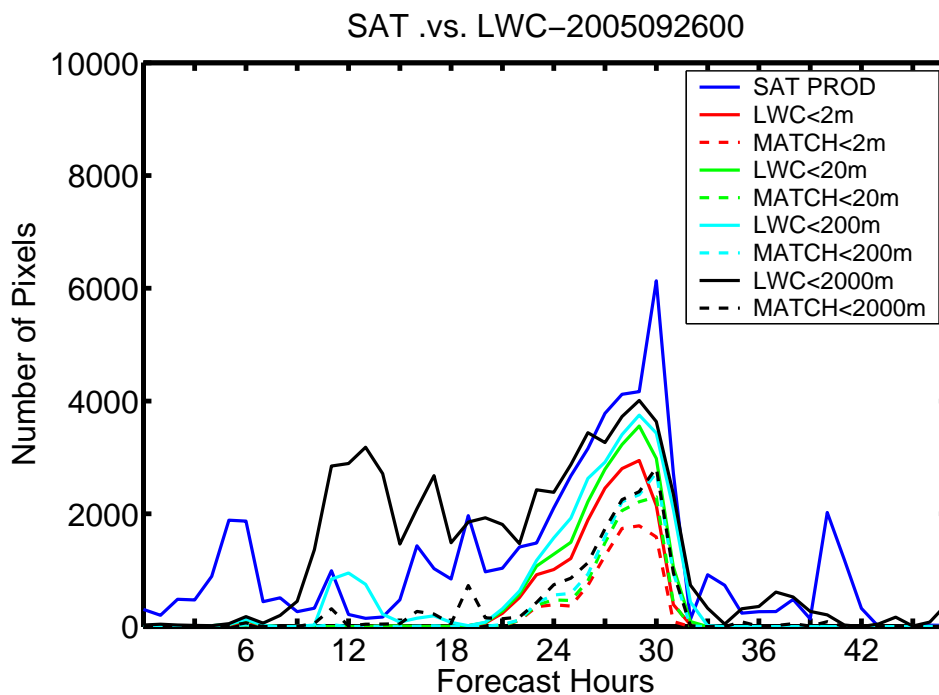
Figure 6.4: Comparison of the time evolution of LM-PAFOG fog spatial distribution forecast with the spatial distribution extracted from the Meteosat 8 satellite products on the Lindenberg area at 2005 September, 26-27th.
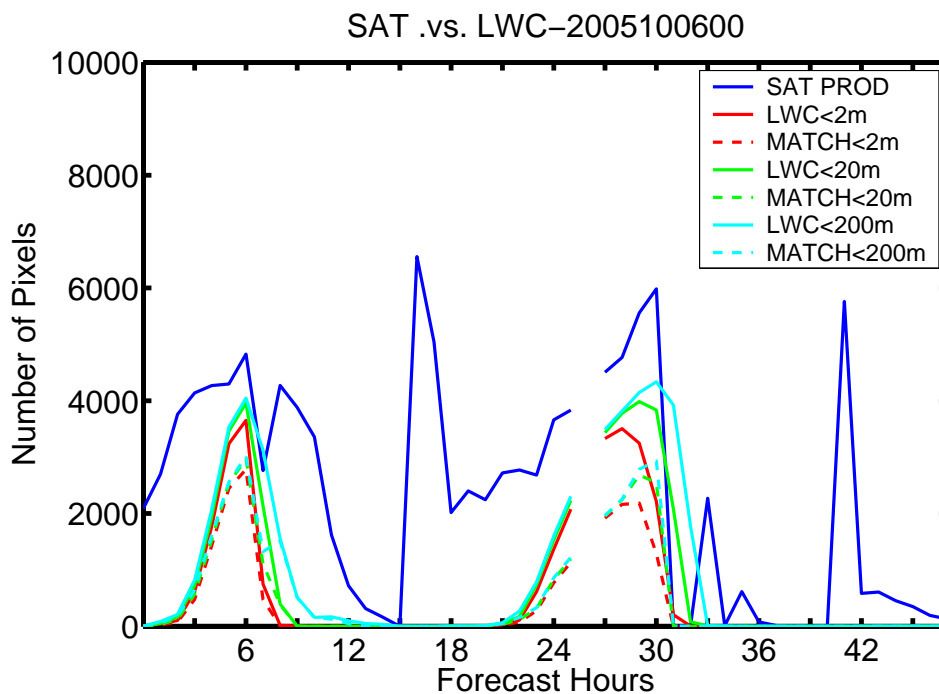
Figure 6.5: Same as Figure 6.4 at 2005 October, 6-7th.

In order to limit the uncertainty about the cloud base height of the satellite fog mask, the comparison of the forecasted liquid water with the satellite observations was extended to the other model levels. The liquid water contained in the model column was integrated from the ground until a defined altitude (2m, 20m, 200m and 2000m). The resulting surface of this integrated liquid water content was compared with the satellite observations. The results are presented in the Figures 6.4 and 6.5. With this new point of view, the LM-PAFOG forecast quality can be better quantified. LM-PAFOG forecasts show significant improvements if the liquid water contained in the first 20 m are compared with the satellite data. It underlines some difficulty of LM-PAFOG to keep fog clouds in contact with the ground. Moreover, the comparison with the liquid water in the first 200 m or 2000 m shows only a weak improvement of the coincidence with the satellite data. This weak improvement of the hit quantity between both surfaces underlines the good quality of the satellite observations for these chosen fog events. However, it also means that the satellite products detects always relatively high clouds in their observations.

6.3   Conclusions

The comparison between the above-described satellite products and the model data is practical, because a quick estimation of area coincidence is possible. From this satellite product, no information is available on cloud ground contact, i.e. whether humidity levels are elevated near the ground. Therefore, a comparison of this product with modelled ground fog is not possible. Another difficulty to be considered in a comparison of model and satellite data is the issue of multiple cloud layers. In the satellite product, only the uppermost cloud layer is considered. Any clouds below are not detected and therefore model and satellite output will disagree. A comparison could be envisaged in case of very low cloud cover and after a verification of the satellite data with ground measurements. Instead however, the model can be validated regarding liquid water distribution when the integrated liquid water column is considered rather than the lowermost layer alone. The first tests, made with the integrated liquid water are encouraging. Moreover, their results introduce information about the cloud compositions and not only its spatial distribution. In case of fog event, the satellite products cannot be used in a verification process, however they supply additional information necessary for the development of a three-dimensional forecast model.

Chapter 7

Conclusions and outlook

Conclusions

Fog has a significant impact on economical and safety aspects. Accurate forecasts of fog spatial distribution are decisive information. Nevertheless, the numerical modelling of fog is a complex exercise. The formation of fog results from a combination of cooling, moistening and turbulent mixing processes. Only an accurate prediction of boundary layer temperature, humidity and wind associated with a detailed treatment of cloud microphysics can ensure a successful fog forecast. One of the most important processes is the radiative cooling of the lowest atmospheric layers during the night. For the numerical modelling of the radiative fog, the treatment of the boundary layer by means of a one-dimensional numerical model is often sufficient. It is one of the reasons why numerous one-dimensional fog models have been developed in the last decades. Nevertheless, this fog modelling approach is insufficient while considering other processes, such as advection and topographically induced dynamic flows which are determinant factors in the fog formation. In these cases, it is necessary to use a three-dimensional approach for the numerical fog forecast. So far, three-dimensional approaches are limited to the operational mesoscale model forecast, which are not developed for the specificity of the fog forecast.

The central aim of this thesis was to develop new three-dimensional fog forecasts dealing with the spatial heterogeneity involved in the boundary layer processes. In the first step, the detailed fog microphysics, PAFOG, have been introduced in the model structure of the nonhydrostatic mesoscale model, LM, of the German Meteorological Service. The bulk microphysics of LM, with the respect to the condensation and evaporation, have been substituted by the PAFOG microphysics. The total droplet number concentration was introduced as new prognostic variable. The microphysics influence on the formation, persistence and dissipation of fog is now controlled by the growth and shrink of the cloud droplets in the activation, condensation/evaporation and sedimentation processes. A better representation of gravitational settling based on cloud droplet size is thus used. The heteorogene structure of fog is also better reproduced in the visibility parametrisation by combined relations including cloud droplet concentration and cloud liquid water content.

In a second step, the modelling environment has been adjusted to the specificity of the fog formation. During the growth phase, radiative fog steadily gains thickness, start-

ing from a thin layer above the surface. In order to consider these processes occurring at the soil/atmosphere interface, it is necessary to have a high vertical resolution, which is not available in the operational mesoscale model. A high vertical resolution with 25 atmospheric layers in the lowest 2000 m has been adapted in the dynamical core of the LM. In order to consider the spatial heterogeneity of the topography or vegetation, a grid spacing of 2.8 km has been used. With this higher resolution, LM-PAFOG reproduced the horizontal transport of moist or cold air masses involved in fog formation.

An extensive study of the three-dimensional model's performance was made by participation in the COST 722 intercomparison. A statistical study and case study analysis of selected fog events allowed an assessment of the fog forecast quality. Moreover, a statistical forecast system, MOS-ARPEGE, as well as three-dimensional models such as ALADIN-AUSTRIA, DMI-HIRLAM and NMM-PAFOG have also been involved in this campaign. LM-PAFOG forecasts have therefore been successively compared with a large set of measurements and with other participating models' forecasts.

Skill scores for a four month period of continuous forecasts pointed out the influence of the diurnal cycle on the forecast performances. LM-PAFOG has some difficulties to form fog in the afternoon, while it forecasts the observed fog episodes in the calm atmosphere accurately. Despite the skill score variations, our model is able to increase the discrimination with an equitable threat score of 20%. These results have been achieved following an automatical procedure based on a single point comparison. The subjective interpretation by a human forecaster who knows the models would improve the skills further.

In three chosen fog events covering different periods of the day and controlled by different physical processes, the physical parametrisation of LM-PAFOG has been analysed in detail. Comparisons with surface observations reporting the evolution of thermodynamic and dynamic parameters, as well as the visibility were necessary to assess the value of our three-dimensional approach. Regarding the parametrisation of cooling, moistening and mixing processes in the boundary layer, the accuracy of the energy balance at the surface, as well as a well-reproduced wind field, have been confirmed. However, the turbulent mixing parametrisation adjusted to the high vertical resolution has shown evident shortcomings of the chosen turbulence scheme. It has been clearly identified as responsible for the inaccurate afternoon fog forecasts. Current researches and sensitive tests concerning a new turbulent mixing parametrisation are in progress.

In this approach, it was difficult to illustrate the gains of our three-dimensional fog forecast model. The local patterns of fog were only compared with a sparse surface observation network. The verification of the spatial distribution of fog has been restrained to 38 grid points of the forecast domain. Nevertheless, the influence of the surface parameters on the local formation have been demonstrated. The lack of information concerning the surface parameters remains a limitation in the development of an accurate three dimensional fog forecast. The definition of urban island as well as a more detailed vegetation parametrisation would significantly improve the accuracy of the predicted fog extension.

The confrontation of our model with other European fog forecast systems revealed that the primary factor affecting the forecast performance is not based on the complexity of the physical parametrisation or on the high spatial resolution, but an accurate fog forecast can only occur with an adapted initialisation scheme and an optimised empirical

visibility function. Both operational mesoscale models, ALADIN-AUSTRIA and DMI-HIRLAM, delivered more accurate fog forecasts than the research model, NMM-PAFOG and LM-PAFOG. The computing experience of the operational models stays a decisive factor for an accurate forecast. The initial conditions of LM-PAFOG are simply interpolated from the operational forecast model outputs of LM. The development of a high resolution data assimilation system will be an decisive improvement for the LM-PAFOG forecasts.

The evaluation of our three-dimensional fog forecast model highlighted the needs for the verification of fog spatial distribution. The MSG satellite products adapted to the detection of fog and very low stratus fields have been tested to verify the accuracy of spatial distribution of LM-PAFOG fog forecasts. Case studies outlined the good appraisal of forecasted fog extension and the potential of advanced satellite products which can be used for verification purposes. However, an evaluation only based on the satellite product comparison is not sufficient in presence of multilayer clouds since the lower atmosphere can be hidden from the satellite. A product combining surface observations and satellite products for fog and very low stratus is necessary to evaluate the gains in spatial distribution rendition by our model.

Outlook

The development of our three-dimensional fog forecast model LM-PAFOG with parametrised microphysics opens a new field in the domain of fog prediction. Despite the promising results of LM-PAFOG in comparison with well-attended operational models, numerous improvements are still necessary to obtain an operational fog forecast model which considers the influence of the three-dimensional environment.

The results of this thesis highlighted among other things the difficulty to consider the evolution of the boundary layer with a high vertical resolution approach. In this field, only few turbulence schemes are dimensioned to be used on such resolutions, and generally are computing time consuming. Finding an adapted turbulence parametrisation to the LM-PAFOG grid resolution is the proposed next development to improve the system. However, the continuous reducing of the horizontal grid resolution with the always faster supercomputer will need to consider the turbulent mixing processes as a fully three-dimensional transport.

Moreover, the influence of the soil/atmosphere interactions plays a decisive role in the formation of fog. However, the surface transfer parametrisation of LM, which is used in this work, describes these exchanges only partially. The heterogeneity of the soil properties is restrained to ten basic soil types in the LM. The implementation of a more accurate soil and landuse dataset will be a first step. The improvement of the soil/atmosphere interactions through the introduction of a detailed vegetation scheme considering processes such as moisture storage in the lowermost atmosphere would lead to more realistic fog formation.

The localised fog extent is strongly influenced by the initialisation value of the dynamic and thermodynamic fields. The use of a high vertical resolution was negatively affected by the lack of information concerning the boundary layer's current state for the initialisation.

A data assimilation approach incorporating numerous vertical profiles of temperature, humidity and wind measurements in the boundary layer could help to better reproduce the evolution of processes occurring in the lowest atmosphere. Another solution can be the development of a three-dimensional ensemble forecast system for fog. The variations of the dynamic and thermodynamic fields in the initialisation phase give the necessary disturbance to define a probability of fog occurrence. Nevertheless, this last approach is extremely computing time consuming and the current computation possibilities are still insufficient.

Chapter 8

Schlussfolgerung und Ausblick

Schlussfolgerung

Nebel hat einen bedeutenden Einfluss auf die Wirtschaft und Sicherheitsaspekte im Verkehrswesen. Präzise Vorhersagen der räumlichen Verteilung von Nebel gelten als eine wichtige Information. Die Modellierung des Nebels ist jedoch eine komplexe Aufgabe. Die Nebelbildung resultiert aus einer Kombination von Abkühlungs-, Befeuchtungs- und Turbulenzmischungsprozessen. Nur eine exakte Vorhersage von Temperatur, Feuchte und Wind in der Grenzschicht, verbunden mit einer detaillierten Behandlung der Wolkenmikrophysik, kann eine erfolgreiche Nebelvorhersage gewährleisten. Einer der wichtigsten Prozesse ist die Abkühlung der niedrigsten atmosphärischen Schichten durch Strahlungsverluste während der Nacht. Für die Modellierung des Strahlungsnebels ist die Behandlung der Grenzschicht mithilfe eines eindimensionalen Modells meistens ausreichend. Dies ist einer der Gründe, warum mehrere eindimensionale Nebelmodelle in den letzten Jahrzehnten entwickelt wurden. Dieser Ansatz zur Nebelmodellierung ist jedoch unzureichend um die anderen Prozesse wie Advektion und dynamische Flüsse, induziert durch die Topographie, zu berücksichtigen. In diesen Fällen ist es notwendig, einen dreidimensionalen Ansatz zur Nebelvorhersage heranzuziehen. Der dreidimensionale Ansatz ist bisher nur von mesoskaligen Modellvorhersagen benutzt worden, die nicht speziell für die Nebelvorhersage entwickelt wurden.

Das Hauptziel dieser Arbeit war die Entwicklung einer neuen dreidimensionalen Nebelvorhersagemodell, das die räumliche Heterogenität in den Prozessen der Grenzschicht berücksichtigt. Zuerst wurde eine detaillierte Nebelmikrophysik, PAFOG, in die Modellstruktur des nicht-hydrostatischen mesoskaligen Modells, LM, des Deutschen Wetterdienstes hinzugefügt. Die Mikrophysik des LM, die Kondensation und Evaporation betrachtend, wurde durch die Mikrophysik von PAFOG ersetzt. Die Gesamtkonzentration der Tropfen wurde als neue Variable der Vorhersage eingeführt. Der Einfluss der Mikrophysik auf die Bildung, die Dauer und die Auflösung von Nebel wird nun vom Wachsen und Schrumpfen der Wolkentropfen im Aktivierungs-, Kondensations-/Evaporations- und Sedimentationsprozess kontrolliert. Eine bessere Beschreibung der gravitativen Sedimentation, die auf der Größe der Wolkentropfen basiert, wird dafür benutzt. Die heterogene Struktur des Nebels wird besser durch die Parametrisierung der Sichtweite mit Hilfe der

Kombination aus der Konzentration des Wolkentropfens und des Wolkenwassergehalts dargestellt.

Im Anschluss wurde die Modellierungsumgebung an die Besonderheiten der Wolkenbildung angepasst. Während der Wachstumsphase gewinnt Strahlungsnebel regelmäßig an Dicke, beginnend mit einer dünnen Schicht nahe der Bodenoberfläche. Um diese an der Schnittstellle zwischen Boden und Atmosphäre ablaufenden Prozesse zu betrachten, benötigt man eine feine vertikale Auflösung, die nicht im operationalen mesoskaligen Modell verfügbar ist. Eine feine vertikale Auflösung mit 25 atmosphärischen Schichten bis zu 2000 m wurde im dynamischen Kern des LM angepasst. Um die räumliche Heterogenität der Topographie und Vegetation zu berücksichtigen, wurde ein Gitterabstand von 2.8 km verwendet. Mit einer solchen höheren Auflösung stellt LM-PAFOG den horizontalen Austausch von feuchter oder kalter Luftmasse, der an der Nebelbildung beteiligt ist, dar.

Eine ausführliche Validierung des Modells wurde durch die Teilnahme in dem COST 722 Projekt ermöglicht. Eine statistische Studie und Fallstudie von ausgewählten Ereignissen garantierten eine Evaluierung der Qualität der Nebelvorhersage. Ein statistisches Vorhersagesystem, MOS-ARPEGE, sowie die dreidimensionale Modelle, ALADIN-AUSTRIA, DMI-HIRLAM und NMM-PAFOG wurden ebenfalls in das Projekt einbezogen. Die Vorhersagen von LM-PAFOG wurden deswegen mit zahlreichen Beobachtungen und anderen teilhabenden Vorhersagemodellen verglichen.

Skill Scores zeigten während einer viermonatigen Dauer von kontinuierlichen Vorhersagen den Einfluss des Tagesgangs auf die Vorhersageleistung. LM-PAFOG hat einige Schwierigkeiten Nebel am Nachmittag zu bilden, obwohl es die beobachteten Nebelereignisse in der ruhigen Atmosphäre genau vorhersagt. Trotz der Schwankungen der Skill Scores ist unser Modell in der Lage, die Erkennung von Nebel mit einem equitable Threat Score von 20% gegenüber die Nebelklimatologie zu verbessern. Diese Ergebnisse wurden in einem automatischen Prozess ausgeführt, der auf einem Vergleich eines einzigen Punktes basierte. Die subjektive Interpretation eines Meteorologen, der das Modell kennt, würde die Skills verbessern.

In drei ausgewählten Nebelereignissen, die unterschiedliche Tageszeiten abdecken und durch verschiedene physikalische Prozesse kontrolliert werden, wurde die physikalische Parametrisierung von LM-PAFOG detailliert analysiert. Vergleiche mit Bodenbeobachtungen, die die Entwicklung der thermodynamischen und dynamischen Parameter sowie die Sichtweite verfolgen, waren notwendig, um den Wert unseres dreidimensionalen Ansatzes zu bestimmen. Mit Blick auf die Parametrisierung von Abkühlungs-, Befeuchtungs- und Mischungsprozessen in der Grenzschicht wurde die Genauigkeit der Energiebilanz an der Oberfläche sowie gut dargestellte Windfelder bestätigt. Die Parametrisierung der turbulenten Durchmischung, die an die feine vertikale Auflösung angepasst ist, hat eindeutige Nachteile des gewählten Schemas gezeigt. Dieses konnte für die ungenaue Nebelvorhersage am Nachmittag verantwortlich gemacht werden. Aktuelle Forschungen und Sensitivitätsstudien hinsichtlich einer neuen Parametrisierung der turbulenten Durchmischung sind bereits in Arbeit.

Bei dieser Arbeit war es nur schwer möglich, die Vorteile eines dreidimensionalen Nebelvorhersagemodells aufzuzeigen. Die lokalen Muster der Nebelausbreitung wurden nur mit einigen Bodenbeobachtungen verglichen. Sowohl die Verifikation der räumlichen

Verteilung des Nebels war auf 38 Gitterpunkte im Modellgebiet eingeschränkt. Trotzdem konnte der Einfluss der Bodenparametrisierung auf die Nebelbildung nachgewiesen werden. Die Defizite in der Bodenparametrisierung bleiben ein großes Problem bei der Entwicklung eines präzisen dreidimensionalen Vorhersagemodells. Die Definition von Städt-Wärmeinseln als auch eine genauere Beschreibung der Pflanzenparametrisierung würde die Genauigkeit der Nebelausbreitung wahrscheinlich signifikant verbessern.

Der Vergleich des PAFOG-Modells mit anderen europäischen Nebelvorhersagesystemen zeigte, dass der größte Einfluss auf die Vorhersagegüte nicht von der Komplexität der physikalischen Parametrisierung oder der hohen räumlichen Auflösung abhängt. Stattdessen wird eine gute Vorhersage nur bei einem adaptiven Initialisierungsschema und einer optimierten empirischen Sichtweitenfunktion erreicht. Die Initialisierung vom LM-PAFOG wird einfach durch Interpolation der operationellen LM-Vorhersage bestimmt. Die Entwicklung eines hochauflösenden Assimilationsschemas wird wahrscheinlich eine entscheidende Verbesserung mit sich bringen.

Die Bewertungen der Nebelvorhersagen in dieser Arbeit verdeutlichen die Notwendigkeit besserer Verifikationsmethoden für die räumliche Verteilung von Nebel einzusetzen. Die MSG-Satellitenprodukte, die Nebel und tiefliegende Stratusbewölkung identifizieren, wurden getestet, um die Genauigkeit der räumlichen Verteilung von LM-PAFOG Vorhersagen zu überprüfen. Einige Fallstudien zeigen eine gute Bewertungsmöglichkeit der Modellvorhersage durch Satellitenmessungen. Jedoch ist eine Modellvalidierung nur durch Satellitenprodukte nicht ausreichend, wenn vielschichtige Bewölkung auftritt, da die untere Atmosphäre vom Satelliten nicht gemessen werden kann. Eine Kombination von Boden- und Satellitenmessungen ist notwendig, um die verbesserte Wiedergabe der räumliche Struktur von Nebel durch LM-PAFOG zu beurteilen.

Ausblick

Die Entwicklung des dreidimensionalen Nebelvorhersagemodells mit parametrisierter Mikrophysik, LM-PAFOG, eröffnet neue Möglichkeiten im Bereich der Nebelvorhersage. Trotz der vielversprechenden Ergebnisse von LM-PAFOG sind im Vergleich mit etablierten operationellen Modellen allerdings noch zahlreiche Verbesserungen nötig, um ein operationelles Nebelvorhersagemodell zu erhalten, welches auch den Einfluss der dreidimensionalen Umgebung berücksichtigt.

Die Ergebnisse dieser Arbeit unterstreichen die Schwierigkeit, die mit der Beschreibung der Entwicklung der Grenzschicht bei hoher vertikaler Auflösung einher geht. Nur wenige Turbulenzschemata sind für solche hohe Auflösungen ausgelegt; zudem sind sie meistens sehr rechenzeitaufwendig. Ein Vorschlag für die Zukunft ist eine Turbulenzparametrisierung zu finden, die an die LM-PAFOG Gitterauflösung angepasst ist. Dennoch ist es auch nötig, die turbulenten Durchmischungsprozesse als vollständigen, dreidimensionalen Transport zu berücksichtigen; vor allem vor dem Hintergrund, dass mit Hilfe von immer schnelleren Großrechnern die horizontale Auflösung immer weiter verfeinert werden kann.

Weiterhin spielt auch der Einfluss der Wechselwirkungen zwischen Boden und Atmosphäre eine entscheidende Rolle bei der Entstehung von Nebel. Die Parametrisierung im

LM für den Austausch an der Oberfläche, die hier benutzt wird, beschreibt diese Wechselwirkungen nur teilweise. Die Heterogenität der Bodeneigenschaften ist im LM auf zehn elementare Bodenarten beschränkt. Die Implementierung von genaueren Boden- und Landnutzungsdatensätzen wird ein erster Schritt sein. Des Weiteren würde die Einführung eines detaillierten Vegetationsschemas zu einer verbesserten Simulation von Boden/Atmosphärenwechselwirkungen und schließlich zu einer realistischeren Nebelvorhersage führen.

Für die lokale Ausdehnung des Nebelgebiets spielt die Initialisierung der Dynamik- und Thermodynamikfelder eine wichtige Rolle. Die Ergebnisse der hohen Vertikalauflösung in dieser Arbeit lassen vermuten, dass genauere Informationen für die Initialisierung der Grenzschicht nötig sind. So könnte ein Datenassimilationsansatz, der eine große Anzahl gemessener Vertikalprofile von Temperatur, Feuchte und Wind in der Grenzschicht enthält, zu einer besseren Simulation der Prozesse in der untersten Atmosphäre führen.

Eine weitere Möglichkeit ist die Entwicklung eines dreidimensionalen Ensemble-Vorhersage-Systems für Nebel. Variationen der dynamischen und thermodynamischen Anfangsfelder liefern die dafür nötigen Störungen bei der Initialisierung, um letztendlich eine Wahrscheinlichkeitsaussage über das Auftreten von Nebel machen zu können. Dieser Ansatz ist jedoch äußerst rechenzeitaufwendig, die aktuellen Computerkapazitäten sind dafür noch nicht ausreichend.

Chapter 9

Conclusions et perspectives

Conclusions

Le brouillard a un impact majeur dans les domaines de l'économie et de la sécurité des transports. Des prévisions précises sur la distribution spatiale du brouillard sont une information cruciale. Or, la modélisation du brouillard est un exercice complexe. La formation du brouillard résulte d'une combinaison des processus de refroidissement, d'humidification et de phénomènes de turbulences. Seule une prévision précise de la température, de l'humidité et du vent dans la couche limite, associée à un traitement détaillé de la microphysique du nuage peut engendrer une prévision réussie du brouillard. L'un des processus les plus importants est le refroidissement par pertes radiatives des couches atmosphériques basses durant la nuit. Pour la modélisation du brouillard radiatif, le traitement de la couche limite par un modèle unidimensionnel est généralement suffisant. C'est l'une des raisons pour lesquelles de nombreux modèles unidimensionnels ont été développés durant les dernières décennies. Ce type d'approche de la modélisation du brouillard est insuffisant pour prendre en compte les autres processus, tels que l'advection et les flux dynamiques induits par la topographie, qui sont des facteurs déterminants pour le brouillard. Dans ces cas, il est nécessaire d'utiliser une approche tridimensionnelle. Jusqu'ici l'approche tridimensionnelle est limitée aux modèles de prévisions méso-échelles, qui ne sont pas développés pour les spécificités de la prévision du brouillard.

L'objectif central de cette thèse était de développer un nouveau modèle tridimensionnel de prévision de brouillard prenant en compte l'hétérogénéité spatiale induite par les processus de la couche limite.

Dans la première étape, la microphysique détaillée du brouillard, PAFOG, a été introduite dans la structure du modèle méso-échelle non-hydrostatique, LM, du Service Allemand de Météorologie. Les paramétrisations microphysiques de LM, pour ce qui concerne la condensation et l'évaporation, ont été remplacées par celles de PAFOG. La concentration du nombre total de gouttes a été introduite comme nouvelle variable de prévision. L'influence de la microphysique sur la formation, la persistance et la dissipation du brouillard est maintenant contrôlée par la croissance et la diminution du nuage de gouttes dans les processus d'activation, condensation/évaporation et sédimentation. Une meilleure représentation de la précipitation gravitationnelle, basée sur la taille des gouttes du nuage, est utilisée dorénavant. La structure hétérogène du brouillard est ainsi mieux re-

produite dans la paramétrisation de la visibilité grâce aux relations entre la concentration de gouttes et le contenu d'eau liquide du nuage.

Dans une deuxième étape, le modèle a été ajusté à la spécificité de la formation du brouillard. Durant la phase de croissance, le brouillard radiatif gagne régulièrement en épaisseur, à partir d'une fine couche au dessus de la surface. Pour prendre en considération ces processus qui se passent à l'interface terre/atmosphère, il est nécessaire d'avoir une haute résolution verticale, qu'on ne peut obtenir avec le modèle méso-échelle opérationnel. Une haute résolution verticale, avec 25 niveaux atmosphériques dans les 2000 premiers mètres, a été adaptée dans le cœur de la dynamique de LM. Pour prendre en compte l'hétérogénéité spatiale de la topographie et de la végétation, un pas de grille de 2.8 km a été utilisé. Avec une telle résolution, LM-PAFOG a reproduit le transport horizontal d'humidité ou de masses d'air froid impliqués dans la formation du brouillard.

Une vaste étude des performances du modèle tridimensionnel a été conduite en participant à l'inter-comparaison COST 722. Une étude statistique et l'analyse de cas d'études d'événements de brouillard choisis ont permis d'évaluer la qualité de la prévision du brouillard. Un système de prévision statistique, MOS-ARPEGE, ainsi que des modèles tridimensionnels tels qu'ALADIN-AUSTRIA, DMI-HIRLAM et NMM-PAFOG ont été également impliqués dans cette campagne. Les prévisions de LM-PAFOG ont donc été successivement comparées à un large panel de mesures et aux prévisions des autres modèles participants.

Durant une période de quatre mois de prévisions continues, les indicateurs Skill Scores mettent en avant l'influence du cycle diurne sur les performances des prévisions. LM-PAFOG a quelques difficultés à former du brouillard dans l'après-midi, alors qu'il prévoit précisément les épisodes de brouillard observés dans une atmosphère calme. Malgré les variations de Skill Scores, notre modèle est capable d'augmenter la reconnaissance des épisodes de brouillard par rapport à la climatologie observée avec un bon indicateur Equitable Threat Score de 20%. Ces résultats ont été obtenus en suivant une procédure automatique reposant sur une comparaison en un seul point. L'interprétation subjective d'un prévisionniste qui connait les modèles améliorerait les résultats des Skills.

Dans les trois évènements de brouillard choisis couvrant différentes périodes da la journée et contrôlés par différents processus physiques, la paramétrisation physique de LM-PAFOG a été analysée en détails. Des comparaisons avec les observations portant sur l'évolution des paramètres thermodynamiques et dynamiques et de la visibilité étaient nécessaires pour estimer la pertinence de notre approche tridimensionelle. En considérant la paramétrisation des processus de refroidissement, d'humidification et de mélange dans la couche limite, la précision de l'équilibre énergétique à la surface ainsi que la bonne reproduction du vent ont été confirmées. Cependant, la paramétrisation des phénomènes de turbulences ajustée à la haute résolution verticale a mis en évidence des imperfections dans le schéma de turbulence choisi. Il a été clairement identifié comme responsable des prévisions inexactes de l'après-midi. Dans le cadre des recherches en cours, des tests de sensibilité concernant une nouvelle paramétrisation des mélanges turbulents sont entrepris.

Dans cette approche, il était difficile d'illustrer les gains de notre modèle de prévision de brouillard tridimensionnel. Les exemples locaux de brouillard ont seulement été comparés avec un réseau d'observation clairsemé. La vérification de la distribution spatiale du brouillard a été réduite à 38 points du domaine de prévision. Cependant, l'influence des

paramètres de surface sur la formation locale a été démontrée. Le manque d'informations concernant les paramètres de surface reste une limitation dans le développement d'une prévision exacte en trois dimensions du brouillard. La définition d'un îlot urbain ainsi qu'une paramétrisation plus détaillée de la végétation améliorerait significativement la précision des prévisions de l'étendue du brouillard.

La confrontation de notre modèle avec les autres systèmes européens de prévision du brouillard a révélé que le principal facteur affectant les performances de prévision ne dépendait pas de la complexité de la paramétrisation physique ou d'une haute résolution spatiale, mais d'un schéma d'initialisation adapté et d'une fonction empirique optimisée de la visibilité. Les deux modèles opérationnels méso-échelle ALADIN-AUSTRIA et DMI-HIRLAM, ont donné de meilleurs prévisions de brouillard que les modèles de recherche NMM-PAFOG et LM-PAFOG. L'expérience des modèles opérationnels, acquises par les nombreuses heures de calculs, reste un facteur décisif d'une prévision exacte. Les conditions initiales de LM-PAFOG sont simplement l'interpolation des résultats du modèle opérationnel de prévision LM. Le développement d'un système d'assimilation de données pour des résolution spatiale plus fine sera un pas décisif dans l'améliorations des prévisions de LM-PAFOG.

L'évaluation de notre modèle tridimensionnel de prévision de brouillard souligne les besoins de vérification de la distribution spatiale du brouillard. Les produits du satellite MSG, adaptés à la détection du brouillard et des nuages très bas ont été testés pour vérifier l'exactitude de la distribution spatiale des prévisions de brouillard de LM-PAFOG. Les études de cas ont souligné la bonne estimation de l'étendue du brouillard prévu et le potentiel des produits satellite avancés qui peuvent être utilisés pour les vérifications. Cependant une évaluation reposant seulement sur la comparaison avec le produit satellite n'est pas suffisante en présence de nuages multicouches qui peuvent cacher l'atmosphère basse aux satellites. Un produit associant les observations de surface et celles par satellite du brouillard et des nuages très bas est nécessaire pour progresser dans l'interprétation de la distribution spatiale de notre modèle.

Perspectives

Le développement de notre modèle tridimensionnel de prévision de brouillard à microphysique paramétrée, LM-PAFOG, ouvre un nouvel horizon dans le domaine de la prévision de brouillard. Malgré les résultats prometteurs de LM-PAFOG dans les comparaisons avec les modèles opérationnels, de nombreuses améliorations sont encore nécessaires pour obtenir un modèle de prévision de brouillard opérationnel qui prend en compte l'influence de l'environnement en trois dimensions.

Les résultats de cette thèse mettent en lumière, parmi d'autres choses, la difficulté de prendre en compte l'évolution de la couche limite avec une haute résolution verticale. Dans ce domaine, seuls quelques schémas de turbulence sont dimensionnés pour être utilisés avec de telles résolutions et sont généralement consommateurs de temps de calcul. Trouver une paramétrisation de turbulence adaptée à la résolution de LM-PAFOG est le prochain développement à envisager. Cependant, la réduction continue du pas de résolution horizontale avec des ordinateurs toujours plus rapides nécessitera la prise en compte des phénomènes de turbulence en tant que déplacements tridimensionnels.

De plus, l'influence des interactions sol/atmosphère joue un rôle décisif dans la formation du brouillard. Pourtant la paramétrisation des transferts à la surface de LM, qui est utilisée dans ce travail, décrit ces échanges de manière seulement partielle. L'hétérogénéité des caractéristiques du sol est réduite à dix types de sols dans LM. La mise en œuvre d'un fichier plus précis des paramètres du sol sera une première étape. Pourtant, pour une amélioration des interactions sol/atmosphère l'introduction d'un système de végétation détaillé prenant en compte des processus tels que le stockage de l'humidité dans les couches les plus basses de l'atmosphère pourrait permettre une formation de brouillard plus réaliste.

L'extension d'un brouillard localisé est fortement influencée par la valeur d'initialisation des champs dynamiques et thermodynamiques. L'utilisation d'une haute résolution verticale met en évidence le manque d'informations sur l'état de la couche limite lors de l'initialisation. Un processus d'assimilation de données incorporant de nombreux profils verticaux de mesure de température, d'humidité et de vent dans la couche limite pourrait permettre de mieux reproduire l'évolution des processus se déroulant dans les basses couches de l'atmosphère. Une autre solution peut être le développement d'un Ensemble basé sur des prévisions tridimensionnelles du brouillard. Les variations des champs dynamiques et thermodynamiques dans la phase d'initialisation introduisent des perturbations nécessaires pour définir la probabilité d'apparition du brouillard. Cependant cette dernière approche est extrêmement consommatrice de temps de calcul et les possibilités de calcul actuelles sont encore insuffisantes.

Appendix A

Analysis of selected fog event-Episode 2: September 27th, 2005

In this section, the comparisons of each SYNOP station with the forecast of the corresponding LM-PAFOG grid point are detailled for the radiative fog episode occurring at September, 27th 2005. The time evolution of the available dynamic and thermodynamic variables is presented:

- differences in terms of 2m visibility (figure A.1)

- bias of 2m temperature (figure A.2)

- bias of 2m relative humidity (figure A.3)

- bias of 10m wind speed (figure A.4)

The position of the SYNOP station in the forecast area as well as the corresponding numbering used in this study is highlighted in figure 4.2.
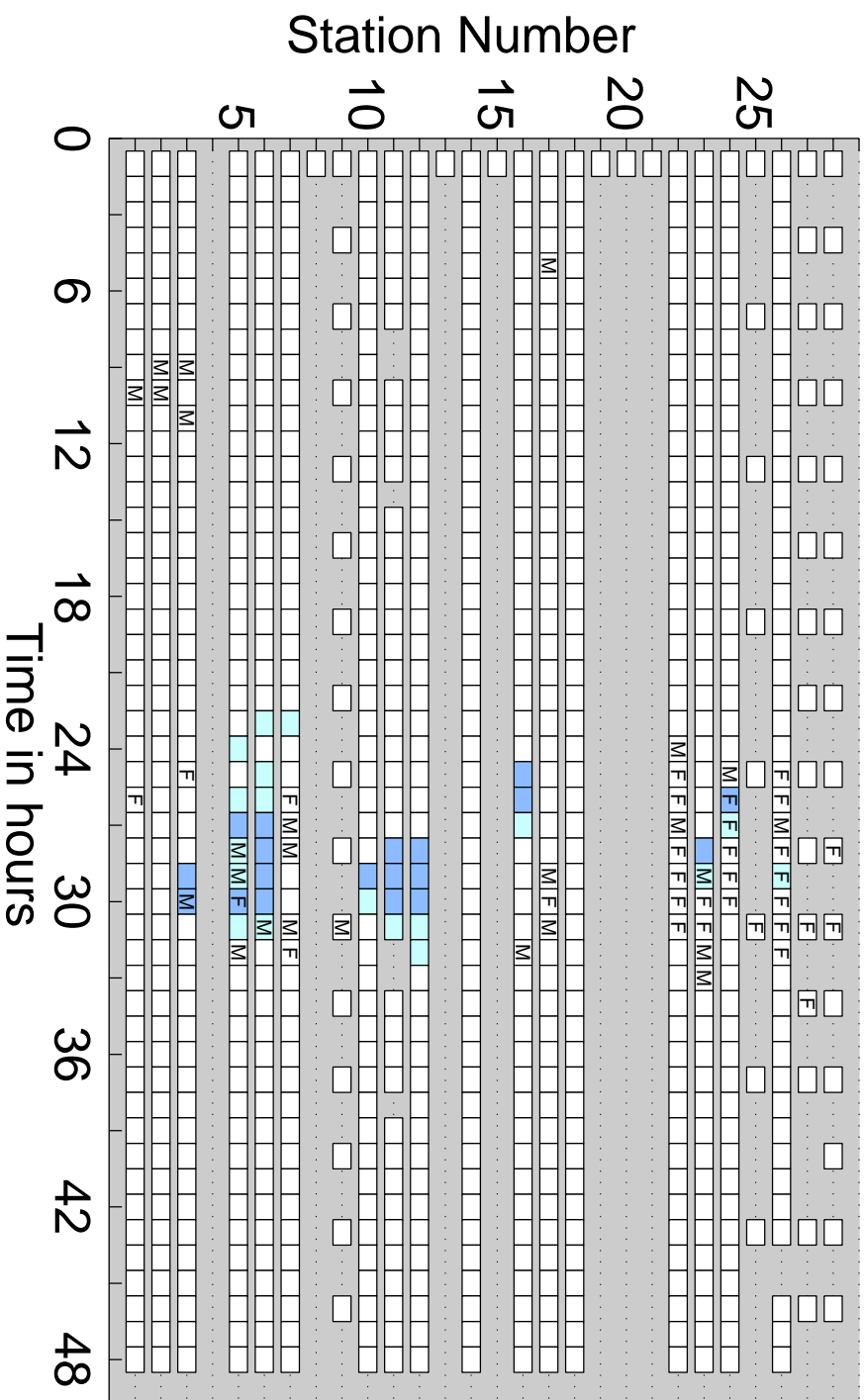
Figure A.1: Comparison of forecasted 2m-visibility with each SYNOP station measurement in the Lindenberg area at September 26-27th, 2005. Capital letters notify the presence of fog reported from each SYNOP station: **F** corresponds to a fog with a visibility below 1000m; **M** marks a mist with a visibility between 1000 and 3000 m. The colour scale points out the presence of fog issued from the LM-PAFOG forecasts: **deep blue** corresponds to a fog with a visibility below 1000m; **cyan** represents a mist with a visibility between 1000 and 3000m; **white** is the period without fog, i.e. visibility higher than 3000m. Boxes are only plotted where measurements were available. Initialisation: September 26th, 2005 at 00UTC.
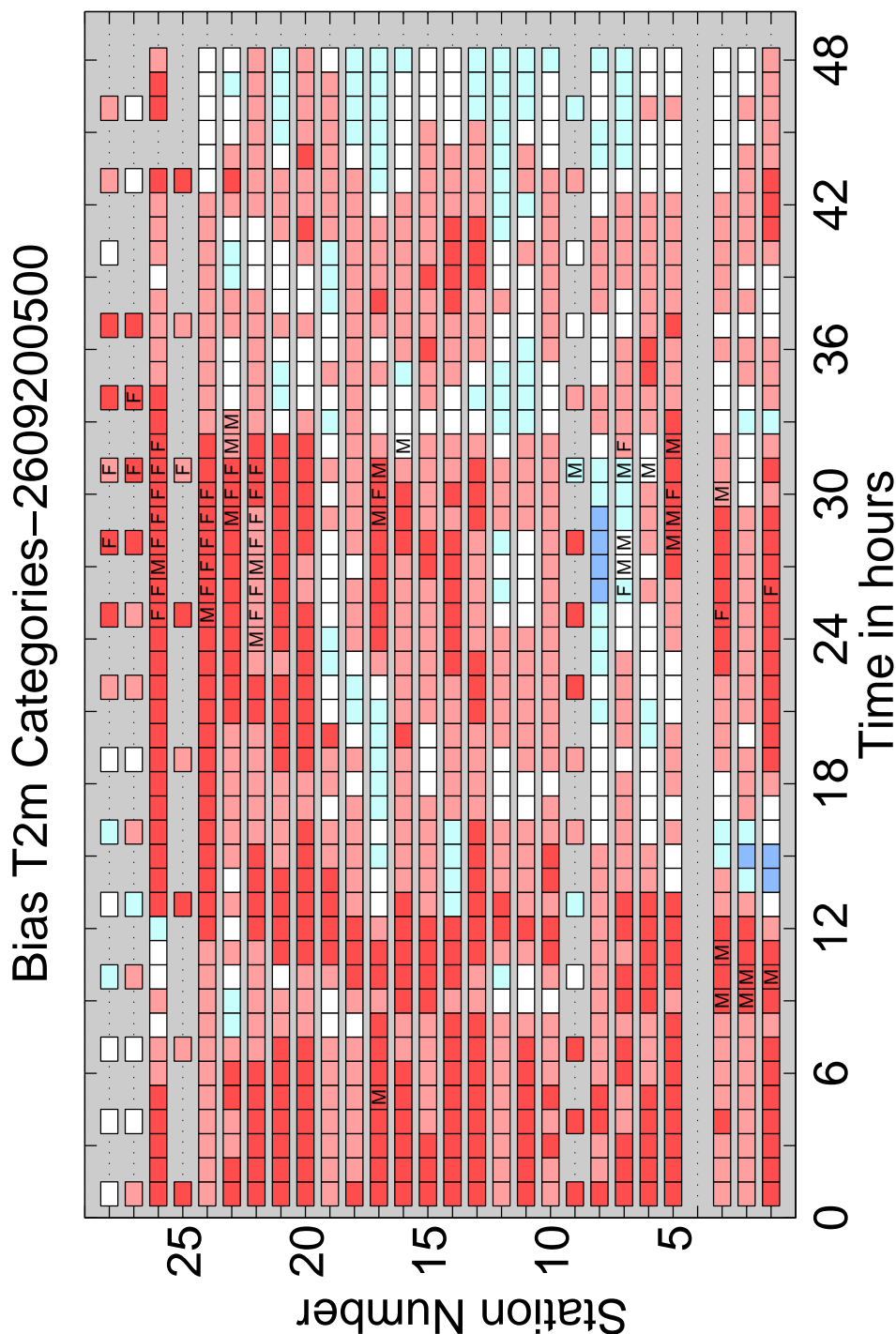
Figure A.2: Comparison of forecasted 2m-temperature with each SYNOP station in the Lindenberg area at September 26-27th, 2005. The colour scale sorts the bias in 5 categories: **deep red** corresponds to an overestimation of the model, with a bias larger than 2°C; **red** corresponds to an overestimation of the model, with a bias between 0.5°C and 2°C; **white** marks the agreement between measurements and forecasts, with a bias between 0.5°C and -0.5°C; **cyan** corresponds to an underestimation of the model, with a bias between -0.5°C and -2°C; **deep blue** corresponds to an underestimation of the model, with a bias lower than -2°C. Boxes are only plotted where measurements were available. Initialisation: September 26th, 2005 at 00UTC.

Figure A.3: Comparison of forecasted 2m-relative humidity for each SYNOP station in the Lindenberg area at September 26-27th, 2005. The colour scale sorts the bias in 5 categories: **deep red** corresponds to an overestimation of the model, with a bias larger than 5%; **red** corresponds to an overestimation of the model, with a bias between measurements and forecasts, with a bias between 1% and 5%; **white** marks the agreement between measurements and forecasts, with a bias between 1% and -1%; **cyan** corresponds to an underestimation of the model, with a bias between -1% and -5%; **deep blue** corresponds to an underestimation of the model, with a bias lower than -5%. Boxes are only plotted where measurements were available. Initialisation: September 26th, 2005 at 00UTC.

Figure A.4: Comparison of forecasted 10m-wind for each SYNOP station in the Lindenberg area at September 26-27th, 2005. The colour scale sorts the bias in 5 categories: **deep red** corresponds to an overestimation of the model, with a bias larger than 2 m.s^{-1}; **red** corresponds to an overestimation of the model, with a bias between 0.5 m.s^{-1} and 2 m.s^{-1}; **white** marks the agreement between measurements and forecasts, with a bias between 0.5 m.s^{-1} and -0.5 m.s^{-1}; **cyan** corresponds to an underestimation of the model, with a bias between -0.5 m.s^{-1} and -2 m.s^{-1}; **deep blue** corresponds to an underestimation of the model, with a bias lower than -2 m.s^{-1}. Boxes are only plotted where measurements were available. Initialisation: September 26th, 2005 at 00UTC.

Appendix B

Analysis of selected fog event-Episode 3: December 6-7th, 2005

In this section, the comparisons of each SYNOP station with the forecast of the correspon-ding LM-PAFOG grid point are detailled for the fog episode occurring at the December, 6-7th 2005. The time evolution of the available dynamic and thermodynamic variables is presented:

- differences in terms of 2m visibility (figure B.1)

- bias of 2m temperature (figure B.2)

- bias of 2m relative humidity (figure B.3)

- bias of 10m wind speed (figure B.4)

The position of the SYNOP station in the forecast area as well as the corresponding numbering used in this study is highlighted in figure 4.2.

Figure B.1: Comparison of forecasted 2m-visibility with each SYNOP station in the Lindenberg area at December 6-7th, 2005. Capital letters notify the presence of fog reported from each SYNOP station: **F** corresponds to a fog with a visibility below 1000m; **M** marks a mist with a visibility between 1000 and 3000 m. The colour scale points out the presence of fog issued from the LM-PAFOG forecasts: **deep blue** corresponds to a fog with a visibility below 1000m; **cyan** represents a mist with a visibility between 1000 and 3000m; **white** is the period without fog, i.e. visibility higher than 3000m. Boxes are only plotted where measurements were available. Initialisation: December 6th, 2005 at 00UTC.

Figure B.2: Comparison of forecasted 2m-temperature with each SYNOP station in the Lindenberg area at December 6-7th, 2005. The colour scale sorts the bias in 5 categories: **deep red** corresponds to an overestimation of the model, with a bias larger than 2°C; **red** corresponds to an overestimation of the model, with a bias between 0.5°C and 2°C; **white** marks the agreement between measurements and forecasts, with a bias between 0.5°C and -0.5°C; **cyan** corresponds to an underestimation of the model, with a bias between -0.5°C and -2°C; **deep blue** corresponds to an underestimation of the model, with a bias lower than -2°C. Boxes are only plotted where measurements were available. Initialisation: December 6th, 2005 at 00UTC.

Figure B.3: Comparison of forecasted 2m-relative humidity for each SYNOP station in the Lindenberg area at December 6-7th, 2005. The colour scale sorts the bias in 5 categories: **deep red** corresponds to an overestimation of the model, with a bias larger than 5%; **red** corresponds to an overestimation of the model, with a bias between 1% and 5%; **white** marks the agreement between measurements and forecasts, with a bias between 1% and -1%; **cyan** corresponds to an underestimation of the model, with a bias between -1% and -5%; **deep blue** corresponds to an underestimation of the model, with a bias lower than -5%. Boxes are only plotted where measurements were available. Initialisation: December 6th, 2005 at 00UTC.
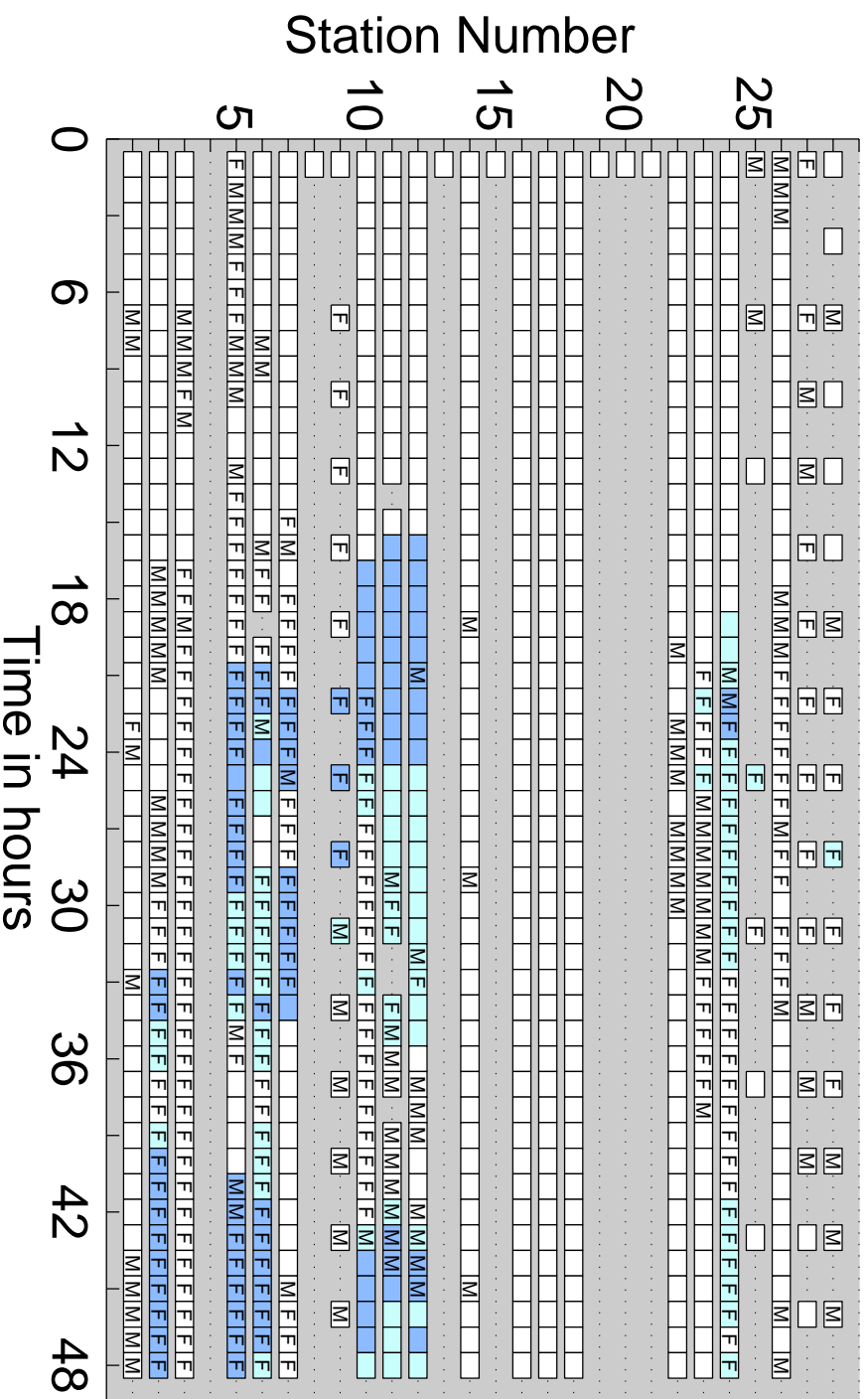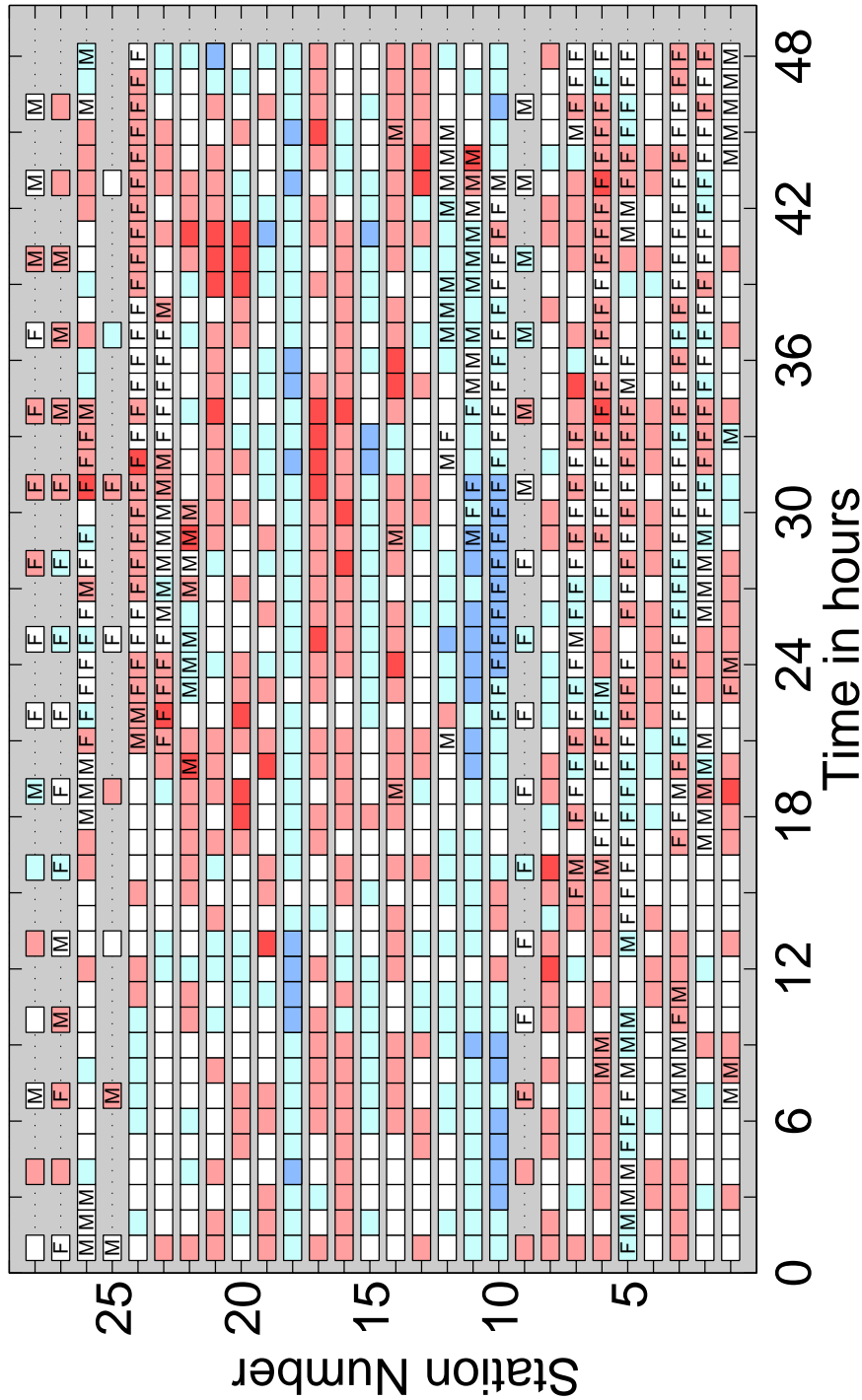
Figure B.4: Comparison of forecasted 10m-wind for each SYNOP station in the Lindenberg area at December 6-7th, 2005. The colour scale sorts the bias in 5 categories: **deep red** corresponds to an overestimation of the model, with a bias larger than 2 m.s^{-1}; **red** corresponds to an overestimation of the model, with a bias between 0.5 m.s^{-1} and 2 m.s^{-1}; **white** marks the agreement between measurements and forecasts, with a bias between 0.5 m.s^{-1} and -0.5 m.s^{-1}; **cyan** corresponds to an underestimation of the model, with a bias between -0.5 m.s^{-1} and -2 m.s^{-1}; **deep blue** corresponds to an underestimation of the model, with a bias lower than -2 m.s^{-1}. Boxes are only plotted where measurements were available. Initialisation: December 6th, 2005 at 00UTC.

Appendix C

List of symbols

Symbols	Definition
β_{ext}	extinction coefficient
$\beta_{scat,D}$	scattering coefficient for fog droplets
c_{pd}	heat capacity of dry air for a constant pressure
c_{vd}	heat capacity of dry air for a constant volume
D	droplet diameter
D_0	mean value of the droplet diameters
$D(\eta)$	soil hydraulic diffusivity
e_{sat}^{v}	saturation vapour pressure over a plane water surface
E	global evapotranspiration at the surface
E_b	bare soil evaporation
E_i	evaporation of the interception store
E_p	potential evaporation rate
E_s	snow sublimation
E_{trans}	plant transpiration
η_{ADP}	air dryness point of the soil
η_{PV}	pore volume of the soil
η_g	volumetric moisture content at the ground
f_h	stability function of heat turbulent fluxes
f_i	fraction of water cover
f_m	stability function of momentum turbulent fluxes

Symbols	Definition
f_s	fraction of snow cover
f_{veg}	fraction of plant cover
F_{sfc}^v	moisture fluxes at the surface
F_η	vertical soil water flux
F_h	heat soil fluxes
F^f	turbulent atmospheric flux of frozen water
F^l	turbulent atmospheric flux of liquid water
F^v	turbulent atmospheric flux of water vapour
F^t	turbulent atmospheric fluxes of heat
$\mathbf{g}$	apparent acceleration of gravity
G_p	latent heat flux caused by freezing rain at the ground
G_s	latent heat flux caused by melting snow at the ground
$\mathbf{H}$	turbulent flux of sensible heat
I^l	rate of phase change of liquid water
I^f	rate of phase change of ice
$K(\eta)$	soil hydraulic conductivity
K_h	turbulent diffusion coefficient for heat at the surface
K_h^v	turbulent diffusion coefficient for heat
K_m	turbulent diffusion coefficient for momentum at the surface
K_m^v	turbulent diffusion coefficient for momentum
κ	von-Karman constant ($\kappa = 0.4$)
l	turbulent length scale
l_∞	asymptotic of the turbulent length scale
LWC	Liquid Water Content
L_v	latent heat of vaporisation
L_s	latent heat of solidification
λ	soil heat capacity
$m(D_{c,0})$	mass of a cloud water droplet
N_a	cloud condensed nuclei concentration

Symbols	Definition
N_c	cloud droplet concentration
$\boldsymbol{\Omega}$	constant angular velocity of earth rotation
p	pressure
P^l	precipitation fluxes of water
P^f	precipitation fluxes of ice
q_{atm}	specific humidity in the atmosphere
q_{sat}^v	specific humidity at saturation
q_c	mass fraction of cloud water
q_v	mass fraction of water vapour
q_l	mass fraction of liquid water
q_f	mass fraction of frozen water
q_{sfc}	virtual specific humidity at the surface
$Q_{rad,net}$	total radiation budget at the surface
t	time
T	temperature
T_{atm}	temperature in the lowest model layer
T_{sfc}	temperature at the ground
T_{so}	soil temperature
$\underline{\mathbf{T}}$	turbulent flux of momentum (Reynolds stress tensor)
θ	potential temperature
θ_{atm}	potential temperature in the lowest model layer
θ_{sfc}	potential temperature at the ground
θ_v	virtual potential temperature
r_a	atmospheric resistance
r_f	foliage resistance
$\mathbf{R}$	flux density of solar and thermal radiation
R_d	gas constant for dry air
R_v	gas constant for water vapour
R_w	specific gas constant for moist air

Symbols	Definition
Re	Reynolds number
Ri	Richardson number
Ri_B	bulk Richardson number
ρ	total density of the air mixture
ρ_w	density of water
S	supersaturation
$S_{q,c}$	sedimentation fluxes of specific liquid water
$S_{n,c}$	sedimentation fluxes of cloud droplet concentration
σ_c	standard deviation of the log normal droplet size distribution
$\mathbf{v}$	barycentric velocity
$|v_h|$	horizontal wind speed
VIS	visibility in m
z	altitude
z_0	aerodynamical roughness length
z_h	roughness length for turbulent heat exchange

Appendix D

List of acronyms

ALADIN	Air Limitée Adaptation dynamique Développement InterNational
ARPEGE	Action de Recherche Petite Echelle Grande Echelle
CCN	Cloud Condensed Nuclei
COSMO	COnsortium Small Scale Modelling
COST	Co-operation in the field of Scientific and Technical Research
DEM	Digital Elevation Model
DMI	Danish Meteorological Institute
DWD	Deutscher Wetterdienst (German Meteorological Service)
ECMWF	European Centre for Medium-Range Weather Forecasting
ESF	European Science Foundation
GFS	Global Forecasting System
GME	Global Model of the German meteorological service
HIRLAM	High Resolution Limited Area Model
LM	Lokal Modell
MOS	Model Output Statistic
NCEP	National Center for Environmental Prediction
NMM	Nonhydrostatic Mesoscale Model

NOAA	National Oceanic and Atmospheric Administration
ROC	Relative Operative Characteristic
SEVIRI	Spinning-Enhanced Visible and Infrared Imager
UTC	Universal Time Co-ordinated
WMO	World Meteorological Organisation
ZAMG	Zentralanstalt für Meteorologie und Geodynamik (Central Institute for Meteorology and Geodynamics)

Bibliography

Allan, S. S., S. Gaddy, and J. Evans, Delay causality and reduction at the New York city airports using terminal weather information systems, Massachusetts Institute of Technology, Lincoln Laboratory, 2001, Project Report ATC-291.

Andre, P., C. Silva, E. Balocco, J. Boreux, V. Cavallo, M. Colomb, J. Dore, J. Dufour, J. Hannay, K. Hirech, N. Kelly, P. Lacôtte, and L. Mealares, The main results of a European research project:"Improvement of transport safety by control of fog production in a chamber" ("FOG"), in *Third International Conference on Fog, Fog Collection and Dew*, C60, 2004.

Arakawa, A., Computational design for long term numerical integration of the equations of fluid motion: 1. Two-dimensional incompressible flow, *Journal of Computational Physics*, 1, 119–143, 1966.

Ballard, S., B. Golding, and R. Smith, Mesoscale Model Experimental Forecasts of the Haar of Northeast Scotland, *Monthly Weather Review*, 119, 2107–2123, 1991.

Bergeron, T., On the physics of cloud and precipitation, in 5th *Assembly of U.G.G.I Paul Dupont, Paris*, pages 156–178, 1935.

Bergot, T. and D. Guedalia, Numerical Forecasting of Radiation Fog. Part I: Numerical Model and Sensitivity Tests, *Monthly Weather Review*, 122, 1218–1230, 1994.

Berry, E. and M. Pranger, Equations for calculating the terminal velocities of water drops, *Journal of Applied Meteorology*, 13, 108–113, 1974.

Blackadar, A., The Vertical distribution of wind and turbulent exchange in a neutral atmosphere, *Journal of Geophysical Research*, 67, 3095–3102, 1962.

Bott, A., A Positive Definite Advection Scheme Obtained by Nonlinear Renormalization of the Advective Fluxes, *Monthly Weather Review*, 117, 1006–1015, 1989.

Bott, A., On the influence of the physico-chemical properties of aerosols on the life cycle of radiation fogs, *Boundary Layer Meteorology*, 56, 1–31, 1991.

Bott, A., *Theoretical and Numerical Investigations on the Physico-Chemical Microstructure of Radiation Fogs*, Institut für Physik der Atmosphäre, Johannes Gutenberg-Universität Mainz, 1992, Habilitationsschrift.

Bott, A., U. Siewers, and W. Zdunkowski, A Radiation Fog Model with a Detailed Treatment of the Interaction between Radiative Transfer and Fog Microphysics, *Journal of Atmospheric Sciences*, 47, 2153–2166, 1990.

Bott, A. and T. Trautmann, PAFOG-a new efficient forecast model of radiation fog and low-level stratiform clouds, *Atmospheric Research*, 64, 191–203, 2002.

Bremnes, J. and S. Michaelides, Probabilistic forecasting of visibility using neural networks, *Pure and Applied Geophysics*, 2007, in press.

Brooks, H. E. and A. I. Doswell, A comparison of measures-oriented and distributions-oriented approaches to forecast verification, *Weather and Forecasting*, 11, 288–303, 1996.

Brown, R., A numerical study of radiation fog with an explicit formulation of the microphysics, *Quarterly Journal of the Royal Meteorological Society*, 106, 781–802, 1980.

Brown, R. and W. Roach, The physics of radiation fog: Part II - a numerical study, *Quarterly Journal of the Royal Meteorological Society*, 102, 335–354, 1976.

Businger, J., J. Wyngaard, Y. Izumi, and E. Bradley, Flux profile relationships in the atmospheric surface layer, *Journal of Atmospheric Sciences*, 28, 181–189, 1971.

Cermak, J., *SOFOS - A New Satellite-based Operational Fog Observation Scheme*, Ph.D. thesis, Philipps-Universität Marburg, 2006.

Cermak, J. and J. Bendix, A novel approach to fog/low stratuc detection using Meteosat 8 data, *Atmospheric Research*, 87, 279–292, 2008.

Cermak, J., M. Schneebeli, D. Nowak, L. Vuilleumier, and J. Bendix, Characterization of low clouds with satellite and ground-based remote sensing systems, *Meteorologische Zeitschrift*, 15, 65–72, 2006.

Chapelon, J. and F. Loones, Analysis of road traffic injury accidents occurring at night and/or in foggy conditions, in *Vehicle and Infrastructure Safety improvement in Adverse conditions and night driving*, 2001.

Chaumerliac, N., E. Richard, J.-P. Pinty, and E. Nickerson, Sulfur Scavenging in a Mesoscale Model With Quasi-Spectral Microphysics: Two-Dimensional Results for Continental and Maritime Clouds, *Journal of Geophysical Research*, 92, 3114–3126, 1987.

Chen, F. and J. Dudhia, Coupling an advanced land-surface/hydrology model with the Penn state/NCAR MM5 modeling system. Part I: Model description and implementation, *Monthly Weather Review*, 129, 569–585, 2001.

Clark, P. and W. Hopwood, One-dimensional site specific forecasting of radiation fog. Part 1: Model formulation and idealized sensitivity studies, *Meteorological Applications*, 8, 279–286, 2001.

Colomb, M., I. Gultepe, and P. Morange, A comparison of visibility parameterization using surface observations, in *Reprint of the fourth International Conference of Fog, Fog collection and Dew*, pages 17–20, La Serena, Chile, 2007.

Costa, S., F. Carvalho, R. Amorin, A. Campos, J. Ribeiro, V. Cavalho, and D. D. Santos, Fog forecast for the international airport of Maceió, Brazil using artificial neural network, in *Proc. 8th ICSHMO*, pages 1741–1750, Foz do Iguacu, Brazil, 2006.

Courtier, P. and J. F. Geleyn, A global numerical weather prediction model with variable resolution: Application to the shallow water equations, *Quarterly Journal of the Royal Meteorological Society*, 114, 1321–1346, 1988.

Crank, J. and P. Nicolson, A practical method for numerical evaluation of solutions of partial differential equations of the heat-conduction type, in *Proceedings of the Cambridge philosophical society*, volume 43, pages 50–67, 1947.

Cullen, M., The Unified Forecast/Climate model, *Meteorological Magazine*, 122, 81–94, 1993.

Cuxart, J., P. Bourgeault, and J. Redelsperger, A turbulence scheme allowing for mesoscale and large eddy simulations, *Quarterly Journal of the Royal Meteorological Society*, 126, 1–30, 2000.

Davies, H., A lateral boundary formulation for multilevel prediction models, *Quarterly Journal of the Royal Meteorological Society*, 102, 405–418, 1976.

Dingman, S. L., *Physical Hydrology*, Prentice Hall, Second edition, 2002.

Doms, G., J. Förstner, E. Heise, H.-J. Herzog, M. Raschendorfer, R. Schrodin, T. Reinhardt, and G. Vogel, A Description of the Nonhydrostatic Regional Model LM. Part II: Physical Parameterization., Technical report, German Weather Service, Research Department, P.O. 100465, 63004 Offenbach, Germany, 2005, available at http://www.cosmo-model.org.

Doms, G. and U. Schättler, A description of the Nonhydrostatic Regional Model LM. Part I: Scientific documentation., Technical report, German Weather Service, Research Department, P.O. 100465, 63004 Offenbach, Germany, 2002, available at http://www.cosmo-model.org.

Donaldson, R., R. Dyer, and M. Kraus, An objective evaluator of techniques for predicting severe weather events, in *Preprints, 9th Conference on severe local storms*, edited by A. M. Society, pages 321–326, Norman, Oklahoma, 1975.

Doswell, C. A. I., R. Davies-Jones, and D. L. Keller, On summary measures of skill in rare event forecasting based on contingency tables, *Weather and Forecasting*, 5, 576–585, 1990.

Dudhia, J., A nonhydrostatic version of the Penn State / NCAR mesoscale model: Validation tests and simulation of an Atlantic cyclone and cold front, *Monthly Weather Review*, 121, 1493–1513, 1993.

Duynkerke, P., Radiation Fog: A Comparison of Model Simulation with Detailed Observations, *Monthly Weather Review*, 119, 324–341, 1991.

Duynkerke, P., Turbulence, Radiation and Fog in Dutch Stable Boundary Layers, *Boundary Layer Meteorology*, 90, 447–477, 1999.

Fels, S. and M. Schwarzkopf, The simplified exchange approximation: a new method for radiative tranfer calculations, *Journal of Atmospheric Sciences*, 32, 1475–1488, 1975.

Ferrier, B., A new grid-scale cloud and precipitation scheme in the NCEP Eta model, in *Spring Colloquium on the Physics of Weather and Climate: Regional weather prediction modeling and predictability*, Trieste, Italy, 2002.

Finley, J., Tornado predictions, *American Meteorological Journal*, 1, 85–88, 1884.

Fischer, R., The use of Multiple Measurements in Taxonomic Problems, *Annals of Eugenics*, 7, 179–188, 1936.

Fisher, C., The variational computations inside ARPEGE/ALADIN: CY25T1., Technical report, Meteo France, CNRM/GMAP, 2002, Available from authors on request.

Fisher, E. and P. Caplan, An Experiment in Numerical Prediction of Fog and Stratus, *Journal of Atmospheric Sciences*, 20, 425–437, 1963.

Fitzjarrald, D. R. and G. G. Lala, Hudson Valley Fog Environments, *Journal of Applied Meteorology*, 28, 1303–1328, 1989.

Fletcher, N., *The Physics of Rainclouds*, Cambridge University Press, 1962.

Flossmann, A. I., W. Hall, and H. Pruppacher, A Theoretical Study of the Wet Removal of Atmospheric Pollutants. Part I: The Redistribution of Aerosol Particles Captured through Nucleation and Impaction Scavenging by Growing Cloud Drops., *Journal of Atmospheric Sciences*, 42, 583–606, 1985.

Geleyn, J. and A. Hollingsworth, An Economical Analytical Method for the Computation of the Interaction Between Scattering and Line Absorption of Radiation, *Contribution to Atmospheric Physics*, 52, 1–16, 1979.

Georgii, W., Die Ursachen der Nebelbildung, *Annalen der Hydrographie und Maritime Meteorologie*, 48, 207–222, 1920.

Gilbert, G., Finley's tornado predictions, *American Meteorological Journal*, 1, 166–172, 1884.

Glahn, H. and D. Lowry, The use of model output statistic (MOS) in objective weather forecasting, *Journal of Applied Meteorology*, 11, 1203–1211, 1972.

Golding, B., A study of the Influence of Terrain on Fog Development, *Monthly Weather Review*, 121, 2529–2541, 1993.

Golding, B., Review of state of the art of prediction methods for fog and low clouds, *COST-722 report-Phase 1*, 2002.

Guedalia, D. and T. Bergot, Numerical Forecasting of Radiation Fog. Part II: A Comparison of Model Simulations with Several Observed Fog Events, *Monthly Weather Review*, 122, 1231–1246, 1994.

Gultepe, I., J. Milbrandt, and S. Belair, Visibility parameterization from microphysical observations for warm fog conditions and its application to Canadian MC2 mode, in *AMS meeting*, Atlanta, USA, American Meteorological Society, 2006a.

Gultepe, I., M. Müller, and Z. Boybeyi, A new visibility parameterization for warm fog applications in numerical weather prediction models, *Journal of Applied Meteorology*, 45, 1469–1480, 2006b.

Gunn, K. and J. Marshall, The distribution with size aggregate snowflakes, *Journal of Atmospheric Sciences*, 15, 452–461, 1958.

Hess, R., Assimilation of screen-level observations by variational soil moisture analysis, *Meteorology and Atmospheric Physics*, 77, 145–154, 2001.

Hilliker, J. and J. Fritsch, An observation-based statistical system for warm season hourly probabilistic forecast of low ceiling at the San Francisco International airport, *Journal of Applied Meteorology*, 38, 1692–1705, 1999.

Hobbs, P. and A. Rangno, Ice particle concentrations in clouds, *Journal of Atmospheric Sciences*, 42, 2523–2549, 1985.

Jacobs, W., V. Nietosvaara, S. Michaelides, and H. Gmoser, Short Range forecasting methods of fog, visibility and low clouds-COST action 722 phase I report, European scientific foundation, 2005.

Jacobsen, I. and E. Heise, A new economic method for the computation of the surface temperature in numerical models, *Contribution to Atmospheric Physics*, 55, 128–141, 1982.

Janjic, Z., The step-mountain coordinate: physical package, *Monthly Weather Review*, 118, 1429–1443, 1990.

Janjic, Z., The Mellor-Yamada level 2.5 scheme in the NCEP Eta model, in *11th Conference on numerical weather prediction*, pages 333–334, Norfolk, VA, American Meteorological Society, 1996.

Janjic, Z., Nonsingular implementation of the Mellor-Yamada level 2.5 scheme in the NCEP Meso model, Technical Report 437, NCEP Office, 2002, 61pp.

Johnson, J., *Physical Meteorology*, MIT Press, 1954, Cambridge, Massachusetts, USA, 393p.

Kessler, E., *On the Distribution and Continuity of water substance in the atmospheric circulations*, American Meteorological Society, Boston, 1969, Volume 32 of Meteorological Monographs, 10.

Klein, W., B. Lewis, and I. Enger, Objective prediction of five-day mean temperatures during winter, *Journal of Atmospheric Sciences*, 16, 672–682, 1959.

Klemp, J. B. and R. B. Wilhelmson, The simulation of three-dimensional convective storm dynamics, *Journal of Atmospheric Sciences*, 35, 1070–1096, 1978.

Kloesel, K., A 70-year history of marine stratocumulus cloud field experiments off the coast of California, *Bulletin of the American Meteorological Society*, 73, 1581–1585, 1992.

Köhler, H., The nucleus in and the growth of hygroscopic droplets, *Transaction of the Faraday Society*, 32, 1152–1161, 1936.

Köppen, W., Landnebel und seenebel, Part I, *Annalen der Hydrographie und Maritime Meteorologie*, 44, 233–257, 1916.

Köppen, W., Landnebel und seenebel, Part II, *Annalen der Hydrographie und Maritime Meteorologie*, 45, 401–405, 1917.

Koracin, D., J. Lewis, W. Thompson, C. Dorman, and J. Businger, Transition of Stratus into Fog along the California Coast: Observations and Modelling, *Journal of Atmospheric Sciences*, 58, 1714–1731, 2001.

Koschmieder, H., Theorie der horizontalen Sichtweite, *Beiträge zur Physik der freien Atmosphäre*, 12, 33–35, 1924.

Kunkel, B., Parameterization of Droplet terminal velocity and Extinction Coefficient in Fog Models, *Journal of Applied Meteorology*, 23, 24–41, 1984.

Lacis, A. and J. Hansen, A parameterization for the absorption of solar radiation in the earth's atmosphere, *Journal of Atmospheric Sciences*, 31, 118–133, 1974.

Lala, G., E. Mandel, and J. Juisto, A Numerical Investigation of Radiation Fog Variables, *Journal of Atmospheric Sciences*, 32, 720–728, 1975.

Leigh, R., Economic benefits of terminal aerodrome forecasts (TAFs) for Sydney airport, Australia, *Meteorological Applications*, 2, 239–247, 1995.

Leipper, D., Fog on the US west coast: A review, *Bulletin of the American Meteorological Society*, 75, 229–240, 1994.

Leporini, M., *Développement et évaluation d'un modèle tridimensionnel de nuage chaud à microphysique détaillée*, Ph.D. thesis, University Blaise Pascal, Clermont-Ferrand, France, 2005.

Lopez, P., Implementation and validation of a new prognostic large-scale cloud and precipitation scheme for climate and data assimilation purposes, *qjrms*, 128, 229–257, 2002.

Louis, J.-F., A parametric model of vertical eddy fluxes in the atmosphere, *Boundary Layer Meteorology*, 17, 187–202, 1979.

Marschall, J. and W. Palmer, The distribution of raindrops with size, *Journal of Meteorology*, 5, 165–166, 1948.

Marzban, C., Scalar measures of performance in rare-event situations, *Weather and Forecasting*, 13, 753–763, 1998.

Marzban, C., The ROC curve and the area under it as performance measure, *Weather and Forecasting*, 19, 1106–1114, 2004.

Masbou, M., A. Bott, H. Petithomme, C. Petersen, N. Nielsen, H. Seidl, A. Kann, M. Müller, J. Cermak, and W. Adam, COST 722 Model Intercomparison on Lindenberg area, *COST-722 Final Report*, 2007.

Mason, I., Decision-theoretic evaluation of probabilistic predictions, in *WMO Symposium on Probabilistic and Statistical Methods in Weather Forecasting*, pages 219–228, Nice, France, 1980.

Mason, I., A model for assessment of weather forecasts, *Australian Meteorological Magazine*, 30, 291–303, 1982.

Mason, I., Dependence of the critical success index on sample climate and threshold probability, *Australian Meteorological Magazine*, 37, 75–81, 1989.

Mellor, G. and T. Yamada, Development of a Turbulence Closure Model for Geophysical Fluid Problems, *Review of Geophysics and Space Physics*, 20, 851–875, 1982.

Meyers, M., P. Demott, and W. Cotton, New primary ice-nucleation parameterizations in an explicit cloud model, *Journal of Applied Meteorology*, 31, 708–721, 1992.

Miles, N., J. Verlinde, and E. Clothiaux, Cloud Droplet Size Distributions in Low-Level Stratiform Clouds, *Journal of Atmospheric Sciences*, 57, 295–311, 2000.

Monin, A. and A. Obukhov, Basic Regularity in Turbulent Mixing in the Surface Layer of the Atmosphere, *Akad. Nauk. S.S.S.R. Trud. Geofiz. Inst.*, 24, 163–187, 1954.

Mouskos, M., Transferability of a statistical diagnostic model for fog and low visibility from Denmark to Cyprus, *COST-722 Final Report*, 2007.

Müller, M., *Numerical Simulation of fog and radiation in complex terrain*, Ph.D. thesis, University of Basel, 2006.

Murphy, A. H., What is a good forecast ? An essay on the nature of goodness in weather forecasting, *Weather and Forecasting*, 8, 281–293, 1993.

Musson-Genon, L., Numerical simulation of a fog event with a one-dimensional boundary layer model, *Monthly Weather Review*, 115, 592–607, 1987.

Nickerson, E., E.Richard, R. Rosset, and D. Smith, The Numerical Simulation of Clouds, Rain, and Airflow over the Vosges and Black Forest Mountains: A Meso- β Model with Parameterized Microphysics, *Monthly Weather Review*, 114, 398–414, 1986.

NOAA, Geostationary Operational Environmental Satellite System (GEOS) GEOS-R Souder and Imager Cost/benefit Analysis (CBA), National Environmental Satellite, Data, and Information service (NESDIS), 2002, Prepared for the Departement of Commerce by National Oceanic and Atmospheric Administration.

Noilhan, J. and S. Planton, A simple parameterization of land surface processes for meteorological models, *Monthly Weather Review*, 117, 536–549, 1989.

Olsson, E., S. Gollvik, and L. Unnerstad, Development of a one-dimensional version at SMHI, *COST-722 Final Report*, 2007.

Pagowski, M., I. Gultepe, and P. King, Analysis and modeling of and extremely dense fog event in southern ontario, *Journal of Applied Meteorology*, 43, 3–16, 2004.

Pasini, A., V. Pelino, and S. Potestà, A neural network model for visibility nowcasting from surface observations: Results and sensitivity to physical input variables, *Journal of Geophysical Research*, 106, 14951–14959, 2001.

Petersen, C. and N. Nielsen, Diagnosis of visibility in DMI-HIRLAM, scientific report 00-11, DMI, 2000, available at http://www.dmi.dk/dmi/sr00-11.pdf.

Petithomme, H., Determine how to evaluate the potential of the existing methods, *COST-722 Final Report*, 2007.

Pruppacher, H. and J. Klett, *Microphysics of Clouds and Precipitation*, Kluwer Pub. Inc, Boston, 1997.

Pruppacher, H. and R. Rasmussen, A wind tunnel investigation of the rate of evaporation of large water drops falling at terminal velocity in air, *Journal of Atmospheric Sciences*, 36, 1255–1260, 1979.

Rijtema, P., Soil moisture forecasting, Technical report, Instituut voor Cultuurtechniek en Waterhuishouding, Wageningen, 1969, Nota 13.

Ritter, B. and J. Geleyn, A Comprehensive Radiation Scheme for Numerical Weather Prediction Models with Potential Applications in Climate Simulations, *Monthly Weather Review*, 120, 303–325, 1992.

Roach, W., Back to basics: Fog: Part 1 - Definitions and basics physics, *Weather*, 49, 411–415, 1994.

Roach, W., Back to basics: Fog: Part 2 - The formation and dissipation of land fog, *Weather*, 50, 7–11, 1995.

Roach, W., R. Brown, S. Caughey, J. Garland, and C. Readings, The physics of radiation fog: I - a field study, *Quarterly Journal of the Royal Meteorological Society*, 102, 313–333, 1976.

Sakakibara, H., A Scheme for Stable Numerical Computation of the Condensation Process with a Large Time Step, *Journal of the Meteorological Society of Japan*, 57, 349–353, 1979.

Sass, B., Reduction of numerical noise connected to the parameterization of cloud and condensation processes in the HIRLAM model, *HIRLAM Newsletter*, pages 37–45, 1997.

Savijäri, H., Fast radiation parameterization scheme for mesoscale and short-range forecast models, *Journal of Applied Meteorology*, 29, 437–447, 1990.

Schaefer, J., The critical success index as an indicator of forecast skill, *Weather and Forecasting*, 5, 570–575, 1990.

Schemenauer, R. and P. Cereceda, A proposed standard fog collector for use in high-elevation regions, *Journal of Applied Meteorology*, 33, 1313–1322, 1994.

Schraff, C., Mesoscale data assimilation and prediction of low stratus in the Alpine region, *Meteorology and Atmospheric Physics*, 64, 21–50, 1997.

Schraff, C. and R. Hess, A description of the Nonhydrostatic Regional Model LM. Part III: Data Assimilation, Technical report, German Weather Service, Research Department, P.O. 100465, 63004 Offenbach, Germany, 2003.

Schrodin, R. and E. Heise, The Multi-Layer Version of the WD Soil Model TERRA-LM, Technical report, Consortium for Small-Scale Modelling (COSMO), 2001, available at http://www.cosmo-model.org.

Schwarzkopf, M. and S. Fels, The simplified exchange method revisited-An accurate, rapid method for computation of infrared cooling rates and fluxes, *Journal of Geophysical Research*, 96(D5), 9075–9096, 1991.

Seidl, H. and A. Kann, New approaches to stratus diagnosis in Aladin, *ALADIN Newsletter*, 2002.

Seidl, H., A. Kann, and T. Haiden, Low stratus and fog forecast for central Europe introducing an empirical enhancement scheme for sub-inversion cloudiness, *COST-722 Final Report*, 2007.

Shettle, E. and R. Fenn, Models for the aerosols of the lower atmosphere and the effects of humidity variations on their optical properties, Environmental research papers No.676, Air Force Geophysics Laboratory, Massachusetts, USA, 1979.

Siebert, J., A. Bott, and W. Zdunkowski, Influence of a vegetation-soil model on the simulation of radiation fog, *Beiträge zur Physik der Atmosphäre*, 65, 93–106, 1992a.

Siebert, J., U. Sievers, and W. Zdunkowski, A One-Dimensional Simulation of the Interaction between Land Surface Processes and the Atmosphere, *Boundary Layer Meteorology*, 59, 1–34, 1992b.

Squires, P., The spatial variation of liquid water and droplet concentration in cumuli, *Tellus*, 10, 256–262, 1958.

Stephenson, D. B., Use of "odds ratio" for diagnosing forecast skill, *Weather and Forecasting*, 15, 221–232, 2000.

Steppeler, J., G. Doms, U. Schättler, H. Bitzer, A. Gassmann, U. Damrath, and G. Gregoric, Meso-gamma scale forecasts using the nonhydrostatic model LM, *Meteorology and Atmospheric Physics*, 82, 75–96, 2003.

Sundqvist, H., *Parameterization of condensation and associated clouds in models for weather prediction and general circulation simulation. Physically based Modelling and Simulation of Climate and Climate Change.*, volume 1, pages 433–461, M.E. Schlesinger. Ed. Kluwer Academic, 1988.

Sundqvist, H., Inclusion of Ice Phase of Hydrometeor in cloud parameterization for Mesoscale and Largescale Models, *Contribution to Atmospheric Physics*, 66, 137–147, 1993.

Sundqvist, H., E. Berge, and J. Kristjánsson, Condensation and cloud parameterization studies with a Mesoscale Numerical Weather Prediction Model, *Monthly Weather Review*, 117, 1641–1657, 1989.

Swets, J., Indices of discrimination or diagnostic accuracy: their ROCs and implied models, *Psychological Bulletin*, 99, 100–117, 1986.

Taylor, G., The formation of fog and mist, *Quarterly Journal of the Royal Meteorological Society*, 43, 241–268, 1917.

Texeira, J., Simulation of fog with the ECMWF prognostic cloud scheme, *Quarterly Journal of the Royal Meteorological Society*, 125, 529–552, 1999.

Texeira, J. and P. Miranda, Fog prediction at Lisbon airport using a one dimensional boundary layer model, *Meteorological Applications*, 8, 497–505, 2001.

Thomas, S., C. Girard, G. Doms, and U. Schättler, Semi-implicit scheme for the DWD Lokal-Modell, *Meteorology and Atmospheric Physics*, 73, 105–125, 2000.

Thornes, J. E. and D. B. Stephenson, How to judge the quality and value of weather forecast products, *Meteorological Applications*, 8, 307–314, 2001.

Tiedtke, M., A comprehensive mass flux scheme for cumulus parameterization in large-scale models, *Monthly Weather Review*, 117, 1779–1799, 1989.

Turton, J. and R. Brown, A comparison of a numerical model of radiation fog with detailed observations, *Quarterly Journal of the Royal Meteorological Society*, 113, 37–54, 1987.

Twomey, S., The nuclei of natural cloud formation. part II: The supersaturation in natural clouds and the variation of cloud droplet concentration, *Pure and Applied Geophysics*, 43, 243–249, 1959.

Unden, P., L. Rontu, H. Järvinen, P. Lynch, J. Calvo, G. Cats, J. Cuxart, K. Eerola, C. Fortelius, J. Garcia-Moya, C. Jones, G. Lenderlink, A. McDonald, R. McGrath, B. Navascues, N. Nielsen, V. Odegaard, E. Rodriguez, M. Rummukainen, R. Room, K. Sattler, B. Sass, H. Savijärvi, B. Schreur, R. Sigg, H. The, and A. Tijm, HIRLAM-5 Scientific documentation, Technical report, HIRLAM Programme, 2002, available on http://hirlam.org.

Vislocky, R. and J. Fritsch, Improved Model Output Statistics Forecasts through Model Consensus, *Bulletin of the American Meteorological Society*, 76, 1157–1164, 1995.

von Glasow, R. and A. Bott, Interaction of radiation fog with tall vegetation, *Atmospheric Environment*, 33, 1333–1346, 1999.

Wang, Y., T. Haiden, and A. Kann, The operational limited area modelling system at ZAMG: ALADIN-AUSTRIA, *Contribution to Meteorology and Geophysics*, 37, 2006.

Wantuch, F., Visibility and fog forecasting based on decision tree method, *IDOJARAS*, 105, 29–38, 2001.

Wicker, L. and W. Skamarock, A time-splitting scheme for the elastic equations incorporating second-order Runge-Kutta time differencing, *Monthly Weather Review*, 126, 1992–1999, 1998.

Willett, H., Fog and haze, their causes, distribution, and forecasting, *Monthly Weather Review*, 56, 435–468, 1928.

Wilson, L. J. and W. R. Burrows, Spatial verification using the relative operating characteristic curve, in *Proceedings of the 17th Conference on probability and statistics in the atmospheric sciences*, number 2.8.1-2.8.6, Seattle, Washington, USA, American Meteorological Society, 2004.

WMO, International Meteorological Vocabulary, *World Meteorological Organization*, 182, 1992, Geneva, Switzerland, 2nd edn.

WMO, Guide to meteorological instruments and methods of observation, *World Meteorological Organization*, 8, 1996, Geneva, Switzerland, 6th edn.

Zdunkowski, W. and A. Barr, A radiative-conductive model for the prediction of radiation fog , *Boundary Layer Meteorology*, 3, 152–177, 1972.

Zdunkowski, W. and B. Nielsen, A preliminary prediction analysis of radiation fog, *Pure and Applied Geophysics*, 75, 278–299, 1969.

Zhang, H. and T. Casey, Verification of categorical probability forecasts, *Weather and Forecasting*, 15, 80–89, 2000.

LM-PAFOG: ein neues dreidimensionales Nebelvorhersagemodell mit parametrisierter Mikrophysik

Nebel und tief hängende Wolken beeinträchtigen häufig den Luft- und Straßenverkehr; schwere Unfälle sind immer wieder die Folge. Vor diesem Hintergrund leistet eine verbesserte Nebelvorhersage, bezüglich der Lokalisierung von Nebelereignissen, der Vorhersage von der Nebeldauer sowie der Schwankungen der Sichtweite, einen immensen Beitrag zur Effizienz im Transportwesen. Nebel als ein kleinräumiges Phänomen wird durch advektiven Transport, turbulente Durchmischung an der Erdoberfläche, sowie mikrophysikalische Prozesse beeinflusst. Daher ist für eine realistische Nebelvorhersage eine detaillierte Beschreibung der mikrophysikalischen Prozesse unerlässlich. Eine verbesserte Beschreibung der mikrophysikalischen Prozesse wurde durch die Kopplung des eindimensionalen Nebelmodells PAFOG mit parametrisierter Nebelmikrophysik (*Bott and Trautmann*, 2002) mit dem mesoskaligen numerischen Wettervorhersagemodell des Deutschen Wetterdienstes (*Steppeler* et al., 2003), erreicht. Durch die Einführung einer neuen prognostischen Variable, die Wolkenkondensationskerne, werden die Sedimentationsprozesse sowie die Sichtweitenschwankungen besser beschrieben. Neben der erweiterten Mikrophysik zeichnet sich das Nebelmodell LM-PAFOG vor allem durch eine höhere horizontale Auflösung von 2.8 km und eine feine vertikale von 4 m aus, wodurch eine bessere Beschreibung der Grenzschichtprozesse erreicht wird. Mit Hilfe der im Rahmen der COST 722 durchgeführten Vergleichsstudie wurde LM-PAFOG evaluiert. Eine statistische Analyse sowie einige Fallstudien zeigen die Modellvariabilität zwischen Tag und Nacht. Auch der Vergleich mit anderen europäischen Nebelvorhersagemodellen zeigt die herausragende Bedeutung eines adaptiven Datenassimilationsschemas für hoch aufgelöste Modelle. Des weiteren hat die Kalibrierung der Sichtweitenparametrisierung einen groen Einfluss auf die Nebelvorhersage. Da es nur wenig Beobachtungen gibt, die die Nebelausbreitung beschreiben, wurde ein Verifikationsschema auf Grundlage von MSG-Satelliten für Nebel und tief hängenden Stratus (*Cermak and Bendix*, 2008) getested.

Schlagwörte: Nebel, Sichtweite, dreidimensionale Modellierung, parametrisierte Mikrophysik, Cost 722 Projekt, Modellvergleichsstudie, Sattelitenverifikation, LM-PAFOG

LM-PAFOG: a new three dimensional fog forecast model with parametrised microphysics

The presence of fog and low clouds in the lower atmosphere can have a critical impact on both airborne and ground transports and is often connected with serious accidents. An improvement of fog forecasts in terms of localisation, duration and variations in visibility therefore holds an immense operational value for the field of transportation in conditions of low visibility. However, fog is generally a small scale phenomenon which is mostly affected by local advective transport, turbulent mixing at the surface as well as its microphysical structure. Therefore, a detailed description of the microphysical processes within the three-dimensional dynamical core of the forecast model is necessary. For this purpose, a new microphysical parametrisation based on the one-dimensional fog forecast model, PAFOG (*Bott and Trautmann*, 2002), was implemented in the Lokal Modell (LM), the nonhydrostatic mesoscale model of the German Meteorological Service (*Steppeler* et al., 2003). The implementation of cloud water droplets as a new prognostic variable allows a detailed definition of the sedimentation processes and the variations in visibility. A horizontal resolution of 2.8 km and a vertical resolution of 4 m describe the boundary layer processes, forecasted by LM-PAFOG. In the framework of the COST 722 intercomparison campaign, the evaluation of the LM-PAFOG forecasts, based on statistical study and case studies, points out the variability of the model performance between day and night time periods. Moreover, the comparisons with other fog forecast systems highlight the decisive influence of an adapted data assimilation scheme for the high grid resolution model, as well as the necessary calibration of a visibility parametrisation. Finally, due to the lack of information concerning the observed fog spatial extension, a verification scheme with MSG satellite products for fog and low stratus (*Cermak and Bendix*, 2008) is tested.

Keywords: fog, visibility, three-dimensional modelling, parametrised microphysics, "Lokal Modell", PAFOG, COST 722 project, model intercomparison, satellite verification.

LM-PAFOG: un nouveau modèle tridimensionnel de prévision du brouillard à microphysique parametrée

La présence de brouillard et de nuages bas occasionne des perturbations des transports aériens et routiers et peut être à l'origine d'accidents graves. Une amélioration des prévisions de brouillard en termes de localisation, durée de l'épisode et des variations de visibilité serait un apport considérable pour la gestion des transports et la sécurité en condition de visibilité réduite. Cependant, le brouillard est en général un phénomène de petite échelle, influencé aussi bien par les transports advectifs locaux, les échanges turbulents à la surface ainsi que par sa structure microphysique. Une description détaillée des processus microphysiques dans une dynamique atmosphérique tridimensionnelle est essentielle. Une paramétrisation microphysique basée sur le modèle unidimensionnel de prévision du brouillard, PAFOG (*Bott and Trautmann*, 2002), a été introduite dans le modèle méso-échelle tridimensionnel non-hydrostatique, "Lokal Modell" (*Steppeler* et al., 2003). L'introduction de la concentration en goutte d'eau nuageuse comme nouvelle variable pronostique donne une description detaillée des processus de sédimentation et des variations de la visibilité. De plus, une résolution horizontale de 2.8 km et une résolution verticale de 4 m décrivent les processus de la couche limite simulés par LM-PAFOG. Dans le cadre de la campagne d'intercomparaison COST 722, l'évaluation des prévisions de LM-PAFOG, basée sur une étude statistique et des études de cas, montre la dispersion des performances du modèle entre les périodes de jour et de nuit. De plus, des comparaisons avec d'autres systèmes de prévision du brouillard pointent l'influence d'un schéma d'assimilation adapté pour un modèle ayant une haute résolution, ainsi que celle de la calibration nécessaire de la paramétrisation de la visibilité. Enfin, à cause d'un manque d'informations concernant l'extention spatial du brouillard observé, un schéma de verification utilisant des produits satellites (*Cermak and Bendix*, 2008) pour le brouillard et les stratus bas a été testé.

Mots clés: brouillard, visibilité, modélisation tridimensionnelle, microphysique paramétrée, "Lokal Modell", PAFOG, projet COST 722, inter-comparaison de modèles, vérification satellite.